

# Dynamic Response of Spar-type Offshore Floating Wind Turbines

---

**Roberts Proskovics**

A thesis presented in partial fulfilment of the  
requirements for the degree of Doctor of Philosophy

Centre for Doctoral Training in Wind Energy Systems

Department of Electronic and Electrical Engineering

University of Strathclyde

Glasgow G1 1XW

Scotland, UK

**June 2015**

This thesis is the result of the author's original research. It has been composed by the author and has not been previously submitted for examination which has led to the award of a degree.'

'The copyright of this thesis belongs to the author under the terms of the United Kingdom Copyright Acts as qualified by University of Strathclyde Regulation 3.50. Due acknowledgement must always be made of the use of any material contained in, or derived from, this thesis.

Dedicated to my parents.

### **Acknowledgements**

I would like to express my deepest gratitude to my supervisors Shan Huang, Sandy Day and Julian Feuchtwang. It would have been an immense task finishing my PhD without their guided support and expertise in the various areas that this thesis touched upon.

I would like to acknowledge The Centre for Doctoral Teaching in Wind Energy system and its staff, in particular, David Infield, Bill Leithead, Drew Smith, Olimpo Anaya-Lara and Nigel Barltrop for helping overcome various obstacles along this 4 year journey. A special thank you goes to Peter Davies and Lloyd's Register for sharing their knowledge and organising my industrial placement. Last but not least, Jason Jonkman from The National Renewable Energy Laboratory for always finding time to answer my questions.

# Table of Contents

<b>TABLE OF CONTENTS</b> .....	<b>V</b>
<b>LIST OF FIGURES</b> .....	<b>VIII</b>
<b>LIST OF TABLES</b> .....	<b>XII</b>
<b>ABSTRACT</b> .....	<b>XIV</b>
<b>ABBREVIATIONS</b> .....	<b>XVI</b>
<b>NOMENCLATURE</b> .....	<b>XVII</b>
<b>CHAPTER 1: INTRODUCTION</b> .....	<b>19</b>
1.1. OFFSHORE WIND RESOURCE .....	19
1.1.1. <i>Europe</i> .....	19
1.1.2. <i>The United States</i> .....	20
1.1.3. <i>Japan</i> .....	21
1.2. BATHYMETRY AND DISTANCE TO SHORE .....	22
1.3. SUPPORT STRUCTURE TYPES .....	27
1.4. FLOATING SUBSTRUCTURE CLASSIFICATION .....	28
1.4.1. <i>Ballast Stabilised</i> .....	29
1.4.2. <i>Buoyancy Stabilised</i> .....	29
1.4.3. <i>Mooring line stabilised</i> .....	30
1.5. MOORING SYSTEM AND ANCHORING .....	31
1.6. VERTICAL-AXIS FLOATING WIND TURBINES .....	32
1.6.1. <i>Vertiwind</i> .....	33
1.6.2. <i>DeepWind</i> .....	34
1.6.3. <i>Other concepts</i> .....	36
1.7. HORIZONTAL-AXIS FLOATING WIND TURBINES .....	37
1.7.1. <i>Hywind</i> .....	38
1.7.2. <i>Nautica</i> .....	38
1.7.3. <i>Sway</i> .....	39
1.7.4. <i>WindFloat</i> .....	40
1.7.5. <i>Fukushima Mirai</i> .....	41
1.7.6. <i>WindSea</i> .....	43
1.7.7. <i>Blue-H</i> .....	43
1.8. FLOATING OFFSHORE WIND TURBINE COMPARISON .....	44
1.9. COST OF FLOATING WIND TURBINES .....	46
1.10. OC3-HYWIND .....	49
1.11. THESIS OBJECTIVES .....	51
1.12. CO-ORDINATE SYSTEMS .....	55
<b>CHAPTER 2: ATTACHED FLOW</b> .....	<b>57</b>
2.1. REDUCED FREQUENCY .....	58
2.2. THEODORSEN'S THEORY .....	61
2.2.1. <i>Theodorsen's function</i> .....	62
2.2.2. <i>Plunging</i> .....	65
2.2.3. <i>Pitching</i> .....	70
2.3. WAGNER'S FUNCTION .....	74
2.4. VELOCITY PERTURBATION NORMAL TO BLADE .....	76
2.5. VAN DER WALL AND LEISHMAN .....	77
2.5.1. <i>Code validation</i> .....	79
2.5.2. <i>Downwash</i> .....	81
2.5.3. <i>Non-circulatory aerodynamics</i> .....	82

2.5.4. Axial induction factor.....	84
2.5.5. Lift versus drag .....	85
2.5.6. Thin aerofoil theory .....	87
2.5.7. Wake development.....	91
2.5.8. Simulations .....	92
2.5.8.1. Excitation.....	95
2.5.8.2. Initial Conditions .....	95
2.5.8.3. Flow Chart .....	96
2.5.9. Results .....	96
2.5.9.1. Surge .....	96
2.5.9.2. Sway .....	107
2.5.9.3. Heave .....	114
2.5.9.4. Roll .....	115
2.5.9.5. Pitch .....	118
2.5.9.6. Yaw.....	122
2.6. CONCLUSION.....	125
<b>CHAPTER 3: UNSTEADY FLOW .....</b>	<b>128</b>
3.1. FAST.....	129
3.1.1. Hydrodynamic loading.....	131
3.1.1.1. Wave particle kinematics .....	131
3.1.1.2. Morison's equation .....	132
3.1.2. Control of the OC3-Hywind.....	133
3.1.3. Shortcomings of FAST.....	133
3.1.3.1. Induced velocities.....	134
3.1.3.2. Hydrodynamics.....	134
3.1.3.3. Flow separation .....	135
3.1.3.4. Mooring system.....	139
3.1.3.5. Small-angle approximations.....	140
3.1.3.6. Disabling degrees-of-freedom of the spar.....	141
3.1.3.7. Vortex ring state.....	145
3.1.4. Sanity check .....	146
3.1.4.1. Natural frequencies.....	148
3.1.5. Damping .....	150
3.1.5.1. Aerodynamic damping .....	150
3.1.5.2. Damping in different degrees-of-freedom .....	155
3.2. FULLY-UNSTEADY AERODYNAMICS .....	156
3.2.1. Unsteady aerodynamic effects .....	158
3.2.2. Most detrimental degree-of-freedom .....	166
3.2.2.1. Surge and pitch.....	167
3.2.2.2. Below-rated.....	168
3.2.2.3. Example.....	172
3.2.3. Correlational approach.....	180
3.3. CONCLUSIONS .....	185
<b>CHAPTER 4: ALTERNATIVE SPAR DESIGNS .....</b>	<b>189</b>
4.1. EXCEL SPREAD SHEET.....	189
4.1.1. OC3-Hywind.....	192
4.1.2. Design parameters .....	195
4.1.2.1. Steel thickness.....	195
4.1.2.2. Inertia .....	196
4.1.2.3. Added inertia.....	198
4.1.2.4. Static heel angle .....	198
4.1.2.5. Roll and pitch natural period.....	199
4.1.2.6. Ballast.....	199
4.1.2.7. Spar dimensions .....	201
4.1.2.8. Metacentric height.....	201
4.2. PARAMETRIC STUDY.....	203

4.2.1. <i>Uniform spar</i> .....	204
4.2.1.1. Spar diameter.....	204
4.2.1.2. Spar length.....	205
4.2.2. <i>OC3-Hywind</i> .....	206
4.2.2.1. Draft.....	207
4.2.2.2. Ballast density.....	211
4.2.2.3. Steel thickness.....	213
4.2.2.4. Draft diameter.....	214
4.2.3. <i>Design limits</i> .....	217
4.2.4. <i>Trade-offs</i> .....	219
4.3. SPAR FOR MEDIUM-DEEP WATERS.....	226
4.3.1. <i>Natural frequencies</i> .....	229
4.3.1.1. Surge and sway.....	229
4.3.1.2. Heave.....	229
4.3.1.3. Roll and Pitch.....	230
4.3.1.4. Yaw.....	231
4.4. MATHIEU INSTABILITY.....	233
4.5. SPAR MODIFICATION.....	233
4.6. SECOND-ORDER HYDRODYNAMICS.....	235
4.7. STRAKES AND DAMPING PLATES.....	237
4.8. CONCLUSION.....	239
<b>CHAPTER 5: SUMMARY</b> .....	<b>242</b>
5.1. REVIEW OF CONCLUSIONS.....	242
5.2. RECOMMENDATIONS.....	247
5.3. FUTURE WORK.....	250
<b>REFERENCES</b> .....	<b>252</b>
<b>APPENDIX</b> .....	<b>260</b>
A1.1. UK ROUND 1, 2 AND 3 WIND FARMS.....	260
A1.2. COMPARISON OF DIFFERENT FLOATING HAWTS.....	262
A1.3. APPROXIMATIONS TO THEODORSEN'S FUNCTION.....	263
A1.4. VAN DER WALL AND LEISHMAN - DISCRETISATION.....	264
A1.5. 6 DSOF.....	268
A1.6. VAN DER WALL AND LEISHMAN - RESULTS.....	276
A1.7. CHANGES IN AXIAL FORCE.....	299
A1.8. NON-CIRCULATORY LIFT OF OSCILLATORY PITCHING.....	302
A1.9. EXCEL SPREADSHEET.....	303
A1.10. WAMIT RAOS.....	305
A1.11. MAXIMAL STRESS POINTS.....	309
A1.12. MOST DAMAGING DEGREE-OF-FREEDOM.....	316
A1.13. CORRELATIONAL APPROACH.....	320

# List of Figures

FIGURE 1 – WIND ATLAS OF EUROPE [4] .....	20
FIGURE 2 – THE U.S. OFFSHORE WIND RESOURCES AT 90 M ABOVE THE WATER SURFACE [8] .....	21
FIGURE 3 – OFFSHORE WIND RESOURCE MAP OF JAPAN [10] .....	22
FIGURE 4 – UK ROUND 1, 2 AND 3 WIND FARMS AND ZONES .....	24
FIGURE 5 – BATHYMETRY MAP OF EUROPE .....	25
FIGURE 6 – BATHYMETRY MAP OF THE U.S. [8] .....	26
FIGURE 7 – BATHYMETRY MAP OF JAPAN .....	26
FIGURE 8 – FIXED BOTTOM OFFSHORE FOUNDATION TYPES (MONOPILE, TRIPILE, JACKET AND GRAVITY BASE) [18] .....	28
FIGURE 9 – STATIC STABILITY TRIANGLE .....	29
FIGURE 10 – THREE MAIN PRINCIPLES OF ACHIEVING STATIC STABILITY FOR FLOATING WIND TURBINES [19] .....	30
FIGURE 11 – TYPES OF MOORING SYSTEMS AND THEIR FOOTPRINTS .....	31
FIGURE 12 – VERTIWIND CONCEPT .....	33
FIGURE 13 – DEEPWIND CONCEPT .....	35
FIGURE 14 – G WIND CONCEPT .....	37
FIGURE 15 – HYWIND (STATOIL) .....	38
FIGURE 16 – NAUTICA CONCEPT .....	39
FIGURE 17 – SWAY CONCEPT .....	40
FIGURE 18 – WINDFLOAT CONCEPT .....	41
FIGURE 19 – INSTALLATION OF FUKUSHIMA MIRAI .....	42
FIGURE 20 – FUKUSHIMA KIZUNA .....	42
FIGURE 21 – WINDSEA CONCEPT .....	43
FIGURE 22 – BLUE H .....	44
FIGURE 23 – CAPITAL COST BREAKDOWN FOR A TYPICAL ONSHORE AND OFFSHORE WIND FARM [38] .....	46
FIGURE 24 – CAPITAL EXPENDITURE FOR FIXED AND FLOATING OFFSHORE WIND [40] .....	47
FIGURE 25 – COSTS BREAKDOWN FOR 3 DIFFERENT FLOATING OFFSHORE WIND TURBINE MODELS [43] .....	48
FIGURE 26 – OC3-HYWIND TOWER NATURAL FREQUENCIES .....	49
FIGURE 27 – FLOWCHART OF THE THESIS .....	54
FIGURE 28 – DEGREES-OF-FREEDOM FOR SPAR-TYPE FOWT IN CHAPTER 2 [51] .....	55
FIGURE 29 – DEGREES-OF-FREEDOM FOR SPAR-TYPE FOWT IN CHAPTER 3 [51] .....	56
FIGURE 30 – UNSTEADINESS ASSOCIATED WITH THE NREL 5MW OFFSHORE BASELINE TURBINE .....	60
FIGURE 31 – MAGNITUDE AND PHASE OF THEODORSEN’S FUNCTION .....	63
FIGURE 32 – COMPARISON OF THEODORSEN’S AND R.T JONES’ APPROXIMATION FOR THE NREL 5MW ( $F = 0.2$ Hz) ..	63
FIGURE 33 – THEODORSEN’S FUNCTION .....	64
FIGURE 34 – UNSTEADY LIFT RESPONSE IN PLUNGE MOTION .....	66
FIGURE 35 – THRUST FORCE ON A BLADE IN OSCILLATORY PLUNGING .....	67
FIGURE 36 – TORQUE ON A BLADE IN OSCILLATORY PLUNGING .....	68
FIGURE 37 – COMPARISON BETWEEN THE QUASI-STEADY AND UNSTEADY RESPONSES IN PLUNGING .....	68
FIGURE 38 – REDUCED FREQUENCY DISTRIBUTION ALONG THE BLADE LENGTH .....	69
FIGURE 39 – UNSTEADY LIFT RESPONSE TO PITCH .....	70
FIGURE 40 – THRUST FORCE ON A BLADE IN OSCILLATORY PITCHING .....	71
FIGURE 41 – TORQUE ON A BLADE IN OSCILLATORY PITCH .....	72
FIGURE 42 – COMPARISON BETWEEN THE QUASI-STEADY AND UNSTEADY RESPONSES IN PITCHING .....	73
FIGURE 43 – COMPARISON OF WAGNER’S FUNCTION APPROXIMATIONS .....	75
FIGURE 44 – UNSTEADY OVER QUASI-STEADY LIFT RATIO FOR AN AEROFOIL AT A CONSTANT ANGLE-OF-ATTACK AND OSCILLATING FREE-STREAM VELOCITY .....	80
FIGURE 45 – EFFECTS OF THE FREE-STREAM VELOCITY FLUCTUATIONS ON THE UNSTEADY LIFT OF AN AEROFOIL AT A CONSTANT ANGLE-OF-ATTACK [56] .....	81

FIGURE 46 – NON-CIRCULATORY FORCES ON AN NREL 5MW TURBINE BLADE (SURGE $A=1$ M AND $T=5$ s).....	83
FIGURE 47 – AXIAL INDUCTION FACTOR DISTRIBUTION FOR THE NREL 5MW TURBINE.....	84
FIGURE 48 – FORCES ON AN AEROFOIL.....	85
FIGURE 49 – DRAG AND LIFT CONTRIBUTIONS TO THRUST FORCE ON A BLADE EXPERIENCING SINUSOIDAL SURGE MOTION OF $A = 1$ M, $T = 10$ s.....	86
FIGURE 50 – DRAG AND LIFT CONTRIBUTIONS TO IN-PLANE FORCE ON A BLADE EXPERIENCING SINUSOIDAL SURGE MOTION OF $A = 1$ M, $T = 10$ s.....	87
FIGURE 51 – DIFFERENT LIFT COEFFICIENT SLOPES.....	88
FIGURE 52 – DISTRIBUTION OF LIFT COEFFICIENT AT ZERO ANGLE-OF-ATTACK FOR THE NREL 5MW TURBINE.....	89
FIGURE 53 – COMPARISON BETWEEN DIFFERENT METHODS OF CALCULATING LIFT VALUES.....	90
FIGURE 54 – NORMAL LOADING ON A BLADE ON A SYSTEM THAT IS SURGING WITH 4 M AMPLITUDE AND 5 S PERIOD....	91
FIGURE 55 – SETTling OF INITIAL VALUES FOR FULLY-ATTACHED LOADING.....	94
FIGURE 56 – SIMPLIFIED FLOWCHART OF THE FULLY-ATTACHED AERODYNAMICS MATLAB CODE.....	96
FIGURE 57 – SURGE MOTION (SIDE VIEW).....	97
FIGURE 58 – VELOCITY COMPONENTS IN SURGE MOTION.....	97
FIGURE 59 – NORMAL FORCE ON AN NREL BLADE FOR 1 M AMPLITUDE AND 10 S PERIOD SURGE MOTION.....	99
FIGURE 60 – NORMAL FORCE ON A BLADE IN SURGE MOTION OF 1 M AMPLITUDE AND 5 S PERIOD.....	100
FIGURE 61 – MEAN OF NORMAL FORCE ON A BLADE IN SURGE (THIN AEROFOIL THEORY).....	101
FIGURE 62 – MEAN OF NORMAL FORCE ON A BLADE IN SURGE (LOOK-UP TABLES).....	103
FIGURE 63 – NORMAL FORCE ON A BLADE IN SURGE MOTION OF 5 M AND 5 S AMPLITUDE AND PERIOD.....	103
FIGURE 64 – STALLING EFFECT [1].....	104
FIGURE 65 – DIFFERENCE IN AMPLITUDE OF THRUST IN SURGE MOTION (THIN AEROFOIL THEORY).....	105
FIGURE 66 – DIFFERENCE IN AMPLITUDE OF THRUST IN SURGE MOTION (LOOK-UP TABLES).....	106
FIGURE 67 – AMPLITUDE OF OUT-OF-PLANE BENDING MOMENT IN SURGE MOTION (THIN AEROFOIL THEORY).....	107
FIGURE 68 – NORMAL FORCE ON A BLADE IN SWAY.....	108
FIGURE 69 – NORMAL FORCE ON A BLADE IN SWAY WITH 5 M AMPLITUDE AND 5 S PERIOD.....	109
FIGURE 70 – DIFFERENCE IN THE MEAN THRUST IN SWAY FOR DIFFERENT COMBINATIONS OF $A$ AND $T$ .....	109
FIGURE 71 – DIFFERENCE IN HALF-RANGE VALUES OF THRUST FOR SWAY MOTION COMBINATIONS.....	110
FIGURE 72 – DIFFERENCE IN HALF-RANGE VALUES IN OUT-OF-PLANE BENDING MOMENT IN SWAY DoF.....	111
FIGURE 73 – DIFFERENCE IN THE MEAN LOADING OF $F_T$ IN SWAY.....	112
FIGURE 74 – DIFFERENCE IN THE HALF-RANGE VALUES OF IN-PLANE BM IN SWAY.....	113
FIGURE 75 – IN-PLANE FORCE ON A BLADE IN SWAY OF 2 M AMPLITUDE AND 20 S PERIOD.....	113
FIGURE 76 – IN-PLANE BM FOR A BLADE IN SWAY OF 3 M AMPLITUDE AND 20 S PERIOD.....	114
FIGURE 77 – IN-PLANE FORCE ON A BLADE IN HEAVE OF 2 M AMPLITUDE AND 5 S PERIOD.....	114
FIGURE 78 – NORMAL FORCE ON A BLADE IN ROLL DoF OF 1 DEG. AMPLITUDE AND 10 S PERIOD.....	115
FIGURE 79 – DIFFERENCE IN HALF-RANGE VALUES OF THE NORMAL FORCE ON A BLADE IN ROLL (LOOK-UP TABLE).....	116
FIGURE 80 – OUT-OF-PLANE BM ON A BLADE IN 1 M AMPLITUDE AND 15 S PERIOD MOTION IN ROLL.....	116
FIGURE 81 – IN-PLANE FORCE ON A BLADE IN 5 DEG. AND 25 S ROLL MOTION.....	117
FIGURE 82 – IN-PLANE BM FOR 2 DEG. AND 10 S ROLL MOTION.....	117
FIGURE 83 – NORMAL FORCE ON A BLADE IN 1 DEG. AMPLITUDE AND 10 S PERIOD IN THE PITCH DoF.....	118
FIGURE 84 – DIFFERENCE IN THE NORMAL FORCE HALF-RANGE VALUES BETWEEN THE QUASI-STEADY AND UNSTEADY RESULTS (PITCH).....	119
FIGURE 85 – PLATEAUING OF LOOK-UP TABLE RESULTS IN THE PITCH DoF.....	120
FIGURE 86 – DIFFERENCE IN HALF-RANGE VALUES IN THE NORMAL FORCE ON A BLADE (PITCH).....	120
FIGURE 87 – DIFFERENCE IN THE MEAN NORMAL FORCE IN THE PITCH DoF (THIN AEROFOIL THEORY).....	121
FIGURE 88 – DIFFERENCE IN THE MEAN NORMAL FORCE IN PITCH DoF (LOOK-UP TABLE).....	121
FIGURE 89 – IN-PLANE FORCE ON A BLADE IN PITCH DoF.....	122
FIGURE 90 – NORMAL FORCE ON A BLADE IN YAW MOTION.....	123
FIGURE 91 – NORMAL FORCE ON A BLADE IN YAW.....	124
FIGURE 92 – FREQUENCY COMPONENT OF THE SIGNAL IN FIGURE 91.....	124
FIGURE 93 – THE OC3-HYWIND SPAR (IN WAMIT).....	130
FIGURE 94 – DIAMETER TO WAVELENGTH RATIO FOR THE OC3-HYWIND.....	136

FIGURE 95 – KEULEGAN-CARPENTER NUMBER FOR THE OC3-HYWIND .....	138
FIGURE 96 – REYNOLDS NUMBER DISTRIBUTION FOR THE OC3-HYWIND .....	138
FIGURE 97 – DISPLACEMENT IN ROLL WITH OTHER DSOF DISABLED.....	141
FIGURE 98 – ROLL DISPLACEMENT IN THE FREQUENCY-DOMAIN .....	142
FIGURE 99 – DISPLACEMENT IN ROLL WITH ALL DSOF ACTIVE .....	144
FIGURE 100 – ROLL DISPLACEMENT IN THE FREQUENCY-DOMAIN (ALL DSOF ACTIVE).....	144
FIGURE 101 – DEPICTION OF THE VORTEX RING STATE ON A HELICOPTER ROTOR.....	146
FIGURE 102 – HYDRODYNAMIC WAVE-EXCITATION PER UNIT AMPLITUDE FOR THE OC3-HYWIND (NO MOORING OR WT) .....	147
FIGURE 103 – HYDRODYNAMIC ADDED MASS AND DAMPING FOR THE OC3-HYWIND SPAR (NO MOORING OR WT) ...	147
FIGURE 104 – RADIATION IMPULSE-RESPONSE FUNCTIONS FOR THE OC3-HYWIND SPAR (NO MOORING OR WT).....	148
FIGURE 105 – FREE-DECAY TESTS FOR THE OC3-HYWIND SYSTEM.....	148
FIGURE 106 – DISPLACEMENTS IN 4 DIFFERENT DSOF FOR THE OC3-HYWIND.....	151
FIGURE 107 – DISPLACEMENT AND THRUST FORCE IN THE SURGE DOF .....	152
FIGURE 108 – LOGARITHMIC DECREMENT METHOD .....	152
FIGURE 109 – TOWER TOP DISPLACEMENT AND THE ASSOCIATED DAMPING RATIO.....	153
FIGURE 110 – FLOWCHART OF AERODYN.....	158
FIGURE 111 – SURGE DISPLACEMENT .....	160
FIGURE 112 – THRUST FORCE ON THE ROTOR .....	160
FIGURE 113 – TORQUE RESPONSE.....	161
FIGURE 114 – AMPLITUDE SPECTRUM FOR TORQUE RESPONSE .....	162
FIGURE 115 – TOWER BASE SS MOMENT .....	163
FIGURE 116 – FFT OF TOWER BASE SIDE-TO-SIDE MOMENT .....	164
FIGURE 117 – TOWER BASE FORE-AFT MOMENT .....	165
FIGURE 118 – FLAPWISE MOMENT RESPONSE.....	165
FIGURE 119 – FFT OF BLADE ROOT FLAPWISE MOMENT .....	166
FIGURE 120 – FLOW DIAGRAM OF APPROACH USED TO COMPARE THE PITCH AND SURGE DSOF .....	169
FIGURE 121 – WAVE-EXCITATION FORCE-VECTOR SCALED IN THE SURGE DOF.....	169
FIGURE 122 – SURGE AND PITCH RESPONSE (SCALED SURGE WAVE-EXCITATION FORCE-VECTOR) .....	170
FIGURE 123 – WAVE-EXCITATION FORCE-VECTOR SCALED IN THE PITCH DOF.....	171
FIGURE 124 – SURGE AND PITCH RESPONSE (SCALED PITCH WAVE-EXCITATION FORCE-VECTOR) .....	171
FIGURE 125 – SURGE AND PITCH DISPLACEMENT RESPONSE .....	173
FIGURE 126 – TOWER BASE FA MOMENT.....	174
FIGURE 127 – TOWER FA BENDING MOMENT AT 9.7 M FROM THE BASE .....	176
FIGURE 128 – BLADE ROOT FLAPWISE MOMENT .....	177
FIGURE 129 – AMPLITUDE SPECTRUM FOR BLADE ROOT FLAPWISE MOMENT .....	177
FIGURE 130 – BLADE FLAPWISE MOMENTS AT 2 DIFFERENCE LOCATIONS ALONG THE BLADE LENGTH .....	178
FIGURE 131 – THE OC3-HYWIND RESPONSE IN SURGE AND PITCH DSOF.....	181
FIGURE 132 – FLOWCHART OF EXCEL SPREADSHEET .....	191
FIGURE 133 – THE OC3-HYWIND HULL STRUCTURAL PROPERTIES [111] .....	196
FIGURE 134 – STATIC HEEL ANGLE, AND ROLL AND PITCH NATURAL PERIOD VARIATION WITH VARYING STEEL THICKNESS .....	196
FIGURE 135 – SECTIONS OF SPAR-TYPE FLOATING OFFSHORE WIND TURBINE’S HULL .....	197
FIGURE 136 – METACENTRIC RADIUS DISTRIBUTION FOR VARYING DRAFT OF THE OC3-HYWIND .....	203
FIGURE 137 – DIMENSIONS OF THE OC3-HYWIND SPAR IN METERS [46] .....	207
FIGURE 138 – INFLUENCE DIAGRAM OF SHORTENING THE DRAFT OF THE OC3-HYWIND .....	208
FIGURE 140 – METACENTRIC HEIGHT AND INERTIA ABOUT THE X- AND Y-AXIS FOR VARYING DRAFT .....	209
FIGURE 141 – STATIC HEEL ANGLE AND NATURAL PERIODS FOR VARYING DRAFT .....	210
FIGURE 142 – INFLUENCE DIAGRAM OF INCREASING BALLAST DENSITY.....	211
FIGURE 143 – METACENTRIC HEIGHT AND INERTIA VARIATION WITH BALLAST DENSITY .....	212
FIGURE 144 – STATIC HEEL ANGLE AND NATURAL PERIOD VARIATION WITH BALLAST DENSITY .....	212
FIGURE 145 – MASS VARIATION WITH VARYING STEEL THICKNESS.....	213

FIGURE 146 – METACENTRIC HEIGHT AND INERTIA VARIATION WITH VARYING STEEL THICKNESS .....	214
FIGURE 148 – MASS OF HULL CHANGE WITH INCREASING SPAR DIAMETER .....	215
FIGURE 149 – INFLUENCE DIAGRAM OF INCREASING SPAR DIAMETER .....	216
FIGURE 151 – STATIC HEEL ANGLE AND NATURAL PERIOD VARIATIONS FOR VARYING SPAR DIAMETER.....	217
FIGURE 152 – TRADE-OFF BETWEEN BALLAST DENSITY AND SPAR DIAMETER FOR 80 M DRAFT DESIGN .....	220
FIGURE 153 – TRADE-OFF BETWEEN BALLAST DENSITY AND NATURAL PERIOD IN ROLL AND PITCH DsoF FOR 80 M DRAFT DESIGN .....	221
FIGURE 154 – TRADE-OFF BETWEEN SPAR DIAMETER AND NATURAL PERIOD IN ROLL AND PITCH DoF FOR 80 M DRAFT DESIGN .....	222
FIGURE 155 – TRADE-OFF BETWEEN BALLAST DENSITY AND SPAR DIAMETER FOR 70 M DRAFT DESIGN .....	223
FIGURE 156 – TRADE-OFF BETWEEN BALLAST DENSITY AND ROLL AND PITCH NATURAL PERIOD FOR 70 M DRAFT DESIGN .....	223
FIGURE 157 – TRADE-OFF BETWEEN BALLAST DENSITY AND SPAR DIAMETER FOR 60 M DRAFT DESIGN .....	224
FIGURE 158 – TRADE-OFF BETWEEN BALLAST DENSITY, AND ROLL AND PITCH NATURAL PERIOD FOR 60 M DRAFT DESIGN .....	224
FIGURE 159 – TRADE-OFF BETWEEN BALLAST DENSITY AND SPAR DIAMETER FOR 50 M DRAFT DESIGN .....	225
FIGURE 160 – TRADE-OFF BETWEEN BALLAST DENSITY, AND ROLL AND PITCH NATURAL PERIOD FOR 50 M DRAFT DESIGN .....	225
FIGURE 161 – OC3-HYWIND AND SHORTENED SPAR PLATFORM DIMENSIONS.....	227
FIGURE 162 – MASS OF HULL AND BALLAST CHANGE WITH DRAFT .....	228
FIGURE 163 – DIAMETER AT THE KEEL, COG AND METACENTRIC HEIGHT VARIATION WITH DRAFT .....	229
FIGURE 164 – NATURAL PERIODS AND ROLL/PITCH INERTIA VARIATION WITH DRAFT .....	232
FIGURE 165 – STRATEGIES FOR REDUCING RESPONSE OF A SYSTEM.....	234
FIGURE 166 – DAMPED VIBRATION OF A SYSTEM .....	234
FIGURE 167 – DIAMETER TO WAVELENGTH RATIO FOR 50 M DRAFT SPAR .....	236
FIGURE 168 – HELICAL STRAKES ON A SPAR.....	237
FIGURE 169 – SWAY MOTION .....	268
FIGURE 170 – SWAY INFLUENCE ON THE IN-PLANE VELOCITY SEEN BY A BLADE ELEMENT .....	268
FIGURE 171 – HEAVE MOTION .....	269
FIGURE 172 – HEAVE INFLUENCE ON THE IN-PLANE VELOCITY SEEN BY BLADE ELEMENT.....	270
FIGURE 173 – ROLL MOTION .....	271
FIGURE 174 – PITCH DOF .....	272
FIGURE 175 – SIMPLIFIED PITCH DOF .....	273
FIGURE 176 – RAO FOR SURGE/SWAY.....	305
FIGURE 177 – RAO FOR HEAVE .....	306
FIGURE 178 – RAO FOR PITCH/ROLL .....	307
FIGURE 179 – RAO FOR YAW .....	308
FIGURE 180 – MAX. STRESS DISTRIBUTION ALONG THE TOWER’S LENGTH .....	310
FIGURE 181 – STRESS DISTRIBUTION ALONG THE BLADE’S SPAN.....	314
FIGURE 182 – MAXIMUM STRESS POINTS ALONG THE BLADE’S LENGTH .....	315
FIGURE 183 – SURGE AND PITCH RESPONSE IN RATED CONDITIONS AND MODIFIED WAVE-EXCITATION FORCE-VECTOR	316
FIGURE 184 – SURGE AND PITCH RESPONSE AT ABOVE RATED CONDITIONS FOR SCALED WAVE-EXCITATION FORCE-VECTOR .....	318

# List of Tables

TABLE 1 – SUPPORT STRUCTURE TYPES .....	27
TABLE 2 – TYPES OF ANCHORS .....	32
TABLE 3 – COMPARISON OF DEEPWIND AND HYWIND CONCEPTS [9] .....	36
TABLE 4 – FLOATING OFFSHORE HAWT DESIGN COMPARISON.....	45
TABLE 5 – HYWIND AND OC3-HYWIND CORE PARAMETERS .....	50
TABLE 6 – CLASSIFICATION OF FLOW UNSTEADINESS [5] .....	59
TABLE 7 – INITIAL CONDITIONS .....	95
TABLE 8 – DSOF OF FLOATING HAWT IN FAST .....	131
TABLE 9 – REGULAR WAVE DEFINITIONS [46] .....	135
TABLE 10 – NATURAL FREQUENCIES OF THE OC3-HYWIND PLATFORM .....	149
TABLE 11 – SIMILARITIES AND DIFFERENCES BETWEEN THE QUASI-STEADY AND UNSTEADY AERODYNAMIC SETTINGS IN FAST .....	157
TABLE 12 – SURGE AND PITCH DISPLACEMENT FOR TWO DIFFERENT WAVE-EXCITATION FORCE-VECTORS .....	172
TABLE 13 – BLADE DELS IN SURGE AND PITCH DSOF IN BELOW-RATED CONDITIONS .....	179
TABLE 14 – LOADS AND DELS FOR TOWER AND BLADE IN SURGE AND PITCH DSOF IN BELOW-RATED CONDITIONS.....	179
TABLE 15 – ENVIRONMENTAL CONDITIONS USED.....	180
TABLE 16 – CORRELATION MATRIX FOR TOWER LOADS FOR BELOW-RATED, ALIGNED WIND AND WAVES .....	182
TABLE 17 – CORRELATION MATRIX FOR TOWER LOADS FOR BELOW-RATED, MISALIGNED WIND AND WAVES .....	182
TABLE 18 – CORRELATION MATRIX FOR BLADE LOADS FOR BELOW-RATED, ALIGNED WIND AND WAVE.....	183
TABLE 19 – CORRELATIONS MATRIX FOR BLADE LOADS FOR BELOW-RATED, MISALIGNED WIND AND WAVES.....	184
TABLE 20 – THE OC3-HYWIND WIND TURBINE DATA.....	192
TABLE 21 – THE OC3-HYWIND SPAR DATA .....	193
TABLE 22 – THE OC3-HYWIND STATIC HEEL ANGLE, INERTIA AND NATURAL PERIODS .....	194
TABLE 23 – OLIVINE PRODUCTION BY COUNTRY IN THOUSAND METRIC TONS FOR YEAR 1995 AND 1999 .....	199
TABLE 24 – DIFFERENT TYPES OF OLIVINE AND SEAWATER SLURRIES .....	200
TABLE 25 – DIFFERENT TYPES OF HAEMATITE AND SEAWATER SLURRIES .....	201
TABLE 26 – THREE ALTERNATIVE DESIGNS OF THE OC3-HYWIND WITH A SHORTENED SPAR OBTAIN USING EXCEL SOLVER .....	226
TABLE 27 – UK ROUND 1 AND 2 WIND FARMS AND THE CORRESPONDING WATER DEPTHS AND DISTANCES TO SHORE ..	260
TABLE 28 – UK ROUND 3 WIND FARM ZONES AND THE CORRESPONDING WATER DEPTHS AND DISTANCES TO SHORE ..	261
TABLE 29 – FLOATING HAWT ASSESSMENT CRITERIA .....	262
TABLE 30 – APPROXIMATIONS TO GENERALISED THEODORSEN’S FUNCTION .....	263
TABLE 31 – VARIABLES USED IN CALCULATING MAXIMUM STRESS POINT ON A BLADE .....	313
TABLE 32 – MEAN DISPLACEMENTS IN SURGE AND PITCH DSOF FOR 3 DIFFERENT OPERATION STATES (ORIGINAL, PITCH X 0.25 (SCALED 1) AND SURGE X 1.35 (SCALED 2)) .....	317
TABLE 33 – SURGE AND PITCH RESPONSE RANGES FOR RATED SIMULATIONS .....	317
TABLE 34 – LOADS AND DELS FOR TOWER AND BLADE IN SURGE AND PITCH DsoF IN RATED CONDITIONS .....	317
TABLE 35 – SURGE AND PITCH RESPONSE RANGES FOR ABOVE-RATED SIMULATIONS .....	318
TABLE 36 – LOADS AND DELS FOR TOWER AND BLADE IN SURGE AND PITCH DsoF IN ABOVE-RATED CONDITIONS .....	319
TABLE 37 – CORRELATION MATRIX FOR TOWER LOADS WITH ALIGNED WIND AND WAVE INPUTS IN RATED CONDITIONS ..	320
TABLE 38 – CORRELATION MATRIX FOR BLADE LOADS WITH ALIGNED WIND AND WAVE INPUTS IN RATED CONDITIONS ..	321
TABLE 39 – CORRELATION MATRIX FOR TOWER LOADS WITH MISALIGNED WIND AND WAVE INPUTS IN RATED CONDITIONS .....	321
TABLE 40 – CORRELATION MATRIX FOR BLADE LOADS IN MISALIGNED WIND AND WAVE INPUTS IN RATED CONDITIONS ..	322
TABLE 41 – CORRELATION MATRIX FOR TOWER LOADS IN ALIGNED WIND AND WAVE INPUTS IN ABOVE-RATED CONDITIONS .....	322

TABLE 42 – CORRELATION MATRIX FOR BLADE LOADS IN ALIGNED WIND AND WAVE INPUTS IN ABOVE-RATED CONDITIONS .....	323
TABLE 43 – CORRELATION MATRIX FOR TOWER LOADS IN MISALIGNED WIND AND WAVE INPUTS IN ABOVE-RATED CONDITIONS .....	323
TABLE 44 – CORRELATION MATRIX FOR BLADE LOADS IN MISALIGNED WIND AND WAVE INPUTS IN ABOVE-RATED CONDITIONS .....	323

# Abstract

In recent years there has been a significant increase in the interest in floating offshore wind turbines from the wind energy industry, governments and academia. Partially driven by the recent nuclear disaster in Japan, but also by the lack or complete absence of shallow waters in various countries around the globe (making fixed offshore wind turbines infeasible), multiple different topology floating offshore wind turbines have been proposed and, in some cases, prototypes built and installed offshore. The most well-known of these is Hywind by Statoil, which has been operational off the coast of Norway since the end of 2009. While small scale prototypes had been installed even before Hywind, for example Blue-H in 2007, no guidelines have yet emerged that would give recommendations and guiding principles in designing new floating offshore wind turbines.

The aim of this thesis is to provide some knowledge base for future design of floating offshore wind turbines by looking at what simplifications could be made and what effect these would have on the preliminary designs of new floating offshore wind turbines.

This thesis starts by comparing different topology floating offshore wind turbines and choosing one, deemed the most promising, as the base case scenario for use in the subsequent analysis and calculations.

This thesis also looks at the importance of unsteady representations of the aerodynamics compared with quasi-steady when designing a new floating offshore wind turbine, by comparing quasi-steady aerodynamic loads first with fully-attached unsteady loads and later with fully-unsteady (fully-attached, separated and dynamic stall).

A chapter is allocated to identifying which degree-of-freedom of loading is the most damaging to the system, as floating offshore wind turbines operate in very harsh and unstable environments. Once identified, this knowledge can be used to further improve floating offshore wind turbines, hence making them even more feasible.

Finally, the wind turbine previously chosen as a base case has its floating support shortened and four different draft designs proposed that would allow it to be deployed in medium-to-deep waters, in which fixed supports for wind turbines are not economical.

# Abbreviations

AFT	Advanced Floating Turbine
AM	Added Mass
ASL	Above Sea Level
BEM	Blade Element Momentum Theory
BOS	Balance of System
CoB/CB	Centre of Buoyancy
CoG/CM	Centre of Gravity/Centre of Mass
CoE	Cost of Energy
DoF	Degree of Freedom
DOWEC	Danish Offshore Wind Energy Converter
EWEA	European Wind Energy Association
FA	Fore-Aft
FOWT	Floating Offshore Wind Turbine
FSV	Field Support Vessel
GDW	Generalised Dynamic Wake
HAWT	Horizontal Axis Wind Turbine
HLV	Heavy Lift Vessel
HVDC	High Voltage Direct Current
IEC	International Electrotechnical Commission
IRENA	International Renewable Energy Agency
KC	Keulegan–Carpenter number
LCoE	Levelised Cost of Energy
MWL	Mean Water Level
NACA	National Advisory Committee for Aeronautics
NREL	National Renewable Energy Laboratory
OC3	Offshore Code Comparison Collaboration
OPEX	Operational Expenditure
RAOs	Response Amplitude Operators
ROCs	Renewable Obligation Certificates
ROI	Rate of Investment
ROR	Rate of Return
SS	Side-to-Side
SWL	Still Water Level
TLP	Tension Leg Platform
VAWT	Vertical Axis Wind Turbine
VIM	Vortex Induced Motion
VIV	Vortex Induced Vibration
WT	Wind Turbine
ZVI	Zone of Visual Influence

# Nomenclature

a	axial induction factor (-) or pitch axis location measured from mid-cord in half-chords (-)
b	half-chord (m)
$b_i$	exponents of indicial function (-)
c	chord (m) or restoring constant/stiffness ( $\text{Nm}^{-1}$ )
g	gravitational acceleration ( $\text{ms}^{-2}$ )
h	plunge displacement (m) or section height (m)
$\bar{h}$	amplitude of plunging (m)
k	reduced frequency (-) or stiffness of a body ( $\text{Nm}^{-1}$ )
l	distance from the centre-of-mass to hub (m)
m	mass (kg)
$m'$	added-mass (kg)
r, R	distance from the centre of hub (m)
$r_1$	inner radius (m)
$r_2$	outer radius (m)
s	non-dimensional time (-) or complex argument of frequency domain (-)
t	time (s) or thickness (m)
$w_{3/4}$	downwash at $\frac{3}{4}$ of chord ( $\text{ms}^{-1}$ )
A	amplitude of motion (m or deg.) or area ( $\text{m}^2$ )
$A_i$	coefficient of indicial function (-)
BM	bending moment (Nm)
$\overline{\text{BM}}$	metacentric radius (m)
C	Theodorsen function (-)
$C_L$	coefficient of lift (-)
$C_L^c$	circulatory lift coefficient (-)
$C_L^{nc}$	non-circulatory lift coefficient (-)
$C_{L_0}$	coefficient of lift at zero angle-of-attack (-)
$C_D$	coefficient of drag (-)
$C_T$	coefficient of thrust (-)
$\overline{\text{CM}}$	centre of mass measured from SWL (m)
$\overline{\text{CB}}$	centre of buoyancy measured from SWL (m)
D	drag (N)
F	real part of Theodorsen function (-) or force (N)
G	imaginary part of Theodorsen function (-)
$\overline{\text{GM}}$	metacentric height (m)
H	Hankel function (-) or hub height (m)
$H_s$	significant wave height (m)
I	moment of inertia ( $\text{kgm}^2$ ) or second moment of area ( $\text{m}^4$ )
$I'$	added-inertia ( $\text{kgm}^2$ )
J	Bessel function of the first kind (-)
$\overline{\text{KB}}$	centre of buoyancy above the keel (m)

$\overline{KG}$	centre of gravity above the keel (m)
$\overline{KM}$	metacentre (m)
L	lift (N) or distance to shore (m)
Q	torque (Nm)
R	distance from the centre of hub (m) or radius of the Earth (m)
S	section modulus (m <sup>3</sup> )
T	thrust (N) or period of motion (s)
T <sub>p</sub>	peak spectral period (s)
U, U <sub>∞</sub>	free-stream velocity (ms <sup>-1</sup> )
V	total displacement (m <sup>3</sup> )
V, W	resultant velocity (ms <sup>-1</sup> )
Y	Bessel function of the second kind (-)
α	angle-of-attack (rad)
α <sub>eff</sub>	effective angle-of-attack (rad)
α <sub>qs</sub>	quasi-steady angle-of-attack (rad)
β	pitch angle + aerodynamic twist (deg.)
δ	Logarithmic decrement (-)
θ	displacement in pitch/roll/yaw degree-of-freedom (deg.)
θ <sub>heel</sub>	static heel angle (deg.)
ρ	air density (kgm <sup>-3</sup> )
ρ <sub>l</sub>	liquid density (kgm <sup>-3</sup> )
ρ <sub>s</sub>	solid density (kgm <sup>-3</sup> )
ρ <sub>sl</sub>	slurry density (kgm <sup>-3</sup> )
σ	dummy variable of integration (-) or stress (Nm <sup>-2</sup> )
φ	Wagner function (-)
φ	yaw angle (deg.)
φ <sub>sl</sub>	concentration of solids in the slurry (%)
ω	frequency of flow (rads <sup>-1</sup> )
Ω	rotational velocity of rotor (rads <sup>-1</sup> )

# Chapter 1: Introduction

---

## 1.1. Offshore wind resource

Around 70% of the Earth surface is covered by water. This, together with the knowledge that the winds are steadier and stronger offshore than onshore (on average 1 m/s higher, when 10 km from the shore), makes offshore wind, potentially, a very viable solution for meeting our energy demands and renewable targets. The fatigue loading due to aerodynamic loads is normally smaller offshore than onshore, as the offshore wind exhibits much lower turbulence, which is caused by lower surface roughness at sea [1]. Gust factors are also smaller, wind shear is reduced and wind directionality is much more stable, whilst the average and extreme wind speeds are higher.

In a report by the EWEA (European Wind Energy Association) [2] 3 main regions have been identified that are competing in the deep offshore technology race: Europe, the United States and Japan. For this reason, the analysis of offshore wind resource and bathymetry is limited to these 3 regions.

### *1.1.1. Europe*

The offshore wind resource is immense. In Europe alone it could meet Europe's demand seven times over [3] with an estimated 25% of it concentrated in Scotland, as highlighted by the strong wind in Figure 1.

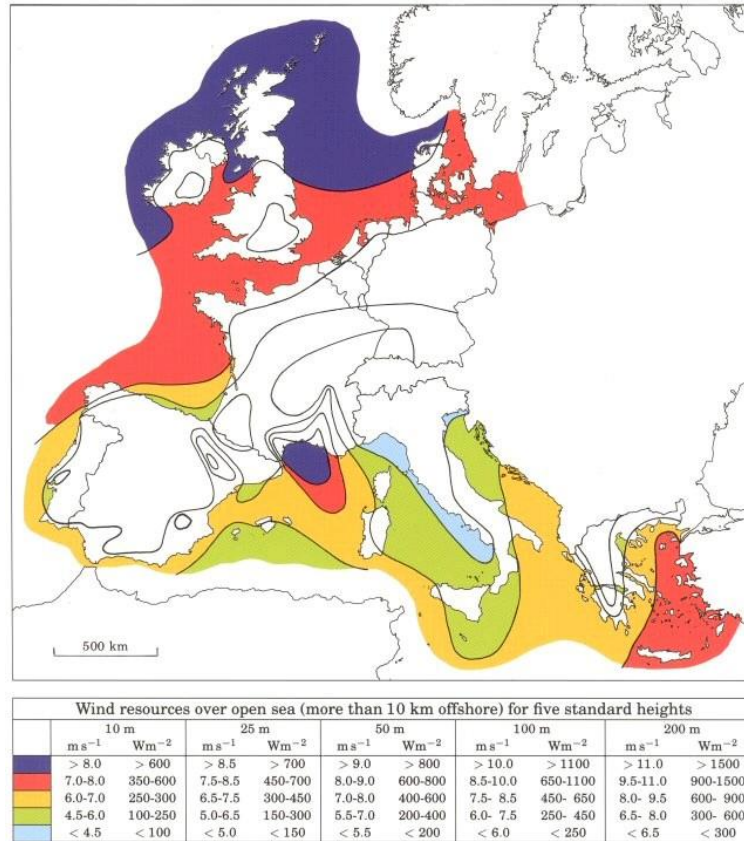


Figure 1 – Wind atlas of Europe [4]

By the end of 2013, 6,562 MW of offshore wind power had been connected to the grid in Europe, from which 72% in the North Sea, 22% in the Baltic Sea and 6% in the Atlantic Ocean [5]. This trend, of having the majority of installations in the North Sea, is highly likely to continue for the foreseeable future, due to both political and financial mechanisms set in place by the UK, Germany and Denmark to develop offshore wind, and relatively shallow waters compared to the Atlantic Ocean and the Mediterranean Sea.

### 1.1.2. The United States

A thorough report by the U.S. Department of Energy had looked at a potential scenario, where 20% of the U.S. electricity would come from wind by 2030 [6]. As the report details, a share of this would have to be met by the offshore wind.

Only 28 of the 48 contiguous states have coastal boundaries. At the same time, they consume 78% of the U.S. electricity [7]. Only 6 of these states have enough onshore wind resource to meet more than 20% of their electricity demand, meaning that offshore wind,

including floating offshore wind, will have to play a significant role in the future generation mix.

Figure 2 shows an offshore wind resource map for the U.S. at 90 m above the SWL (still water level) and up to 50 nautical miles offshore, with the exception of some of the Southern States and Alaska.

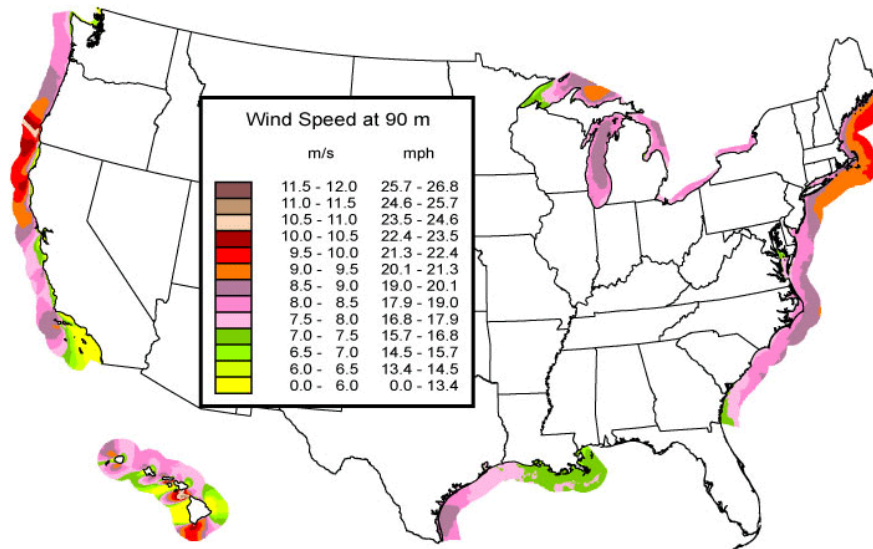


Figure 2 – The U.S. offshore wind resources at 90 m above the water surface [8]

Also worth mentioning is that the U.S. offshore wind energy potential is ranked 2<sup>nd</sup> in the world, trailing only behind China [9]. However, due to its geographical location, some areas of the U.S. are very prone to hurricanes, making some parts, especially the South and South-East, not viable for building wind farms.

### 1.1.3. Japan

In the light of the recent nuclear disaster in Fukushima, Japan has set very ambitious targets for renewable energy generation. In wind alone, 11 GW are expected to be operational by 2020 (of which 1 GW of floating wind), 28 GW by 2030 and 50 GW by 2050. To meet these targets, the majority of the turbines will have to be placed offshore due to lack of suitable areas onshore (densely populated, highly mountainous, etc.).

The total potential of offshore wind in Japan is around 1600 GW [10].

Figure 3 shows the offshore wind resource map of Japan with the wind speeds split into 3 wind ranges. The North of Japan, around Hokkaido Island, has the best wind resource. However, the majority of Japan's population lives in the central belt of Japan on Honshu Island (approx. 5.5 million people on Hokkaido and 103 million on Honshu). Theoretically, the area south of Tokyo could meet some of Japan's renewable targets, as it has a very good wind resource ( $> 8.5$  m/s) and is also situated very close to large load centres.

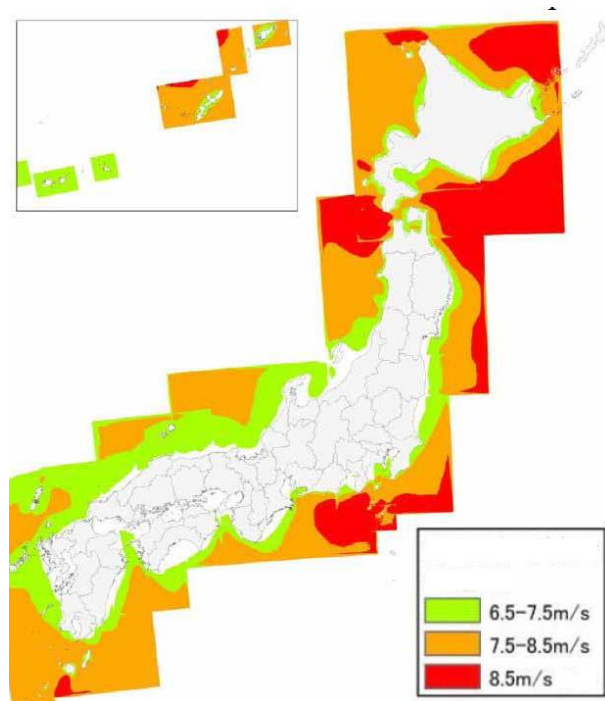


Figure 3 – Offshore wind resource map of Japan [10]

Similarly to the U.S., the risk of highly destructive environmental conditions, such as tsunamis, should be considered when planning offshore wind farms in Japan.

## 1.2. Bathymetry and distance to shore

Since the beginnings of the 90's, when the first offshore wind turbines were installed in Vindeby wind farm off the coast of Denmark, more and more wind turbines are being installed offshore each year.

In Europe, which is relatively densely populated, wind turbines on land are quite often met with a very strong opposition from public. This, together with stronger and steadier winds offshore, has led to Europe, and in particular the UK (partially due to access to plentiful of shallow waters), becoming a leader in the offshore wind. Table 27 and Table 28 in appendix show the water depth and distance to shore for various projects in Round 1 and 2, and Round 3, respectively.

Offshore wind farms experience higher winds, coupled together with less demanding acoustic requirements and much smaller public opposition due to smaller or no visual pollution.

For an observer standing at sea level at the shore, wind turbines are not visible if their distance to shore is:

$$L > \sqrt{2HR} \quad 1.1$$

where  $L$  is the distance to shore in meters,  $H$  is the hub height in meters and  $R$  is the radius of the Earth in meters [11]. For a typical 5 MW offshore turbine, the tip of the blade at zero azimuth angle (12 o'clock) is approximately 150 m above the SWL, meaning that the turbine has to be put 44 km away from the shore to be completely invisible. However, Sorenson & Hansen [12] reported that for distances greater than 8 km from shore the visual impact to the public is negligible. While Soerensen & Hansen came to this conclusion when offshore wind turbines were in their infancy (report dates back to 2001), it has been proven that the ZVI (Zone of Visual Influence) is highly dependent on the weather conditions and many other factors (see [13, 14]), and can result in wind farms being absolutely undistinguishable from the rest of the view at much closer distances from shore compared with the previous example of 44 km. This, together with very attractive financial incentive mechanisms set by governments (feed-in-tariffs, ROCs (renewable obligation certificates)), makes the offshore wind market very attractive to developers.

Europe leads in the number of offshore wind farms that are currently operating and/or under construction. This is partly due to the 'long' history of modern wind turbines in this region, but also due to the fact that parts of the North Sea are very shallow. This has allowed Europe to emerge as a leader in offshore wind, with the majority of turbines being

installed on monopole-type supports and close to shore using AC power connections to the mainland.

Nowadays, as more and more wind turbines are being installed offshore, the average water depth and distance to shore is increasing (see Figure 4), stretching the limits of the 'standard' technology. Increasing consideration is being given to HVDC connections instead of AC due to the significant losses experienced by the AC cables once their length exceeds 30-40 km [15] or 70-100 km [16] (depending on the study). There is also a need to consider the feasibility of different types of foundation – whether fixed or floating. Installation of a super grid between countries, in particular in Europe, could potentially have a very positive effect for wind turbines moving into deeper waters.

A report by the EWEA [5] shows that the average water depth for turbines installed in 2011 was 22.8 m and for those still under construction 25.3 m. At the same time, monopiles were making up more than 60% of all types of substructures used. Very similar numbers were reported for 2012 [6]; the average water depth of 22 m, 29 km to shore and 73% of substructures being monopiles. Since then, wind farms have been announced that will be up to 200 km offshore and at depths down to 215 m. These wind farms would take advantage of the fact that floating wind turbines do not experience scour effects, which can be up to 2 m in the central and northern parts of the North Sea.

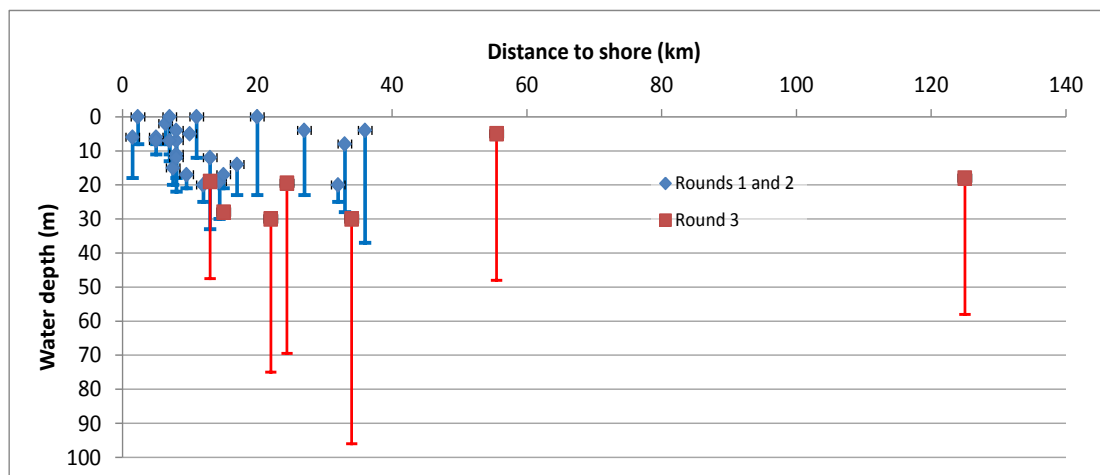


Figure 4 – UK Round 1, 2 and 3 wind farms and zones<sup>1</sup>

<sup>1</sup> Detailed description of each wind farm and zone is given in A1.1

The following 3 figures (Figure 5, Figure 6 and Figure 7) show bathymetry maps for Europe, the U.S. and Japan.

Figure 5 shows that the Mediterranean Sea is very deep, though parts of the Adriatic Sea and the Aegean Sea, and, in particular, the North Sea and the Baltic Sea, have substantial areas of shallow water. Looking at the central and southern parts of the North Sea, while Germany, Belgium and the Netherlands have no sea basin that is deeper than 50 m, Denmark, Norway and the UK have 16,000, 80,000 and 120,000 km<sup>2</sup> of sea basin areas deeper than 50 m [17].

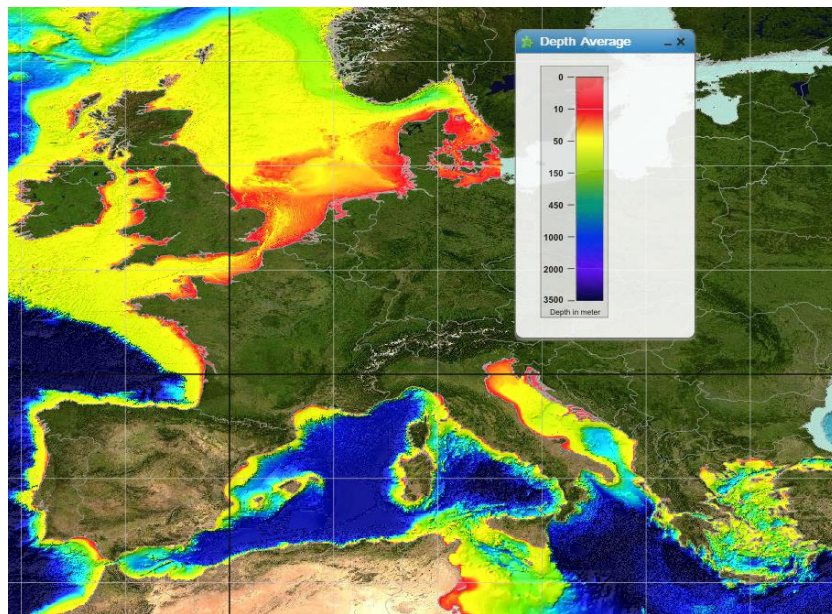


Figure 5 – Bathymetry map of Europe

The West Coasts of the U.S. and Hawaii have very steep drops in the water depths just a few kilometres off the coast. However, the East Coast, from Massachusetts to Florida, and the South Coast have plenty of shallow or medium depth (transitional depth between fixed and floating foundation) waters. In contrast, the Great Lakes are relatively deep and also require innovative solutions as they ice over in winter, though this problem has been encountered and addressed in the Baltic Sea.

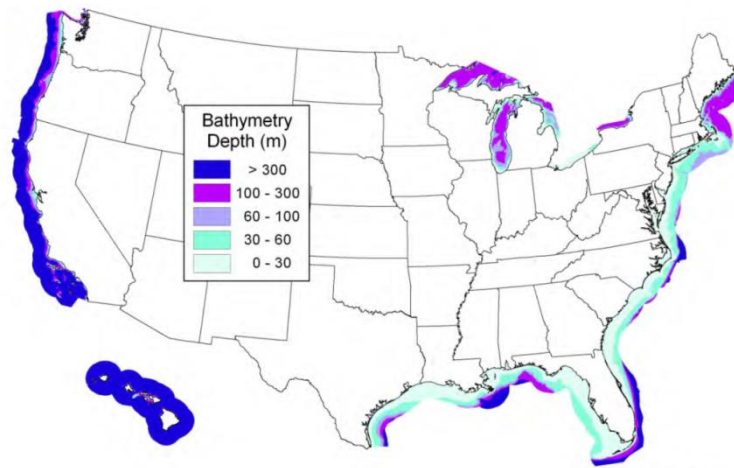


Figure 6 – Bathymetry map of the U.S. [8]

The shallowest waters around Japan are located in the North of Hokkaido and around Kyushu. However, 80% of Japan's offshore wind resources are in waters deeper than 100 m. On the East coast of Japan is the Japan Trench, which is up to 9000 m deep and reaches depths in excess of 120 m when only 20 km off the coast. To the West is the Sea of Japan with an average and maximum depths of 1,752 and 3,742 meters. This makes fixed-bottom offshore wind turbines completely unfeasible in Japan.

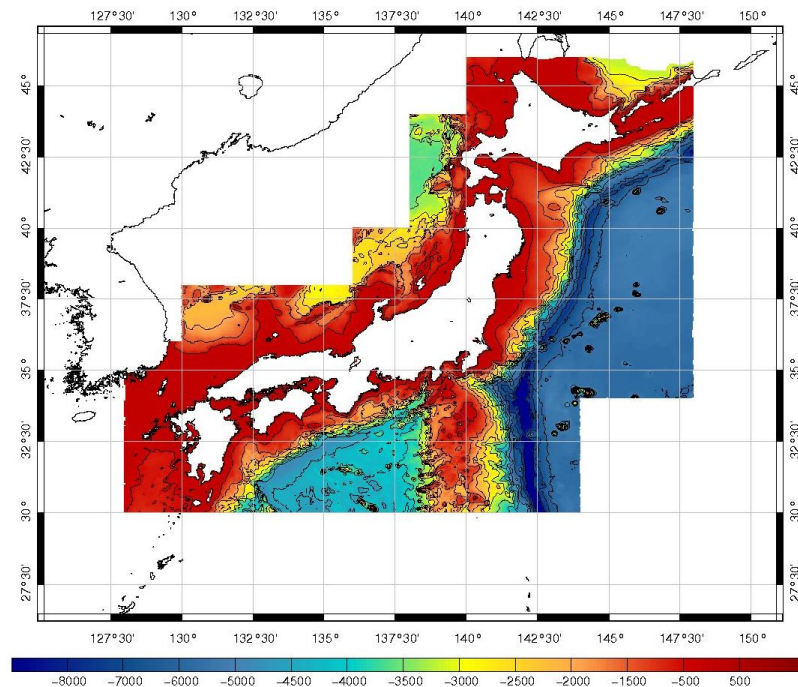


Figure 7 – Bathymetry map of Japan

With the average water depths of new offshore wind farms in Europe increasing by 2-3 m every year, how long will it take before floating substructures will start to dominate the market? One should also keep in mind that for countries like Japan, Norway and the U.S. this time will definitely come much faster, as none of these countries have access to large areas of shallow water, as their coasts are dominated by deep waters.

### 1.3. Support structure types

Support structures for offshore wind turbines come in different sizes and shapes. It was mentioned before that so far monopiles have been the favourite choice by the developers due to long history of usage, simplicity and shallow water depths associated with the current wind farm projects. However, monopiles are not the only option. The main types of support structure are summarised and shown in Table 1 and Figure 8. Three different water depth ranges were used: shallow to medium for 0-30 m depths; medium to deep for 30-50 m depths; and deep to very deep for 50+ m depths, making these consistent with [2].

Table 1 – Support structure types

Type	Water depths
Gravity	shallow to medium
Monopile	shallow to medium
Jacket	medium to deep
Tripod	medium to deep
Tripile	medium-to-deep
Floating	deep to very deep

Up to 2014, three fourths off all foundation installed in Europe have been monopiles (76%), followed by 12% gravity base, 5% jackets and tripods (each), and 2% tripile. Additionally, there have been 2 full-scale grid connected floating wind turbines and 2 downscaled prototypes [5].

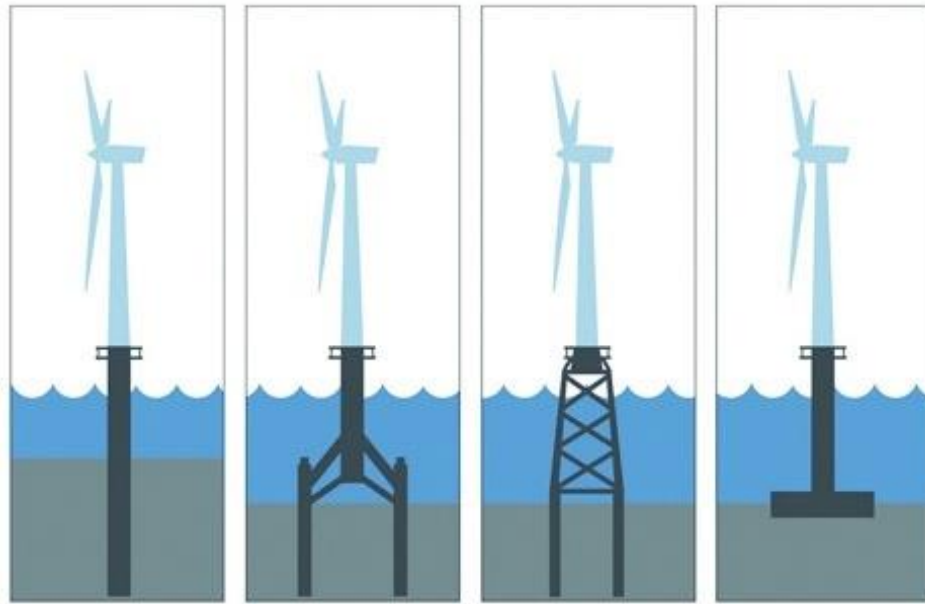


Figure 8 – Fixed bottom offshore foundation types (monopile, tripile, jacket and gravity base) [18]

The list in Table 1 is by no means complete. New designs are being suggested and built as the need for them arises. These include: full-truss structure, suction can monotower, hybrid monopile, etc. A separate field in its own right is floating support, which is discussed next.

## 1.4. Floating substructure classification

There have been many different configuration options proposed for floating offshore wind turbines. Partly due to extensive experience in the offshore oil and gas industry, and partly because of the wide range of different types of mooring, anchoring, tank and ballasting options known and used. In most cases, the treatment of floating wind turbine structures is comparable to those of the platforms in the oil and gas industry, with the main differences being the relatively small size and water depth, and the dominance of aerodynamic loading in the wind turbine case. However, unlike oilrigs, wind turbine controllers can be used to damp-out some motion induced by waves.

A floating structure must provide enough buoyancy to support the weight of the turbine and to restrain pitch, roll and heave motions within acceptable limits.

Typically, the overall architecture of a floating platform is determined by a first-order static stability analysis. Floating platform configurations can vary widely from one design to another. Nevertheless, all floating platforms can be split into three main categories based on the physical principle that is used to achieve stability [9, 19].

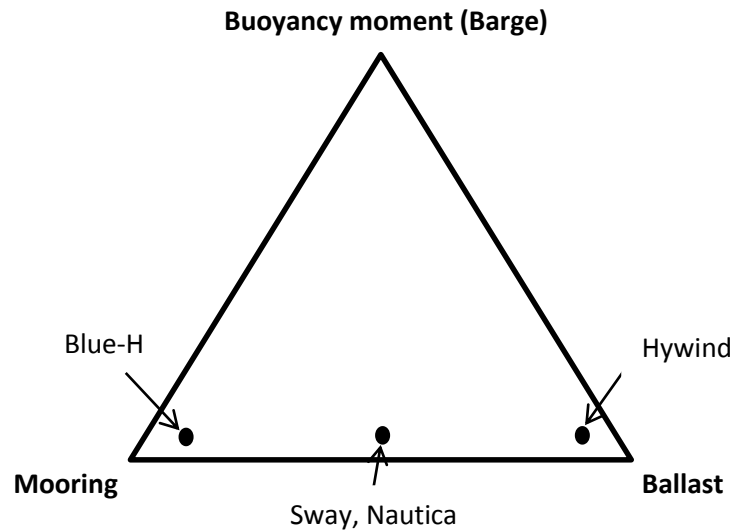


Figure 9 – Static stability triangle

#### 1.4.1. Ballast Stabilised

Floating platforms that use ballast as the main principle for achieving stability create a righting moment and high inertial resistance to pitch and roll degrees-of-freedom (DsoF). This is achieved by lowering the centre of mass (CM) to well below the centre of buoyancy (CB) using ballast. In general, this can only be achieved to an adequate extent with a higher density ballast than with water alone. Concepts such as DeepWind, Hywind and Sway use this strategy. Designs utilising this idea usually have enough draft to offset heave motion.

#### 1.4.2. Buoyancy Stabilised

These are the systems that achieve stability through the use of distributed buoyancy by taking advantage of the weighted water plane area for the righting moment. This principle is used in barges. The drawback of this design is that the main structure is very wave sensitive, as the main part of the body is very close to the water line.

### 1.4.3. Mooring line stabilised

Concepts such as Blue-H, Sway and Nautica achieve their stability through the use of mooring line tension. Tension leg platforms (TLP), such as those used in the oil and gas industry, rely on the mooring line tension for the righting moment, which eliminates heave, roll and pitch motions. These designs are very soil dependent and quite often are considered not feasible for floating wind turbine designs on financial grounds. These are also limited to areas free from significant tidal fluctuations and currents.

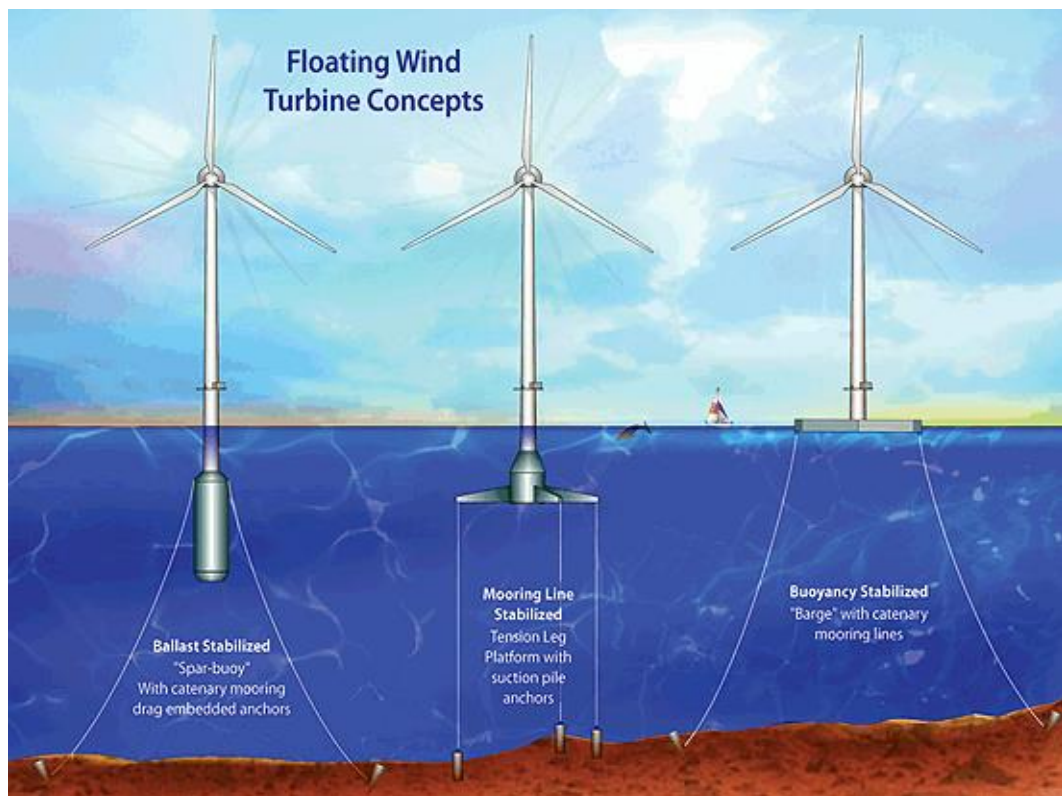


Figure 10 – Three main principles of achieving static stability for floating wind turbines [19]

In practise, all floating concepts are hybrid designs that gain static stability from more than one method, although, generally relying on one primary source for stability, such as Hywind or Blue-H in Figure 9.

## 1.5. Mooring system and anchoring

One of the most convenient ways of categorising mooring systems is by type of mooring technique used. The 3 main ones include: catenary, taut-leg and vertical tension leg. Each technique has its advantages and disadvantages. For example, catenary systems are the cheapest choice, but they are also the most prone to motion. Taut-leg designs have a smaller footprint than catenary, but are more complex and costly. Vertical tension legs have the smallest footprint, but again they are relatively expensive and need anchors that can withstand much higher loads than those used in catenary designs. Also, not always can taut-leg and vertical tension leg designs be employed in shallow waters; however, they do not need large amounts of ballast for stability, as is the case with the catenary systems.

Anchoring principles used with each design are very soil dependent. The deeper the anchor can be embedded, the larger the holding capacity of the anchor (shear force of the soil). The direction in which the force is applied also greatly influences performance of anchors. For example, a catenary moored anchor loading is mainly driven by the horizontal mooring force, whereas vertical load anchors need to have deep embedment to affect as much soil as possible to withstand much higher vertical loads.

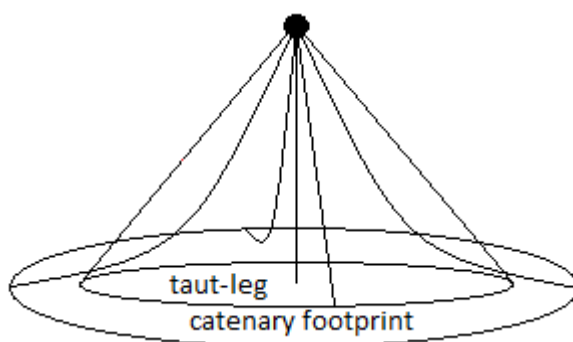


Figure 11 – Types of mooring systems and their footprints

The cost of the mooring system depends on the cost of mooring lines (chain, cable or pipe), and cost of materials and installation of anchors themselves. Some different types of anchors and their characteristics are summarised in Table 2.

Table 2 – Types of anchors

Type	Characteristics
Gravity-base anchor	Can be used with TLPs
Drag-embedded anchor	Very cheap, slight anchor movement
Driven pile anchor	No anchor movement
Suction anchor	Most effective for catenary systems
Driven anchor plate	Similar to suction, but cheaper
Torpedo embedded anchor	Easy to install
Drilled and grouted pile anchor	Good for medium and hard soil conditions, but expensive

By no means does the list in Table 2 include all types of anchors available and used in the offshore industry. However, not all of these types are economically feasible for offshore floating wind turbine installations.

Next, the advantages and disadvantages of floating HAWTs (horizontal-axis wind turbines) and VAWTs (vertical-axis wind turbines) are discussed, and a few prototypes are considered. A full list of all grid connected floating wind turbines and those in design and development stage can be found in [2].

## 1.6. Vertical-axis floating wind turbines

In the last few years a renewed interest has been shown in VAWTs, some of which specifically in the floating offshore wind turbine area. This is due to the advantages that are associated with VAWTs and applicable in the floating case. These include:

- Lower centre of mass (generator on the bottom of the structure, rather than the top as in HAWTs)
- No need for yaw
- Often do not use any pitching mechanism
- Often easier to install than HAWTs
- No reversing gravitational loads

However, there are three main disadvantages to VAWTs:

- Tendency to stall under gusty winds
- Blades prone to fatigue
- Not as proven technology as the HAWT

It should be noted that recent progress in blade manufacture and better control techniques allow alleviating some of these issues to a certain extent.

### *1.6.1. Vertiwind*

Vertiwind project was launched by Technip (French offshore oil and gas engineering giant) and Nénuphar (original developers of this VAWT) in January 2011. Prior to this, Nénuphar had spent three years on designing and testing 1:10 scale model of its VAWT.

Essentially, Vertiwind is a VAWT kept afloat by a three-column semi-submersible floater concept as shown in the figure below.

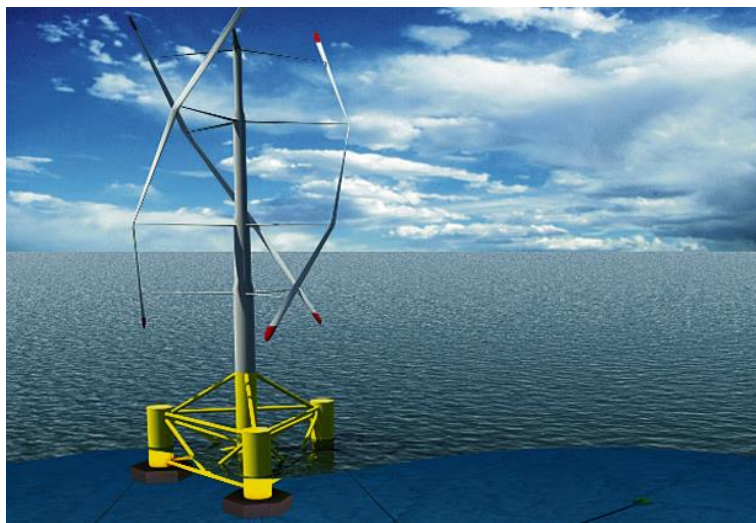


Figure 12 – Vertiwind concept

A 2 MW prototype was due to be operating in water depths of 85 m and should have been launched in 2012 just 5 km off the coast of South of France, but, as with many other floating wind turbine concepts, this has been postponed (installation is expected in mid-2015).

The wind turbine is based on the Darrieus-type rotor of 50 m in diameter and consists of three 70 m long blades. These blades are angled at 120 degrees and attached by struts to the pole at the centre of the floater. The design includes a clearance of 25 metres between the rotor and the sea to protect the rotor from waves, especially in storms. This VAWT concept has no yaw or pitch systems, nor is there a gearbox. A very big advantage of this design and VAWTs overall is that it allows the centre of gravity to be lowered by placing the generator (50 metric ton permanent magnet model) just 20 metres above the sea level, which is significantly lower than for any conventional HAWT.

Its floater utilises a chain and wire three-point spread together with standard drag anchors or piles, depending on the soil conditions at the site of installation. Because of its small draft (only 9 m) it allows for easier construction at the quayside, and easier and cheaper installation, maintenance and decommissioning as the system can be taken to dockside for significant repairs.

[20] provides a much more detailed description of the turbine, its configuration and the proposed installation site.

### *1.6.2. DeepWind*

DeepWind, a 4 year project, was funded by Future Emerging Technologies with an objective to explore technologies needed for development of new floating offshore VAWTs together with the design tools for design and performance evaluation. In other words, instead of “marinising” onshore wind turbines, for floating offshore wind turbines to be cost effective, they need to be designed through dedicated technology.



Figure 13 – DeepWind concept

DeepWind is also a VAWT based on the Darrieus principle. Its floating support uses a spar-buoy concept, which is ballast stabilised.

DeepWind suggests using different generator configurations, but all these topologies involve placing the generator at the bottom of the submerged spar. This is very advantageous in terms of lowering the overall centre of mass. However, this raises the question of accessing the generator for maintenance.

DeepWind has no need for a pitch or yaw control systems and the power control is obtained by control of the rotor speed.

DeepWind (VAWT) and Hywind (HAWT) are compared in Table 3.

Table 3 – Comparison of DeepWind and Hywind concepts [9]

	DeepWind	Hywind
Power (MW)	2	2.3
Rotor diameter (m)	67	82.4
Rotor height (m)	75	65
Chord (m) (blade number)	3.2 (2)	varying (3)
Rotational speed at rated conditions (rpm)	15	18
Total tower length (m) (underwater part (m))	183 (93)	165 (100)
Displacement (tonnes)	3,000	5,300

The following papers give a much more detailed insight into the original DeepWind idea and modifications and developments [21-23].

### 1.6.3. Other concepts

Other floating VAWTs include Skwid [24], which is a Japanese hybrid design with a 3-bladed Darrieus turbine and a Savonius ocean current turbine. It was initially planned as a sub-MW system to provide additional electricity to remote offshore or island installations. However, the prototype sank while being towed by a barge. The future of the project is unclear.

Gwind [25], a Norwegian project, is a gyro-stabilised floating VAWT. It utilises a 3-bladed Darrieus turbine and is mainly intended to provide electricity for oilrigs and fish farms. Since 2013 a 1kW prototype has been operational in Norway.



Figure 14 – Gwind concept

## 1.7. Horizontal-axis floating wind turbines

There are many different type of floating offshore HAWT concepts around, and their number greatly surpasses that of floating offshore VAWTs. For a number of reasons, HAWTs are generally a further developed technology than VAWTs, having seen more than 25 years of commercial development, so it is not surprising that there are more floating HAWT concepts than floating VAWTs. Some of these, but not all, are essentially ‘marinised’ land-based HAWT models.

Floating offshore HAWTs include such models as:

- Hywind
- Sway
- Nautica
- WindFloat
- Fukushima Mirai
- WindSea
- Blue-H
- And many more

At the time of writing only 3 full-scale floating offshore HAWTs have been installed – Hywind, WindFloat and Fukushima Mirai.

### 1.7.1. Hywind

Hywind [26] is probably the most famous of all floating offshore wind turbine concepts. It was the first full-scale prototype to be installed and is still operating in Norwegian waters 10 km off Karmøy, north of Stavanger, where water meets the required depth for design of 120-700 m.



Figure 15 - Hywind (Statoil)

Hywind is based on a long slender cylinder design (spar buoy) for its floater (designed and installed by Technip) with a typical 2.3 MW Siemens offshore wind turbine placed atop. It is moored using 3 catenary lines with extra 60 tonnes of weight attached at the mid-point of each line and drive pile anchors installed 10 m into the seabed. Stability is achieved by lowering the centre of mass using a ballast of water and olivine which is abundant in Norway and has a sufficiently high density.

### 1.7.2. Nautica

Nautica is an advanced floating turbine (AFT), which incorporates a combination of tension-legged and spar buoy designs. A two-bladed downwind turbine is used to increase drivetrain reliability and prevent blade/tower collision by allowing using more flexible and

lighter blades. Nautica aligns itself with wind without a yaw system, but by using passive wind alignment. For a 5 MW wind turbine it requires water depth of at least 70 meters.



Figure 16 – Nautica concept

Nautica claims to be 75% lighter than the competing oil-platform based designs [27], which permits significantly reduce material costs.

### 1.7.3. Sway

Sway [28], another Norwegian design in partnership with Areva-Multibrid, is a very similar design to Nautica with an exception of using 3 blades. It consists of a floating tower which extends far below the water surface with the ballast in the lower end.

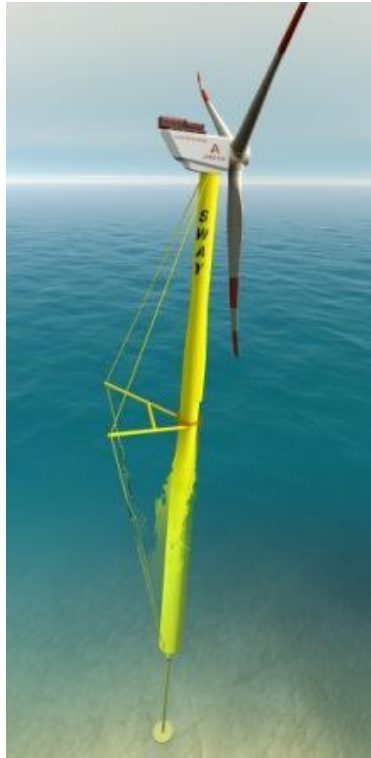


Figure 17 – Sway concept

The first down-scaled model of 1:6, installed on 31.05.2011 off the coast of Norway, sank during a storm called “Berit”. A new prototype was built and launched in summer 2012.

#### *1.7.4. WindFloat*

WindFloat [29] is a floating support structure for offshore wind turbines that is based on a three column design with heave plates and stiffeners mounted on the bottom of each column. An interesting stability feature of this design is the active ballasting system that pumps ballast water between the columns depending on the direction of the wind induced thrust forces.



Figure 18 – WindFloat concept

One of the biggest advantages of this concept is that it can be assembled onshore at a dockyard, allowing saving on the installation cost offshore.

As mentioned before, WindFloat is one of the 3 full-scale floating wind turbines that are currently installed offshore; six miles out to sea from the beach of Aguçadoura, near the northern town of Povoia do Varzim, Portugal.

### 1.7.5. Fukushima Mirai

Fukushima Mirai [30] (*mirai* translates as *future*) is a part of Japan's response to its nuclear disaster in Fukushima in March, 2011 after the nuclear plant was hit by the tsunami. It is a 2 MW floating offshore wind turbine with a 80 m rotor diameter built by Hitachi Ltd. It is installed 23 km off the coast of Fukushima Prefecture in approximately 120 m depth with the floating support based on a 4 column semi-submersible design, as shown in Figure 19. The floater is 32 m high with 16 m above the sea level (ASL). The hub height of the system is 65 m ASL, giving a blade-water clearance of around 25 metres. Six catenary lines, made out of steel chains, are used to hold Fukushima Mirai and Kizuna in place. These steel chains are up to 13.2 cm thick and can withstand a maximum load of 1,070 t.



Figure 19 – Installation of Fukushima Mirai

As part of the first phase of the project, a floating substation called Fukushima Kizuna (*kizuna* translates as *ties*) was also installed next to Fukushima Mirai. It is the world's first 66 kV floating substation, which steps up the 22 kV produced by the turbine to increase transmission efficiency. It is 110 m in height with a 50 m draft and uses an advanced spar design.

The second phase of the project will see the installation of two 7 MW Mitsubishi Heavy Industries turbines in the next two years. The turbines will have a rotor diameter of 167 m, making them amongst the biggest wind turbines ever installed. The floaters will utilise advanced spar designs, identical to Fukushima Kizuna.



Figure 20 – Fukushima Kizuna

### 1.7.6. WindSea

WindSea [31] is based on a semi-submersible three column platform design with a wind turbine mounted on each column. It doesn't include an active yawing system and is self-orientated towards the wind using a turret connected at the vessel's geometric centre. To minimise the shadow effect of one turbine being in the wake of the other two, the tower of the downwind turbine is made longer.



Figure 21 – WindSea concept

### 1.7.7. Blue-H

Blue-H [32] is a tension-legged platform with a 2-bladed upwind wind turbine installed on the top of it. The platform is held semi-submerged under the water by chains or tethers, which connect the buoyant body to the counterweight which lies on the sea bottom. Its anchors have to withstand much larger mooring forces than those of a catenary mooring system. Blue-H can be assembled onshore (in docks) and towed to the location of installation, which must have a minimum water depth of 60 meters.

In the summer of 2008 the first phase of the project was launched. An 80 kW scaled version of the concept was installed in 113 meter deep water 11.5 nautical miles (21.3 km) off the coast of Southern Italy, near the site of the future offshore Tricase project (see Figure 22). After 6 months at sea, the unit was decommissioned in 2009.



Figure 22 – Blue H

Phase 2 of the project was expected to be completed in 2012 and included a full scale prototype (2 MW wind turbine) installed in Tricase wind farm; however, at the time of writing, this has not yet been achieved.

A detailed list of floating wind turbines (both HAWTs and VAWTs) that are grid connected or under development can be found in [2].

## 1.8. Floating offshore wind turbine comparison

Because of the large number of floating wind turbine concepts proposed, concepts were assessed in outline and one specific design chosen to be used as the basis of this thesis.

HAWT concepts were the preferred choice over the VAWT concepts mainly due to the maturity of the HAWT market and the lack of available and verified software packages to design and simulate VAWTs. To date, there has been only one VAWT of near 4MW rating [33]. This allowed VAWT based concepts to be eliminated and the comparison narrowed to HAWTs.

Table 4 contains some core properties used in assessing the HAWT concepts.

**Table 4 – Floating offshore HAWT design comparison**

	Type	Mooring	Depth req.	No. of blades	Turbine type	Wind alignment	Assembly
<b>Hywind</b>	Spar	Catenary	120-700m	3	Upwind	Active	Offshore
<b>Blue-H</b>	Semi-sub. TLP	Tension leg	>60m	2	Upwind	Active	Onshore
<b>WindFloat</b>	Semi-sub.	Catenary	>50m	3	Upwind	Active	Onshore
<b>Nautica</b>	TLP	Tension leg	>70m (5MW)	2	Downwind	Passive	Onshore
<b>Sway</b>	Spar	Tension leg	80-400m	3	Downwind	Passive	Onshore
<b>WindSea</b>	Semi-sub.	Catenary	45-700m	3 x 3	2 upwind, 1 downwind	Passive	Onshore

All the aforementioned HAWT concepts, apart from Fukushima Mirai, which was ‘under the radar’ at the time of writing, were assessed in terms of relevant criteria. These included motion (static heel angle, 6 DsoF), cost of the wind turbine, floater and mooring system, anchors, technology’s maturity, sensitivity to soil conditions and footprint. Costs were divided into contributions from material, fabrication, installation, maintenance and decommissioning.

Different concepts were then compared by giving appropriately weighted scores to each of the assessment criteria, and one final design was chosen to be used as the base case in this thesis. A detailed breakdown of scores for each concept in terms of relevant criteria is given in A1.2<sup>2</sup>.

As the result of concept screening, Hywind was selected. Garrad Hassan (now DNV GL Garrad Hassan) came to a very similar conclusion, as early as 1993, when it performed a technical and economic feasibility study of floating wind turbines. From 6 floater configurations (cylindrical buoy, barge, donut buoy, satellite buoy, semi-submersible buoy and twin-turbine catamaran), the cylindrical buoy configuration was chosen, as it significantly outscored all other configurations [34].

---

<sup>2</sup> Due to involvement of ‘human factor’ in assessing and giving appropriate weighting factors, the overall result would vary depending on the person performing the task.

## 1.9. Cost of floating wind turbines

The levelised cost of energy (LCoE) is still very high for offshore wind and even more so for floating wind. On the other hand, the LCoE for onshore wind has reached levels where it is comparable with the conventional fossil fuel generation [35]. A report by the International Renewable Energy Agency (IRENA) [36] highlights that the LCoE for onshore wind has dropped to 0.06-0.11 USD/kWh in China and India, 0.07-0.11 USD/kWh in North America and 0.08-0.14 USD/kWh in Europe. The same source reports that the LCoE of offshore wind is between 0.14-0.19 USD/kWh, which is a very favourable estimate, as [37] reports the LCoE for 2 offshore site in the UK of 0.14 and 0.144 £/kWh (0.224 and 0.230 USD/kWh using the exchange rate of 05/2012).

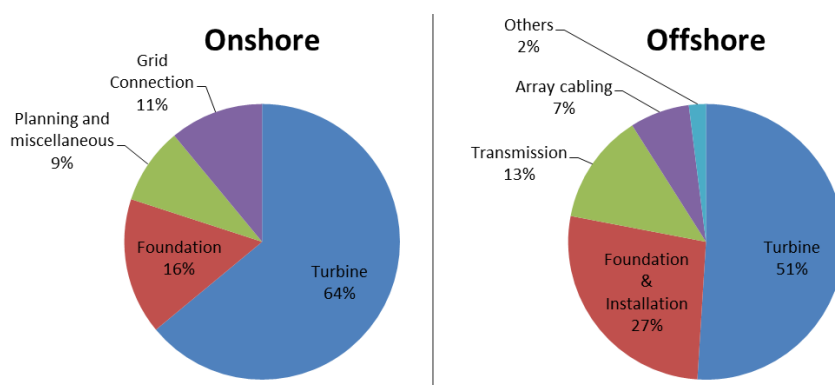


Figure 23 – Capital cost breakdown for a typical onshore and offshore wind farm [38]

Unlike onshore installations, the cost of offshore wind is not dominated to the same extent by the turbine cost, but by the multiple balance-of-station (BOS) and operating expenses (OPEX) factors. [39] shows that the onshore wind sector is very capital intensive with upfront/capital costs making up to 80% of all the costs comparing to 40-60% for other technologies. From Figure 23, the breakdown of the capital costs is very different for the onshore and offshore wind markets. In the offshore case the foundation and installation costs are higher and so are the cabling and transmission costs.

A presentation by GL Garrad Hassan (now DNV GL Garrad Hassan) highlights that the cost of energy (CoE) is becoming comparable for floating and fixed offshore wind [40], due to reduced installation costs and operational expenditure (repair costs) of floating wind.

Figure 24 clearly shows a significant increase in the foundation costs, but also a slight decrease in the transportation and installations costs for floating wind compared to fixed-bottom offshore wind. Smaller installation and transportation costs are associated with the fact that fixed-bottom turbines require heavy lift vessels (HLV) and/or jack-up vessels for foundations installation and jack-up vessels for turbine erection. These come at a great expense (£100,000 and £200,000 day rate on a spot market for jack-up vessel for 35 m and 60 m water depth [41]). On the other hand, some floating wind turbines can be erected onshore (docks) and only require an anchor handling tug for the mooring installation and standard tugs for the tow-out and hook-up to mooring system procedures. These are much cheaper; £10,000 day rate plus fuel and work costs for a field support vessel (FSV) [42].

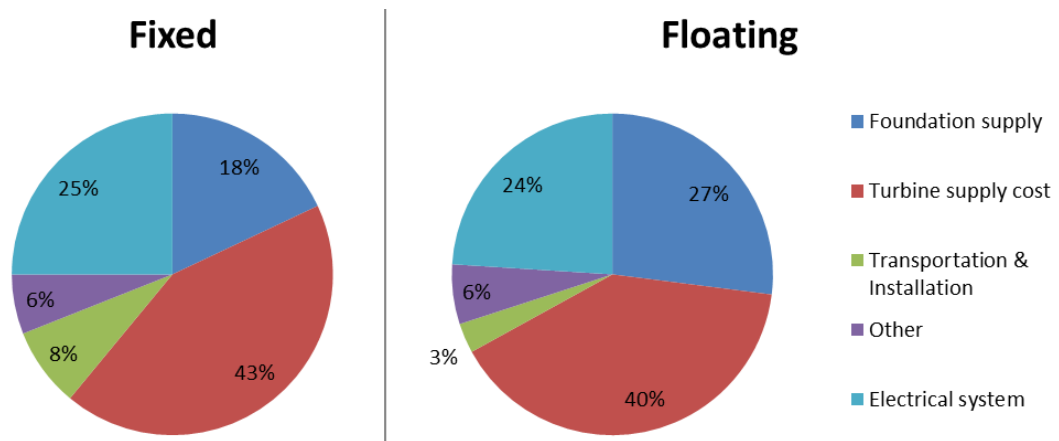


Figure 24 – Capital expenditure for fixed and floating offshore wind [40]

The operational expenditure can be split into repair costs, lost energy costs and management, licence, network costs, etc. For minor repairs, the repair costs should be the same for fixed-bottom and floating wind turbines, as the same access vessels can be used. For major repairs, bottom-fixed turbines generally require jack-up vessels, which are expensive and take time to mobilise. Some floating wind turbines can be disconnected from the mooring lines and brought back to the harbour for repair. Mobilisation of a tug can be achieved quickly, but the actual repair work will take time, as the floating turbine needs to be disconnected from the mooring and grid, towed back to base, repaired, towed back out and connected. Consequently, this may result in equal lost production costs for both cases. However, the dominance of the high mobilisation cost of jack-up vessels may mean that

actual cost of the whole procedure may be cheaper for the floating case where cheaper vessels can be used.

Castro-Santos [43] compared costs for 3 different floating offshore wind topologies (semi-sub, spar and TLP) with the life-cycle costs split into 6 groups: definition (preliminary studies), design (choice of turbine model, number and spacing studies), manufacturing (all manufacturing costs including turbine, platform, mooring, cables, etc.), installation (all installation costs), exploitation (tax, assurance, O&M costs) and dismantling (costs associated with decommissioning). Not surprisingly, TLP showed the highest installation and dismantling costs, due to very complex and expensive mooring system installation and removal procedures.

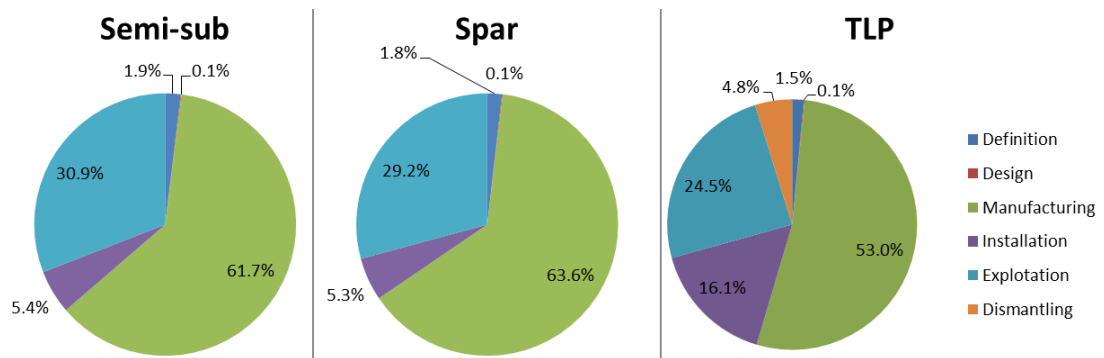


Figure 25 – Costs breakdown for 3 different floating offshore wind turbine models [43]

Semi-submersible and spar buoy topologies showed very similar total life-cycle cost breakdown, but because spar-type designs are less wave sensitive, due to smaller cross-sectional area at the water line, this furthermore confirmed the decision to go with a spar-type floater for further studies.

For floating wind turbines to truly become feasible and to be able to compete with alternative technologies, the rate of return (ROR) or return on investment (ROI) has to be sufficiently low. However, as the technology has not yet reached maturity and as investors see FOWTs as a high risk investment, ROR or ROI that investors require is still quite high.

It should be noted that floating technologies used in offshore wind rely on the knowledge obtained in the oil and gas industry, meaning that they are at the beginning of the learning curve and there is plenty of space for improvement and standardisation, which will eventually drive the cost down.

## 1.10. OC3-Hywind

Hywind is based on a spar-type topology. Originally, the slender cylinder design was selected due to its simplicity (very few parts, proven technology and allows the use of automated welding). After the successful test of a 3 m scaled model, the original Hywind design was launched in 2009 for a two year test [44]. Five years later it is still operational, having withstood 11 m waves [45]. Hywind makes use of an off-the-shelf turbine (Siemens 2.3 MW) with a control system that has been jointly developed by StatoilHydro and Siemens to exploit Hywind's ability to dampen out some of the wave induced motion.

The OC3-Hywind [46], born under Offshore Code Comparison Collaboration (OC3), is a fictitious floating wind turbine based on an NREL 5MW base turbine [47], which is based on the REpower 5 MW and the Dutch Offshore Wind Energy Converter (DOWEC) project [48], and a spar-type floater (modified Hywind).

Table 5 shows some core parameters of the Hywind and OC3-Hywind systems.

The OC3-Hywind system uses the original NREL 5-MW base turbine [47], but with a tower shortened by 10 m to accommodate for the portion of the spar above the SWL [46]. The tower is soft-stiff as it has its first fore-aft (FA) and side-to-side (SS) natural frequencies between the 1P (rotational frequency) and 3P (blade passing frequency) at the rated conditions (Figure 26).

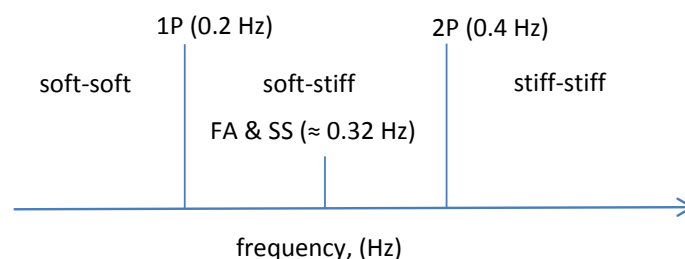


Figure 26 – OC3-Hywind tower natural frequencies

Table 5 – Hywind and OC3-Hywind core parameters

	Hywind	OC3-Hywind
<b>Wind turbine</b>	Siemens 2.3 MW-82	NREL 5 MW offshore WT
<b>Mass of turbine (t)</b>	138	599.7
<b>Hub height (m)</b>	65 above SWL	90 above SWL (tower height is 80 m)
<b>Rotor diameter (m)</b>	82.4	126
<b>Cut-in, rated and cut-out wind speeds (m/s)</b>	4, 13.5 and 25	3, 11.4 and 25
<b>Max. blade pitch rate (°/s)</b>	-	8
<b>Length of floater (m)</b>	117	130
<b>Draft (m)</b>	100	120
<b>Ballast type</b>	water and olivine	water and olivine
<b>Diameter at SWL (m)</b>	6	6.5
<b>Diameter at keel (m)</b>	8.3	9.4
<b>Number of anchoring lines</b>	3	3
<b>Unstretched length of anchoring line (m)</b>	-	902.2
<b>Total mass (t)</b>	≈ 5,300	≈ 8,200
<b>KG (m)</b>	-	42
<b>Suitable water depths (m)</b>	120 – 700	≈ 140+

In late 2013, the Crown Estate agreed to lease Buchan Deep, situated 12 miles off the coast of Peterhead, Aberdeenshire, to Statoil, which plans to install five 6 MW turbines in water depths of 95 to 120 meters. The proposed floating wind turbines, updated versions of the original Hywind, will have drafts of between 75 and 85 m, and displacements of 12,500 m<sup>3</sup> [49].

In the following chapters the OC3-Hywind system is used as the base case. In chapter 2 only the wind turbine (NREL 5 MW) is used to model the fully-attached unsteady aerodynamics. In chapter 3 the OC3-Hywind system is used in FAST [50] to model the unsteady

aerodynamics (fully-attached flow, separated flow, dynamic inflow and dynamic stall). In chapter 4 modifications are made to the OC3-Hywind system to alleviate the most detrimental loads identified in chapters 2 and 3 and to be able to be installed in shallower waters, say, 60 – 90 m depth.

## **1.11. Thesis objectives**

A recent increase in proposals and designs of floating offshore wind turbines has raised the need for design standards for floating offshore wind turbines. The International Electrotechnical Commission (IEC) has since been working on the IEC 61400-3-2 standard that spells out the design requirements for floating offshore wind turbines. At the same time, DNV GL has published its own offshore standard (DNV-OS-J103) on design of floating wind turbine structures. Simultaneously, designers and engineers are still relying on knowledge obtained in the oil and gas industry to come up with new floating offshore wind turbine concepts. This can clearly be seen by the number of different types and variations of floating offshore wind turbines available on the internet (some of which are discussed in this thesis).

The author of this thesis is of the opinion that the industry lacks some very basic design guidelines that could be used in proposing new floating offshore wind turbine concepts.

As mentioned before, there are only three fully operational full-scale prototypes of floating offshore wind turbines installed in the world; Hywind (Norway), WindFloat (Portugal) and Fukushima Mirai (Japan). Most turbines installed on land conform to the 'Danish-model' i.e. 3-bladed up-wind and most recent turbines employ a Doubly-Fed Induction Generator (DFIG). However, it is not yet clear which type of design is most likely to succeed, when floating support becomes necessary.

The three existing floating wind turbines are adaptations of existing wind turbines designed for bottom-mounted offshore installation. These in turn are quite often just 'marinised' versions of their land-based counterparts. In the future, as floating offshore wind turbines evolve, engineers will need to redesign turbines, to be better integrated with their floating

support. For such a design process, it is not enough to be able to analyse an existing design; they will need to know what can be simplified and/or ignored in the initial designs. In particular this thesis will attempt to establish the following:

- The importance of unsteady aerodynamics (compared to quasi-steady)
- The most detrimental degrees of freedom (DsoF) for a floating offshore wind turbine (with an emphasis on spar-type designs)
- The modifications that may be necessary to the support structure to alleviate the most detrimental loads.

Also, the author is of an opinion that there is a need for floating wind turbine designs that could fill in the gap between the conventional bottom-fixed offshore wind turbines (up to 40-50 m of depth) and over-engineered spar-type designs such as Hywind (minimal water depth of 120 m for a 2 MW turbine). This is consistent with the latest proposals by Statoil for a 6 MW turbine with a spar-type floater and a draft of 75 – 85 m [49].

This thesis is split into 5 chapters, where each succeeding chapter is linked and draws on the findings from the previous chapters. A high-level flowchart of the thesis is shown in Figure 27.

Chapter 1 looked at 3 potential FOWT markets; Europe, the U.S. and Japan. Each was examined from the offshore wind resource and bathymetry perspective. This was followed by giving a brief introduction to different types of floating substructures and physics behind achieving static stability. Different types of mooring systems and anchors, with associated advantages and disadvantages, were look at. A variety of different types of FOWT concepts, both VAWTs and HAWTs, were identified and assessed in terms of the relevant criteria, resulting in one specific design being chosen as the base case and used in the subsequent chapters.

Chapter 2 looks at fully-attached unsteady aerodynamics using the wind turbine chosen in Chapter 1 as the base case. It starts by performing a reduced frequency analysis to identify at which areas of the blade and at what operational conditions will the fully-attached unsteady aerodynamic assumption be most applicable. This is followed by simulations of blade in oscillatory plunging and pitching motions using Theodorsen theory. To be able to simulate each of the 6 DsoF of a floating offshore wind turbine separately, Van der Wall and Leishman theory, together with Wagner function, is used. These are implemented in an in-

house written MATLAB code, which has been validated against some previous work by Leishman. All fully-attached results are then compared to quasi-steady and conclusions drawn.

In Chapter 3 the work performed in Chapter 2 is taken one step further by taking into account all unsteady aerodynamic effects (fully-attached and separated flow, dynamic inflow and stall). All simulations are performed in FAST using the base case turbine (the OC3-Hywind) identified in Chapter 1, which has been verified against some previous work by NREL. The main advantages and disadvantages of using FAST are also listed to give reader a better understanding of the software's strengths and weaknesses. Aerodynamic damping and the most detrimental DoF for the OC3-Hywind is also identified by comparing unsteady and quasi-steady aerodynamic loads on the turbine. Findings are then compared to those in Chapter 2 for the fully-attached case.

Chapter 4 looks at how the OC3-Hywind floater could be modified to be made applicable not only for deep waters, but also for medium and medium-deep waters. Before 4 alternative shortened spar designs are proposed, the main design parameters are identified. A parametric study on the identified parameters is performed, which also considers the main design limits and trade-offs. Four shortened spar designs are then proposed and their natural frequencies analysed. The chapter is concluded by identifying some potential hazards and suggesting modifications that could be made to the spar to prolong its life and minimise motion in specific DsoF.

Chapter 5 combines all findings from each previous chapter and provides recommendations in order to be able to confidently design a floating wind turbine. The chapter concludes by suggesting some potential future work that could be performed as a continuation or completely separately from this thesis.

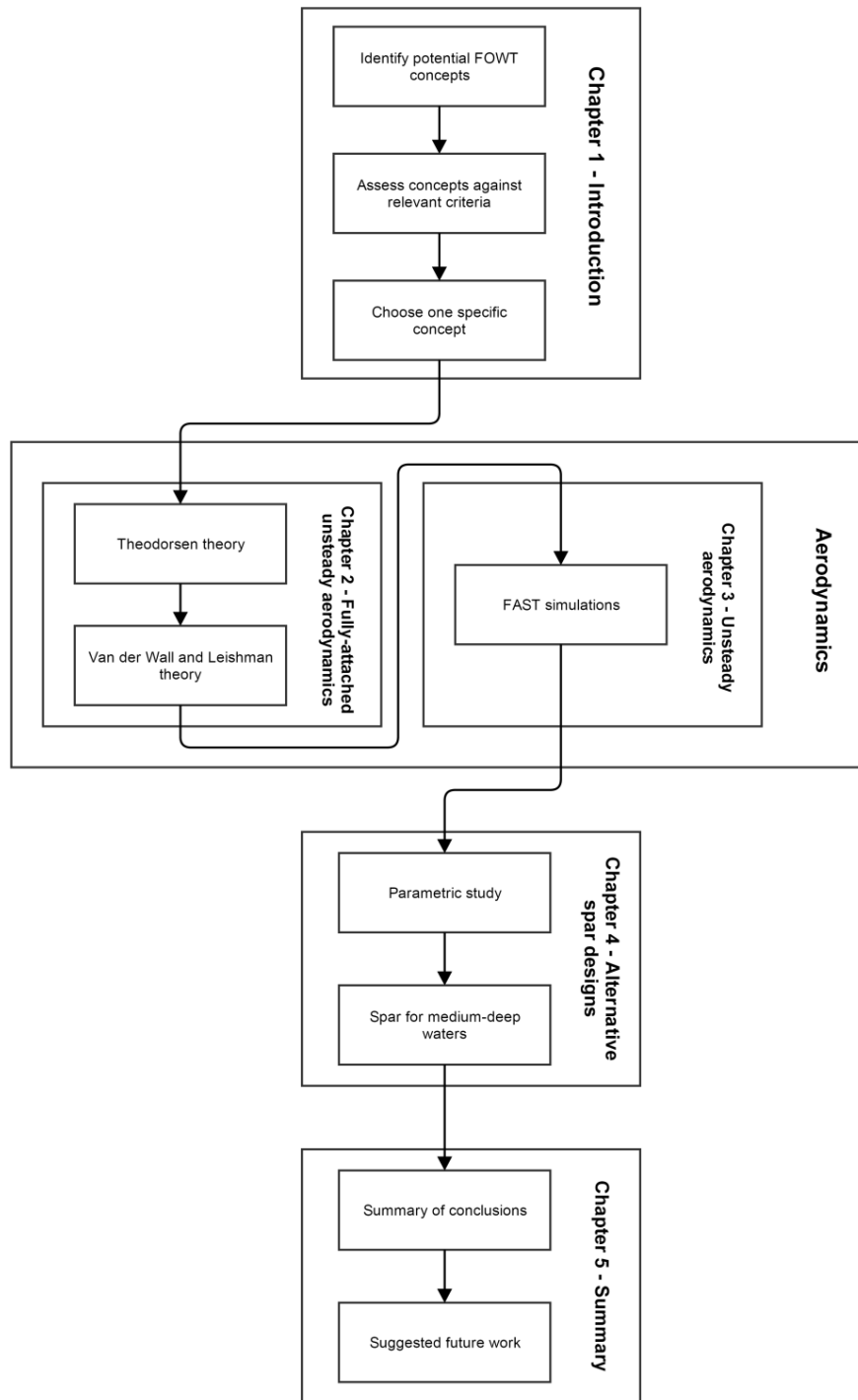


Figure 27 – Flowchart of the thesis

## 1.12. Co-ordinate systems

The following two figures (Figure 28 and Figure 29) show the co-ordinate systems used in this thesis. The inertial frame co-ordinate system used in Chapter 2 has its origin located at the overall CoG of the system (Figure 28). It is around this point that the translational (surge, sway and heave) and rotational (roll, pitch and yaw) motions of the support platform are defined. The x-axis is pointing in the downwind direction, the y-axis is pointing to the left when looking in the downwind direction and the z-axis is pointing vertically upward.

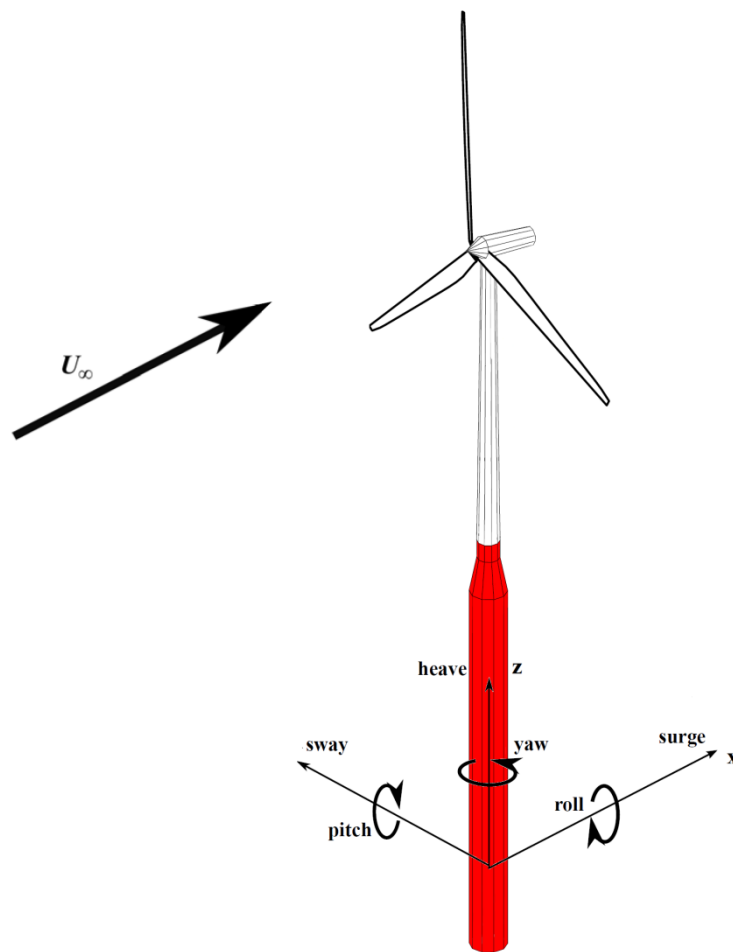


Figure 28 – Degrees-of-freedom for spar-type FOWT in Chapter 2 [51]

The co-ordinate system used in Chapter 3 is shown in Figure 29. This is identical to Figure 28 with exception that the point of the origin of the co-ordinate system has been moved to the SWL. This co-ordinate system was used for all results obtained in FAST and WAMIT. It

should be noted that both of these software packages provide users with the capability to set the point of the origin at any location of their choice.

The pitch and roll restoring of a floating body depends on the vertical distance between the CoB and CoG of the body. In WAMIT, the vertical CoG is also used to determine the pitch and roll restoring associated with platform weight. WAMIT will include these effects in the restoring matrix. However, FAST intrinsically accounts for the platforms weight's influence on the pitch and roll restoring. To avoid double booking these terms, it is important to neglect the terms in WAMIT, which can be achieved by setting the vertical CoG to zero in WAMIT.

A detailed description of co-ordinate systems used by FAST is given in [52].

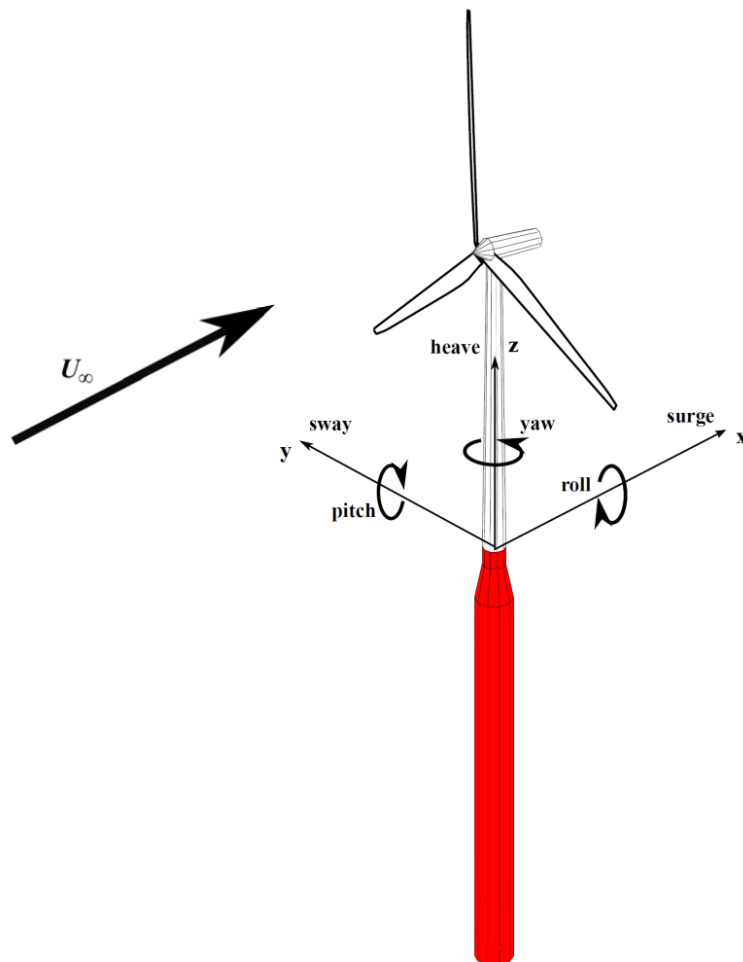


Figure 29 – Degrees-of-freedom for spar-type FOWT in Chapter 3 [51]

# Chapter 2: Attached flow

---

The design of new wind turbines can be greatly improved by accurately predicting aerodynamic loads for all possible conditions that could be encountered by them in their lifetime. However, is not an easy task as wind turbines are exposed to very complex environmental effects such as atmospheric turbulence, horizontal and vertical wind shear, tower shadow, etc. This means that wind turbines operate in a very hostile and unsteady aerodynamic environment that is both hard to accurately define and model. This is even more so true for FOWTs, which, on top of aerodynamic loads, are also subjected to highly complex hydrodynamic loads which can further intensify unsteady aerodynamic effects. In such cases the quasi-steady aerodynamic assumption might not be sufficient and could lead to wrongly predicted loads on a WT.

The importance of precisely modelling the unsteady aerodynamics of FOWTS cannot be underestimated. However, when considering unsteady aerodynamics people tend to think of dynamic stall. However, significant unsteady aerodynamic effects can be experienced by a wind turbine blade/blade element even in fully-attached flow conditions.

Theories based on 2-D assumptions for unsteady aerodynamics for aerofoils in fully-attached flow have been around since 1930's and 50's [53-55].

In [56] Leishman argues that in some situations such as a blade passing through tower shadow or the interaction of a blade with discrete vorticity comprising the blade tip vortices, the assumption of incompressible flow might not be justified and for very precise simulations this issue should be taken into account (at a cost in significantly increased computational overhead). However, because of the comparatively small relative velocities

associated with wind turbine blade elements, as a first approximation, it is sufficiently safe to assume that flow is incompressible.

As previously discussed, in the majority of situations an assumption of incompressibility is adequate. It permits the use of solutions already formulated by Küssner [54], Theodorsen [53] and Wagner [57] for unsteady aerofoil problems. These theories give analytic solutions for aerodynamic coefficients for aerofoils undergoing changes in the angle-of-attack due to translational or rotational motion and/or changes in the free-stream velocity.

In this chapter fully-attached unsteady aerodynamics of WTs is compared to quasi-steady to identify how they differ and whether it has to be accounted for when performing the preliminary designs of FOWTs. The frequency range of excitations was mainly limited to 0.04 – 0.4 Hz. This represents the frequencies which contain the majority of energy stored in waves. Identical frequencies were used in FAST simulations in Chapter 3. Additionally, resonance frequencies of the floater were also considered in Chapter 4. In this chapter two different theories are used; Theodorsen's and Van der Wall and Leishman's. Both theories are coded in MATLAB and verified against published scientific papers.

## 2.1. Reduced frequency

It is common practice that unsteady aerodynamic problems are expressed in terms of reduced frequency (see Theodorsen's theory). For operating wind turbines it is defined as:

$$k = \frac{\omega c}{2W} \quad 2.1$$

where  $\omega$  is some characteristic frequency of the flow in rad/s (for example, motion of the system or blade flapping),  $c$  is the chord length in m and  $W$  is the resultant local flow velocity at the blade element in m/s.

Depending on the reduced frequency, unsteady effects in fully-attached flow conditions manifest themselves as moderate or large amplitude and phase variations compared to the quasi-steady airloads [55]. Reduced frequency thus allows the unsteadiness of the flow to be characterised. A rough guideline is given here in Table 6:

Table 6 – Classification of flow unsteadiness [5]

k (-)	flow state
0	steady
< 0.05	quasi-steady
$0.05 \leq k < 0.2$	unsteady
$\geq 0.2$	highly-unsteady

For reduced frequencies below 0.05, the unsteady effects are assumed to be reasonably small and hence can be ignored. With  $k$  values above 0.05, the unsteady effects become much more pronounced and have to be accounted for. Additionally, for reduced frequency values above 0.2, the unsteady terms will start to dominate the behaviour of the airloads [56].

Figure 30 shows that the NREL 5MW Offshore Baseline Turbine [47] subjected to excitation frequency of the middle of the wave spectrum (0.1 Hz) at 3 different wind and rotor speeds (3 m/s and 6.9 rpm for cut-in, 11.4 m/s and 12.1 rpm for rated and 25 m/s and 12.1 rpm for cut-out [47]), would result in different flow states at different locations along the blade span. For the chosen conditions, one would not expect to see significant unsteady effects close to the tip of the blade, where it really matters from the power and fatigue perspective, when operating in either cut-in, rated or cut-out conditions. However, considering the same turbine operating at rated conditions and being slightly yawed with respect to the free-stream velocity, because the period of rotation at rated conditions is  $\approx 5$  s, the whole plot would be shifted up, resulting in more blade sections being in the unsteady region. A similar effect would be achieved, if the wave period would be decreased to 5 s.

**Note:** The vertical line in Figure 30 represents point on the blade where the aerofoil shape changes from a pure drag device to a lifting surface.

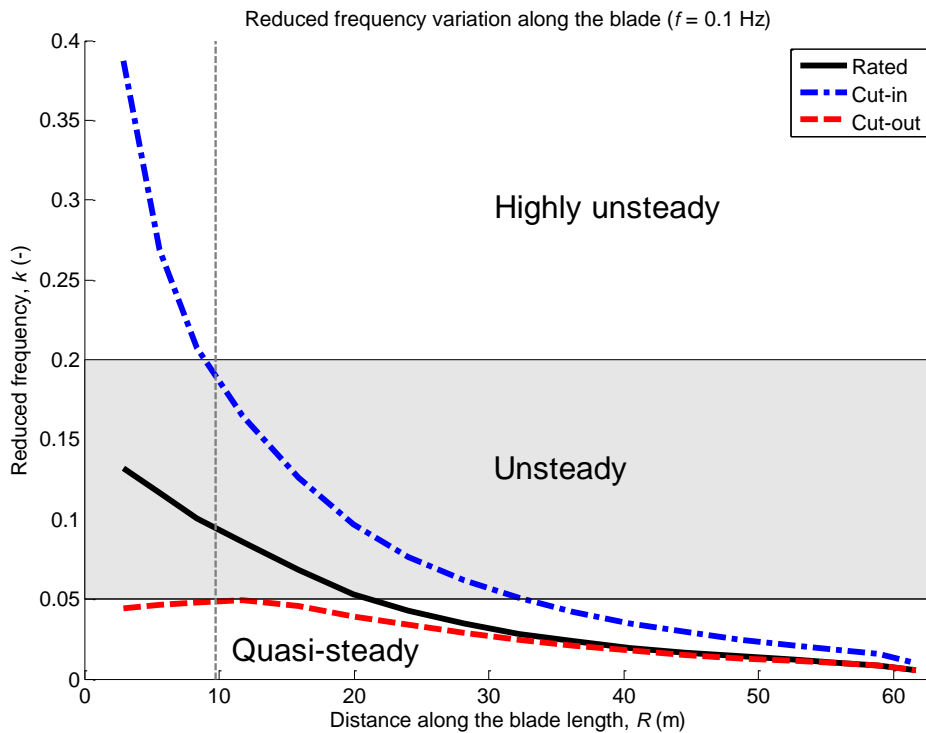


Figure 30 – Unsteadiness associated with the NREL 5MW Offshore Baseline Turbine

There are, however, two big drawbacks to this approach:

- Flow is assumed to be fully-attached,
- Amplitude of oscillation is completely ignored (only frequency considered).

This means that if a blade were vibrating at 1 Hz, it would not matter whether its vibration amplitude was 0.01 or 1 m. Because blade vibration velocity is proportional to the product of the angular frequency and amplitude of vibration, larger amplitudes of vibration would result in larger induced velocities at each blade element. This would lead to larger changes in the angle-of-attack, potentially resulting in increased unsteadiness and flow separation (breaking the first assumption). Conversely, if a small deflection assumption is made (as in the Theodorsen's theory), both assumptions are attained.

Nevertheless, as long as the results are interpreted with care, the reduced frequency can be used as a simple characterisation of flow unsteadiness and may give a reasonable insight into the unsteadiness associated with a particular wind turbine and/or blade element.

## 2.2. Theodorsen's theory

Theodorsen's theory [53] is probably the cornerstone in unsteady aerodynamic solution methods. Initially derived for fixed wing application, it is now regularly used for helicopter analysis, as well as for some wind turbine analysis.

It is a linear, incompressible theory that is based directly on thin-aerofoil theory for a flat plate and thus uses potential flow theory and the Kutta condition<sup>3</sup> but in an unsteady form. Theodorsen's theory separates effects into quasi-steady, added-mass and wake, giving a solution to the oscillatory part of unsteady lift on an aerofoil subjected to harmonic forcing in either pitching or plunging (heaving) in a fully-attached flow.

Being an analytical, frequency-domain unsteady aerodynamic theory, it is expressed in terms of reduced frequency,  $k$ . A solution is based on certain definite integrals that can be expressed using the Hankel function (equation 2.2), which in turn can be expressed as Bessel functions of the first and second kind (equation 2.3). The solution is given in the form of circulatory (wake) and non-circulatory (including added mass) components.

The theory is restricted to rigid body (aerofoil) motion, and is only applicable to pure sinusoidal excitation.

Theodorsen assumed small disturbances, hence fulfilling the requirement of fully-attached flow.

Some other effects that are not accounted for in Theodorsen's theory include: finite span, section shape, deviations from potential flow (frictionless, irrotational flow). It also assumes constant free-stream velocity. If, however, free-stream velocity is not constant, Theodorsen's function breaks down as the pure harmonic wake assumption is not valid anymore.

---

<sup>3</sup> The definition of the Kutta condition by Kuethe and Schetzer: "A body with a sharp trailing edge which is moving through a fluid will create about itself a circulation of sufficient strength to hold the rear stagnation point at the trailing edge."

### 2.2.1. Theodorsen's function

Theodorsen's function,  $C(k)$ , is a complex valued function which accounts for the effects of the shed wake on the unsteady airloads. Theodorsen's function reduces the magnitude of the aerodynamic lift force by an amount that depends on the frequency of oscillation (Figure 31). It is a complex function that can be expressed in form of Hankel functions of the second kind [55]:

$$C(k) = F(k) + iG(k) = \frac{H_1^{(2)}(k)}{H_1^{(2)}(k) + iH_0^{(2)}(k)} \quad 2.2$$

where the Hankel function can be expressed as a complex combination of Bessel functions of the first and second order:

$$H_n^{(2)}(k) = J_n(k) - iY_n(k) \quad 2.3$$

Alternatively, R.T Jones [58] approximated Theodorsen's function<sup>4</sup> numerically as:

$$C(k) = 1 - \frac{0.165}{1 - \frac{0.0455}{k}i} - \frac{0.335}{1 - \frac{0.3}{k}i} \quad 2.4$$

---

<sup>4</sup> See Appendix for more generalised Theodorsen's function approximations.

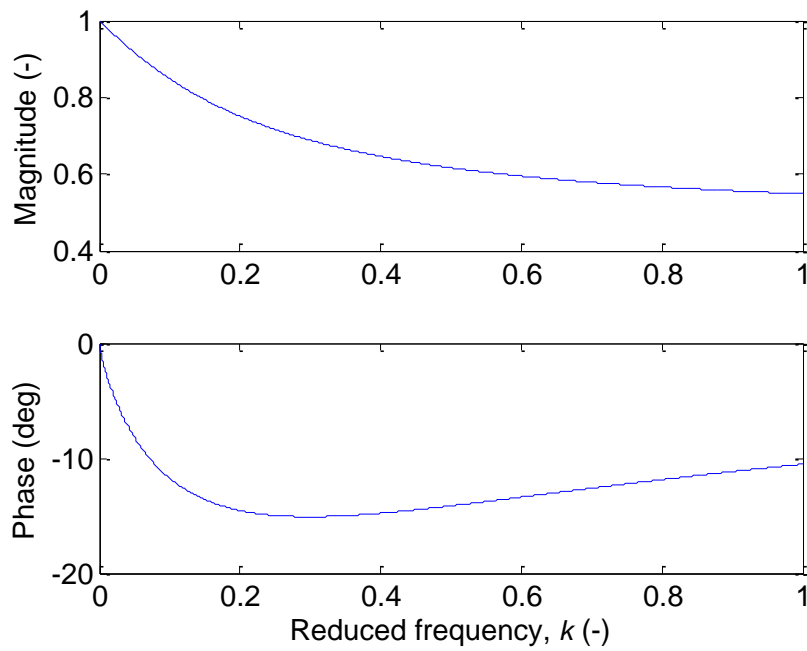


Figure 31 – Magnitude and phase of Theodorsen's function

Figure 32 shows a comparison between the original Theodorsen's function and the approximation by R.T Jones for three different operational states (cut-in, rated, cut-out) of the NREL 5MW wind turbine.

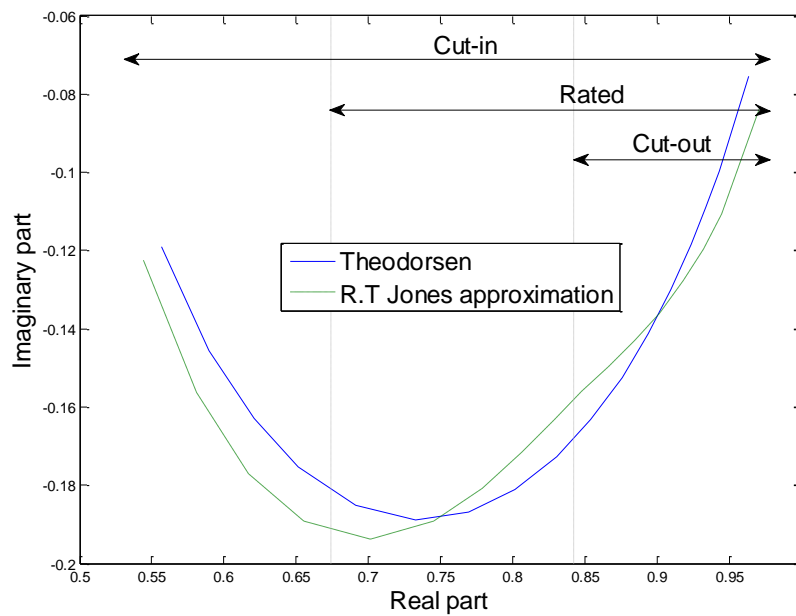


Figure 32 – Comparison of Theodorsen's and R.T Jones' approximation for the NREL 5MW ( $f = 0.2$  Hz)

Figure 32 displays a noticeable deviation between the different operation regions. The original Theodorsen's function is more mathematically and computationally demanding. However, Theodorsen's original function was chosen over Jones' approximation as there was no shortage of computational power and built-in functions available in MATLAB as installed on any reasonable desk-top computer.

A plot of Theodorsen's function is shown in Figure 33, calculated using equations 2.2 and 2.4 for reduced frequency values from 0 to infinity.

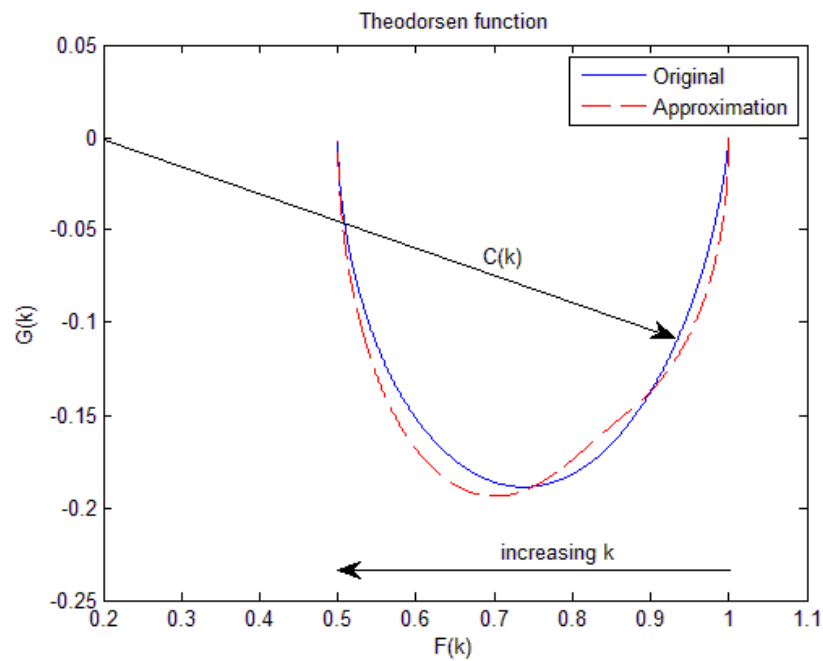


Figure 33 – Theodorsen's function

Theodorsen's function equals 1 when reduced frequency equals 0 (as would be expected in completely steady flow). Then, as  $k$  rises to infinity, the function tends towards 0.5.

Essentially, Theodorsen's function,  $C(k)$ , is a circulatory lift reduction factor as a function of the reduced frequency,  $k$ , which also introduces a shift in phase of the lift relative to the motion in either the plunging or pitching DsoF.

## 2.2.2. *Plunging*

Theodorsen showed that, if an aerofoil is subjected to a pure harmonic plunging motion (blade flapping or heaving), the fully-attached unsteady oscillating lift coefficient can be calculated using:

$$C_L = [2\pi k(iF - G) - \pi k^2] \frac{\bar{h}}{b} e^{i\omega t} \quad 2.5$$

where  $\bar{h}$  is the amplitude of plunging in m and  $b$  is the half-chord length in m. The first term in the outer brackets is the circulatory term and the second term is the non-circulatory term (added mass due to the displacement of the air surrounding the aerofoil).

One of Theodorsen's assumptions is that the aerofoil is aligned with the free-stream wind ( $\alpha = 0$ ). However, this is almost never the case for wind turbines. In normal wind turbine operation conditions, blade elements close to the hub will be encountering large angles-of-attack. The angle-of-attack will gradually decrease with distance from the hub and, eventually, close to the tip (where the relative velocity seen by a blade element is dominated by the rotational velocity) the angle-of-attack will be sufficiently close to fulfilling Theodorsen's assumption of the aerofoil being aligned with the free-stream velocity (in this case the resultant velocity).

With some caution, an aerofoil undergoing oscillatory plunging can represent either a wind turbine in surge motion (low frequency) or blade flapping (high frequency). Figure 28 in 1.12 shows all 6 DsoF for a typical spar-type FOWT and the corresponding point of origin for the co-ordinate system used with calculations in this chapter.

The first harmonic normalised amplitude of the lift coefficient and the corresponding phase shift angles, calculated using Theodorsen's theory of incompressible flow for an aerofoil in heave forcing, are shown in Figure 34.

When an aerofoil is stationary ( $k = 0$ ) the lift is zero, assuming that the aerofoil is aligned with the free-stream velocity, which results in zero angle-of-attack ( $C_L = 2\pi\alpha$ ). As the reduced frequency increases, it is met with a corresponding increase in the lift. In terms of the lift amplitude, the non-circulatory component can be ignored for  $k$  values less than 0.6, as up to this point the lift amplitude is dominated by the circulatory part of equation 2.5. At

reduced frequency values above 0.6, the non-circulatory components become more dominant and the total lift amplitude deviates from the circulatory part, and increases even further.

The phase of the fully-attached lift is very much dependent on the non-circulatory effects. For reduced frequency values as low as 0.05 (boundary between the quasi-steady and unsteady flow) the total lift phase deviates from the phase response of the circulatory term. As the reduced frequency increases and the non-circulatory effects become more dominant, at approximately  $k = 0.35$  the sign of the phase angle changes from lag to lead.

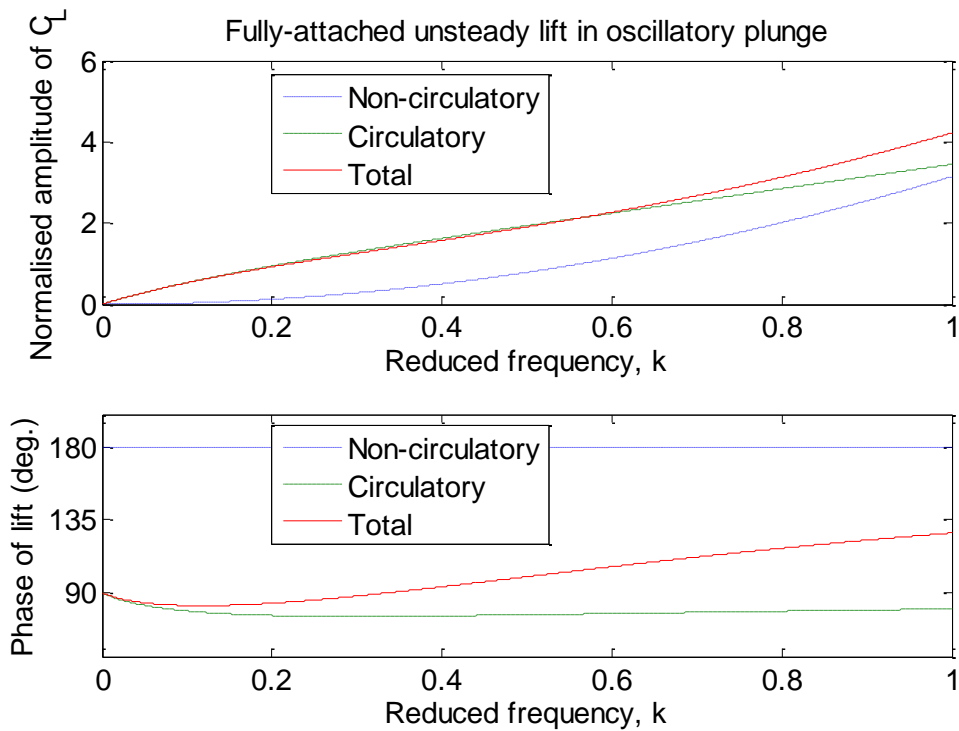


Figure 34 – Unsteady lift response in plunge motion

For a constant free-stream velocity (incident velocity), the non-circulatory lift coefficient is:

$$C_L^{nc} = \frac{\pi c}{2W^2} \left( W\dot{\alpha} + \frac{ac\ddot{\alpha}}{2} + \ddot{h} \right) \quad 2.6$$

where  $a$  is the pitch axis location measured from the mid-chord of the aerofoil in half-chords. It is -0.5, if the pitch axis is located at the quarter chord location (measuring from the leading edge).  $\dot{\alpha}$  and  $\ddot{\alpha}$  are the pitch rate and acceleration, and  $\ddot{h}$  is the plunge acceleration.

The quasi-steady and circulatory lift in plunging motion leads the forcing by a phase angle of  $90^\circ$ . The non-circulatory or the added-mass force leads the forcing by  $180^\circ$ , as shown in equation 2.6.

Thrust force on an NREL 5MW blade in plunging is shown in Figure 35. Only the lift components were used in the calculation (ignored  $C_D$ ). The changes in both the amplitude and the phase are clearly seen. Compared to the quasi-steady case, the unsteady case results in a decrease in the thrust amplitude, which is an effect of reduced lift coefficient values by Theodorsen's function. Also shown in Figure 35 is the phase difference. The unsteady case lags the quasi-steady, meaning that the reduced frequencies are between 0 and 0.35 (see Figure 34).

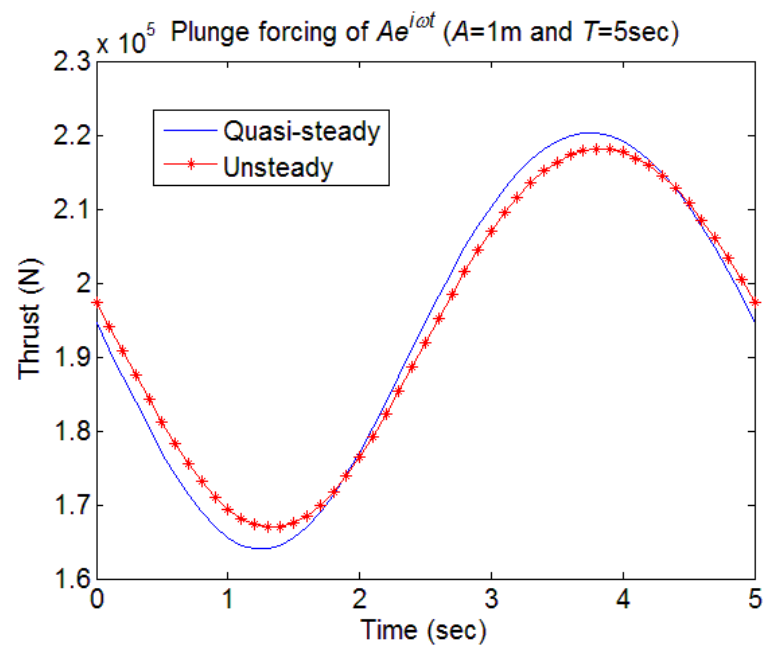


Figure 35 – Thrust force on a blade in oscillatory plunging

The torque response (Figure 36) to oscillatory plunging resembles the thrust with the exception of a smaller difference in the amplitude between the quasi-steady and unsteady results.

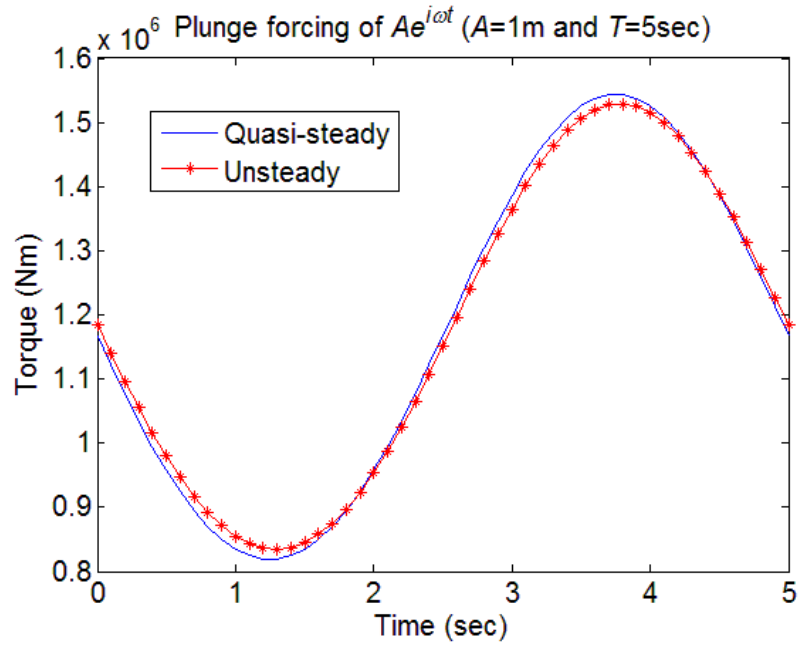


Figure 36 – Torque on a blade in oscillatory plunging

The amplitude and phase response of the quasi-steady and fully-attached unsteady lift along the blade span in plunging motion are shown in Figure 37.

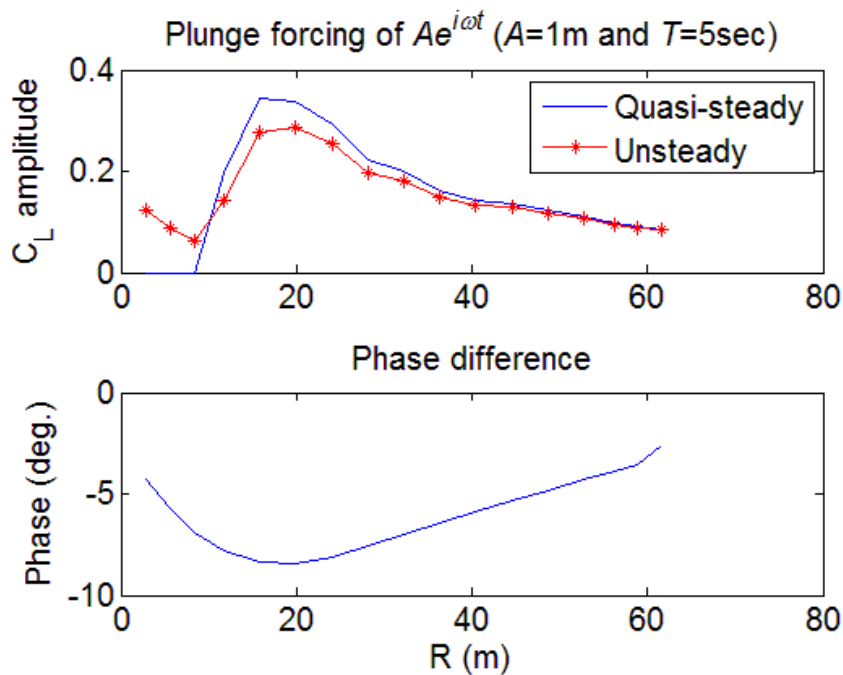


Figure 37 – Comparison between the quasi-steady and unsteady responses in plunging

Except for very close to the hub, the fully-attached unsteady lift response is always of smaller amplitude than quasi-steady. The first three points on the plot are for cylindrical parts of the blade (pure drag devices). These produce zero lift coefficients in the quasi-steady response. However, addition of the added mass in the unsteady calculations produces some lift on an oscillating cylindrical part of the blade. Lift due to the added mass decreases with distance from the hub (decreasing reduced frequency). With the reduced frequency decreasing towards the tip of the blade (Figure 38), the difference between the quasi-steady and unsteady amplitude diminishes.

The phase shift for the associated reduced frequencies (Figure 38), displays a varying lag for the unsteady results at different locations on the blade.

In this report, Theodorsen's function for plunging was used to imitate surge motion of floating offshore wind turbine. Frequencies of flow were kept relatively low (max. 0.2 Hz). However, more often Theodorsen's theory is used to model blade bending, a frequency an order of magnitude higher than the frequencies considered in this report. Potentially, this could result in all blade elements experiencing a highly unsteady flow where non-circulatory effects dominate the loads.

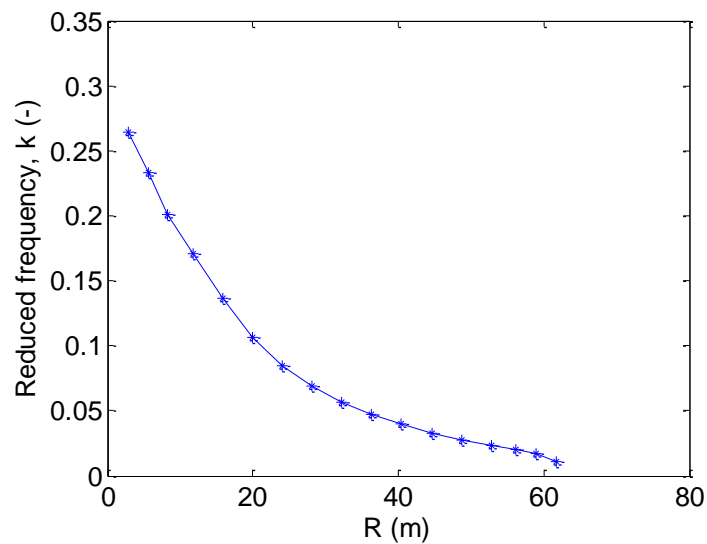


Figure 38 – Reduced frequency distribution along the blade length

Figure 38 applies to both plunging and pitching results described in this report.

### 2.2.3. Pitching

For harmonic pitch oscillation introduced by forcing  $\alpha = \bar{\alpha}e^{i\omega t}$ , the fully-attached unsteady lift coefficient is:

$$C_L = 2\pi[F(1 + ik) + G(i - k)]\bar{\alpha}e^{i\omega t} + \pi k(i - \frac{k}{2})\bar{\alpha}e^{i\omega t} \quad 2.7$$

As in plunging motion, the fully-attached unsteady lift coefficient is a combination of the circulatory and non-circulatory parts. These are the first and second terms in equation 2.7, respectively. The corresponding normalised lift coefficient amplitudes and phase angles are shown in Figure 39.

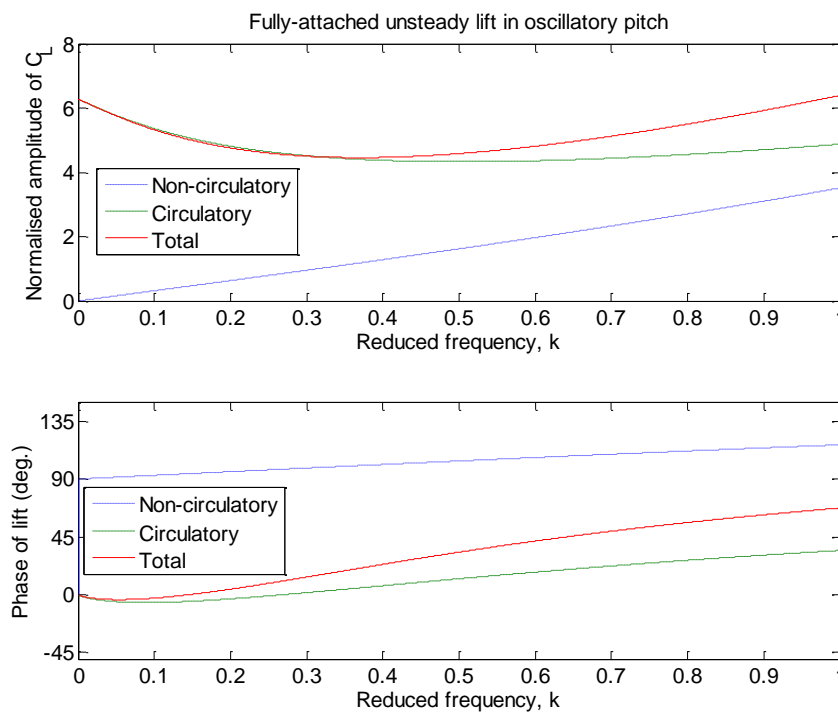


Figure 39 – Unsteady lift response to pitch

At zero reduced frequency the lift amplitude is  $2\pi$  (thin aerofoil theory). It then decreases with increasing reduced frequency. At  $k$  values of around 0.35, the total lift amplitude starts to increase due to, now, increasingly dominant non-circulatory component. For lift amplitude calculations, the non-circulatory component can be ignored up to  $k$  value of around 0.4.

The phase angle changes from lag to lead at  $k \approx 0.15$ . This, just like the lift amplitude, is the result of the non-circulatory forces starting to dominate the loads. Because  $k$  varies along the blade span (Figure 38), different blade stations could potentially experience leading and lagging load responses compared to the pitch forcing.

The derivation of the non-circulatory component of lift to oscillatory forcing in pitch is shown in A1.8.

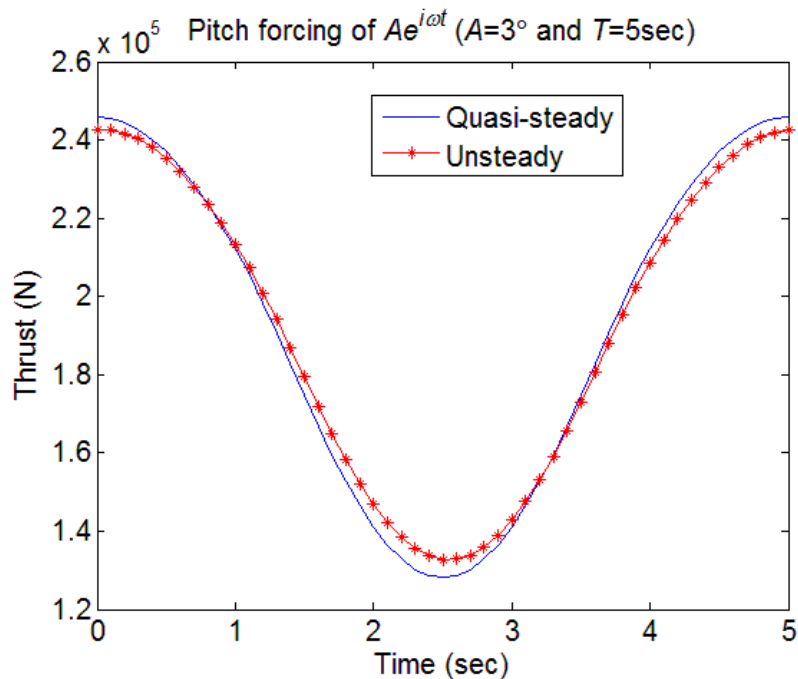


Figure 40 – Thrust force on a blade in oscillatory pitching

The thrust force on a blade forced in oscillatory pitch is shown in Figure 40. The overall results are very similar to those of plunging (Figure 35). A decrease in the force amplitude and a change in the phase are both present. Pitch results lead plunge by a phase angle of  $\pi/2$ . This can be explained by the fact that in pitch oscillation forces are the direct result of displacements in the angle-of-attack, whereas in plunge it is the velocity of the plunging that changes the angle-of-attack.

The torque response (Figure 41) to oscillatory pitching does not exhibit significant difference from thrust results in Figure 40.

Identically to the plunging results (Figure 37), the lift amplitude is always reduced in the unsteady case except for blade stations close to the hub (Figure 42). As the reduced frequency decreases with distance from the hub, the difference between the quasi-steady and unsteady lift amplitudes also decreases.

With an increasing distance from the blade tip towards the hub (increasing reduced frequency), the non-circulatory forces (including added mass) start to dominate the loads. This results in an increasing leading phase in the unsteady results, as shown in Figure 42.

While in plunging the unsteady lift at all blade stations was lagging the quasi-steady response (negative phase angle), in pitching motion different sections of the blade will experience either lead or lag (Figure 42).

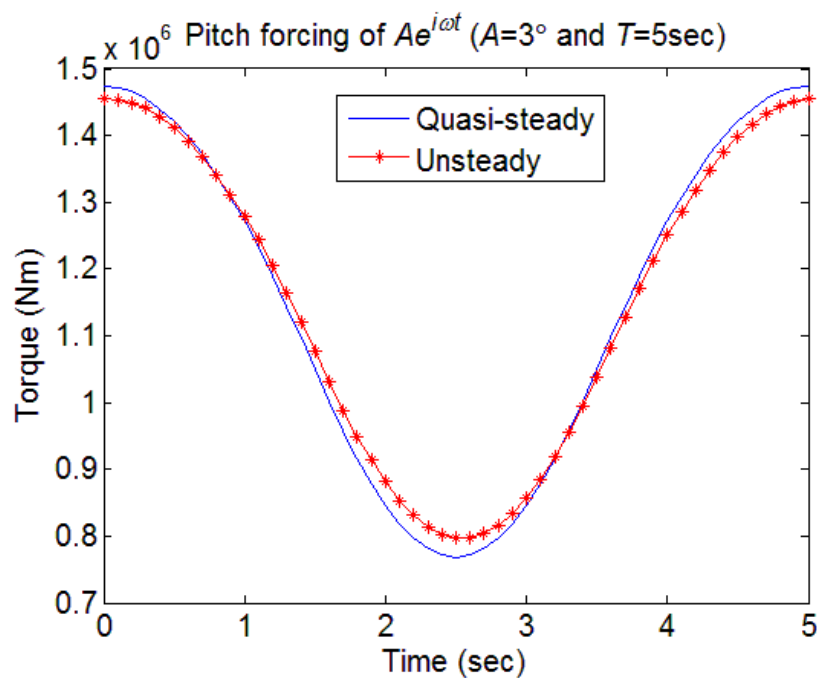


Figure 41 – Torque on a blade in oscillatory pitch

Results obtained using Theodorsen’s theory for blade plunging and pitching show some change in the amplitude and phase in the fully-attached results compared to the quasi-steady results: the quasi-steady results overestimate the fatigue loads on the turbine. This could lead to over-engineered designs of WTs, hence raising the cost and making WTs, in particular FOWTs, less feasible and competitive compared to other types of electricity generating technologies. However, even for highly unsteady conditions of 3 deg. and 5 s

pitching, the overall difference in the amplitude between the quasi-steady and fully-attached unsteady results is very small, with a similar size difference in the thrust (Figure 40) and torque (Figure 41) results. However, this is not consistent across the plunging results. Here the difference between the quasi-steady and fully-attached unsteady results is more prominent in the thrust (Figure 35) compared to the torque response (Figure 36).

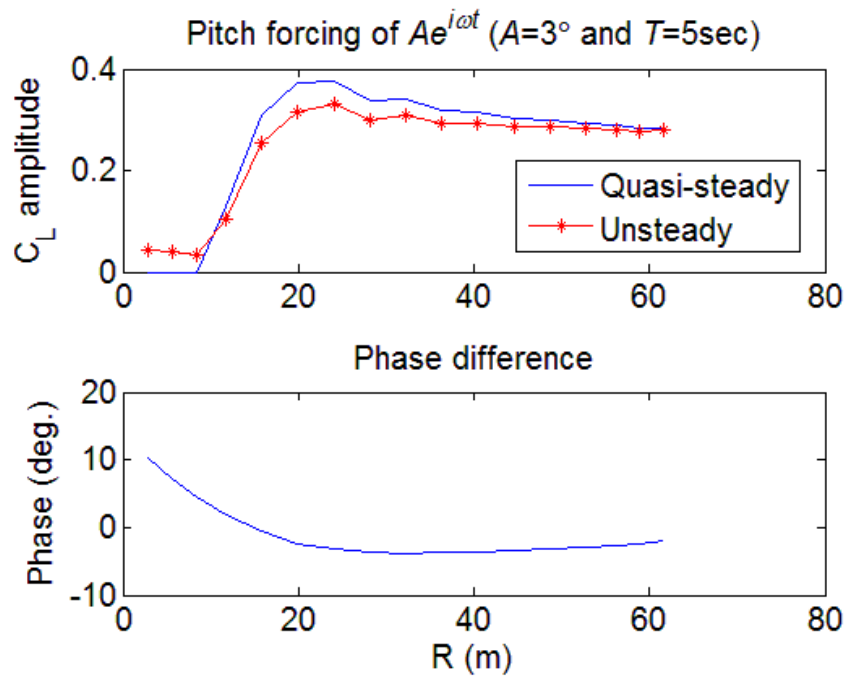


Figure 42 – Comparison between the quasi-steady and unsteady responses in pitching

Whereas the change in the amplitude was shown to be of relatively little importance, change in the phase between both representations of the aerodynamics could lead to very damaging effects on a WT. This is more so applicable to FOWTs, where controllers have an even larger role in providing the overall stability of the system. Here controllers can be used to dampen out some motion in the pitch DoF, hence alleviating tower loads. However, if not accounted for correctly, the phase difference between the quasi-steady and fully-attached unsteady representations of the aerodynamics could lead to negative aerodynamics damping, which could then result in a potential early fail of the system.

## 2.3. Wagner's function

Wagner studied the effect of the wake on an aerofoil in fully-attached unsteady flow in the time-domain. He showed, that for a thin aerofoil undergoing a step change in the angle-of-attack, a solution for indicial lift<sup>5</sup> can be obtained [57].

Wagner solved the problem of an aerofoil that, initially at rest, has an impulsive change in the angle-of-attack. He showed that the circulatory part of the lift coefficient of an aerofoil undergoing some random change in the angle-of-attack in incompressible flow can be expressed as:

$$C_L^c(t) = 2\pi \left[ \alpha(0)\phi(s) + \int_0^s \frac{d\alpha}{d\sigma} \phi(s - \sigma) d\sigma \right] = 2\pi\alpha_{eff} \quad 2.8$$

It should be noted that the non-circulatory terms (including added mass) are not included in this equation and have to be added to obtain the total lift coefficient.

There are different approximations available to Wagner's function. It is often approximated by two time-lags as:

$$\phi(s) \approx 1 - A_1 e^{-b_1 s} - A_2 e^{-b_2 s} \quad 2.9$$

where  $A_1$ ,  $A_2$ ,  $b_1$ ,  $b_2$  vary depending on the application and approximation used.

R.T. Jones's approximation [58] has been shown to agree with the exact solution of the Wagner's function to within 1% [56].

$$\phi(s) \approx 1 - 0.165e^{-0.0455s} - 0.335e^{-0.3s} \quad 2.10$$

Another approximation by W.P. Jones [59] approximates Wagner's function as:

$$\phi(s) \approx 1 - 0.165e^{-0.041s} - 0.335e^{-0.32s} \quad 2.11$$

---

<sup>5</sup> Indicial lift is the lift response to a disturbance that is applied instantaneously at time zero and held constant thereafter; a disturbance given by a step function.

However, in this report an algebraic approximation to Wagner’s function derived by Garrick [60] was used.

$$\phi(s) \approx \frac{s + 2}{s + 4} \quad 2.12$$

While equation 2.12 is not as precise as the equation 2.10 or 2.11, it still agrees with both exponential approximations and the exact solutions to within 2% [61].

A comparison between the previously mentioned Wagner’s function approximations is given in Figure 43.

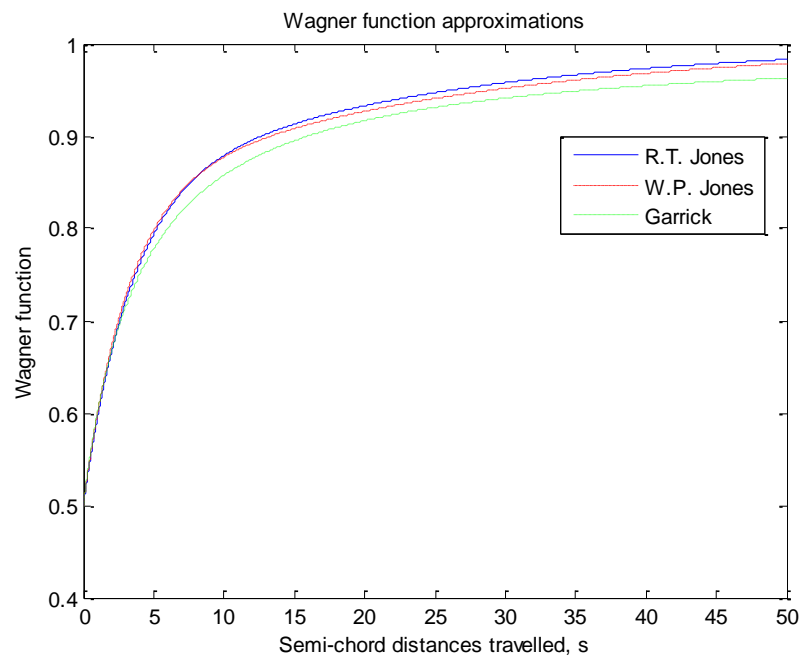


Figure 43 – Comparison of Wagner's function approximations

Wagner’s function states that the instantaneous lift at the start of the motion is equal to a half of the value of the steady lift ( $s = 0 \rightarrow \phi(s) = 0.5$ ). Then, with increasing  $s$ , it increases asymptotically to the steady state value. A more physical explanation would be that with a change in the angle-of-attack there will be a starting vortex shed behind the trailing edge. At the same time, an equal and opposite bound vortex will be formed around the aerofoil.

Garrick and Jones observed that both Theodorsen's transfer and Wagner's indicial response functions are related as a Laplace transform pair.

Wagner's function can be used to model the unsteady motion of a lifting surface by superposition of many small impulsive changes in the angle-of-attack, for which the incremental lift can be calculated.

While Wagner's function can be a very useful tool in modelling unsteady aerodynamics, just as in the case of Theodorsen's function, it loses its validity in the flow situation of wind turbines, where both the free-stream velocity and angle-of-attack are subjected to change. While the angle-of-attack is directly dependent on the free-stream velocity, a non-uniform incident velocity violates the core assumption of both functions.

## **2.4. Velocity perturbation normal to blade**

In [56] Leishman emphasised the importance of distinguishing correctly between the aerodynamic loads that arise from changes in the angle-of-attack over the whole blade (for example, pitching or plunging aerofoil) and those that take time to propagate over the blade. The latter is the result of non-uniform induced velocities over the rotor due to the wake. These can be thought of as a horizontal gust normal to the blade element. While the difference between the two cases can be very inconspicuous, correct methods should be used to model the wind turbine loads.

Theodorsen's and Wagner's theory can be used to model airloads that arise from changes in the angle-of-attack. For aerodynamic loads that arise from velocity perturbations normal to the blade, Küssner and von Karman and Sears [54] solutions to unsteady aerofoil problems should be consulted.

Wind turbines operate in a highly dynamic and unsteady environment with wind turbulence, tower shadow, varying free-stream velocity, blade vibration, pitching of blades, etc. Ideally each effect should be modelled separately and then all combined together through superposition to obtain correct unsteady aerodynamic loads.

Küssner, and von Karman and Sears investigated the problem of an aerofoil entering a vertical gust and found solutions in the time- and frequency-domain, respectively. In a wind

turbine's operation, the equivalent of a vertical gust as referred to by Küssner etc. is a gust in the axial direction, parallel to the free-stream velocity and hence can be superimposed on it, as wind turbine blades, in normal operation, are nearly orthogonal to the free-stream velocity. The problem of an aerofoil entering a vertical gust differs from pitching or plunging of an aerofoil (or any other effect of change in angle-of-attack over the whole blade) in the sense that initially it acts only over some part of an aerofoil and takes time to propagate over the whole blade.

For small reduced frequencies ( $k < 0.1$ ), von Karman and Sears', and Theodorsen's functions converge (see [56] for more details). The biggest drawback of Theodorsen's, and von Karman and Sears' theories is that the solution is in the frequency-domain, which is much harder to code and it also assumes linearity. Solutions for the indicial lift on a thin aerofoil in angle-of-attack change and vertical gust were obtained by Wagner and Küssner.

Finally, Miles [62] obtained results binding together both Wagner and Küssner solutions as a function of convecting gust speeds. Miles showed that as the gust propagation velocity increases from zero to infinity, the solution to the fully-attached unsteady lift changes from the Küssner to the Wagner result.

In this report surge motion was modelled as blade plunging (Theodorsen function), but it also could have been modelled using von Karman and Sears or Küssner solutions (vertical gust). It should be noted that Theodorsen's theory was the preferred choice of this author and this should not be taken as an indication of Küssner's theory inferiority.

## 2.5. Van der Wall and Leishman

Van der Wall and Leishman [63] showed that for moderate values of reduced frequencies all theories that represent unsteady incident velocity as a fore-aft moving aerofoil, such as Isaacs [64, 65], Greenberg [66], Kottapalli [67] and Johnson [68], give the same result as Theodorsen's theory, when the time-varying resultant velocity is inserted in Duhamel's integral form (response of a system to some arbitrary time-varying excitation).

This allows the fully-attached unsteady lift in incompressible flow to be expressed as:

$$L = \pi\rho\frac{c}{4}(V\dot{\alpha} + \dot{V}\alpha + \ddot{h}_{1/2}) + \pi\rho cV\left[w_{3/4}(0)\phi(s) + \int_0^s \frac{dw_{3/4}}{d\sigma}\phi(s-\sigma)d\sigma\right] \quad 2.13$$

where  $\rho$  is the air density,  $c$  is the chord length,  $\alpha$  is the angle-of-attack measured between the chord and the resultant velocity,  $V$ ,  $\ddot{h}_{1/2}$  is the plunge acceleration at the mid-chord,  $w_{3/4}$  is the downwash at the three-quarter point of the chord,  $\phi$  is the indicial function, and  $s$  is the non-dimensional time-scale:

$$s = \frac{2}{c} \int_0^t V dt \quad 2.14$$

describing the distance (in semi-chords) travelled by the wake in the time-varying stream.

The first term in equation 2.13 is the non-circulatory part of the lift, including due to the added mass - acceleration of the air surrounding the blade. The second term in the same equation is the circulatory part of the lift including Duhamel's integral, which describes the 'memory effect' of the vorticity already shed into the wake.

A modified version of the Van der Wall and Leishman formulation (equation 2.13) was taken as the basis for the fully-attached unsteady lift coefficient calculations. Having shown that the non-circulatory effects can be neglected (see **Error! Reference source not found.**) when considering wind turbines, the circulatory part of the lift coefficient can be shown to be:

$$C_L^c(s) = \frac{2\pi}{V(s)} \left[ V(s_0)\alpha(s_0)\phi(s) + \int_{s_0}^s \frac{d(V\alpha)}{d\sigma}\phi(s-\sigma)d\sigma \right] \quad 2.15$$

After some mathematical adaptations (see A1.4 for full derivation), the circulatory part of the lift coefficient discretised in the time-domain becomes:

$$C_L^c(s_n) = \frac{2\pi}{V(s_n)} \left| V(s_n) \alpha(s_n) + \sum_{i=1}^n \left\{ 2 \left[ \frac{d(V\alpha)}{ds} \right]_{s=s_i} \ln \left[ \frac{s_i - (s_n + 4)}{s_{i-1} - (s_n + 4)} \right] \right\} \right| \quad 2.16$$

Alternatively, the effective angle-of-attack can be expressed as:

$$\alpha_{eff}(s_n) = \frac{1}{V(s_n)} \left| V(s_n) \alpha(s_n) + \sum_{i=1}^n \left\{ 2 \left[ \frac{d(V\alpha)}{ds} \right]_{s=s_i} \ln \left[ \frac{s_i - (s_n + 4)}{s_{i-1} - (s_n + 4)} \right] \right\} \right| \quad 2.17$$

From equations 2.16 and 2.17, it can be seen that the circulatory lift coefficient and the effective angle-of-attack can be represented as the sum of two terms. The first is the quasi-steady component and the second is the so-called ‘memory effect’, which takes into account the propagation of the wake. The effective angle-of-attack can be used to look up  $C_L$  values for the NREL 5MW turbine.

Before equations 2.16 or 2.17 could be used to simulate 6 DsoF of a floating wind turbine, the time discretised fully-attached lift code was verified against some previous work of Leishman [56].

### 2.5.1. Code validation

Van der Wall and Leishman’s results were used in the form of equation 2.16 and a sinusoidally varying free-stream velocity was applied (equation 2.18) with a reduced frequency  $k = 0.2$ , whilst keeping the angle-of-attack constant. The ratio between the fully-attached unsteady and the quasi-steady lift coefficients is shown in Figure 44.

$$U(t) = U_\infty [1 + \lambda \sin(\omega t)] \quad 2.18$$

with  $\lambda = 0.2, 0.4, 0.6$  and  $0.8$ .

Results in Figure 44 match very well with those presented by Leishman (Figure 45). The small discrepancies between both figures can be attributed to the fact that the non-circulatory effects, however small they are, were included in Leishman’s calculations and ignored in this report. The discretised (equation 2.16) results show a slight shift to the left of the plot, when compared to Leishman’s results, almost aligning with the Euler (CFD) results. Also to note, different formulations for the Wagner’s function were used in both cases.

The results are accurate enough to be used in floating wind turbine different DoF simulations to gain some insight into the significance of the fully-attached unsteady aerodynamics in floating wind turbine systems.

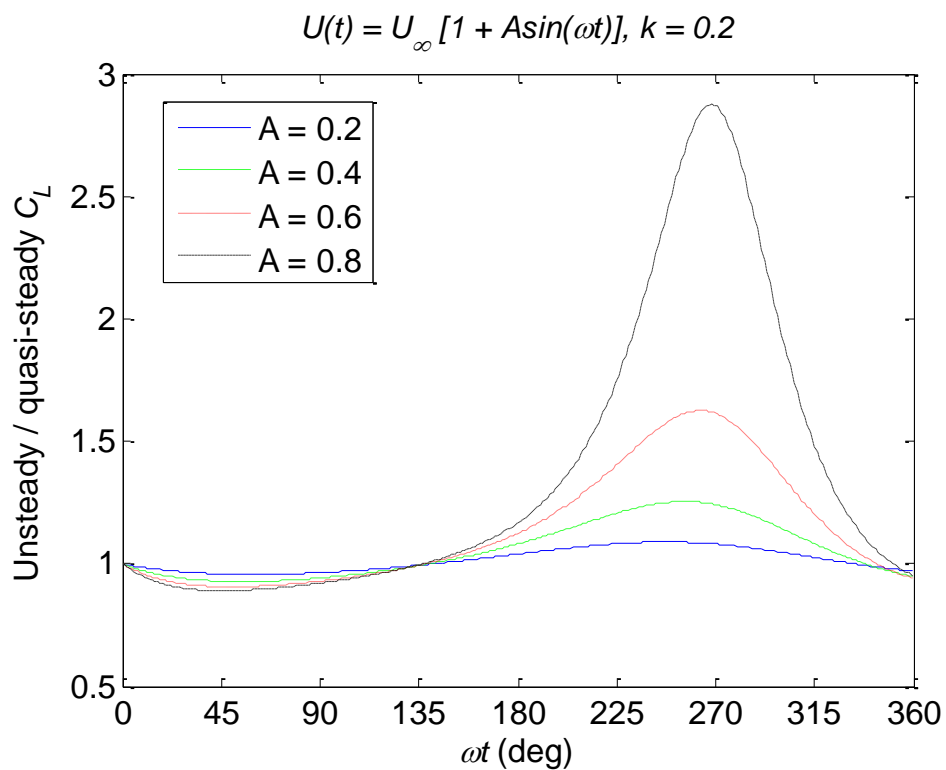


Figure 44 – Unsteady over quasi-steady lift ratio for an aerofoil at a constant angle-of-attack and oscillating free-stream velocity

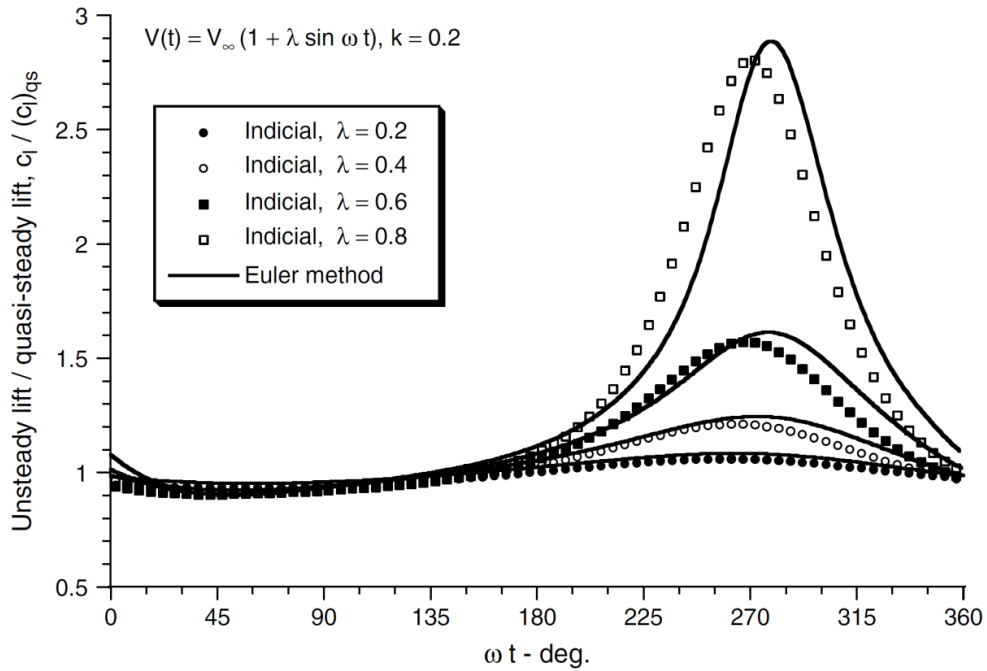


Figure 45 – Effects of the free-stream velocity fluctuations on the unsteady lift of an aerofoil at a constant angle-of-attack [56]

### 2.5.2. Downwash

The downwash used in equation 2.13 is a velocity component that is normal to the chord. Using thin aerofoil theory, the downwash at three quarters of the chord can be expressed as:

$$w_{3/4}(t) = \alpha_{qs}(t)V(t) + \dot{h}(t) + \frac{c}{2} \left( \frac{1-2a}{2} \right) \dot{\alpha}(t) \quad 2.19$$

An unsteady aerofoil can be seen as a problem of both pitching,  $\frac{c}{2} \left( \frac{1-2a}{2} \right) \dot{\alpha}(t)$ , and plunging,  $\dot{h}(t)$ , motion on top of the quasi-steady component,  $\alpha_{qs}(t)V(t)$ .

The first two terms in equation 2.19 are self-explanatory. The third term (pitch rate) produces a linear variation in the normal perturbation velocity. If pitching is about an axis at  $a$  semi-chords from the mid-chord, then downwash at any point on the chord can be expressed as:

$$w(x) = \dot{\alpha} \left( x - \frac{ac}{2} \right) \quad 2.20$$

Fixing the coordinate system to the mid-chord, with  $x$  being positive towards the aft, the downwash at  $\frac{3}{4}$  of a chord due to pitch rate can now be expressed as in equation 2.19.

Because of the way the angle-of-attack is calculated in the in-house written MATLAB code developed to simulate motion of FOWTs in each of the 6 DsoF (see Figure 56 for the flowchart of the code) (assuming that the blades are rigid, plunging is represented as change in the free-stream velocity and no pitching applied), the downwash at  $\frac{3}{4}$  of the chord can be simply expressed as the product of the resultant velocity and quasi-steady geometric angle of attack,  $\alpha_{qs}(t)V(t)$ .

### 2.5.3. Non-circulatory aerodynamics

The non-circulatory part of equation 2.13 is the apparent- or added-mass and other non-circulatory force contributions to the unsteady lift that arise from the  $\frac{\partial \varphi}{\partial t}$  term in the unsteady Bernoulli equation. These account for the pressure forces required to accelerate the fluid in the near vicinity of the aerofoil.

$$\text{Non-circulatory lift} = \pi \rho \frac{c^2}{4} (V\dot{\alpha} + \dot{V}\alpha + \ddot{h}_{1/2}) \quad 2.21$$

For the frequencies and amplitudes of fluctuating velocity that can be found on a helicopter, these non-circulatory forces are very small [61]. Intuitively, the non-circulatory effects associated with wind turbines should be even smaller than those of helicopters.

Figure 46 shows the two main components of the non-circulatory forces associated with wind turbine blades. For a turbine in a pure surge motion of 1 m amplitude and 5 second period, the non-circulatory forces on the blade close to the hub and tip are almost negligible.

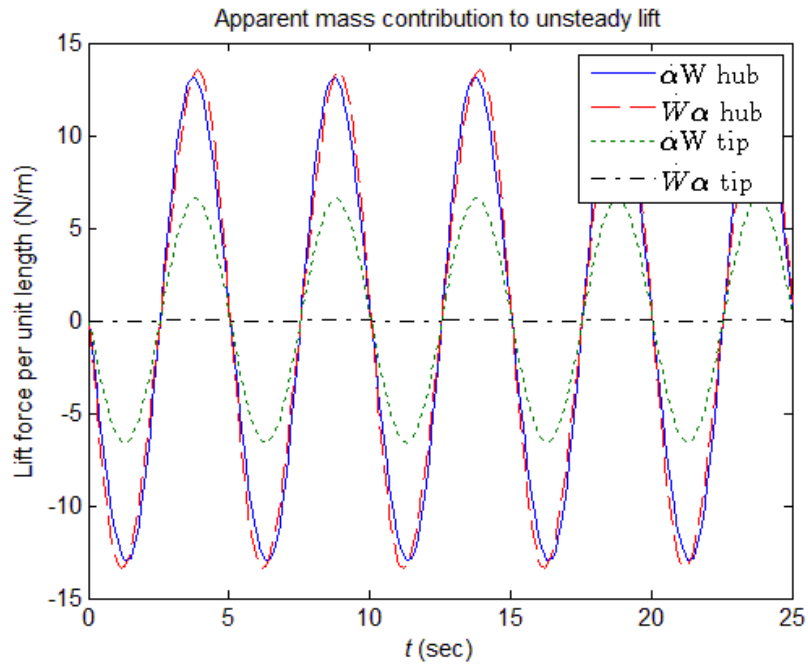


Figure 46 – Non-circulatory forces on an NREL 5MW turbine blade (surge  $A=1$  m and  $T=5$  s)

The last term in equation 2.21 gives the apparent mass force due to the plunging of blades. The explanation below shows that this term is very small and can also be ignored.

Assuming that surge motion of the turbine is a pure plunging motion of the blade:

$$\begin{aligned}
 \text{plunge displacement} &= A \sin(\omega t) \\
 \text{plunge velocity} &= \omega A \cos(\omega t) \\
 \text{plunge acceleration} &= -\omega^2 A \sin(\omega t)
 \end{aligned}
 \tag{2.22}$$

Looking at the somewhat extreme case of a surge amplitude of 1 m and a period of 5 s, plunge acceleration becomes:

$$-1.58 \sin(1.26t)
 \tag{2.23}$$

This leads to maximum absolute values of lift of 38 N/m (assuming the chord is 5 m wide), meaning that, compared to its circulatory counterpart, the non-circulatory components are small enough to be ignored. However, if a blade were to be modelled as elastic with vibrations at low frequencies, added mass terms would have to be considered.

From this point onwards, only the circulatory part of the Leishman and Van der Wall equation is considered, as the turbine blades analysed in this chapter are assumed to be rigid.

#### 2.5.4. Axial induction factor

While the Van der Wall and Leishman derivation takes account of shed vortices, it is the axial induction factor that summarises the bound vorticity on the rotor disc; with the hub and tip loss adjustment for the axial factor allowing trailed vortices to be incorporated.

Figure 47 shows the axial induction factor for the NREL 5MW wind turbine operating at near rated speed.

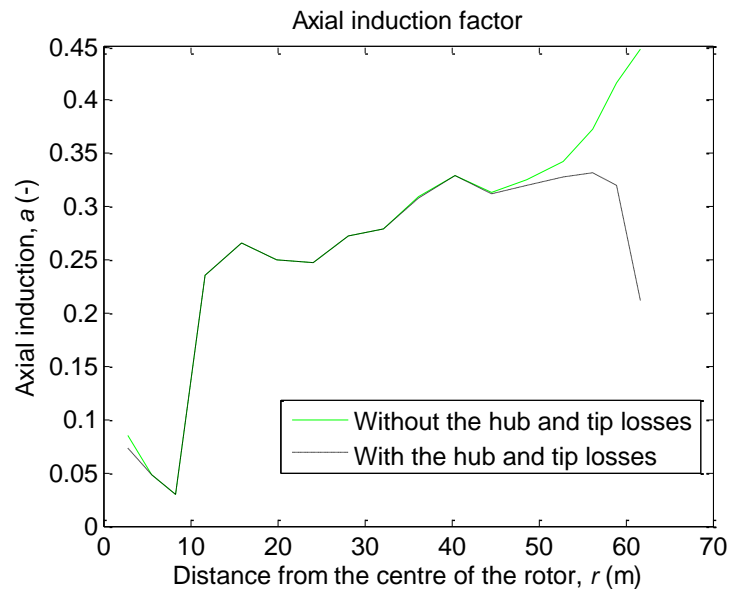


Figure 47 – Axial induction factor distribution for the NREL 5MW turbine

While there is very little change close to the blade root, the values close to the tip can differ as much as two times, when the axial induction factor is calculated with and without the tip loss modification. Because it is close to the tip where the majority of the torque comes from, including or excluding axial induction factor could significantly alter results.

At the initiation of the fully-attached unsteady aerodynamic code in MATLAB, the axial induction factors are calculated and henceforward are kept constant, while the system is undergoing motion in different DsoF. This is consistent with the assumption that for the

majority of the blade it is the in-plane velocity that dominates the resultant velocity seen by each blade element and a small change in the axial induction factor would not alter results significantly.

In future, for more precise and realistic simulations the axial induction factor should be updated at every time step, especially in simulations that involve large induced velocities (small periods and large amplitudes of displacement).

### 2.5.5. Lift versus drag

Van der Wall's and Leishman's fully-attached unsteady aerodynamic theory takes account only of the unsteady lift. Drag is not considered.

In this report unsteady drag was also not considered. However, its significance and contribution to loads is investigated below.

Figure 48 shows a typical cross-section of an aerofoil with lift and drag components that are normal and tangential to the resultant velocity,  $W$ .

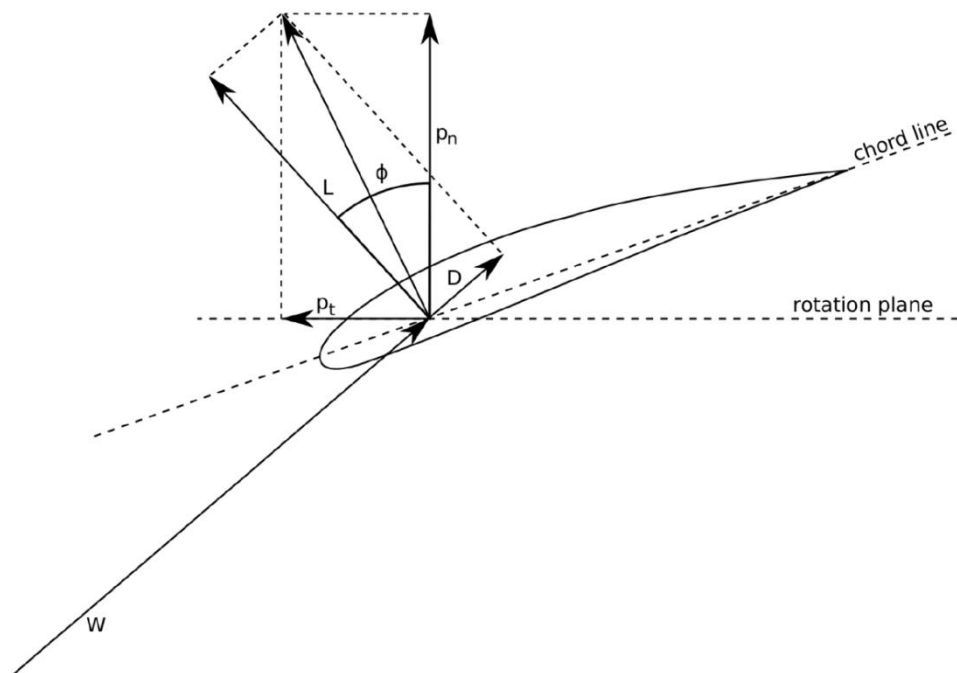


Figure 48 – Forces on an aerofoil

Lift and drag can be split into components that are normal to and parallel to the rotational plane.

$$\begin{aligned} C_n &= C_L \cos \phi + C_D \sin \phi \\ C_t &= C_L \sin \phi - C_D \cos \phi \end{aligned} \quad 2.24$$

Figure 49 and Figure 50 show the thrust and in-plane force on a wind turbine blade that is experiencing surge motion of 1 m amplitude and 10 s period. The NREL 5MW blade geometry and aerofoil data (look-up tables) were used to obtain lift and drag coefficients for the angles-of-attack calculated using the quasi-steady assumption.

As predicted, the total thrust and in-plane force on a blade are highly dominated by the lift components. While at close distances to the hub the angle-of-attack could be relatively high and yield a much higher drag value, at the blade tip, where it really matters from the thrust and torque perspective, angles-of-attack are very small as aerofoils are designed in such a way to produce very high lift to drag ratios.

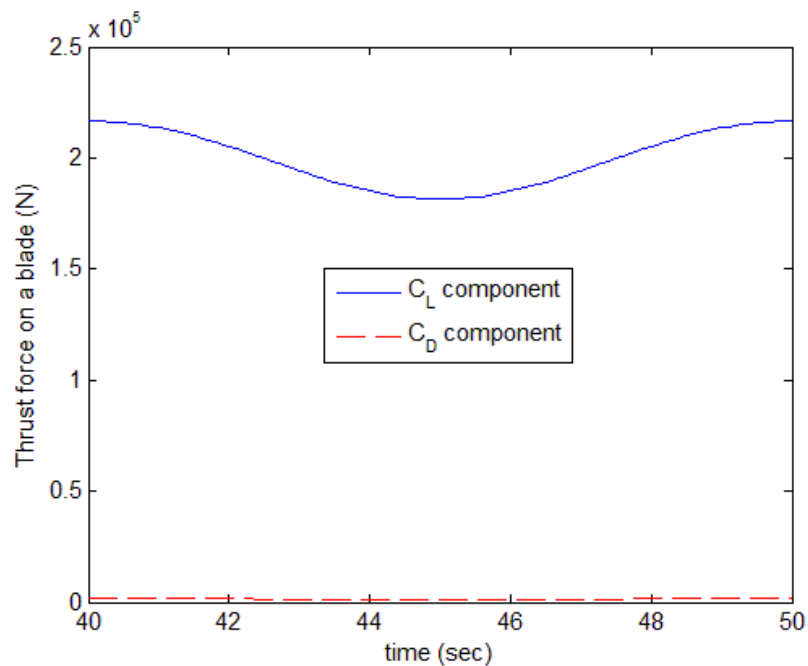


Figure 49 – Drag and lift contributions to thrust force on a blade experiencing sinusoidal surge motion of  $A = 1$  m,  $T = 10$  s

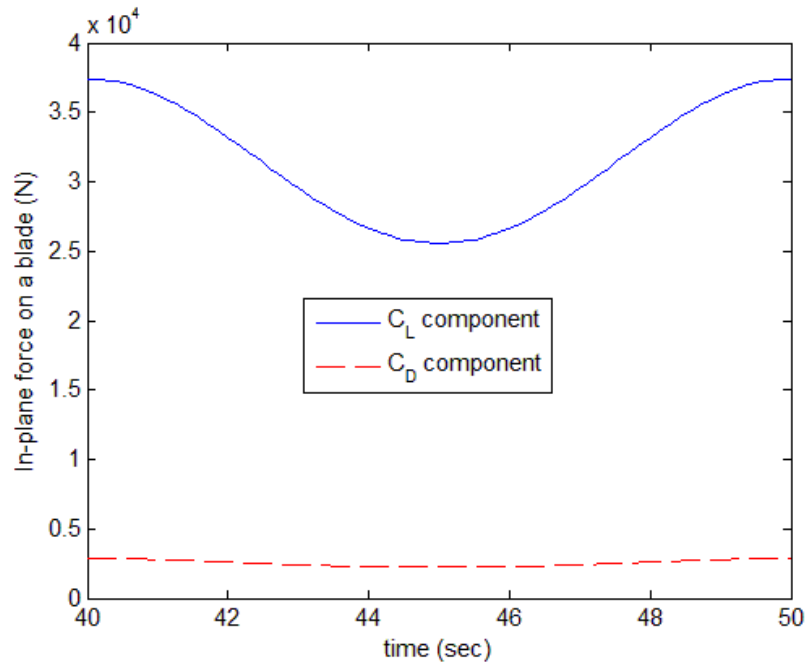


Figure 50 – Drag and lift contributions to in-plane force on a blade experiencing sinusoidal surge motion of  $A = 1$  m,  $T = 10$  s

It should be noted that this assumption of negligible drag is only valid up to rated conditions, where drag is dominated by surface friction and flow is assumed to be fully-attached. Between the rated and cut-off conditions, the pitch to feather procedure would lower  $C_L$  values (while maintaining fully-attached flow) making them more comparable to  $C_D$ , particularly in the in-plane case.

The most likely region of encountering unsteady flow is in below-rated operation (see Figure 30), where lift components dominate the loads on a blade. This allowed drag to be eliminated from the scope of this study.

### 2.5.6. Thin aerofoil theory

All previously discussed theories, including Theodorsen's, and Van der Wall and Leishman's, are based on thin aerofoil theory. This means that lift can be directly calculated and is proportional to the angle-of-attack for incompressible and inviscid flow.

In thin aerofoil theory, the flow around an aerofoil is modelled as a 2-D flow around an aerofoil with zero thickness and infinite span. This, of course, is an idealised case, as real blades (either on aircrafts or wind turbines) have finite thickness and span.

Another very important intrinsic property of thin aerofoil theory is that it doesn't take into account stalling of the aerofoils.

Since the initial development of thin aerofoil theory, a few adjustments have been made specifically for wind turbine calculations. [1] suggests substituting  $2\pi\alpha$  with  $0.1/\text{degree}$  for calculation of the lift coefficient. Figure 51 shows a comparison between two linear  $C_L/\alpha$  curves and NACA64\_A17 lift coefficient data (look-up table).

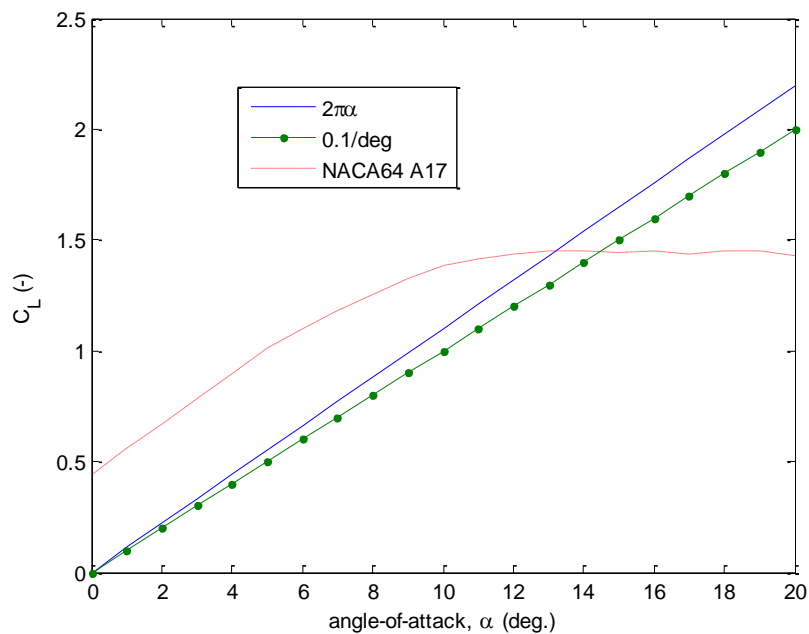


Figure 51 – Different lift coefficient slopes

There are two main differences in Figure 51 between the linear lift coefficient slopes and the data from the look-up table.

- Initial offset on the y-axis due to the camber of the aerofoil.
- Inclusion of 'light' stalling region for NACA64\_A17 aerofoil.

Whereas cambered aerofoil adjustment can be easily made to the thin aerofoil theory, inclusion of stalling of an aerofoil is impossible. This limits usage of the thin aerofoil theory to the linear part of the slope (associated with the fully-attached flow).

There are two different ways to modify thin aerofoil theory, so that it could be used with cambered aerofoils:

1. Use  $C_L = C_{L_0} + 2\pi\alpha$ , where  $C_{L_0}$  is the lift coefficient at 0 angle-of-attack,
2. Use  $C_L = 2\pi\alpha_{C_L=0}$ , where the angle-of-attack is calculated from the zero lift line instead of the chord.

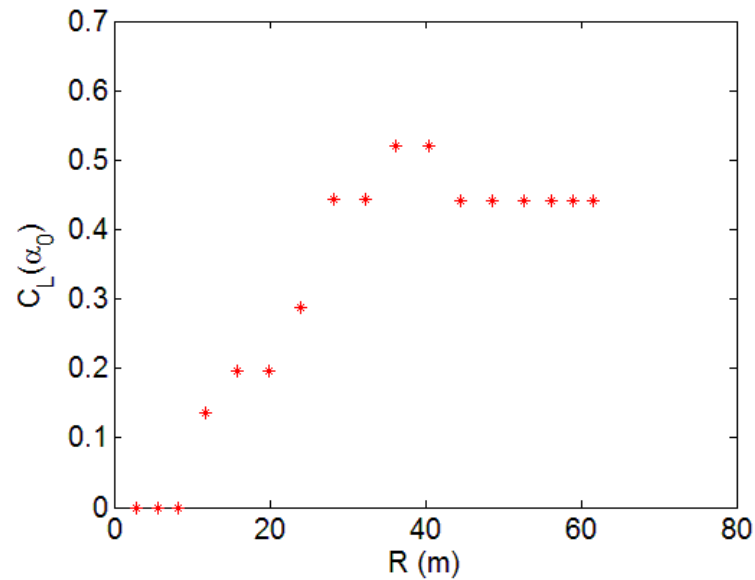


Figure 52 – Distribution of lift coefficient at zero angle-of-attack for the NREL 5MW turbine

In Figure 52, seven different aerofoils can be identified for the NREL 5MW turbine.

The importance of the stalling region is shown in Figure 53, where two different techniques were used to calculate unsteady lift:

1. Thin aerofoil theory together with the effective angle-of-attack (see equation 2.17).
2. Lift coefficient values were looked-up for the NREL 5MW turbine from the appropriate look-up tables for the already calculated effective angles-of-attack.

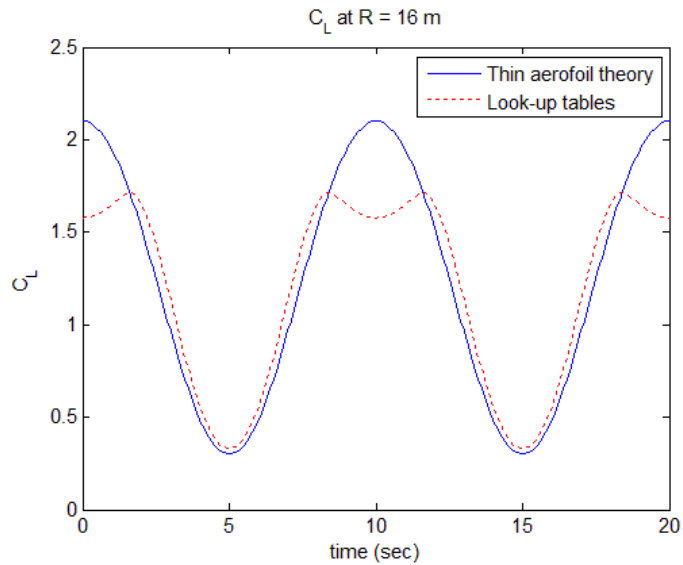


Figure 53 – Comparison between different methods of calculating lift values

Figure 53 shows the unsteady lift for surge motion as experienced by a blade element of the NREL 5MW wind turbine 16 m from the hub. Surge amplitude was set to 5 m and period to 10 s. Aerodynamics were modelled as quasi-steady.

Very high values of lift coefficient can be observed when thin aerofoil theory is used. Such high lift coefficient values are very unlikely. High values of lift are usually expected much closer to the tip of the blade (blade length 61.5 m), and even then for NACA64\_A17 (aerofoil profile at the tip) the maximum achievable values are below 1.5.

The look-up table results in Figure 53 show some small dips at 0, around 10 and 20 seconds. These are attributed to the blade element entering stalling region. As the free-stream velocity increases, due to surging of the turbine, large angles-of-attack are produced.

Figure 54 below shows another example of the comparison of two different techniques (thin aerofoil theory and look-up table). Four different curves represent the normal force on the blade calculated using 4 different methods. These include:

- Quasi-steady loading calculated using look-up tables,
- Quasi-steady loading calculated using thin aerofoil theory,
- Fully-attached unsteady loading calculated using look-up tables,
- Fully-attached unsteady loading calculated using thin aerofoil theory.

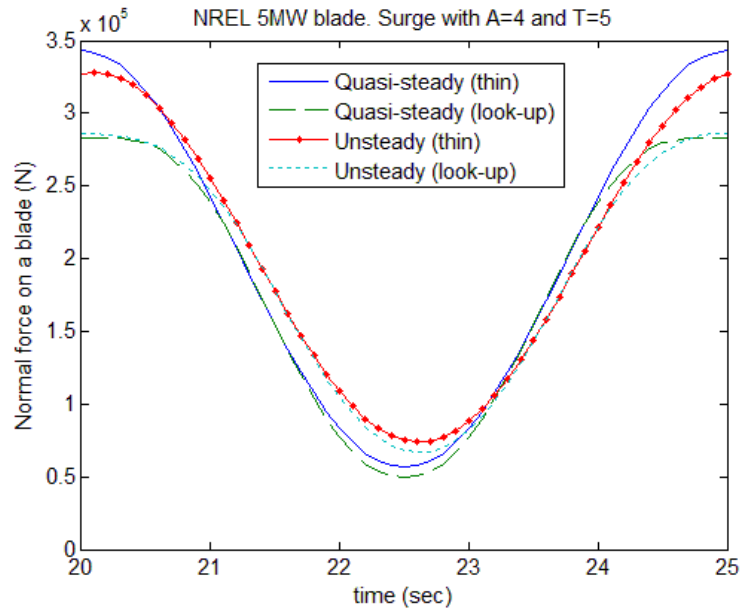


Figure 54 – Normal loading on a blade on a system that is surging with 4 m amplitude and 5 s period

Three main differences between both sets of plots can be observed.

1. Increased amplitude of loading for the thin aerofoil results.
2. A phase difference between the quasi-steady and unsteady results, as expected and described in previous sections.
3. Significant difference in the peak loading at 20 and 25 seconds.

From Figure 53, because of the more realistic results obtained using the look-up table technique, it is the preferred technique in this thesis. However, because the Van der Wall and Leishman formulation is limited to the fully-attached region of operation, and flow separation is unavoidable for some combinations of amplitudes and periods used with DoF simulations, the results for severe wave states (small periods and large amplitude of motion) should be interpreted with some care.

As a potential suggestion for future work, the MATLAB code could be modified to raise a flag every time the stalling region is entered.

### 2.5.7. Wake development

The Leishman and Van der Wall theory incorporates two components: quasi-steady and 'memory effect'. Because the 'memory effect' takes into account the history of the

resultant velocity with which the wake convects downstream, it is important to implement a time lag for the wake to develop and results to settle down.

Figure 55 shows 3 different plots for the normal force on a blade that is surging with 1 m amplitude and 5 s period calculated using the look-up tables and thin aerofoil theory. The main plot shows the overall response of a blade while plots 2 and 3 concentrate on the peak and trough of the loading.

The effect that development of the ‘memory effect’ has on the overall loading on a blade can clearly be seen in plots 2 and 3 of Figure 55. While the difference is not large, it takes a few periods for the ‘memory effect’ to develop and extremes of the loading to settle to some ‘steady’ values.

While one could use simulation results starting with the first period of the motion, they would not represent a real case scenario, as there is no ‘memory effect’ before time equals zero (it takes time for the wake to develop). This is also very unlikely as there is always some history of wind, except for the rare occasions when there was no wind at all and system started moving in some DoF. Having said that, it is very hard to imagine a wake that is perfectly sinusoidal.

All Van der Wall and Leishman theory’s results presented in this thesis use values from the 5<sup>th</sup> period onwards, which sanctions to assume that the results/simulations have reached their steady periodic values.

### *2.5.8. Simulations*

A floating spar-type offshore wind turbine’s motion in each DoF was simulated by imposing change in the free-stream velocity and/or the rotational velocity that would be seen by each blade element for some enforced floater displacement amplitude and period. By doing it this way, it permitted to decouple the wind turbine from the floater, hence significantly reducing the computational complexity.

It should be noted that the environment around the wind turbine was simplified. This included ignoring the following:

- Wind shear,

- Tower shadow,
- Tangential induction factor,
- Turbulence in wind.

By defining floating wind turbine motions as purely oscillatory with some amplitude and period of displacement, underwater currents, icing and similar issues were ignored. The wind turbine blades and tower were assumed to be rigid.

Also, worth mentioning is that no controller was used. The specified blade rotational velocity, axial induction factors and blade pitch were kept constant and not adjusted during simulations.

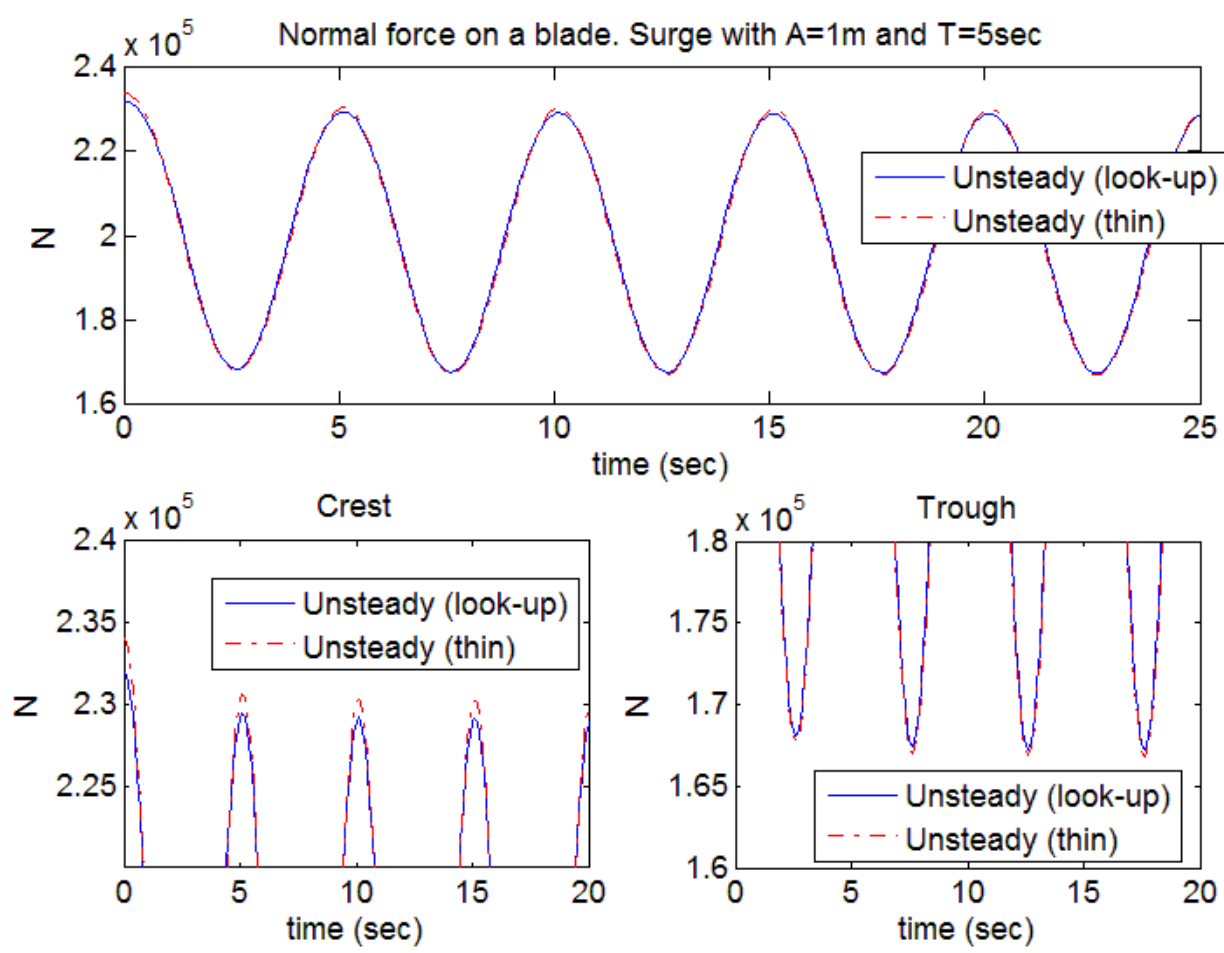


Figure 55 – Settling of initial values for fully-attached loading

### 2.5.8.1. Excitation

All MATLAB simulations were run with amplitudes from 1–5 m or deg. with a step size of one and periods from 5–25 s with a step size of 5 s. The extreme ends of the simulations results, such as 5 m or 5° amplitude with 5 s period, or 1 m, or 1 deg. amplitude with 20-25 s periods, can be discarded as they represent either cases that are highly unsteady, leading to separated flow, or are so ‘slow’ that the quasi-steady assumption can be used with them.

One should note not to mix-up motion of 1 m amplitude and 5 second period with say 5 m amplitude and 25 second period. While the ration of  $A/T$  and the peak velocities  $\omega A$  are the same, there is much less time to achieve this acceleration and deceleration in the first case (1 m and 5 s) leading to a much more unsteady conditions.

When calculating the normal force on a blade, only the lift force was split into the normal and tangential components. Components of drag were ignored. Firstly, because of its relatively small size in the fully-attached flow (drag mainly coming from surface friction). Secondly, because of the lack of available formulation for calculating the unsteady drag coefficients for the fully-attached unsteady flow.

### 2.5.8.2. Initial Conditions

The table below summarises all initial conditions and data used in the simulations.

Table 7 – Initial conditions

NREL 5MW	
Chord distribution	
Aerodynamic twist	
$C_L$ look-up tables	
Rotor velocity	1.2 rad/s
Blade pitch angle	0°
Free-stream velocity	10 m/s
Distance from CoG to hub	150 m

### 2.5.8.3. Flow Chart

Shown below is a simplified version of the MATLAB code flowchart, which is based on equation 2.17.

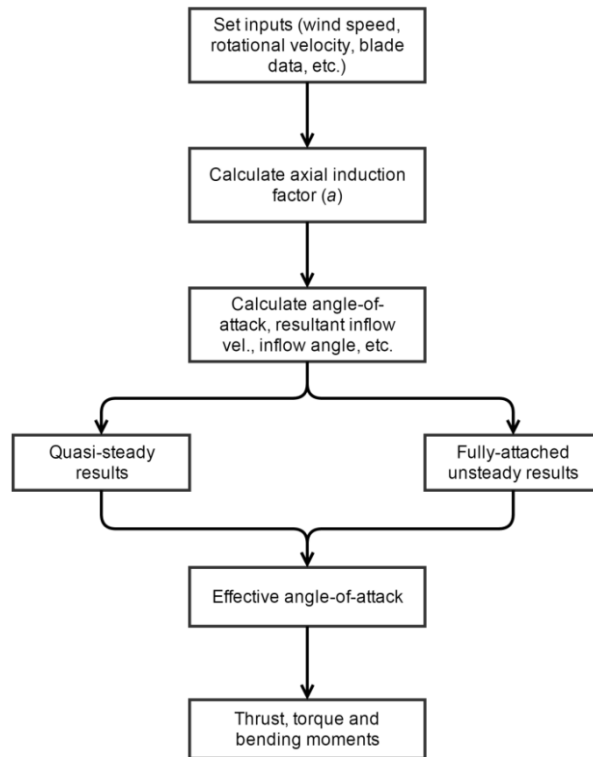


Figure 56 – Simplified flowchart of the fully-attached aerodynamics MATLAB code

## 2.5.9. Results

Each DoF was modelled as a change in the free-stream velocity or the rotational velocity, or both. The derivation for the surge DoF is given below. For other DoF please see A1.5. The results presented below are for the whole blade.

### 2.5.9.1. Surge

Surge is a translational DoF which is characterised by the fore-aft movement of the system (see Figure 57). Oscillatory motion of the system can be represented as an oscillatory change in the free-stream velocity seen by each blade element (Figure 58). Any change in the free-stream velocity, due to surge motion of the system, is experienced equally by all blade elements.

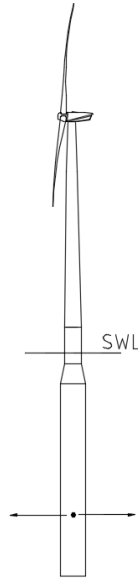


Figure 57 – Surge motion (side view)

Defining surge displacement as  $A \sin(\omega t)$ , surge velocity is  $\omega A \cos(\omega t)$ . This can then be superimposed on the free-stream velocity (as shown in Figure 58 using the red arrows).

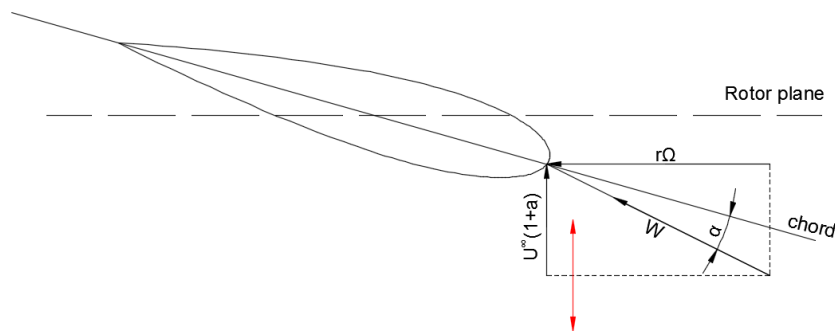


Figure 58 – Velocity components in surge motion

From Figure 58, the apparent wind speed and the corresponding angle-of-attack ‘seen’ by each blade element at each time step can now be expressed as:

$$W(t) = \sqrt{(r\Omega)^2 + [U_\infty(1-a) + \omega A \cos(\omega t)]^2} \quad 2.25$$

$$\alpha(t) = \tan^{-1} \left[ \frac{U_\infty(1-a) + \omega A \cos(\omega t)}{r\Omega} \right] - \beta \quad 2.26$$

where  $\beta$  is the blade twist angle together with the blade pitch angle.

In equations 2.25 and 2.26 the axial induction factor,  $a$ , is only applied to the free-stream velocity,  $U_\infty$ . However, because motion in the surge DoF will induce change in the free-stream velocity as seen by the blade, it might have been more appropriate for the axial induction factor to be applied to the total out-of-plane of rotation velocity as shown in equations 2.27 and 2.28.

$$W(t) = \sqrt{(r\Omega)^2 + \{[U_\infty + \omega A \cos(\omega t)] \times (1 - a)\}^2} \quad 2.27$$

$$\alpha(t) = \tan^{-1} \left[ \frac{[U_\infty + \omega A \cos(\omega t)] \times (1 - a)}{r\Omega} \right] - \beta \quad 2.28$$

This way of expressing the total relative wind speed normal to the rotor disc may be particularly valid as the motion in the surge DoF is of low-frequency compared to blade structural vibrations at high frequencies and hence could have a large overall effect on the axial induced velocity. However, in this study equations 2.25 – 2.26 were used because – as described in 2.5.4 – the axial induction factor was only calculated at the initiation of the MATLAB code and henceforward kept constant. The approach used in this thesis is consistent with how this issue is currently treated in FAST. However, as discussed in 3.1.3.1 this might be a potential shortcoming of FAST. It should be noted that this point is also valid for the pitch and yaw DsoF as motion in these DsoF will induce change in the free-stream velocity as seen by the blade.

The normal force on a blade, for a platform in pure surge with 1 m amplitude and 10 s period, is shown below in Figure 59. While there is no large difference between the four curves, the fully-attached unsteady aerodynamics shows a smaller range of loading, when compared to the quasi-steady counterparts. The expected change in the phase of the fully-attached unsteady aerodynamics can also be seen in the plot (the unsteady results lagging behind the quasi-steady).

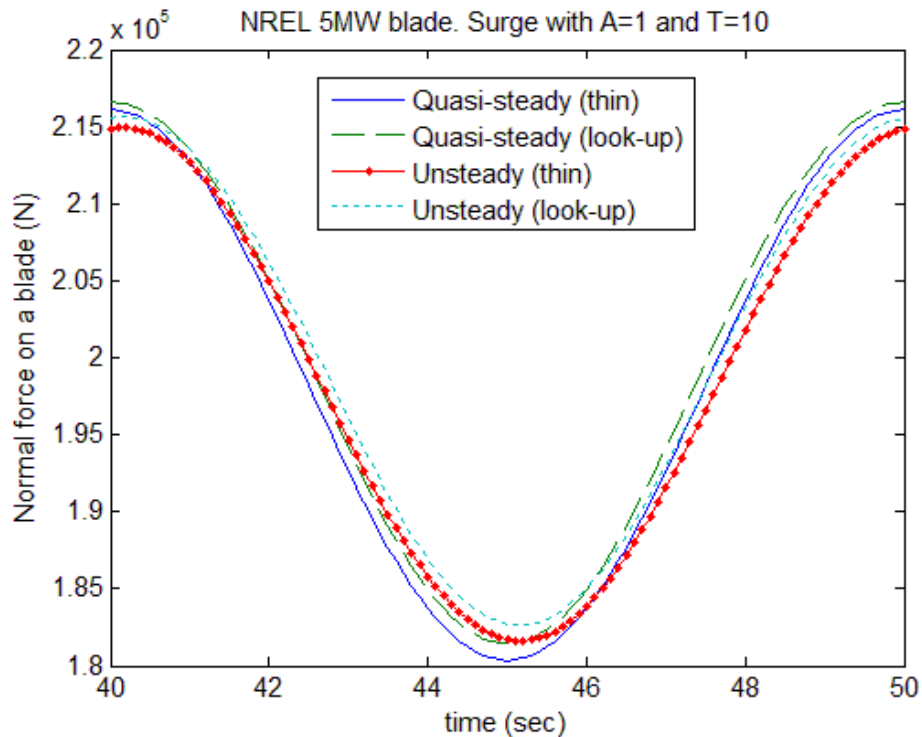


Figure 59 – Normal force on an NREL blade for 1 m amplitude and 10 s period surge motion

In surge simulations, like in all the other DsoF, the lift coefficient values were calculated using thin aerofoil theory and from the NREL 5MW look-up tables.

The following forces and bending moments were calculated:

- Normal force on a blade (also called thrust),
- In-plane force on a blade,
- Out-of-plane bending moment at the root,
- In-plane bending moment at the root.

It is not necessarily correct to assume that the normal force and thrust force is the same thing. Slight coning of the blades will lead to a misalignment between the two forces. Also, twisting of the blades will lead to coordinate system that is rotating along the blade span. However, as mentioned before, because we are only looking for a rough estimate, both these issues were ignored at the time of writing.

Figure 60 shows the normal force on a blade imitating surge motion of the floating wind turbine of 1 m amplitude and 5 s period.

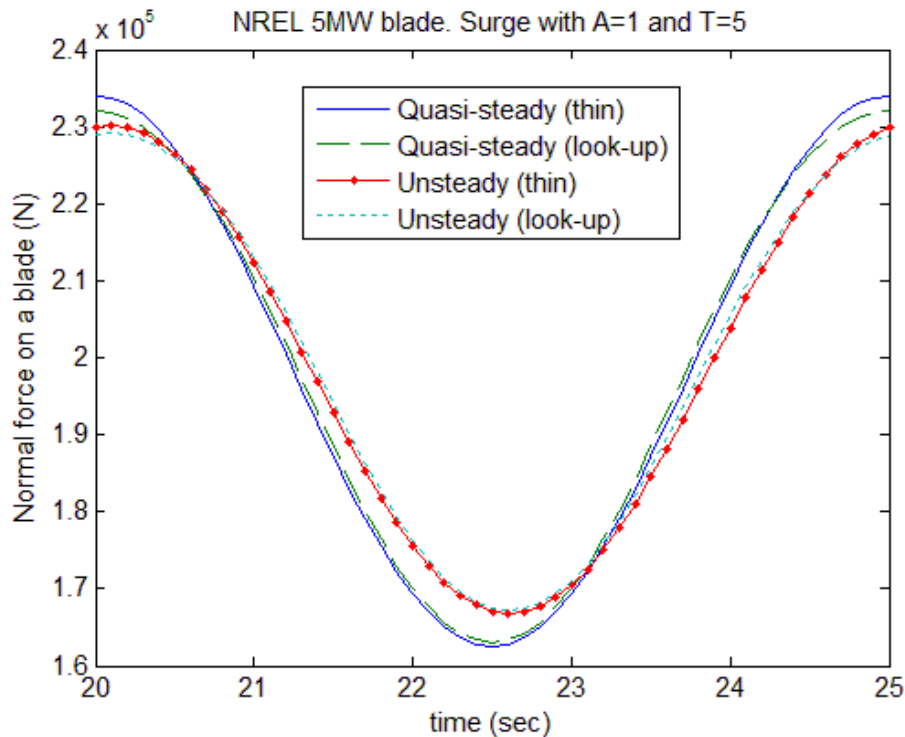


Figure 60 – Normal force on a blade in surge motion of 1 m amplitude and 5 s period

Compared to Figure 59 there is a noticeable difference in the amplitude between the quasi-steady and fully-attached unsteady results.

Differences in the mean loading between quasi-steady and fully-attached unsteady aerodynamics for the thin aerofoil and look-up table techniques are shown in Figure 61 and Figure 62.

From Figure 61:

- The fully-attached unsteady results have higher mean loading compared to the quasi-steady.
- The difference between the both cases diminishes with increasing period and diminishing amplitude.

The second point is also very intuitive as one would expect to see larger unsteady effects at large amplitudes and small periods of motion (large and rapid changes in induced velocities).

The results presented in Figure 61 are not completely linear and show a small difference between the mean thrust values calculated using both aerodynamic representations. This is

unexpected as linear thin aerofoil theory was used to obtain these results. The author believes that this is a direct result of using small angle approximations, which with increasing unsteadiness (small periods and large amplitudes of motion) will lead to increasing errors. This is consistent with other results presented in A1.6.

Comparing the mean loading calculated using the thin aerofoil theory (Figure 61) and the NREL 5MW look-up tables (Figure 62), an overall matching trend can be observed between both plots with the difference between the quasi-steady and unsteady results decreasing with increasing period.

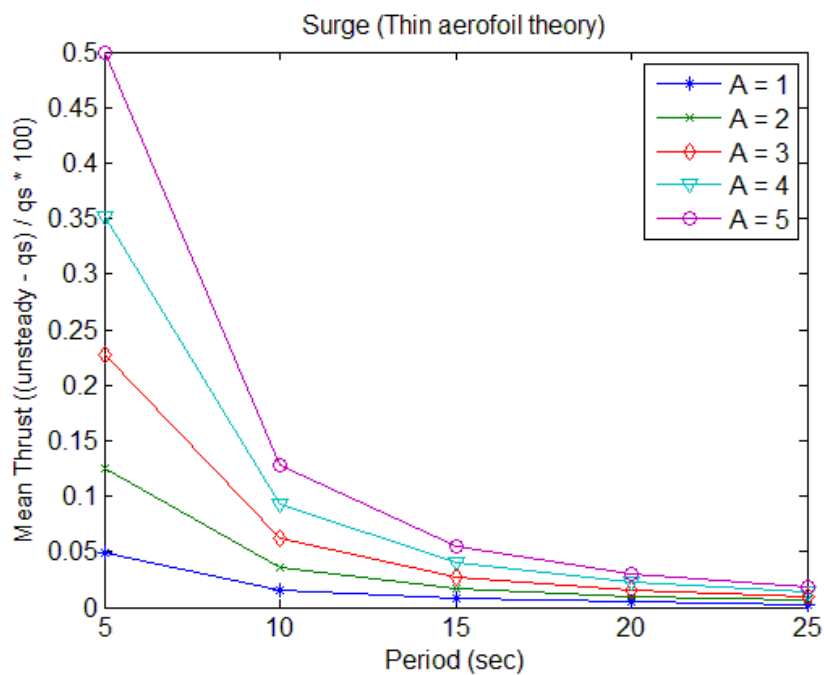


Figure 61 – Mean of normal force on a blade in surge (thin aerofoil theory)

A more detailed examination of the normal force results obtained using the look-up table technique (Figure 63) shows that in time ranges from 20 to 21 and 24 to 25 seconds the peaks are noticeably flattened. This is due to the effective angle-of-attack exceeding the stall onset angle.

Increasing amplitude and decreasing period of motion leads to growth in the range of angles-of-attack ‘seen’ by each blade element. At some point this will result in the angle-of-attack exceeding the stall onset angle. Once off the linear part of the  $C_L$  curve the gradient will decrease dramatically (or even become negative) leading to smaller values of  $C_L$  and the

normal force. This is shown in Figure 64, where the red dot on the static  $C_L$  curve represents some operating condition and the green arrows illustrate maximum and minimum  $C_L$  values for a hypothetical gentle or moderate motion in the surge DoF (large periods and small amplitudes of motion). If the motion in the surge DoF were to be intensified (increased amplitude and decreased period), the green arrows would extend far enough to enter the stalling region (marked by a vertical line at around 12.5 deg.). However, because the aerodynamics is modelled as unsteady (fully-attached unsteady), the return path of the arrow would not follow the original or static curve, but instead deviate from it. Whilst the return path would not be as extreme as shown by the loop labelled 'dynamic' – which represents dynamic stall which is not modelled in this chapter – it would join the static  $C_L$  curve at some lower angle-of-attack. However, if the  $C_L$  were to be calculated using thin aerofoil theory this would never happen as the lift curve would be completely linear. Similarly, the difference in the mean thrust values in Figure 62 is a direct result of blade stalling. At highly unsteady conditions (large amplitudes and small periods of surge motion) blades will encounter large angles-of-attack. This will lead to stalling. However, using fully-attached unsteady aerodynamics will result in smaller angles-of-attack when compared to quasi-steady (direct effect of unsteady effects). This can be explained by looking at Figure 64. In a hypothetical case of a highly unsteady motion in surge, the quasi-steady angle-of-attack will reach 20 degrees, at the same time the unsteady results could lead to an angle-of-attack of 17.5 degrees and a much higher lift coefficient.

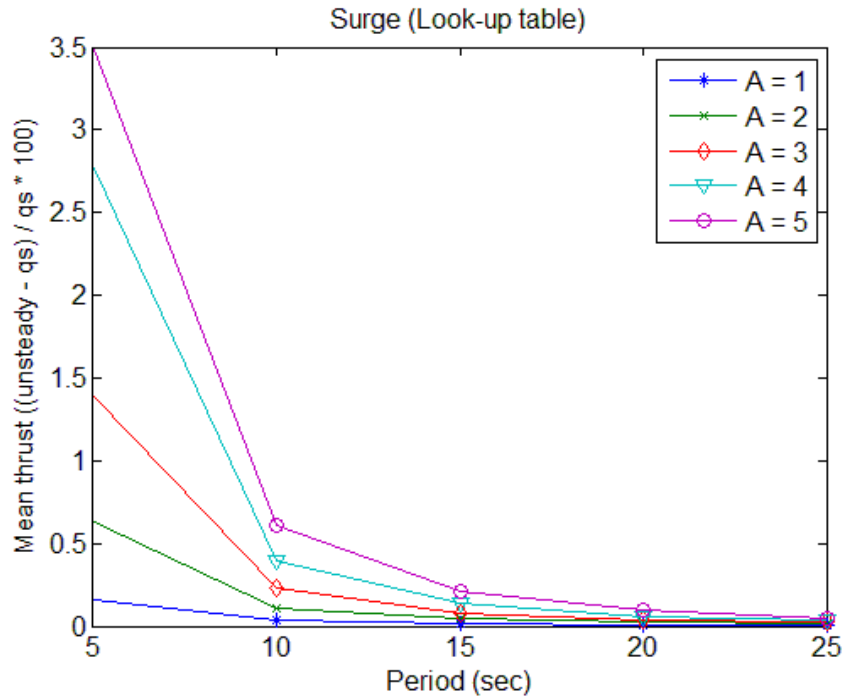


Figure 62 – Mean of normal force on a blade in surge (look-up tables)

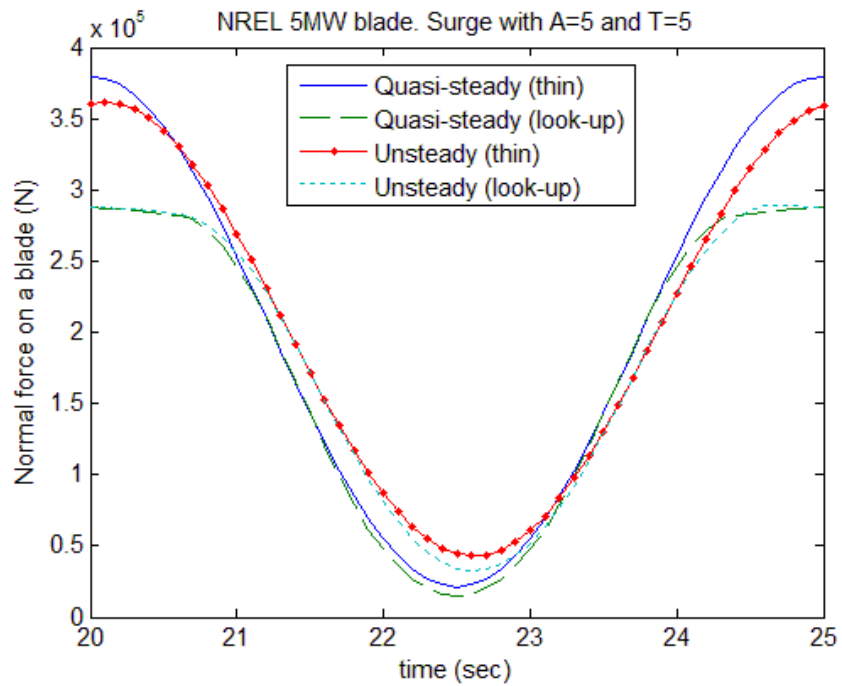


Figure 63 – Normal force on a blade in surge motion of 5 m and 5 s amplitude and period

Another way of looking at it is using the blade element velocity triangle (Figure 58). The oscillatory component of top of the free-stream velocity is  $\omega A \cos \omega t$ . With the most severe

conditions of  $A = 5$  m and  $T = 5$  s, the amplitude of oscillatory component is 6.28 m/s. This, however, is quite a significant increase compared to the steady free-stream value of 10 m/s, which will inevitably results in very large and small angles-of-attack.

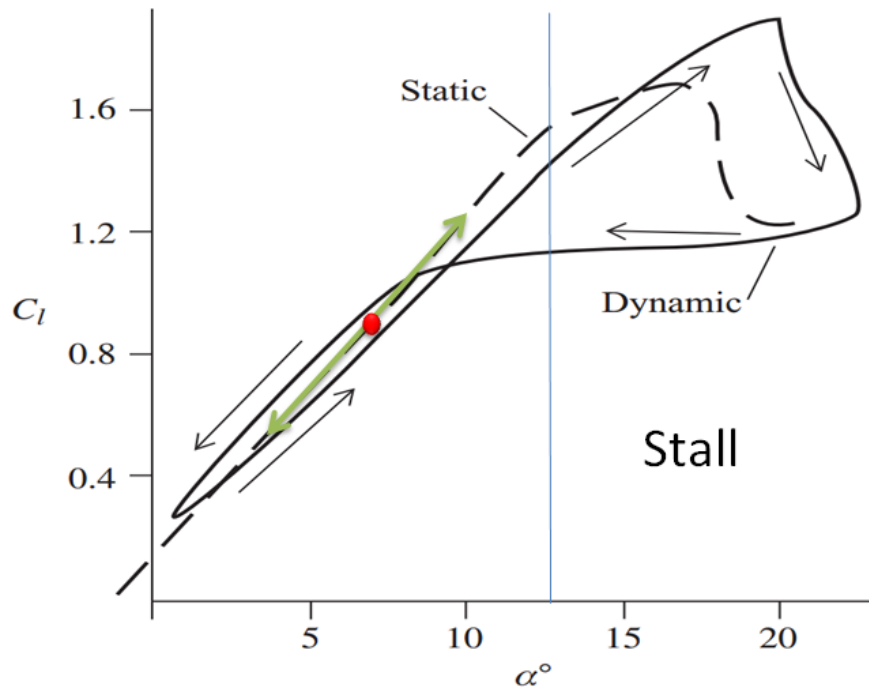


Figure 64 – Stalling effect [1]

Figure 65 and Figure 66 show difference in the amplitude/half-range of thrust between the quasi-steady and unsteady results. In Figure 65 two distinct trends can be observed. Firstly, the difference in the amplitude decreases with increasing period. Secondly, the results are completely independent of the amplitude of motion (result of the thin aerofoil theory being a purely linear theory).

When the thin aerofoil theory (Figure 65) is compared to the look-up table (Figure 66), it shows a very similar pattern to the mean thrust results discussed above. The overall trend between the curves is very similar. However, because the look-up table method is not linear (except over a small range at low angles-of-attack), the results are not amplitude independent. The whole plot also seems to be shifted up – showing a smaller difference between the quasi-steady and unsteady results as a result of stalling.

Figure 66 shows that the difference in the amplitude values of thrust between the quasi-steady and unsteady results is increasing with decreasing amplitude ( $T = 5$  s), which is counterintuitive. However, a closer comparison of Figure 60 and Figure 63 shows that increasing amplitudes and decreasing periods of motion will eventually result in stalling of the flow. This can clearly be seen in Figure 63, where the peaks of the look-up results are flattened.

Where the mean loading for the unsteady results was larger, the opposite can be said about the amplitude. Amplitudes or half-range values of loading in the unsteady case are much smaller than those of the quasi-steady results. Also, the maximum difference in the mean loading was very small (max 0.5% for the thin aerofoil theory), whereas the difference in amplitude can be significant (> 11% - thin aerofoil theory).

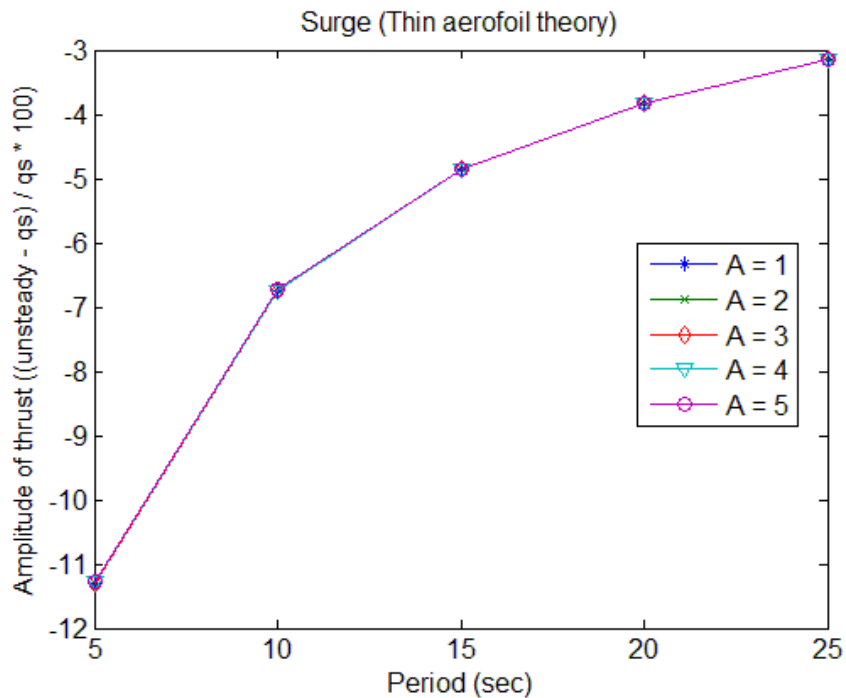


Figure 65 – Difference in amplitude of thrust in surge motion (thin aerofoil theory)

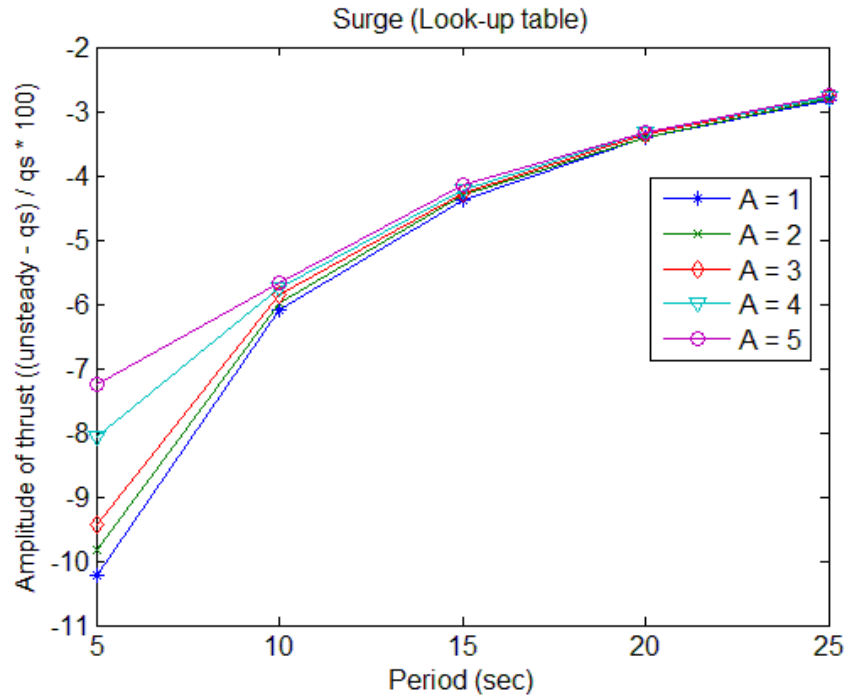


Figure 66 – Difference in amplitude of thrust in surge motion (look-up tables)

The out-of-plane bending moment results are very similar to the thrust results. They follow the same pattern with exception of showing a slightly smaller difference between the unsteady and quasi-steady results. This is because the out-of-plane bending moment is simply the product of the thrust force and distance to the blade root. The reduced frequency results (Figure 30) show that blade elements close to the blade tip experience smaller reduced frequencies. However, the largest contributors to the bending moment are the sections that are at furthestmost distances along the blade span. Combining these two effects together leads to ‘averaging’ of the thrust results.

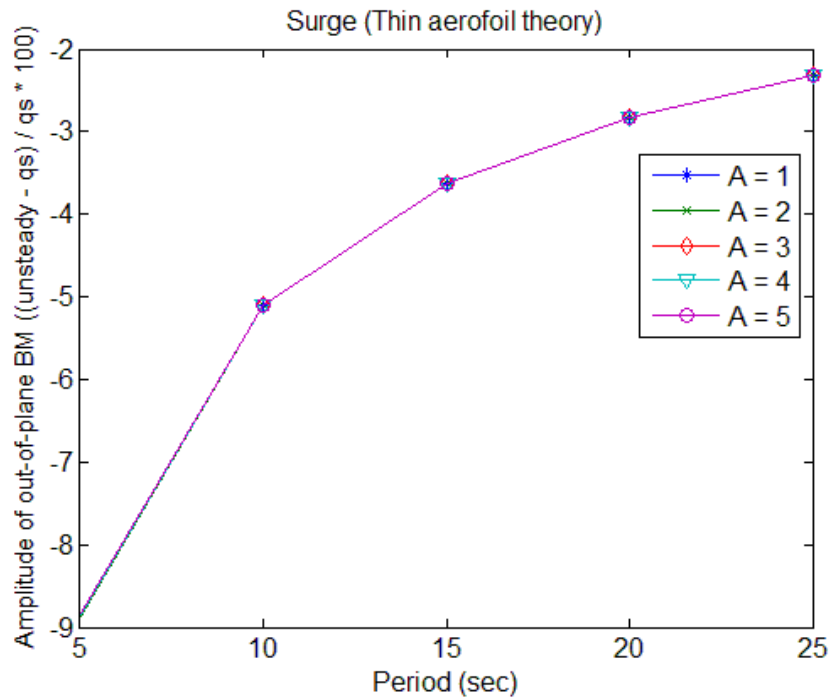


Figure 67 – Amplitude of out-of-plane bending moment in surge motion (thin aerofoil theory)

In-plane force and bending moments also show a very similar trend to the thrust and out-of-plane bending moments with one exception. The thin aerofoil results for the mean in-plane force and bending moment are larger for the quasi-steady theory.

**Note:** See A1.6.1 for more results on surge.

#### 2.5.9.2. Sway

The sway DoF is represented as an increase and decrease in the in-plane velocity of blade elements; however it could have also been modelled as a sinusoidally yawing turbine (see A1.5.1).

Figure 68 shows the normal components of the lift force on an NREL 5MW wind turbine blade. Compared to Figure 59, where surge motion decreased the amplitude of the fully-attached unsteady force, the opposite effect is seen in sway DoF.

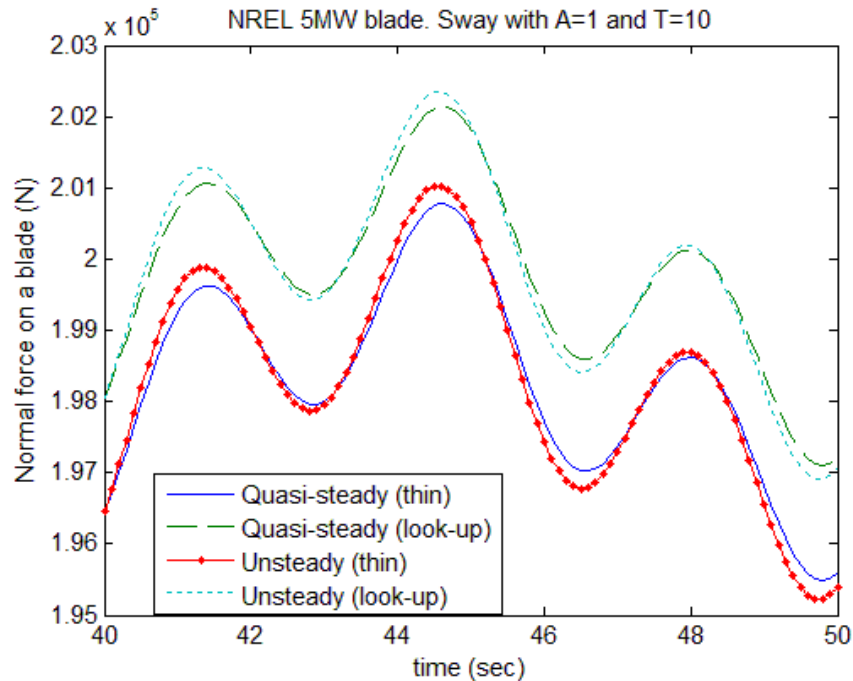


Figure 68 – Normal force on a blade in sway

Figure 69 shows the normal force on an NREL 5MW blade on a turbine that is swaying with 5 m amplitude and 5 s period. Compared to Figure 63 there is no plateauing of the peaks. Compared to surge, the oscillatory component due to motion is added to the rotational velocity of the blade element and for the majority of the blade length it is an order of a magnitude smaller than the rotational velocity. For example, at the tip of the blade the rotational velocity will be around 75 m/s and addition/subtraction of 6.26 m/s will not make as near much a difference as in adding/subtracting it to/from 10 m/s (surge case). However, it is possible for changes in in-plane velocity to lead to more significant changes in the axial force on the rotor, as shown in A1.7.

Also, compared to surge response, the phase difference between the quasi-steady and unsteady results is not noticeable. On a more thorough check it actually appears that unsteady results are leading those of quasi-steady. This does not depict the real case and is a result of modelling sway DoF as a change in the rotational velocity of the rotor.

When analysing the results, it is clear that the difference in the mean values, at least for the thrust force, is negligible (as shown in Figure 70). This applies to both the thin aerofoil theory and the results obtained using the NREL 5MW  $C_L$  look-up tables.

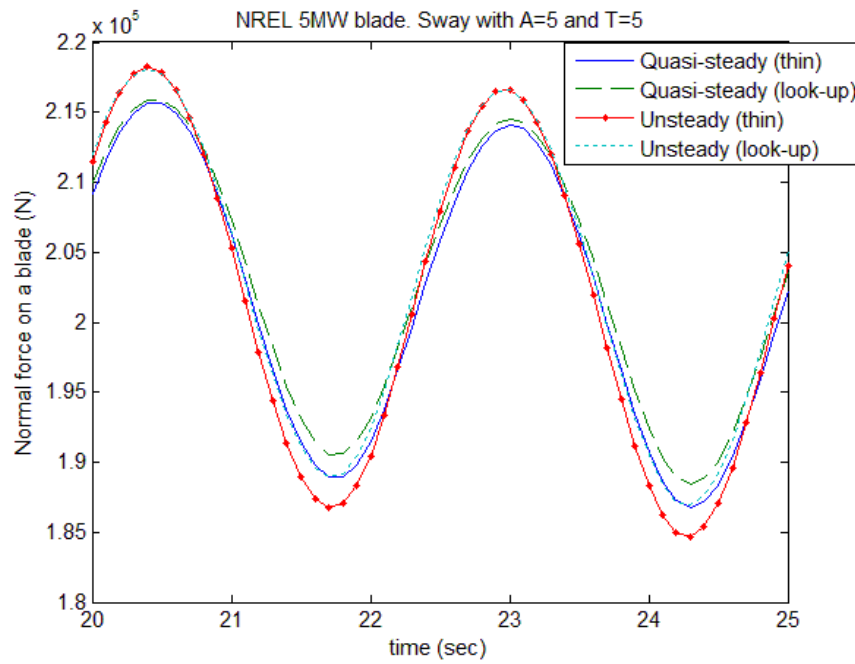


Figure 69 – Normal force on a blade in sway with 5 m amplitude and 5 s period

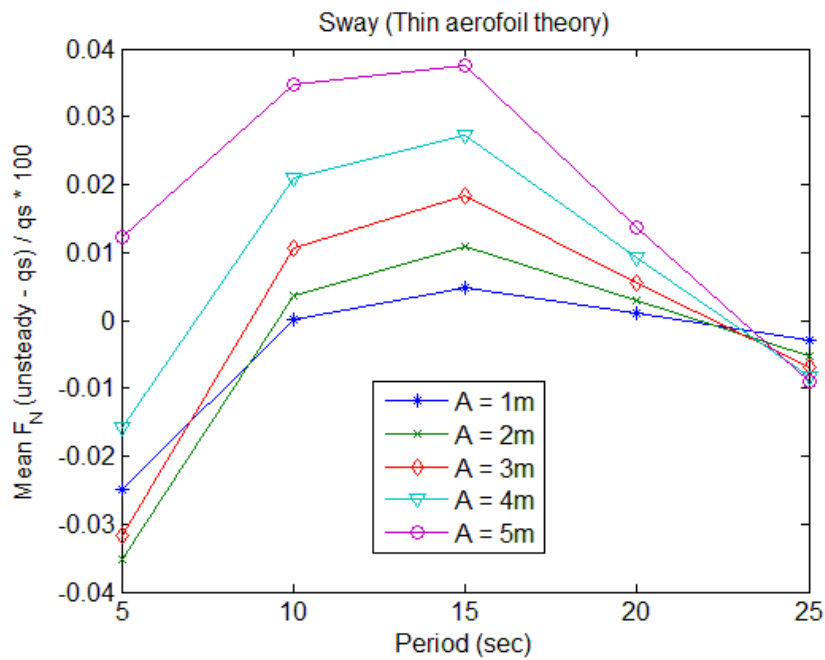


Figure 70 – Difference in the mean thrust in sway for different combinations of  $A$  and  $T$

It is clearly evident from Figure 69 that there is a difference in the amplitude between the quasi-steady and unsteady results (very clearly seen between the blue and red lines). This is

further confirmed in Figure 71, where the difference in the amplitude between both cases is plotted for different combinations of  $A$  (amplitude) and  $T$  (period).

Compared to the surge DoF, sway seems to exhibit a larger range of thrust in the unsteady case. Also, from Figure 71, whilst the difference between both cases decreases with increasing period, at  $T = 20$  s an opposite effect is experienced. This can be attributed to how sway motion or, in particularly, the variation in the rotational velocity was defined. While the response to the surge DoF had a single sinusoid, in sway the in-plane velocity component depends both on the motion of the platform and on the rotational velocity of the rotor. A combination of two different frequencies makes it much harder to measure and show results consistently. Two different fundamental frequencies will lead to peak and trough values varying with time. For this reason the amplitude (as shown on y-axis) should be thought of as a half-range value of the signal.

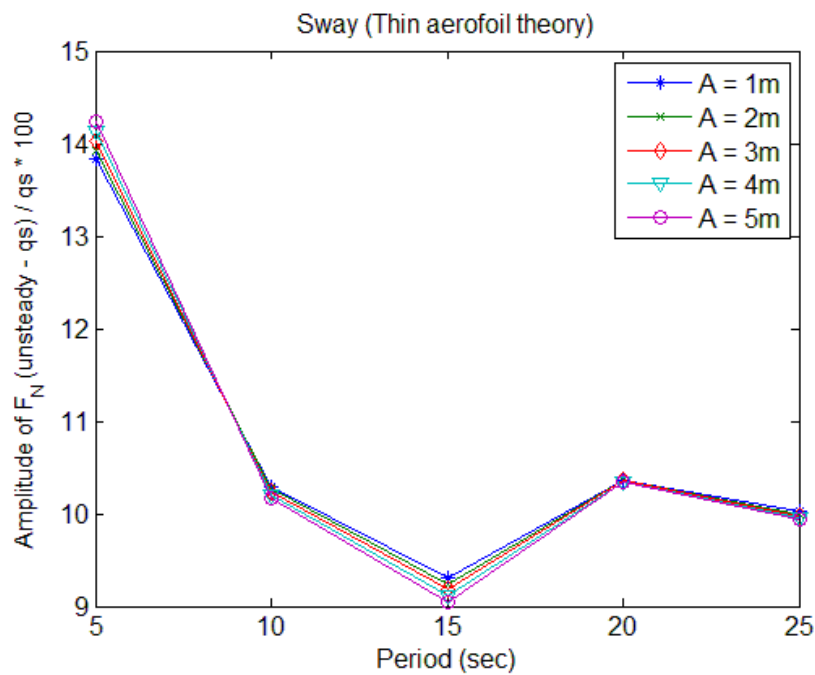


Figure 71 – Difference in half-range values of thrust for sway motion combinations

The out-of-plane bending moment results are very similar to the thrust results. Like in the surge DoF, it will average the thrust results producing a slightly smaller difference between the quasi-steady and unsteady cases, as shown in Figure 72.

In both thrust and out-of-plane bending moment, there is no significant difference between the means calculated by quasi-steady and unsteady methods. However the amplitudes differ significantly. For thrust, the look-up table shows a 7-12% difference and the thin aerofoil theory shows a 9-14% difference. These differences are 4.5-7.5% and 5-8%, respectively, for the out-of-plane bending moment.

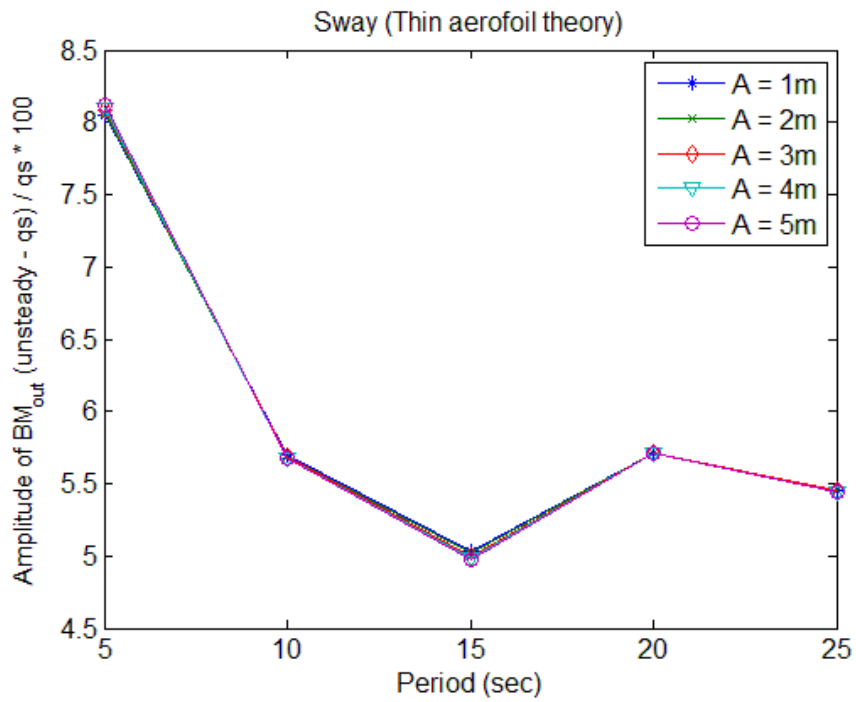


Figure 72 – Difference in half-range values in out-of-plane bending moment in sway DoF

No significant difference in the mean loading in the in-plane force and in-plane bending moment were observed between the quasi-steady and unsteady results (Figure 73).

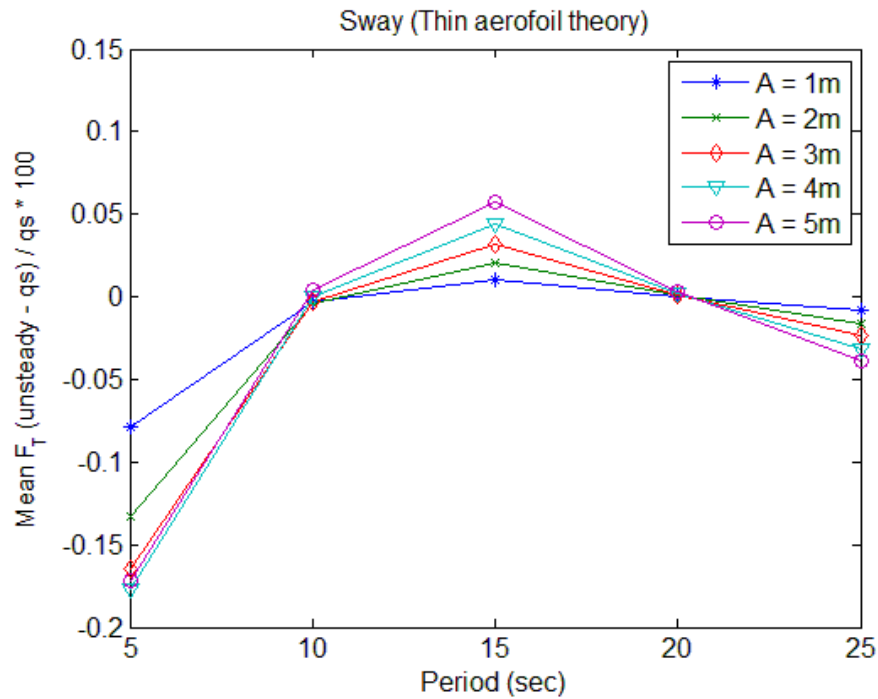


Figure 73 – Difference in the mean loading of  $F_T$  in sway

A very large % difference between the quasi-steady and unsteady half-range values of the in-plane bending moment can be observed in Figure 74. Similarly to the surge results, the quasi-steady amplitude is larger than that of its unsteady counterpart. However, this is potentially misleading. On a closer inspection of Figure 75 and Figure 76, it is clear that the magnitude of the range of the signals is very small. Hence, a slightest difference between the quasi-steady and unsteady results in the in-plane force and bending moment will show up as a large percentage difference.

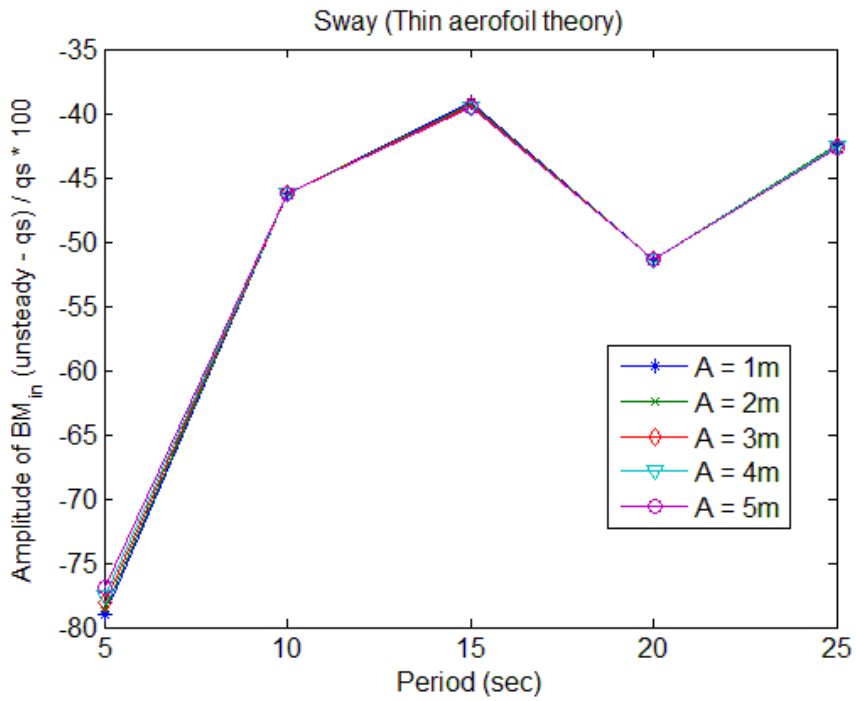


Figure 74 – Difference in the half-range values of in-plane BM in sway

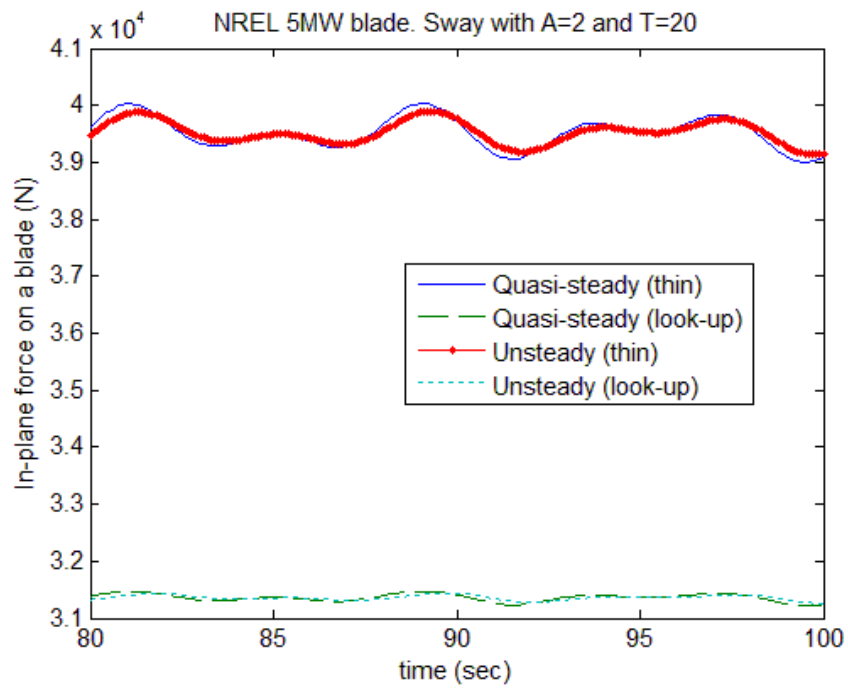


Figure 75 – In-plane force on a blade in sway of 2 m amplitude and 20 s period

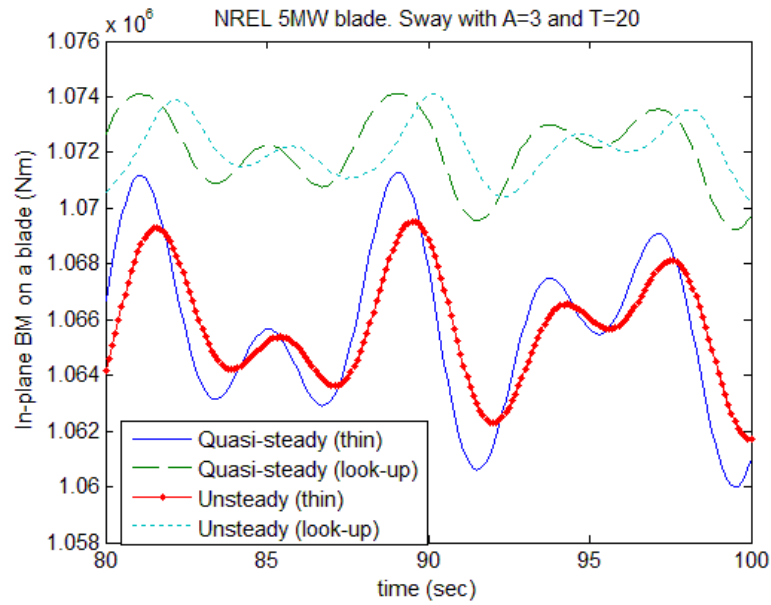


Figure 76 – In-plane BM for a blade in sway of 3 m amplitude and 20 s period

**Note:** See A1.6.2 for more results on sway.

### 2.5.9.3. Heave

Figure 77 shows the in-plane force on an NREL 5MW blade in heave motion of 2 m and 5 s amplitude and period.

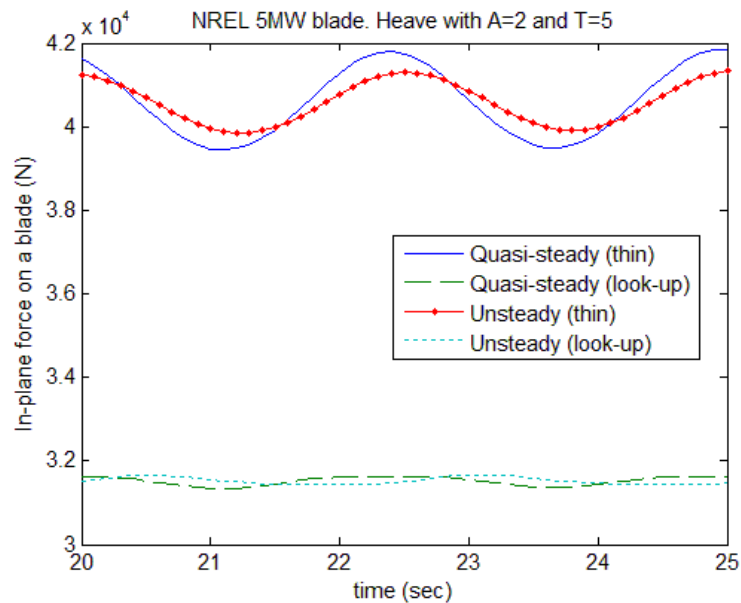


Figure 77 – In-plane force on a blade in heave of 2 m amplitude and 5 s period

Because heave and sway DsoF are modelled almost identically, for more discussion and results see sway DoF.

**Note:** See A1.6.3 for more results on heave.

#### 2.5.9.4. Roll

Not included in this model is the enormous inertia of the rotor. In reality, any rolling side-to-side motion would be resisted by the rotor's inertia. Hence, the results to follow should only be used as a first approximation.

Response for roll DoF is expected to be very similar to that of sway.

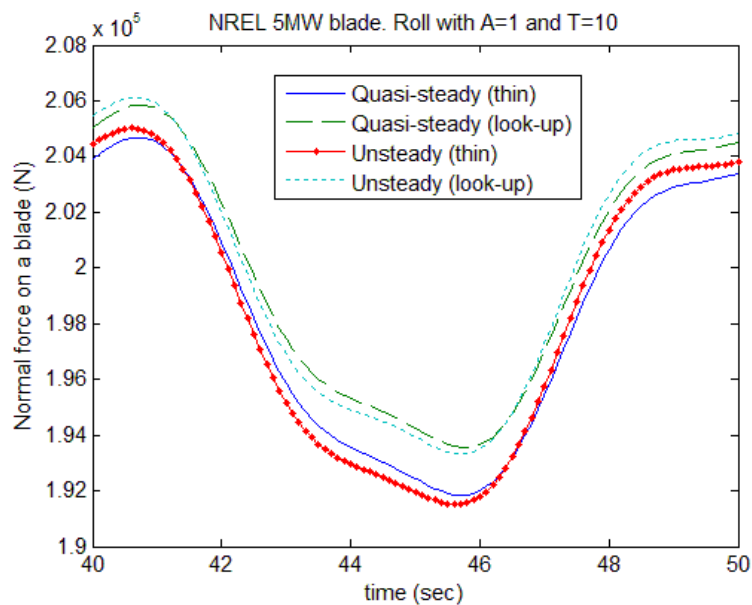


Figure 78 – Normal force on a blade in roll DoF of 1 deg. amplitude and 10 s period

Figure 78 clearly shows a larger range of values for the unsteady calculation (both thin aerofoil and look-up table). This is consistent with the sway results (Figure 68 and Figure 69). This is further confirmed in Figure 79, which shows that the difference in the half-range values between the quasi-steady and fully-attached unsteady methods decreases with increasing period. It is also always positive, meaning that the fully-attached unsteady results always produce larger half-range values.

Looking at the out-of-plane bending moment (Figure 80) there is no significant difference between the quasi-steady and unsteady results (both in the thin aerofoil theory and look-

up table results). However, there is a steady mean difference between the thin aerofoil and look-up table results. This is normal as the thin aerofoil uses  $2\pi$  gradient for the lift coefficient calculation, whereas the look-up tables have a smaller gradient which differs along the blade span and is always smaller than  $2\pi$ .

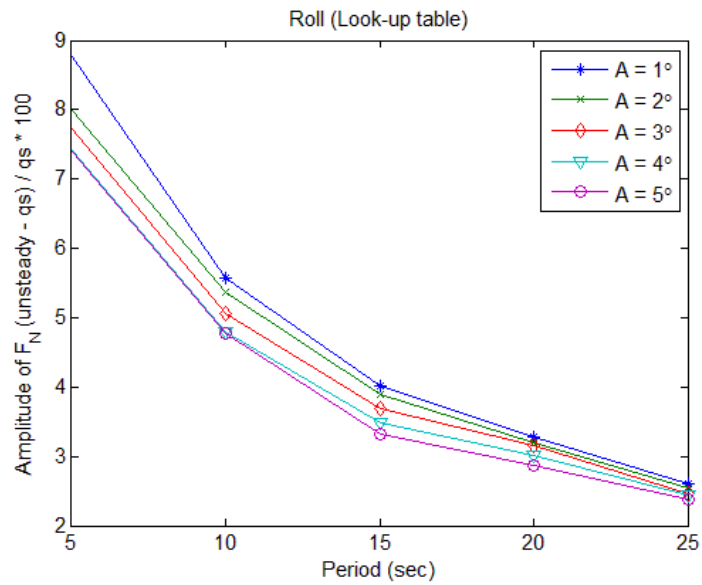


Figure 79 – Difference in half-range values of the normal force on a blade in roll (look-up table)

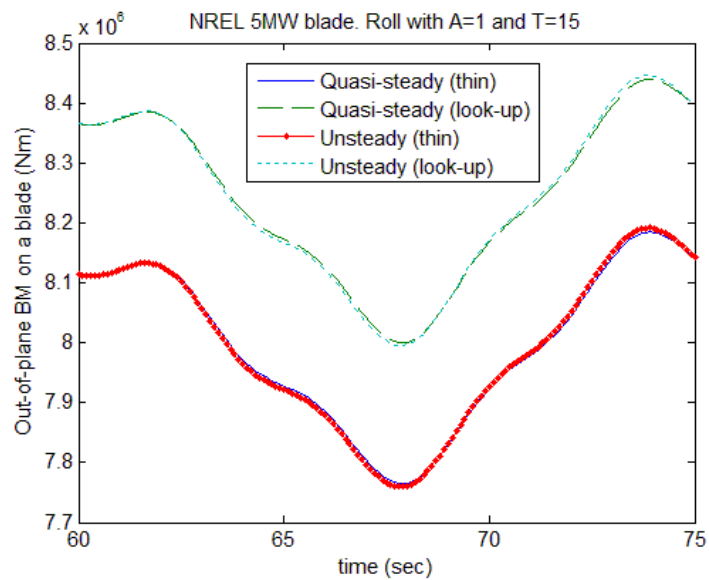


Figure 80 – Out-of-plane BM on a blade in 1 m amplitude and 15 s period motion in roll

Figure 81 and Figure 82 show the in-plane force and bending moment on a blade at different roll amplitudes and periods of motion. Both figures show two distinctive features.

Firstly, a phase difference between the quasi-steady and fully-attached unsteady results, and secondly, a larger range of loading in the quasi-steady case (which is a reversal on the normal force results). The previously mentioned steady displacement between the thin aerofoil and look-up table results is also present.

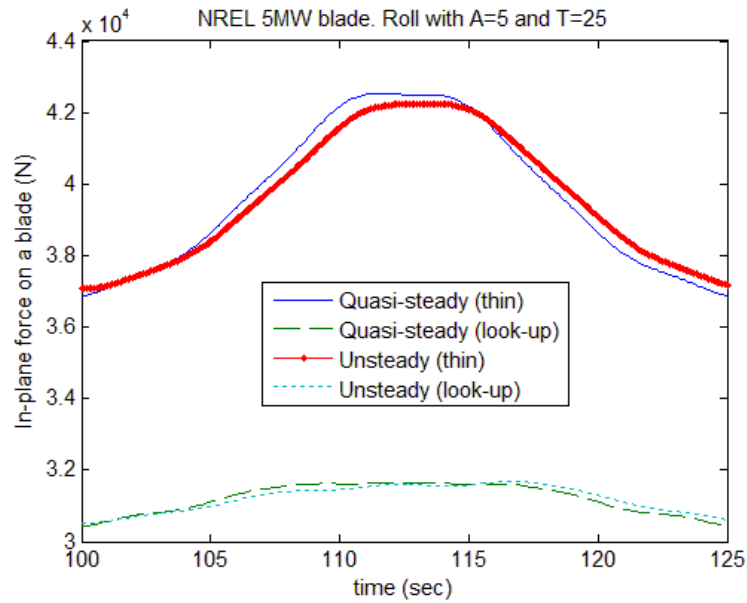


Figure 81 – In-plane force on a blade in 5 deg. and 25 s roll motion

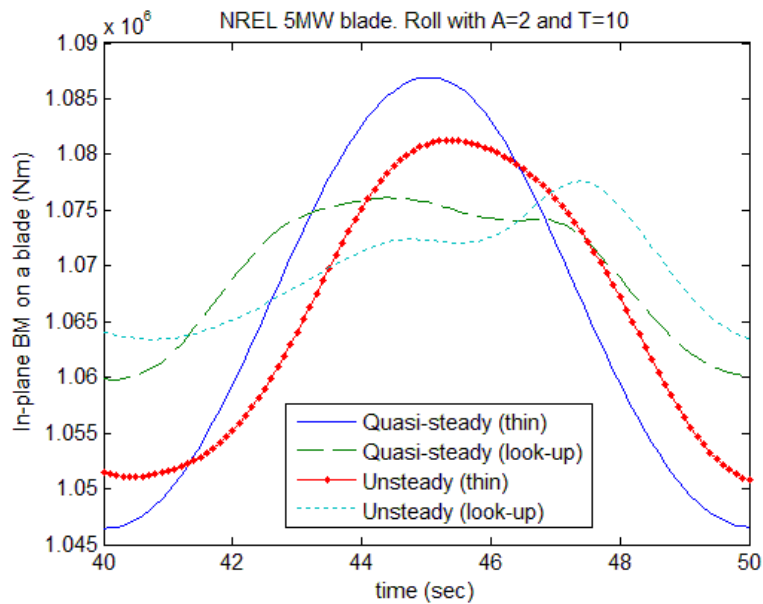


Figure 82 – In-plane BM for 2 deg. and 10 s roll motion

Overall, roll results are very similar to those of sway with almost no difference in the mean loading, and larger ranges of loading for the normal loading in the fully-attached case and vice-versa in the in-plane loading.

**Note:** See A1.6.4 for more results on roll.

#### 2.5.9.5. Pitch

The pitch DoF of a floating wind turbine can be thought of as a combination of surge and heave DsoF, where surge dominates the overall response. However, the changing difference in velocity between the top and bottom of the rotor means that there will be additional 3P components in overall thrust and 1P components in individual BMs. In this model heave contribution has been ignored (see Roll in A1.5 for reasoning).

For 1 deg. amplitude and 10 s period of pitch motion of a floating wind turbine, the normal force on a blade is shown in Figure 83.

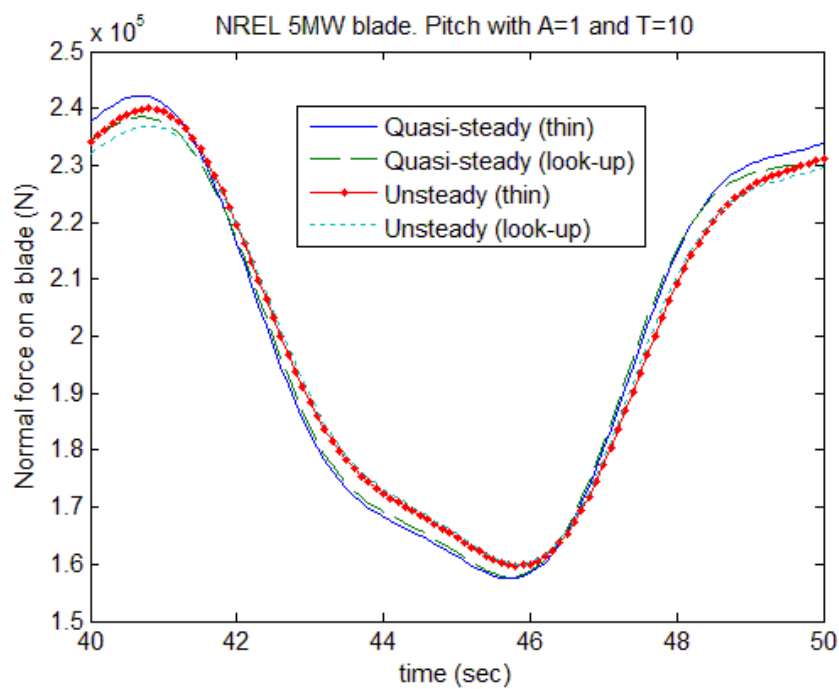


Figure 83 – Normal force on a blade in 1 deg. amplitude and 10 s period in the pitch DoF

Very much like with other DsoF, the range difference between the quasi-steady and fully-attached unsteady is present. This is further confirmed in Figure 84. The thin aerofoil results show that the quasi-steady results have larger half-range values across all amplitude and

period combinations in pitch DoF. This difference between both cases decreases with increasing period of oscillation, as the fully-attach results tend to quasi-steady. Also, a slight difference in the phase between the quasi-steady and unsteady results can be observed.

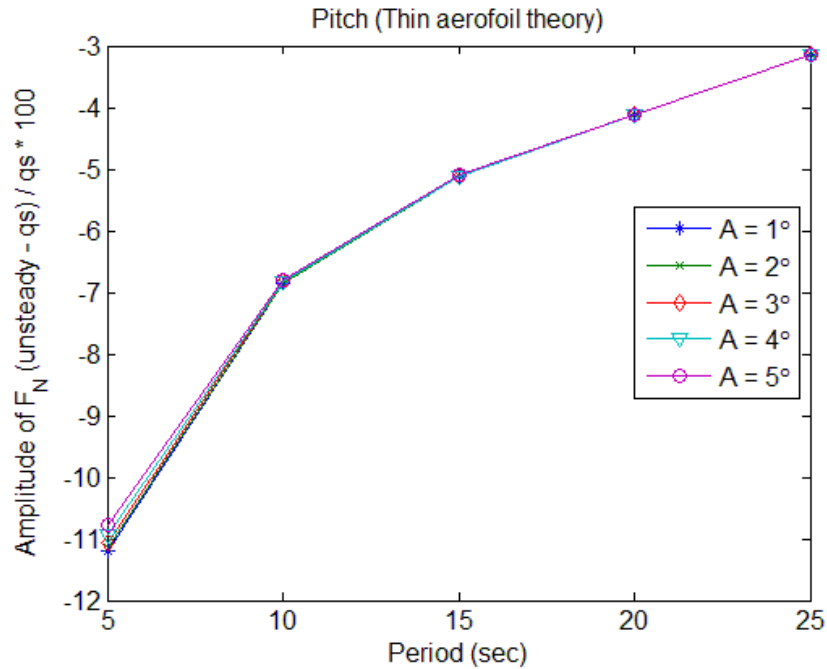


Figure 84 – Difference in the normal force half-range values between the quasi-steady and unsteady results (pitch)

Figure 85 shows plateauing of the look-up tables results in both the quasi-steady and unsteady calculations. The same as in Figure 63, this is a consequence of entering the stalling region. Compared to the surge DoF, the plateauing effect is more pronounced. For a floating turbine that is rocking fore-aft with 5 deg. amplitude and 5 s period (like in Figure 85), which is an extreme case, the induced free-stream velocity at the hub is 16.45 m/s. With the steady free-stream velocity of 10 m/s and no blade pitching mechanisms, this will result in parts of the blade operating in the deep-stall region.

Results of stalling aerofoils can be seen in Figure 86. Compared to the linear thin aerofoil results in Figure 84 (almost purely amplitude independent), the largest amplitude of motion does not lead to the largest difference between the quasi-steady and fully-attached unsteady results. This is a direct result of stalling. The larger the amplitude of motion, the deeper the degree to which the aerofoil stalls, leading to flattening of the peak loading. This in turn results in a smaller difference between the quasi-steady and unsteady results.

A similar effect can also be observed in the in-plane force and bending moment results (see A1.6).

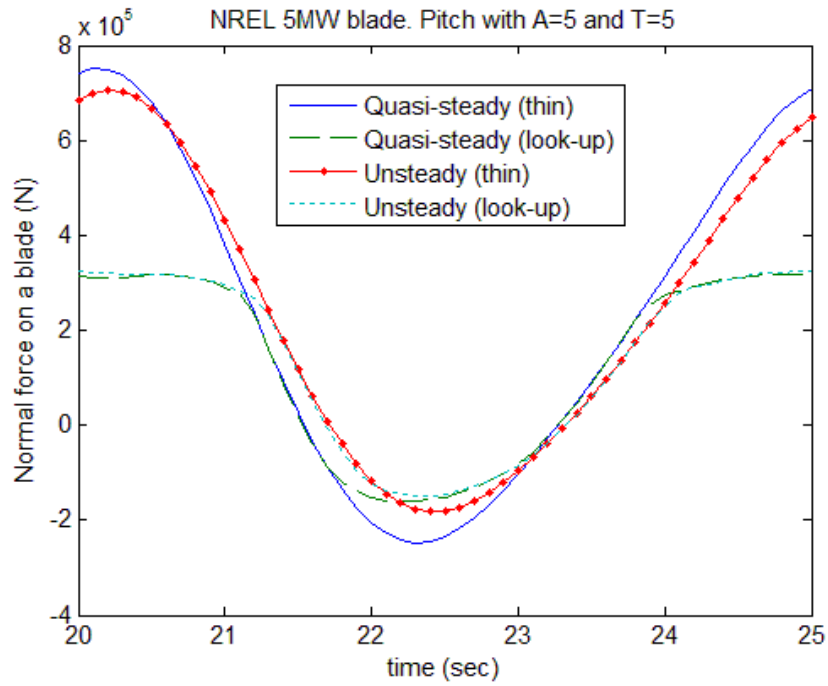


Figure 85 – Plateauing of look-up table results in the pitch DoF

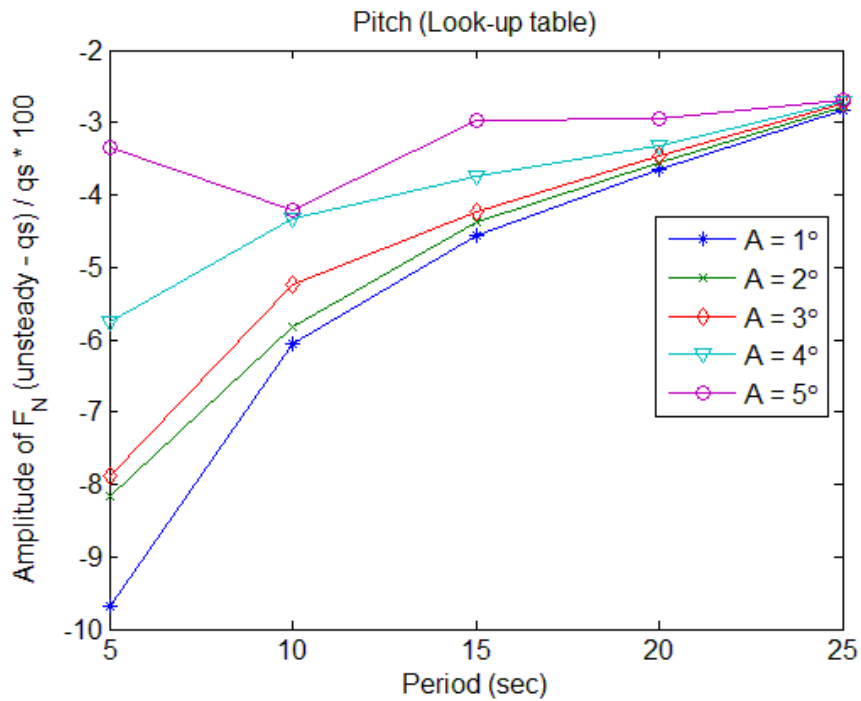


Figure 86 – Difference in half-range values in the normal force on a blade (pitch)

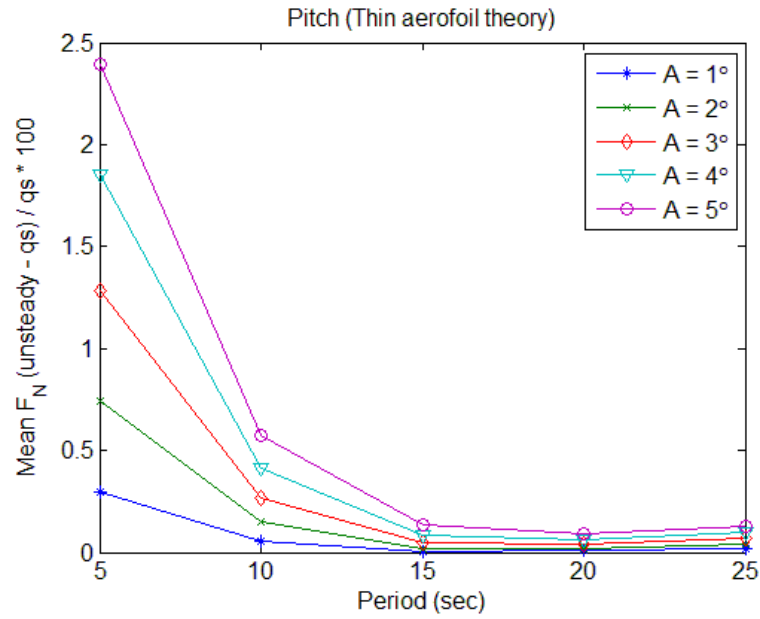


Figure 87 – Difference in the mean normal force in the pitch DoF (thin aerofoil theory)

The mean results for the normal force obtained using the thin aerofoil theory and look-up tables are shown in Figure 87 and Figure 88, respectively. Both figures exhibit a very similar trend. Because flattening of the extremes occurs mainly at the peaks and not troughs of the signal, the mean values of the quasi-steady and unsteady results are displaced by different amounts.

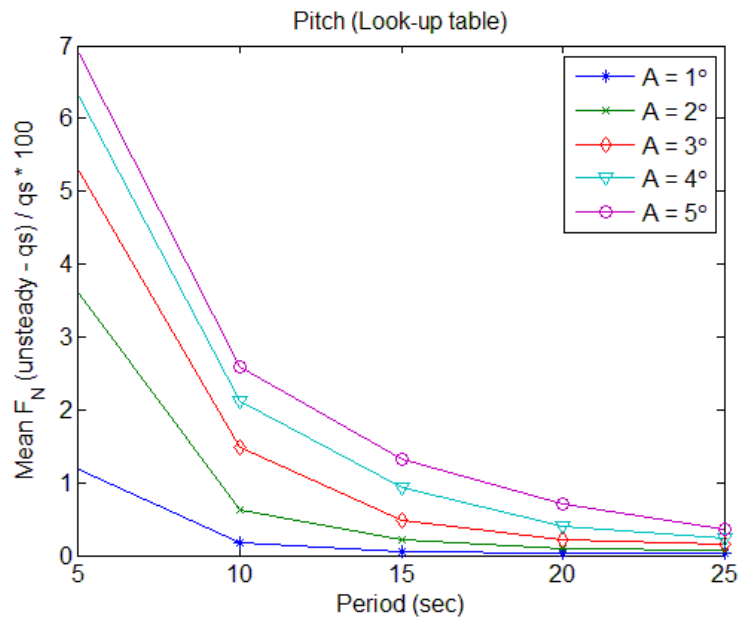


Figure 88 – Difference in the mean normal force in pitch DoF (look-up table)

The in-plane force on a blade that is mounted on a floating turbine that is pitching with 4 deg. amplitude and 5 s period is shown in Figure 89.

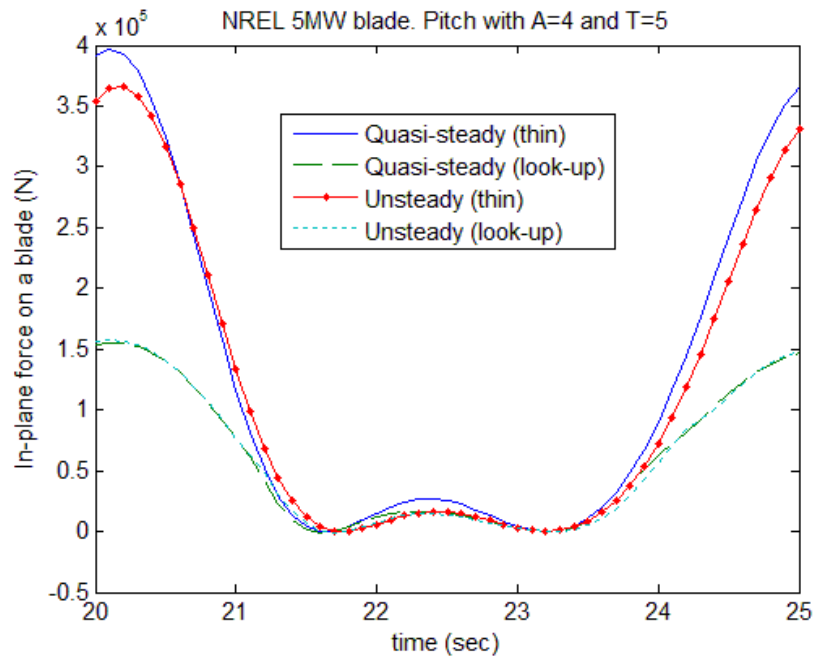


Figure 89 – In-plane force on a blade in pitch DoF

**Note:** See A1.6.5 for more results on pitch.

#### 2.5.9.6. Yaw

Motion in the yaw DoF is probably one of the most common motions in a real wind turbine environment, as very often turbines are not perfectly aligned with the free-stream velocity and are actually operating in a slight yaw. In floating wind turbines motion in this DoF is further amplified by coupling between different DsoF and misalignment between the wave and wind inputs to the system.

Very much like all the other rotational DsoF, yaw can be represented using one of the translational DsoF, in this case surge.

Two different degree-of-complexity representations of yaw DoF were used. Both represented yaw DoF as surge DoF, however, one included modification to the free-stream and in-plane velocity due to the skewed flow, while the other did not. Both representations are given below.

The difference between including and not including the cyclic component modification to the free-stream and in-plane velocity could change the angle-of-attack from 0 deg. at the blade tip to approx. 5 deg. at the blade root.

To calculate the axial induction factor correctly in the yaw DoF, a skewed wake correction has to be used. However, using only very small angles, an assumption was made that it can be overlooked for simple preliminary design calculations.

In the most extreme case ( $A = 5^\circ$  and  $T = 5$  s) the maximum induced free-stream velocity (normal to the rotational plane) is approx. 6.9 m/s.

The figure below shows the normal force on a blade that is mounted on a floating turbine that is yawing with 5 s period and 1 deg. amplitude. Because yaw is modelled as surge, the results are very similar to those of surge. The quasi-steady results show larger range of values than the fully-attached unsteady results. This can be seen across all 4 loads, as shown in A1.6.6.

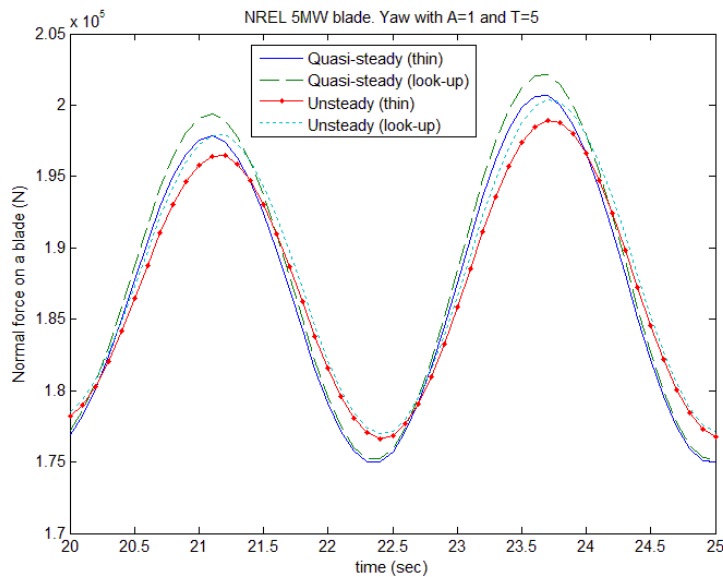


Figure 90 – Normal force on a blade in yaw motion

Figure 90 and Figure 91 show that there is a phase difference between the quasi-steady and unsteady results (a slight lagging of the fully-attached results). The same is observed in the in-plane force and bending moment and out-of-plane bending moment results.

Clearly shown in Figure 91 are the multiple frequency components of the signal. Mathematically these can be explained using product-to-sum and sum-to-product identities. Figure 92 shows the frequency components of the  $F_N$  signal. These are:

- Yawing frequency (0.03906 Hz)
- Sum of yawing and rotational frequencies (0.2295 Hz)
- Difference between the yawing and rotational frequencies (0.1514 Hz)

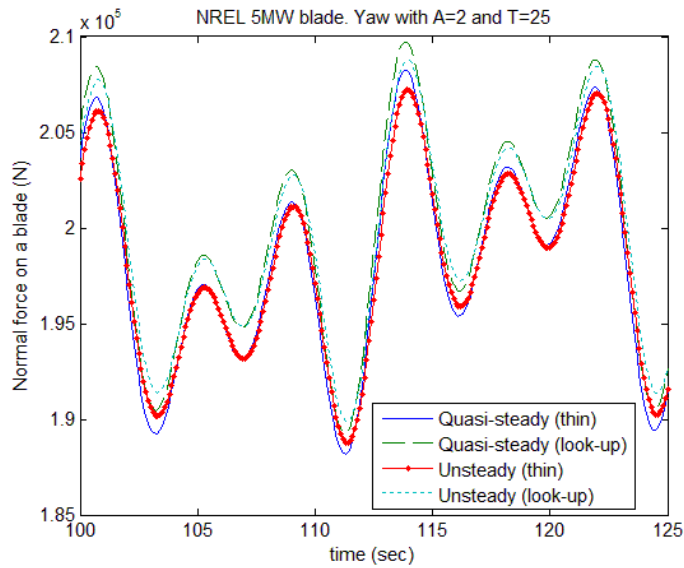


Figure 91 – Normal force on a blade in yaw

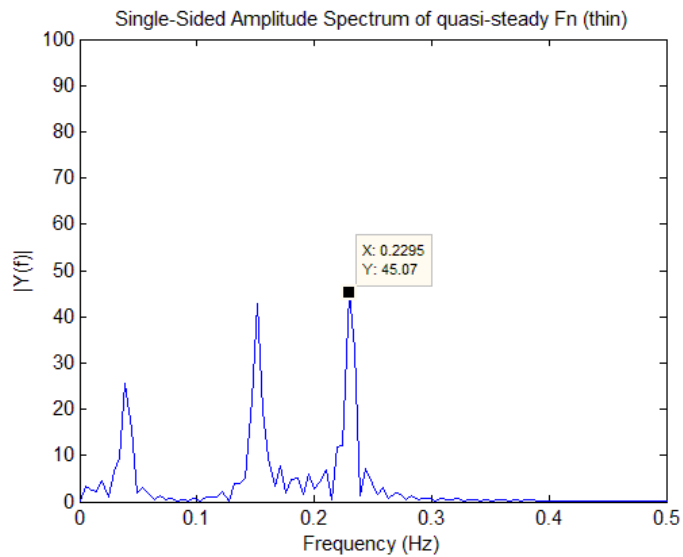


Figure 92 – Frequency component of the signal in Figure 91

**Note:** See A1.6.6 for more results on yaw.

## 2.6. Conclusion

6 DsoF were analysed using the analytical method of Van der Wall and Leishman. Each DoF was modelled as either a change in the free-stream velocity (surge, pitch, yaw DsoF) or in-plane velocity (sway, heave and roll DsoF). Two different flow states, quasi-steady and fully-attached unsteady, were used in combination with two ways of calculating the lift coefficient: thin aerofoil theory and look-up tables. Geometric (chord, aerodynamic twist, etc.) and aerodynamic data ( $C_L/\alpha$  tables) were taken from the NREL 5MW Base Offshore wind turbine [47].

4 different loads on a wind turbine blade were calculated. These included: normal force, in-plane force, out-of-plane and in-plane bending moments at the root of the blade. The corresponding loads, calculated using the quasi-steady and fully-attached unsteady flow assumptions, and thin aerofoil theory and look-up table models, were compared. The analysis concentrated on identifying differences in the mean and amplitude/half-range values of loading, as well as the phase variation between the quasi-steady and fully-attached unsteady results.

With the exception of pitch (look-up) and roll (thin, in-plane force) DsoF, the difference in the mean loading does not vary much between the quasi-steady and fully-attached unsteady flows in both thin aerofoil theory and look-up table cases. Analysing the amplitude/half-range results, 3 prominent trends were spotted. Firstly, for those DsoF that are modelled as a change in the free-stream velocity (surge, pitch and yaw), the normal force and out-of-plane bending moment half-range values are always larger when using the quasi-steady flow assumption. Secondly, for DsoF which are modelled as a change in the in-plane velocity (sway, heave and roll), the normal force and out-of-plane bending moment half-range values are always larger in the unsteady flow case. Thirdly, for the in-plane force and bending moment, the half-range values are always dominated by the quasi-steady results. All three points are valid across both thin aerofoil theory and look-up table results.

Unsteady loads (including the fully-attached) manifest themselves as a phase change compared to the quasi-steady airloads. This phase change can clearly be seen in Figure 60, Figure 76 and Figure 90, where the fully-attached unsteady airloads lag behind the quasi-

steady counterparts. With the majority of cases (different DsoF, loads) the phase difference increases with growing unsteadiness of the flow. For example, there is a larger phase difference between the results of 1 m and 5 s, and 1 m and 25 s amplitude and period in surge DoF. However, this is not completely consistent across all DsoF and loads.

While stalling is not an issue with the thin aerofoil theory results, some results, obtained using the look-up table technique, are questionable. Stalling is the result of some core assumptions and simplifications in the MATLAB model. Firstly, the axial induction factors are calculated at the start of each simulation and kept constant henceforth. Secondly, the absence of a controller means that there is no adjustment made to either the rotational velocity of the rotor or the pitch angle of the blade. Stalling manifests itself as flattening of the peaks. This can clearly be seen in Figure 63, Figure 85 and Figure 89. Some cases see a very deep stall, especially at low periods and high amplitudes of motion. This significantly decreases as the period increases and amplitude decreases.

Keeping in mind the previously stated, it is clear that the fully-attached unsteady aerodynamic effects are important and should be accounted for when performing design (fatigue) and power production calculations. The Van der Wall and Leishman code gives some basic insight into the loads expected on a wind turbine. While no significant mean difference was observed between the quasi-steady and fully-attached unsteady calculation, there was a significant change in the amplitude/half-range and phase values. If not included, the loads could be predicted wrongly, either over-predicted, leading to over-engineering the turbine/power production, or under-predicted, leading to a reduced life-time of the turbine.

To give some analysis recommendations for future development of FOWTs, the author, based on the findings and results presented in this chapter, suggests using a few simple guidelines which are particularly relevant when comparing quasi-steady with fully-attached unsteady aerodynamic representations.

- The phase difference between the quasi-steady and fully-attached unsteady aerodynamic loads has to be considered. If this delay is not accounted for in the model used to design the controller, this will inevitably lead to reduction in the

available phase and gain margins, resulting in instability and higher loads on the system.

- The mean aerodynamic loading can be assumed to be of an equal magnitude between both aerodynamic representations.
- As a first approximation, the range of aerodynamic loads on a system can be modelled using quasi-steady aerodynamics. This will result in larger and hence slightly overestimated load ranges, but will significantly simplify calculations. This rule should be applicable to motion in all 6 DoF of a FOWT. However, the results presented in this chapter only show this to be true for surge, pitch and yaw. The author is of the opinion that this will also hold for sway, heave and roll, if these are not modelled as a change in the rotor rotational velocity but instead as an oscillatory yawing turbine as suggested in 5.3.

The guidelines provided above are very generic and should apply to different types of design of FOWTs (spar, TLP, semi-submersible, etc.).

In future, sway, heave and roll should be modelled using a skewed wake correction instead of modification to the rotational velocity, as latter results in a varying rotational velocity of the rotor along the blade span, which is impossible.

To make calculations more precise and to better understand the effect that each DoF has on the system as a whole, simulations of an offshore floating spar-type wind turbine need to be performed using an aero-elastic simulator. This will account for other dynamic effects, such as, dynamic inflow, unsteady drag and other unsteady aerodynamic effects. In the next chapter the OC3-Hywind model [46] is simulated using FAST [50] under fully-unsteady aerodynamic conditions.

# Chapter 3: Unsteady flow

---

Multiple state-of-the-art computer aided engineering tools for simulating wind turbines exist that can also be used with FOWTs. These include FAST with AeroDyn and HydroDyn by NREL, FAST with Charm3D, Bladed by DNV GL Garrad Hassan, SIMO/RIFLEX with HAWC2 and many others. Almost none of the available packages were originally developed for simulating FOWTs. Instead these are either improved versions of codes originally developed for fixed foundation WTs or aero- and hydro-dynamic codes that had been coupled together to allow for integrated dynamic calculations for FOWTs. However, FOWTs operate in highly dynamic and, quite often, rapidly changing environments (wind, waves, underwater current, mooring system, etc). This makes FOWTs much harder to model accurately. For example, rapid motion of the rotor could result in a blade entering its own wake (and so BEM breaks down), mooring systems are intrinsically highly non-linear, and 2<sup>nd</sup> and higher order hydrodynamic effects such as wave sum- and difference-frequency are not always accounted for even in dedicated hydrodynamics packages. Eventually all the issues associated with modelling FOWTs will have to be addressed to come up with valid and accurate solutions.

In this chapter, 3 different objectives were set and accomplished. Firstly, as the next step towards better understanding of the relative importance and effects of quasi-steady and unsteady aerodynamics on floating wind turbines (compared to the simplified quasi-steady and fully-attached aerodynamic responses of a rigid NREL 5 MW turbine performed in the previous chapter), FAST simulations were used to compare and analyse the response of the complete OC3-Hywind system, when the quasi-steady and fully-unsteady aerodynamic settings were used. Secondly, FAST outputs were used to identify which degree-of-freedom (DoF) is the most detrimental to the system, in particular between surge and pitch, so that

modifications to enhance and prolong the life of a modified OC3-Hywind spar could be suggested in the next chapter. Thirdly, a statistical approach was used to confirm what was already known and to find new links between motions in different DoF, tower and blade loads using a statistical approach.

Before any of the before mentioned results are shown, a brief introduction to FAST is given. This includes the basic structure of FAST and its major shortcomings. A sanity check was also performed to make sure that FAST is working in a correct manner, and the aerodynamic damping calculated for both quasi-steady and unsteady aerodynamic simulations.

### **3.1. FAST**

Theodorsen, and Van der Wall and Leishman theories apply only to fully-attached flow. To account for the full spectrum of unsteady aerodynamics, FAST [50] was used to simulate the OC3-Hywind turbine [46], which is the original 2.3 MW Hywind wind turbine scaled up to 5 MW.

FAST was chosen over other wind turbine simulation packages, such as GH Bladed or HAWC2, as it is free and open source. Furthermore, it allowed each DoF of the OC3-Hywind floater to be modelled separately, which was initially seen as an advantage, but later proven otherwise (see 3.1.3.6), and modifying the wave-excitation force to identify which DoF is the most detrimental to the system (see 3.2.2).

FAST is a non-linear time-domain wind turbine simulation package that can model the coupled aero-hydro-servo-elastic response of different configuration wind turbines, whether they be fixed-bottom, floating, up- or down-wind, 2 or 3-bladed. The wake effects of the rotor aerodynamics are calculated using blade element momentum (BEM) or generalised wake (GDW) theories, and dynamic stall using the Beddoes-Leishman model [69]. Like many other wind turbine (WT) modelling packages, it also includes solutions for hub and tip loss, tower shadow and skewed wake [70]. FAST uses a combination of modal and multi-body dynamics formulation with structural bodies modelled as either rigid or

flexible. For a 3-bladed floating horizontal-axis wind turbine (HAWT) there are 24 DsoF (see table below), with flexible bodies including blades, tower and drive shaft [52]. These are characterised using a linear modal representation that assumes small deflections. This is also true for 3 rotational DsoF of the support platform (roll, pitch and yaw), which also rely on a small-angle approximation (see 3.1.3.5).

The time-domain hydrodynamics of FAST include effects such as the hydrostatic restoring, viscous drag from waves and turbine motion, added mass and damping from wave radiation, and linear wave diffraction. The linearised representation of hydrostatic restoring, added mass and damping, and wave excitation force due to wave diffraction are obtained using WAMIT [71] and are provided in FAST as input data in the form of mass, damping, stiffness and forcing matrices. These were obtained by modelling the OC3-Hywind using two geometric planes of symmetry with 3,900 rectangular panels within each  $\frac{1}{4}$  of the structure beneath the still-water level (SWL).



Figure 93 – The OC3-Hywind spar (in WAMIT)

The mooring system is modelled in FAST as quasi-static and includes effects of stretching, mass density, buoyancy, geometric non-linearity and seabed interaction. However, dynamics effects and drag of the mooring system are not included in FAST [72]. Also not included in FAST are the second-order potential-flow solutions.

Table 8 – DsoF of floating HAWT in FAST

Modes	No. of DsoF
Platform (surge, sway, heave, roll, pitch and yaw)	6
Tower (2 for tower 1 <sup>st</sup> and 2 <sup>nd</sup> for-aft and side-to-side motion)	4
Nacelle yaw	1
Generator	1
Drive-train	1
Blades (2 flap-wise and 1 edge-wise for each blade)	9
Rotor-furl (not used in 3 bladed systems)	1
Tail-furl	1

### 3.1.1. Hydrodynamic loading

Fluid loading on a structure is a very complex problem with many different components. However, these components can be separated out and in most cases can be calculated separately and superimposed in the end to obtain the final result.

Hydrodynamic loading can be classified into:

- Drag loading
- Diffraction
- Inertia loading
- Slam and slap loading
- Water added mass
- Vortex shedding induced oscillating loading.

Whilst some of these, slam and slap loading, are currently not build into FAST and some are mitigated by installing helical strakes along the spar to avoid vortex induced motions (see 4.7), the majority of these loading types are accounted for in FAST.

#### 3.1.1.1. Wave particle kinematics

To calculate hydrodynamic loading on a floating offshore structure in the time-domain, like in FAST, the wave particle kinematics have to be determined. A very popular approach to

calculate the wave particle velocities and accelerations, and the resulting dynamic pressure is to use Airy wave theory [73]. It is also used in FAST and augmented with Wheeler stretching [74] and Morison's equations [75].

The main disadvantage of linear Airy wave theory is that it is linear and cannot account for effects such as breaking and steep-sided waves (slam and slap loading). In Airy theory, waves are modelled as waves of constant amplitude and period. Because linear Airy wave theory only applies to small waves, Wheeler wave stretching is used to account for wave particle kinematics at points above the mean water level (MWL). The assumptions of linearity that is used in this approach is presumed to be reasonable as long as the structure is in deep water, where wave heights are much smaller than wave lengths. To account for the non-linearities in the wave structure due to very large waves or shallow water, stream function wave theory should be used, as it gives a much more accurate representation of wave kinematics than Airy wave theory in shallow waters [76]. However, this is not an option in FAST.

The OC3-Hywind model, as given by the NREL, is modelled in water depth of 320 m. This licenses using FAST and its linear Airy wave theory with Wheeler stretching (as the structure is in deep water, where wave heights are much smaller than wave lengths). Whilst the shortened spar versions of the OC3-Hywind design discussed in Chapter 4 were not simulated in FAST, the same reasoning applies as the shortest spar would be in 60+ m water depth.

#### *3.1.1.2. Morison's equation*

Morison's equation, also known as the MOJS equation, is the standard approach in the offshore industry used for the preliminary estimation of loads on support structures of small diameter relative to the wavelength of the incident waves, such as slender, vertical cylinders. It is a semi-empirical equation derived by Morison, O'Brien, Johnson and Schaaf in [75]. Morison's equation is a function of the diameter of the spar, fluid velocity and acceleration, hydrodynamic drag and inertia coefficients ( $C_D$  and  $C_M$ ). The later can be approximated using works of [77-79]. FAST models the OC3-Hwyind assuming  $C_D=0.6$  and  $C_M=1 + 0.97$ , where 0.97 is the added mass coefficient. In FAST, Morison's equation is used together with Airy wave theory, which provides the wave particle velocities and

accelerations. It accounts for the non-linear viscous drag term that needs to be added in severe sea conditions, when flow-separation occurs, to obtain correct hydrodynamic damping.

Morison's equation assumes that flow acceleration is more-or-less uniform at the location of the body. In the case of the OC3-Hywind, this requires the diameter of the spar to be much smaller than the wavelength. If not, diffraction effects have to be accounted for separately (see 3.1.3.3 and Figure 94 for more discussion and results).

### *3.1.2. Control of the OC3-Hywind*

The OC3-Hywind employs a typical variable-speed, pitch-to-feather control system. It uses a slightly modified version of the controller used in the NREL 5-MW wind turbine [47]. Two main modifications were applied to the NREL 5-MW turbine: reduction of gains in the blade pitch-to-feather control system and swapping constant generator power for a constant generator torque in the rated power operating conditions (control region 3).

The proportional and integral gains and the constant generator torque for the rated operating conditions are given in [46].

These changes were implemented to make sure that the OC3-Hywind does not introduce negative damping as the system is pitching back and forth [80]. Negative damping in the pitch DoF can lead to large resonant platform pitching motions that can be very detrimental to the system in terms of the tower and blade fatigue. This problem has been thoroughly investigated by various researchers and multiple suggestions have been presented, including individual blade pitch control, to eliminate negative damping in the pitch DoF [81-83].

### *3.1.3. Shortcomings of FAST*

In this section the author considers some shortcomings of the FAST code that he has come across and that are particularly relevant to floating offshore wind turbines. By no means is this an exhaustive list of all the limitations and weakness of FAST code. [72] contains a full list of simplifications and detailed description of simplifying assumptions made in FAST.

### 3.1.3.1. Induced velocities

The angle-of-attack calculations in AeroDyn (HAWT aerodynamics module in FAST) assume that the axial induction factor only applies to the free-stream wind velocity. To calculate the total relative wind speed normal to the rotor disc, each blade element's structural velocity is added to the free-stream wind velocity at the rotor disc, as shown below.

$$U_{rel} = U_{\infty}(1 - a) + v_{str} \quad 3.1$$

where  $v_{str}$  is the structural velocity of the blade element normal to the disc (measured positive when pointing upwind).

The assumption made in AeroDyn is that the structural velocities are the product of structural vibrations at high frequencies, which would result in relatively small induced velocities. However, when considering floating offshore wind turbines (FOWT), low-frequency motions, particularly, in surge, pitch and yaw DsoF, which induce change in the free-stream velocity, could lead to high induced velocities. In a low-frequency motion, a better way of expressing the relative wind speed normal to the rotor disc would be:

$$U_{rel} = (U_{\infty} + v_{str}) \times (1 - a) \quad 3.2$$

### 3.1.3.2. Hydrodynamics

The HydroDyn module in FAST, that is responsible for calculating all hydrodynamic loads, is somewhat simplified compared to other purpose-written naval software packages available, such as WAMIT, OrcaFlex, etc. Multiple simplifications are used within HydroDyn, some of which are debatable.

Broadly speaking, hydrodynamic loads can be split into contributions from hydrostatic loads due to stagnant or slow moving water, excitations from incident waves, radiation of waves generated by motion of the system and other non-linear effects. Except for ignoring the non-linear effects, of which only the correction for viscous drag using the Morison's equation is used, all other hydrodynamic loads are assumed to be linear in FAST.

WAMIT [71], based on potential flow wave theory, is a radiation/diffraction panel software developed for the linear analysis of the interaction of surface waves with different types of floating and submerged structures. These can be modelled as freely floating, constrained or

fixed. This means WAMIT uses some fundamental linear assumptions and – except for version 6.4S – cannot analyse any higher order problems, such as sum- and difference-frequency components. It is used in FAST as a pre-processor to obtain the hydrostatic restoring matrix, frequency-dependent added mass and damping matrices, and frequency dependent wave-excitation force vector. Linear solutions are used in obtaining the added-mass and damping, and wave-excitation force in WAMIT. Being based on a linear frequency-domain panel method (also known as the boundary integral equation method), WAMIT assumes that flow is incompressible and with no viscous effects (on top of frictionless and irrotational flow assumption from the potential flow theory). Additionally, the tower and wind turbine can only be modelled as rigid, as WAMIT has no capability of modelling elastic deformations outside of the water. The mooring system is also modelled as linear in WAMIT.

### 3.1.3.3. Flow separation

The hydrodynamic loads on a slender cylinder depend on the flow state, whether flow-separation has occurred or not. Depending on the answer, different formulations have to be used to correctly account for the hydrodynamics loads. The Keulegan-Carpenter number, Reynolds number and diameter-to-wavelength ratio can all be used to assess whether flow separation has occurred.

8 different periodic sea states taken from [46], shown in Table 9, were used to analyse the importance of diffraction effects and the likelihood of flow separation occurring when using the OC3-Hywind spar. The severity of the periodic sea state is in ascending order with 1 being the mildest sea and 8 representing a large storm.

Table 9 – Regular wave definitions [46]

Sea State	T (s)	H (m)
1	2.0	0.09
2	4.8	0.67
3	6.5	1.40
4	8.1	2.44
5	9.7	3.66

<b>6</b>	11.3	5.49
<b>7</b>	13.6	9.14
<b>8</b>	17.0	15.24

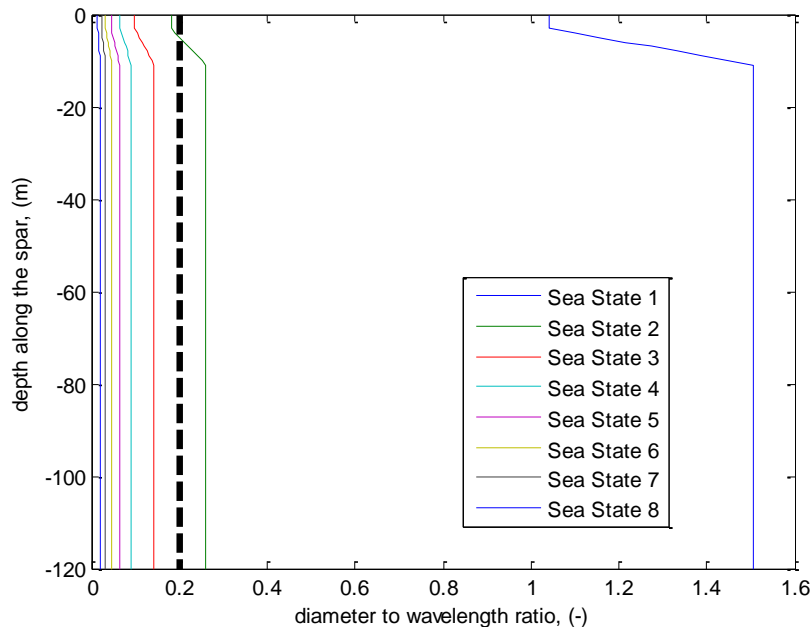


**Figure 94 – Diameter to wavelength ratio for the OC3-Hywind**

The structural members of some offshore installations, especially those of wind turbines, are small compared to the wave length and hence do not alter the flow field significantly. For cylinders, diffraction and refraction effects are assumed only to be important if the diameter-to-wavelength ratio is more than 20%. In such a case the flow has to be corrected to account for these effects.

From Figure 94, diffraction and refraction effects are significant only in very mild sea states, in which case the hydrodynamic loads are small anyway.

The Keulegan-Carpenter number (KC), which is a non-dimensional parameter describing the relative importance of viscous forces over inertia forces for bluff objects in an oscillatory flow, can be used to predict whether flow separation will occur, which occurs when the Keulegan-Carpenter number exceeds 2 [84]. Figure 95 shows that the OC3-Hywind spar should experience flow separation only in very severe weather conditions and

predominantly close to the SWL. For values  $< 2$ , potential flow theory can be used without any major modifications.

The Reynolds number, which is defined as the ratio of inertial forces to viscous forces, can be used to differentiate between different flow regimes, such as a laminar or turbulent flow. Figure 96 shows the distribution of the Reynolds number along the OC3-Hywind spar for the 8 different sea states.

Transition to turbulent flow, which is characterised by chaotic eddies, vortices and other flow instabilities, occurs for Reynolds number of around  $5 \times 10^5$  or higher. For Reynolds numbers below this threshold, the flow can be assumed to be smooth and with constant fluid motion. Figure 96 shows that the unstable and turbulent boundary layer will be experienced in all but the mildest sea state, though to a different extent, depending on the sea state and distance along the spar length.

The previous findings were deemed sufficient by FAST developers to use linear potential-flow theory to obtain the frequency-dependent added-mass and damping, and wave-excitation force for the OC3-Hywind spar.

Only in very severe sea conditions are the hydrodynamic loads obtained from WAMIT augmented with the loads due to flow separation. To do so, FAST uses a simplified hydrodynamic model based on the Morison's formulation. This adjustment for flow-separation is also simplified, as experiments have shown that drag coefficients for oscillating bodies are amplitude and frequency dependent. Any other second- or higher-order potential-flow solutions, such as, mean-drift, slow-drift, and sum- and difference-frequency excitations are not solved and are assumed to be negligible for a slender cylinder such as the OC3-Hywind spar.

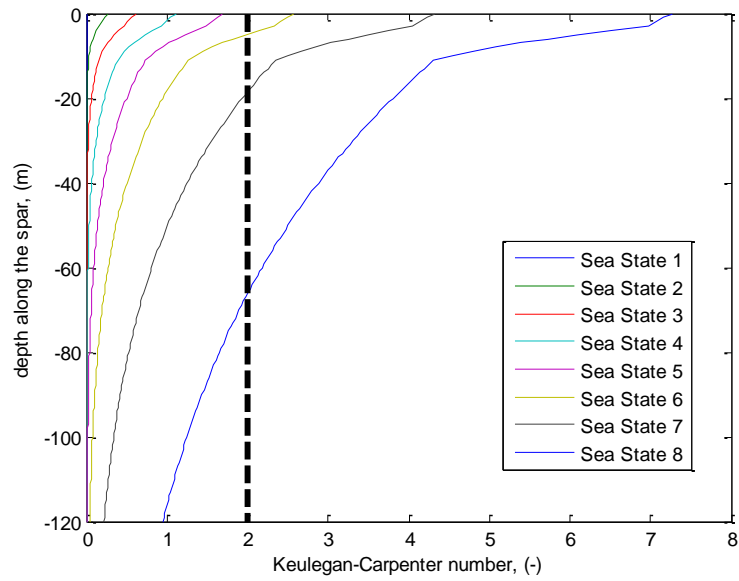


Figure 95 – Keulegan-Carpenter number for the OC3-Hywind

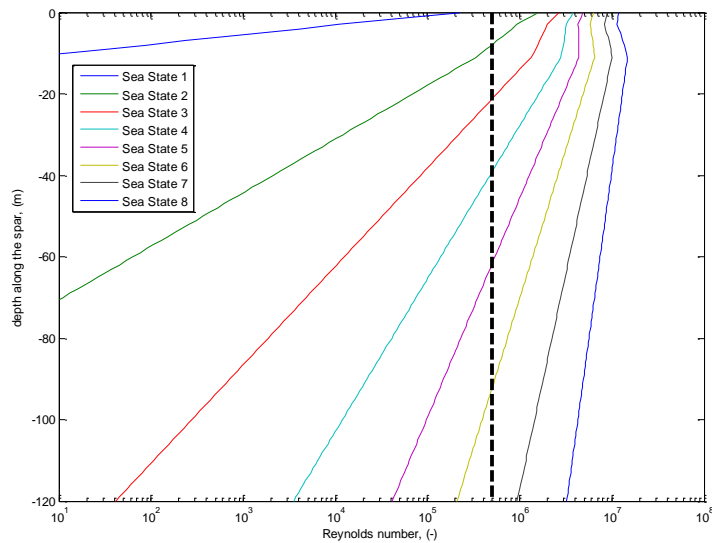


Figure 96 – Reynolds number distribution for the OC3-Hywind

While the use of linear potential-flow theory can be justified for the OC3-Hywind spar, any modification to the spar that would involve shortening the draft and hence increasing the diameter (to maintain buoyancy), will most likely lead to a larger diameter-to-wavelength ratio and an increasing chance of operating in the separated flow state. For this reason, the previous analysis of diameter to wavelength ratio and the Keulegan-Carpenter and the

Reynolds numbers should be revisited once the final, shortened spar design has been chosen.

The effective platform normalised hydrodynamic viscous drag coefficient ( $C_D$ ) of 0.6 is used in FAST to calculate viscous drag term from the Morison's equation for the OC3-Hywind. According to Faltinsen [85], for Keulegan-Carpenter numbers less than 10, the drag coefficient for a cylinder can be approximated as  $C_D \sim 0.2 \times KC$ . This means that FAST already assumes some flow separation as the Keulegan-Carpenter number comes out to be equal to 3 for the OC3-Hywind model.

#### *3.1.3.4. Mooring system*

The OC3-Hywind utilises a 3 point catenary system with each line consisting of multiple segments of varying properties and a clump weight (60 t for the original 2.3 MW Hywind). The catenary lines are attached to the spar using a delta connection as this allows the yaw stiffness of the system to be increased. Without such devices, there is almost no stiffness in the yaw DoF.

In the current version of FAST (FAST v7) the mooring system is modelled as quasi-static. It includes the effects of stretching, mass density, buoyancy, geometric non-linearity and seabed interaction. However, FAST uses 3 simplifications when it comes to modelling the mooring system of the OC3-Hywind:

- The delta (crow-foot) connection of the mooring system to the floater is eliminated (because of this the system has to be augmented with a yaw spring to achieve the proper overall stiffness in the yaw DoF).
- Each of the multi-segment lines is represented as one equivalent homogenous line with weighted average values for mass, weight and stiffness.
- All mooring system damping, including hydrodynamic drag and line-to-seabed drag, is ignored.

As explained in [46], these simplifications are adequate for static analysis, but may not be suitable for simulating dynamic conditions.

The additional yaw spring, which is needed as a result of eliminating the delta connection (crow-foot) from the model, has stiffness of 98,340,000 Nm/rad. A detailed description of the mooring system and the corresponding properties is provided in [46].

Mooring system dynamics are intrinsically non-linear and often include a hysteresis effect, which cannot be modelled in FAST. In the particular system being modelled, the highest non-linearities in the mooring line loads occur when the distance between the fairlead and anchor is between 800 – 870 m (853.87 m in the undisplaced case). This range also includes the transition from when a part of the mooring line rests on the seabed and when it is completely taut [46].

Results from a comparison study between FAST simulations and experiments [86] show that there are significant inconsistencies in the representation of damping behaviour in the model of a spar-type floating offshore wind turbine. In particular in heave, significant differences were observed between experimental and simulation results.

In future releases of FAST (FAST v8) a separate module will be responsible for calculating mooring statics and dynamics [87]. It will be capable of accounting for multi-segmented mooring lines. However, it will still be quasi-static and will still neglect viscous drag and damping [88].

#### *3.1.3.5. Small-angle approximations*

Floating offshore wind turbines operate in very unstable environments. Potentially, this can lead to large deflections in blade, tower and, less likely, platform rotational DsoF. FAST employs linear modal summation for calculating blade and tower deflections. The small-angle approximation in blade and tower deflection formulations is used. This means that at large deflections the accuracy of deflections and loads considerably diminishes. Moreover, large aero-elastic deflections or significant coning of the rotor blades will also diminish the accuracy of the wake modelling as the GDW and BEM models assume that the rotor plane is flat.

The support platform's rotational DsoF (roll, pitch and yaw) also use a small-angle approximation. FAST loses considerable accuracy when any of the displacements greatly exceeds 20 deg. [89].

### 3.1.3.6. Disabling degrees-of-freedom of the spar

A built-in option in FAST allows different DsoF of the floater (flags) to be disabled. In this research, the author has noticed that disabling floater's DsoF influences the system's natural frequencies. This is discussed next.

The following figure (Figure 97) shows displacement in the roll DoF for the OC3-Hywind spar in regular waves of 1 m height and 20 s period, and winds of 10 m/s, when only the roll DoF is ON. Both aerodynamics and hydrodynamic (aero + hydro) and just hydrodynamic (hydro) responses are shown for the quasi-steady (plot 1) and unsteady (plot 2) aerodynamic assumptions. The wind and waves are 90 degrees misaligned (the wind is aligned with the rotor axis) to achieve greater excitation in the side-to-side direction.

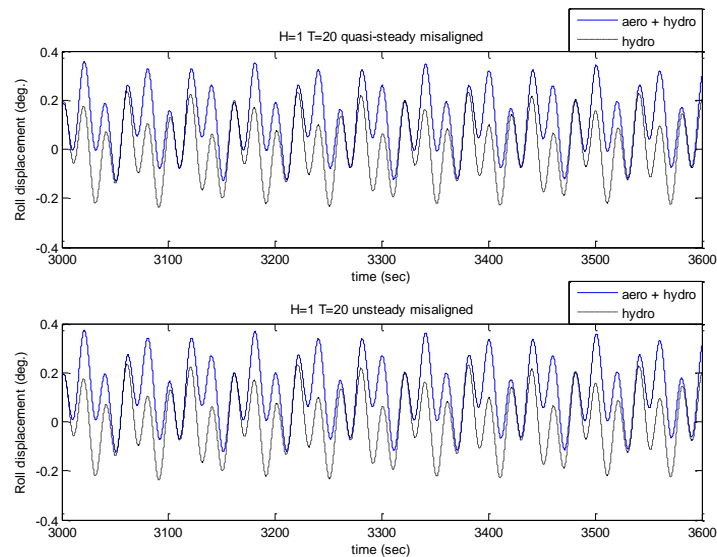


Figure 97 – Displacement in roll with other DsoF disabled

The figure above clearly shows two things:

- Difference between the quasi-steady and unsteady aerodynamic cases is negligible,
- The operating wind turbine (aero + hydro) has a steady mean displacement in the roll DoF due to torque reaction.

The figure below (Figure 98) depicts the single-sided amplitude spectrum for the quasi-steady aerodynamics roll displacement showed in the figure above (Figure 97). Two frequency components are present:

- Wave frequency ( $f = 0.05$  Hz),
- “Unobvious” frequency ( $f = 0.0189$  Hz).

Whilst the presence of the wave frequency is self-explanatory, the “unobvious” frequency does not correspond to any natural frequency of any other DoF of the system.

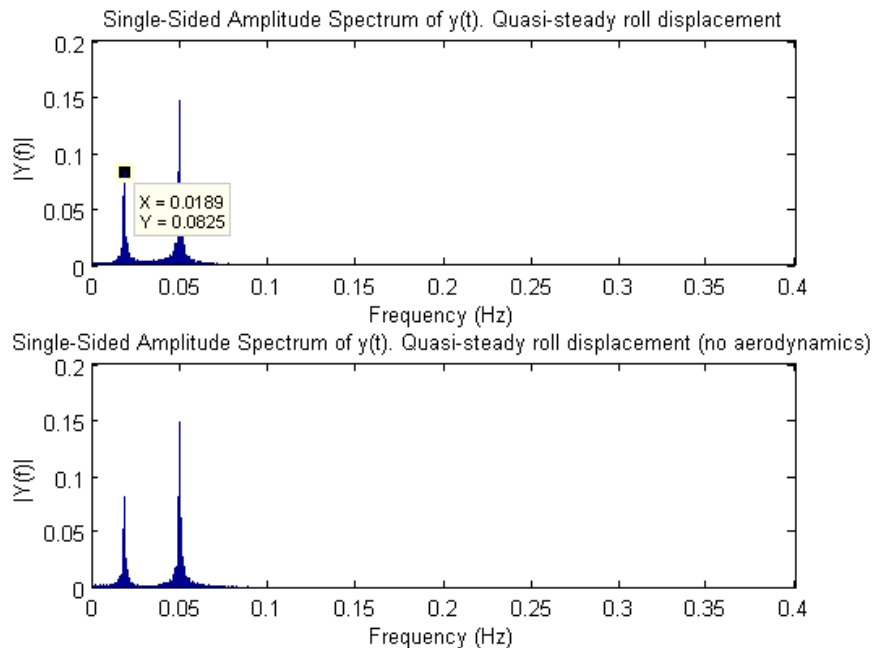


Figure 98 – Roll displacement in the frequency-domain

Another simulation was performed with all 6 DsoF of the supporting platform active (ON), but no aerodynamic loading (disabled aerodynamic calculations flag and 0 air density). Figure 99 and Figure 100 show the corresponding displacement in roll and its FFT (single-sided amplitude spectrum) for the same environmental conditions as in the case above.

The result with all DsoF of the floating support platform active show a mean roll displacement of 0 degrees (as would be expected, as no torque is generated at the rotor). The range of displacement has increased and, also, it now resembles much more a signal that has one dominant frequency component. This can be explained by looking at the signal in the frequency-domain (Figure 100).

Identical to the previous results, two frequency components are present:

- Wave frequency ( $f = 0.05$  Hz),

- Roll frequency ( $f = 0.0336$  Hz).

However, now the “unobvious” frequency, which was present in the previous simulations, has been replaced by the support platform’s roll frequency (0.0342 Hz, as given by the NREL). The natural frequency in roll motion is still present in the response of the OC3-Hywind even after 3,000 s of simulation, as there is very little damping in the side-to-side direction, and any initial transients will take a very long time to dissipate and reach the steady-state response, which would consist only of the wave frequency. Because aerodynamic loads are not calculated, there is no aerodynamic damping; hence all damping must come from the structural and hydrodynamic damping. This means that the initial results with the support platform’s DsoF disabled, except for roll, cannot be used to compare different DsoF and that the “unobvious” frequency is the result of FAST’s internal structure (the way it has been written, or more specifically, how it treats disabled DsoF) and not the result of product-to-sum or sum-to-product expressions of different frequencies, as initially believed by the author. This is also consistent with the e-mail sent by Jason Jonkman, who is responsible for FAST in the NREL, in which he explains that disabling DsoF will change the natural modes of the system (i.e. “fixed-free” versus “free-free” modes). However, the results seen, as presented here, are somewhat perplexing; when a DoF is disabled, the expected result should be an increase in frequency due to the system being, effectively, stiffer.

Similar effects were seen when all but the pitch DoF were disabled, and wind and wave inputs were aligned. The natural frequency in pitch DoF was shifted to some “unobvious” frequency. Both roll and pitch DsoF are strongly coupled to sway and surge. Normally, the OC3-Hywind spar pivots about the location on the spar where the moorings are attached (70 m below the SWL). However, the actual floater DsoF in FAST are defined about the platform reference point, which in this case is about the location where the spar intersects the SWL (Figure 29). Hence enabling only the roll or pitch DoF will result in very different roll or pitch motion than when both roll and sway or pitch and surge DsoF are enabled. Hence the explanation for the shift in the natural frequency in the pitch and roll is due to the coupling effects between these DsoF being disregarded.

This means that disabling different DsoF to model one DoF at a time is not an option. An alternative method was used which involved scaling the wave-excitation force vector in

different DsoF to establish which DoF is the most detrimental to the system in terms of the tower and blade fatigue.

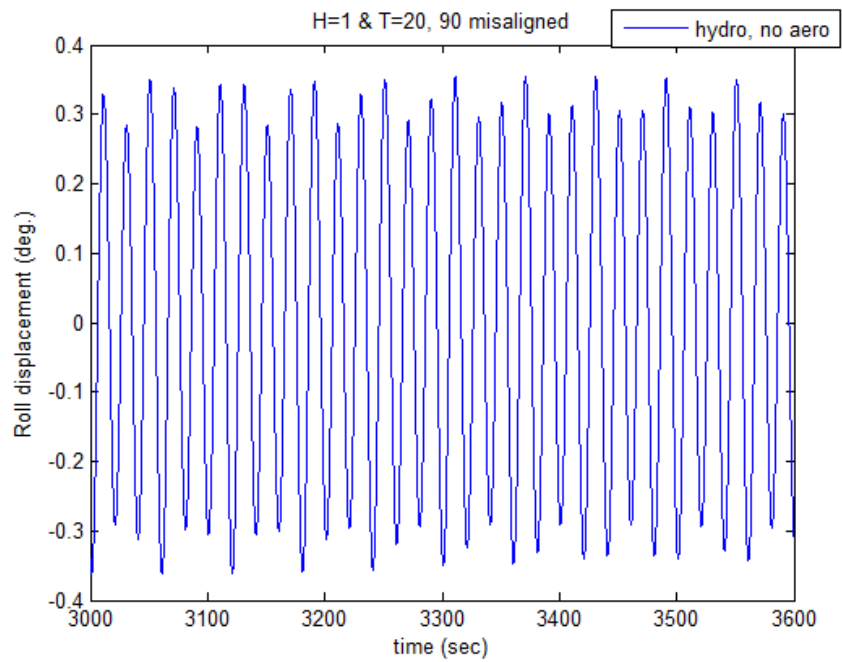


Figure 99 – Displacement in roll with all DsoF active

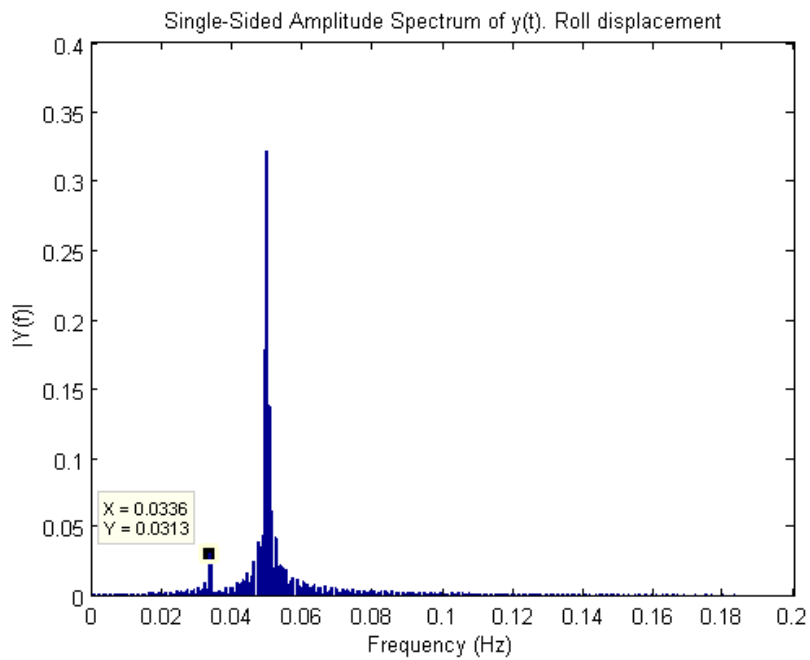


Figure 100 – Roll displacement in the frequency-domain (all DsoF active)

### *3.1.3.7. Vortex ring state*

A vortex ring (toroidal vortex) is a torus shaped vortex in which flow spins around an imaginary axis that forms a closed loop. Vortex rings can be formed by a spinning rotor (helicopter, wind turbine). A vortex ring formation around the rotor of a helicopter is known as the vortex ring state or settling with power. The effects of the vortex ring state have been thoroughly studied by the helicopter industry. This is a very dangerous condition of flow recirculation that can result in significant loss of lift and a potential accident [90].

The vortex ring state can develop in floating offshore wind turbines as these alternate between the turbine (extracting energy) and propeller (inducing energy into the flow) operational states due to the system's motion (particularly in surge, pitch and yaw). When operating in the vortex ring state, turbine will experience large, periodic changes in loads and, more importantly, it will lead to breakdown of the momentum balance equations, which form the basis of the majority of the industry's simulation codes. A detailed description of the breakdown of momentum theory in the vortex ring state is given by Sebastian in [91, 92].

Sebastian, using FAST, analysed how much time is spent in the vortex ring state under three different operating conditions (below-rated, rated and above-rated) for a monopile and for 3 floating offshore wind turbines (barge, spar-buoy and TLP) with the NREL 5MW wind turbine and no dynamic inflow [93]. For the OC3-Hywind, the time spent in the vortex ring state differed significantly between the operating conditions. Below-rated it varied from near 0% close to the blade root to more than 50% at the blade tip, at rated from 0.1% at the root to slightly more than 1% at the blade tip and for above-rated it was less than 0.25% over the whole blade.

Wake simulation in FAST (AeroDyn) is modelled using either BEM or GDW and neither of the two methods can model or account for the vortex ring state.

Sebastian identified the pitch and yaw DsoF of the OC3-Hywind as the most likely to lead to unsteady loads compared to a monopile supported turbine, and hence generating and operating in the vortex ring state [51].

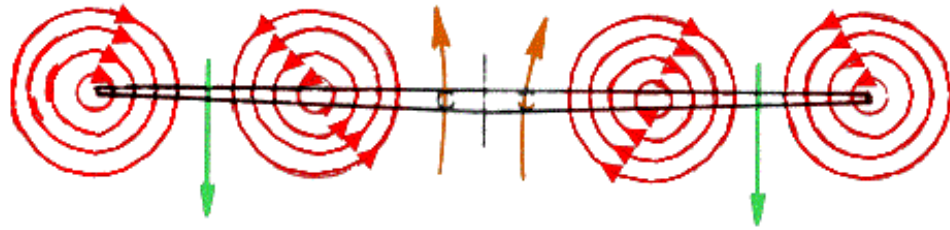


Figure 101 – Depiction of the vortex ring state on a helicopter rotor

### 3.1.4. Sanity check

To make sure that the OC3-Hywind simulations produce meaningful results, a sanity check was performed on the FAST set-up and simulations outputs. Multiple parameters were compared to those published by NREL in papers by Jason Jonkman et al [46, 94]. These included the hydrodynamic wave excitation, hydrodynamic added mass and damping, and radiation impulse response functions for the OC3-Hywind spar obtained using the WAMIT software package [71], and free-decay tests for surge, heave, pitch and yaw DsoF performed in FAST.

The magnitude and phase of the hydrodynamic wave-excitation as a function of wave frequency obtained using WAMIT produced identical results to previously published by Jonkman [46]. Both hydrodynamic added mass and damping, and radiation impulse-response functions for the OC3-Hywind were reproduced identically (Figure 103 and Figure 104).

Free-decay tests for the OC3-Hywind (spar, mooring and WT) for surge, heave and pitch DsoF with initial displacements of 20 m, 5 m and 10 deg. respectively, are shown in Figure 105. Not shown is the platform's response in yaw, but, the same as in the other 3 DsoF, it perfectly matched the results presented in [94].

When modelling the OC3-Hywind spar in FAST v7, it was necessary to use a specially compiled version of FAST that includes additional stiffness and damping, as described in [46]. That is, the default version FAST v7 could not be used with the OC3-Hywind model as there are no means to add and account for additional stiffness and damping that were

added to match the free-decay data provided by Statoil. With the release of FAST v8, the extra stiffness and damping will be able to be provided in the input files.

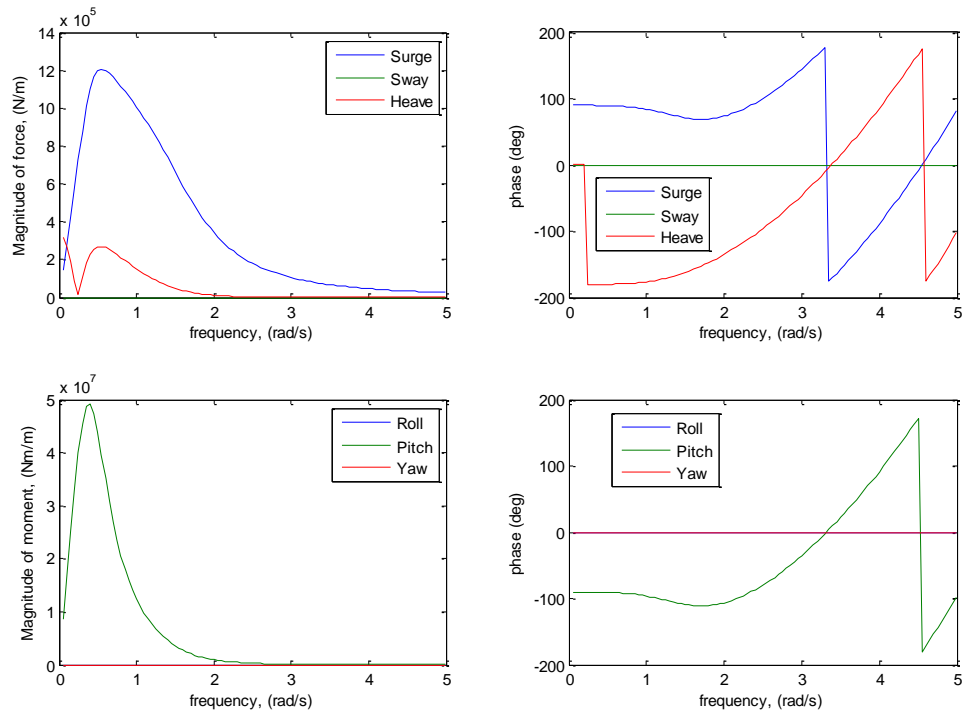


Figure 102 – Hydrodynamic wave-excitation per unit amplitude for the OC3-Hywind (no mooring or WT)

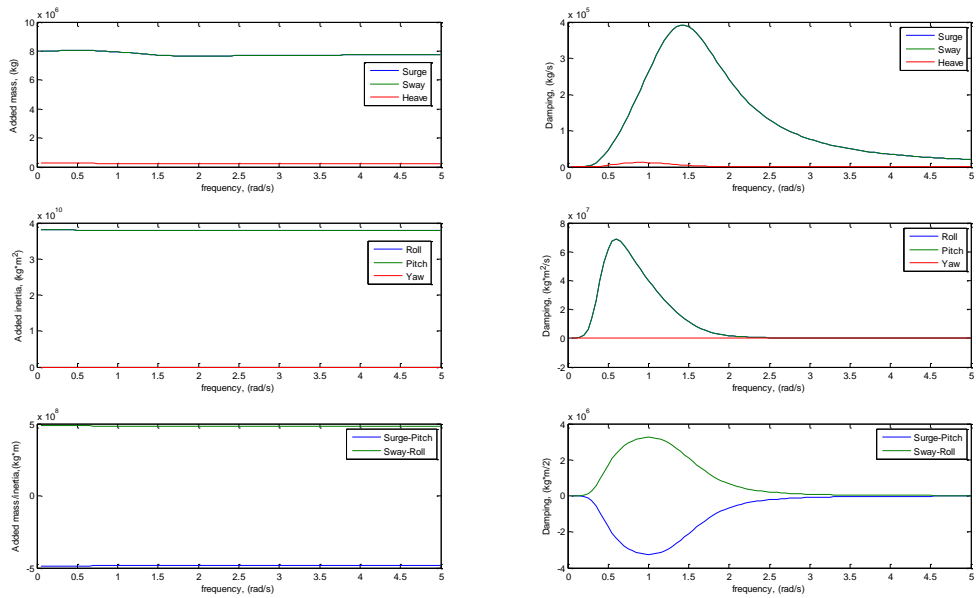


Figure 103 – Hydrodynamic added mass and damping for the OC3-Hywind spar (no mooring or WT)

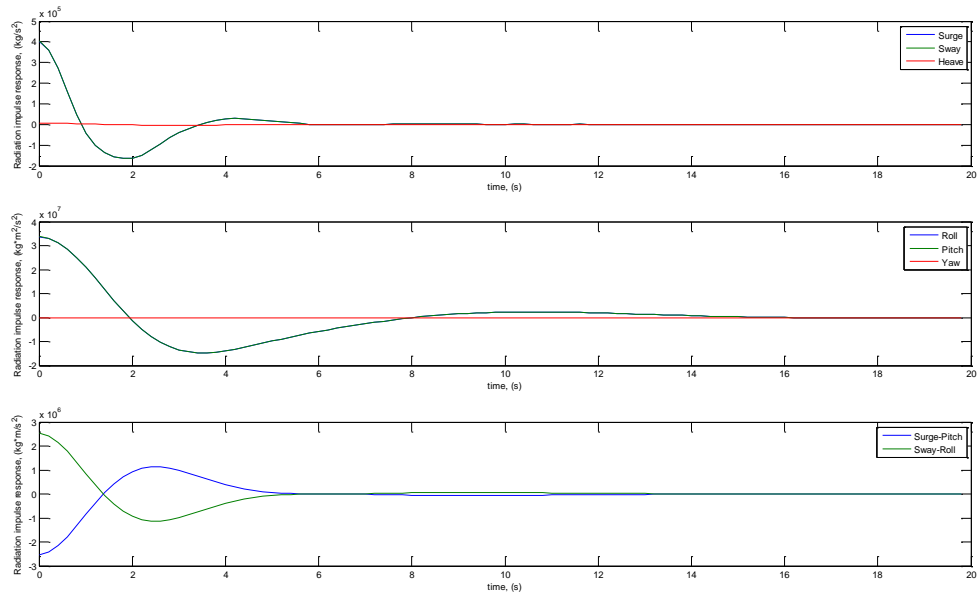


Figure 104 – Radiation impulse-response functions for the OC3-Hywind spar (no mooring or WT)

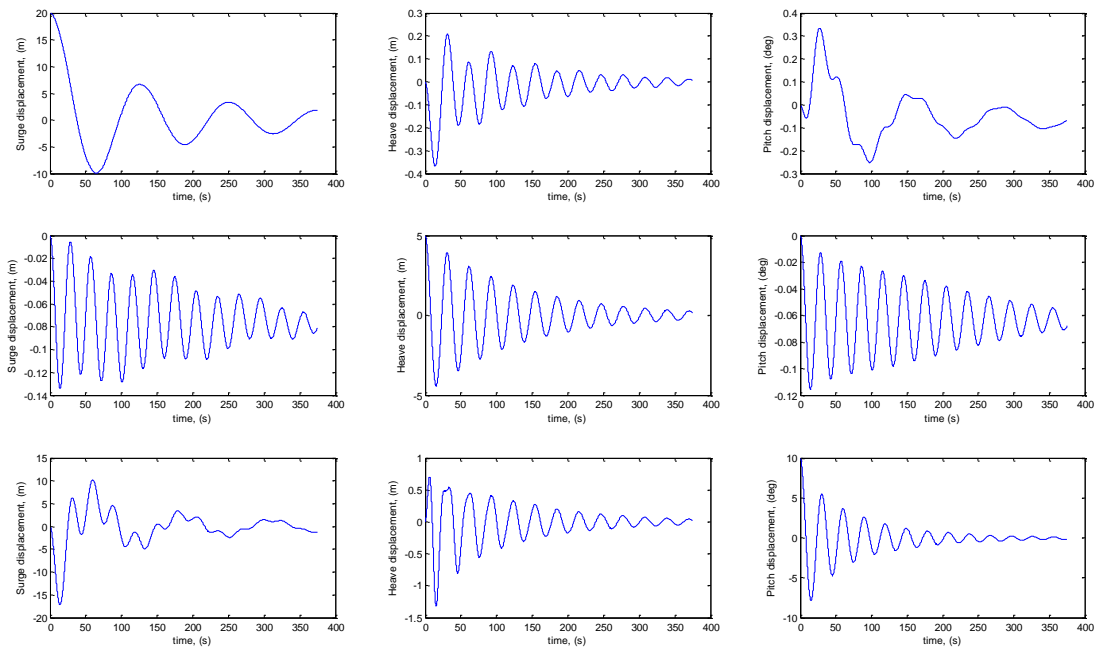


Figure 105 – Free-decay tests for the OC3-Hywind system

### 3.1.4.1. Natural frequencies

To obtain a better understanding of the factors that influence the natural frequencies of the OC3-Hywind, the natural frequencies of the OC3-Hywind, as published by Matha [95],

were compared to those obtained by performing some back-of-the-envelope calculations in Excel (A1.9) and simulations in WAMIT (A1.10).

**Table 10 – Natural frequencies of the OC3-Hywind platform**

	<b>D. Matha</b>	<b>Excel</b>	<b>WAMIT</b>
<b>Surge</b>	0.0080 Hz	0.0080 Hz	0.0080 Hz
<b>Sway</b>	0.0080 Hz	0.0080 Hz	0.0080 Hz
<b>Heave</b>	0.0324 Hz	0.0322 Hz	0.0318 Hz
<b>Roll</b>	0.0342 Hz	0.0364 Hz	0.0303 Hz
<b>Pitch</b>	0.0343 Hz	0.0364 Hz	0.0303 Hz
<b>Yaw</b>	0.1210 Hz	0.1174 Hz	0.1178 Hz

The approach in calculating the natural frequencies of the OC3-Hywind system in the Excel spreadsheet is shown in appendix (A1.9). The obtained results closely matched those of Matha with surge and sway showing no discrepancy at all, and heave, roll and pitch, and yaw having <1%, <6.5% and 3% difference, respectively.

The results obtained using RAOs (response amplitude operators) in WAMIT have a slightly larger deviation from the results by Matha. In particular, the biggest difference was observed in the roll and pitch DsoF (approx. 12%), the same DsoF that showed larger discrepancies as with the Excel calculations. On the other hand, heave, yaw, and surge and sway natural frequencies showed a very good agreement; no deviation in surge and sway results, and <2% and 3% in heave and yaw.

The natural frequencies of the surge, sway and yaw DsoF are purely functions of the mooring system’s stiffness. On the contrary, heave, pitch and roll depend on both the mooring system’s stiffness and restoring forces due to extra buoyancy (heave) and righting moments (pitch and roll). A detailed description and derivation of each DoF is given in A1.9.

RAOs obtained in WAMIT also allowed the cross-coupling between different DsoF to be observed. The results are shown in A1.10.

### *3.1.5. Damping*

The three main types of damping associated with a spar-type floating offshore wind turbines are:

- Hydrodynamic damping (viscous drag),
- Aerodynamic damping (changes in aerodynamic forces),
- Structural damping.

Aerodynamic damping arises due to changes in the inflow of air to the rotor when the system is moving. Changes in the airflow across the rotor due to its own motion result in changes in thrust and torque on the rotor. Aerodynamic damping is a very large source of damping in all wind turbines. In contrast, structural damping comes from internal friction within the material itself and is relatively small for the OC3-Hywind. Tower and blade structural damping ratios in all modes are 1 and 0.477%, respectively. To match the still-water free-decay responses of Hywind provided by Statoil, additional linear damping was added in FAST (100,000 N/(m/s) in surge and sway, 130,000 N/(m/s) in heave and 13,000,000 Nm/(rad/s) in yaw [46]). Other means of damping, such as damping from the mooring system, are relatively small and cannot be modelled in FAST.

#### *3.1.5.1. Aerodynamic damping*

In trying to identify which DsoF are potentially the most detrimental from the fatigue perspective, it is vital not to neglect the importance of the aerodynamic damping, as it can have large effect on the response in each DoF and thus on the lifetime loads on the whole structure.

In onshore and fixed-bottom offshore wind turbines, aerodynamic damping provides the majority of the damping of the system. Typically, it is an order of magnitude larger than the structural damping. Aerodynamic damping can be seen as both active (pitch control) and passive damping (thrust force generated over the rotor due to blade rotation). Generally, for fixed base wind turbines the lateral motions of the tower top tend to persist much longer than longitudinal, as aerodynamic damping from the rotor is an order-of-magnitude smaller in the side-to-side direction [96]. The OC3-Hywind responses to impulse loading in 4

different DsoF for below-rated conditions (10 m/s uniform wind) and 5 meter and 20 second waves is shown in Figure 106.

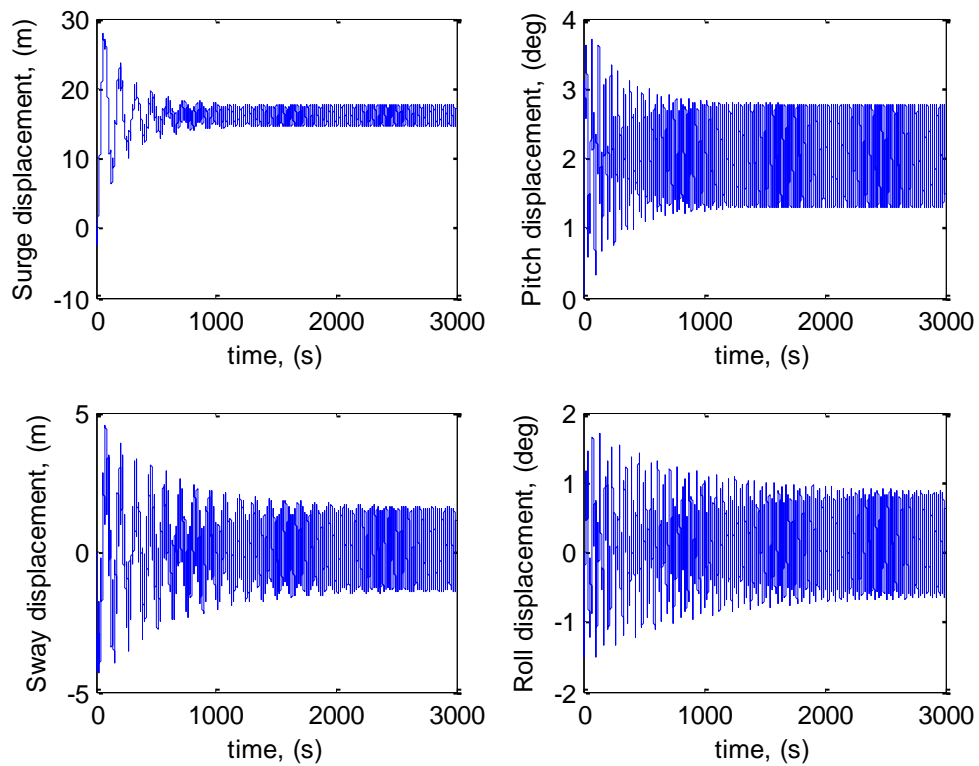


Figure 106 – Displacements in 4 different DsoF for the OC3-Hywind

Figure 106 clearly shows that fore-aft motion (surge and pitch) has much more aerodynamic damping compared to side-to-side motion (sway and roll). With the viscous (hydrodynamic damping) and structural damping being the same for surge and sway, and pitch and roll, due to the symmetry of the system, the difference must come from the aerodynamic damping from the rotor, which seems to be the dominant damping term. Also to note is that surge and sway, and pitch and roll have almost identical natural frequencies.

Figure 107 shows the displacement of the floater and the thrust force on the rotor in the same wind and wave conditions as in Figure 106. Only the last 100 seconds of the simulation's results are shown to ensure that the 'steady-state' values have been reached. The mean surge displacement is slightly larger for the unsteady case, as its mean thrust is also higher. However, while the amplitudes of displacement are almost identical in the quasi-steady and unsteady cases, the amplitude of the thrust force on the rotor in the unsteady aerodynamics simulation is significantly larger. This is suspected to be the result

of differences in the aerodynamic damping between the quasi-steady and unsteady cases. For this reason, the aerodynamic damping is considered in more detail below.

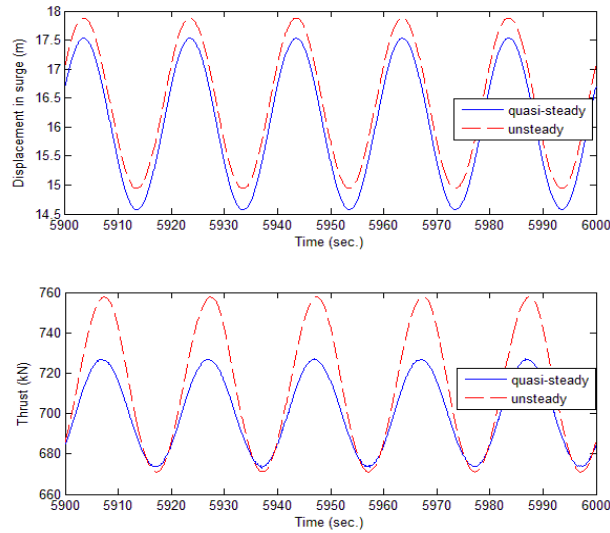


Figure 107 – Displacement and thrust force in the surge DoF

There are multiple methods of calculating the aerodynamic damping associated with wind turbines. Some of these methods for constant and variable speed turbines are presented in [97]. In this report, methods of logarithmic decrement and Van der Temple [98] were used.

Logarithmic decrement,  $\delta$ , can be used to find the damping ratio for an under-damped system in the time-domain.

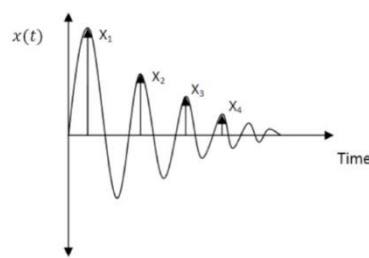


Figure 108 – Logarithmic decrement method

$$\delta = \frac{1}{n} \log \left[ \frac{x(t)}{x(t + nT)} \right] \quad 3.3$$

where  $x(t)$  is the amplitude at  $t$  and  $x(t+nT)$  is the amplitude of the peak in  $n$  periods.

Now the total damping ratio of an underdamped system can be found using:

$$\xi_{total} = \frac{\delta}{\sqrt{4\pi^2 + \delta^2}} \quad 3.4$$

where  $\xi_{total}$  is the total damping ratio and consists of aerodynamic, viscous hydrodynamic and structural terms.

The logarithmic decrement method becomes less accurate for damping ratios above 0.5 (or 50%). However, this is of little importance, as the aerodynamic damping ratio rarely exceeds 10%.

The logarithmic decrement method was used to calculate the aerodynamic damping in the quasi-steady and unsteady aerodynamic simulations. Damping is a function of amplitude and frequency of response. A fixed-foundation WT with modified tower mass and stiffness distribution was used to mimic the aerodynamic damping experienced by the OC3-Hywind under wave input. This approach also allowed removing any contributions from the hydrodynamic damping due to the platform's motion.

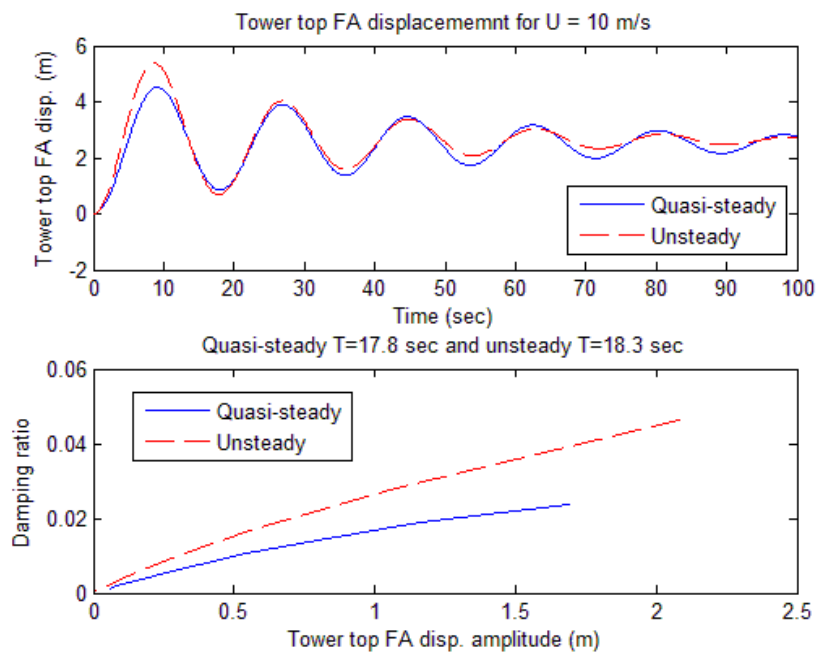


Figure 109 – Tower top displacement and the associated damping ratio

Results, obtained in FAST, showed that for the below-rated conditions of 10 m/s wind and 6 meter and 18 second regular waves, the amplitude of surge displacement for both quasi-steady and unsteady results was 1.57 m. These results were imitated in Figure 109, resulting in the total damping of 2.3 and 3.7% for the quasi-steady and unsteady representations, respectively. In calculations the author assumes that the hydrodynamic damping is identical between the quasi-steady and unsteady aerodynamic calculations, as the amplitude of displacement is the same.

Alternatively, Van der Temple's method [98] expresses the aerodynamic damping directly from the time-domain simulation results by relating it to the change in the thrust force on the rotor caused by a change in the perpendicular wind speed relative to the rotational plane.

$$c_{damping} = \frac{dT}{dU_{normal}} \quad 3.5$$

$$\xi_{aero} = \frac{dT}{dU_{normal}} \times \frac{1}{2M_0\omega_n} \quad 3.6$$

where  $U_{normal}$  is the relative wind speed perpendicular to the rotational plane (includes wind speed, blade flapping and fore-aft movement of the system),  $M_0$  is the modal mass and  $\omega_n$  is the natural frequency.

The Van der Temple method is much simpler to execute, yet it cannot be used directly, as neither FAST, nor AeroDyn outputs the wind speeds relative to the rotational plane. Nonetheless, if blade motions are ignored by neglecting blades flexibility (not strictly valid, as the current wind turbine blades can experience deflections of several meters at the blade tip), the relative wind speed at the rotational plane can be expressed as the difference between the surge velocity and the actual wind speed at the rotor disc, taking into account induced velocity. This will result in almost identical relative wind speeds between the quasi-steady and unsteady cases, though there would be a small difference due to differences in the axial induction factors. With all other variables in equation 3.6 being identical between both simulations (quasi-steady and unsteady), the aerodynamic damping is proportional to the change in thrust. Plot 2 of Figure 107 shows a much greater gradient of thrust for the unsteady results; meaning that the aerodynamic damping is

greater in the unsteady aerodynamic simulations. This matched the results obtained using the logarithmic decrement method.

#### *3.1.5.2. Damping in different degrees-of-freedom*

In [99], Withee has looked at damping in single and multiple modes of motion of a spar-type floating wind turbine with spoke mooring. He found that in some DsoF viscous drag dominated the damping and in others it was the damping of the wind turbine. He also found the aerodynamic damping of the wind turbine to be linear. While he used a different design of a floating offshore wind turbine (draft of 10 m and rated power of 1.5 MW), some of the results can also be expected to apply to the OC3-Hywind.

In surge, the aerodynamic damping due to the wind turbine rotor was found to be linear and an order-of-magnitude smaller than the viscous drag. In sway, the quadratic damping coefficient (viscous drag) is almost identical to surge damping as the floater is symmetrical. However, the linear damping coefficient was found to be around 30% of the surge coefficient. This was to be expected as motion in sway does not affect the axial (out-of-plane) wind inflow much, and mainly influences the rotor thrust through changes in in-plane velocity. For the same amplitude of motion, the percentage change in in-plane velocity is much smaller than for the changes in out-of-plane velocity in surge. The linear damping coefficient in heave was shown to be of the same order of magnitude as in sway (both DsoF have the rotor moving normal to the wind inflow), but the viscous drag damping was found to be 2 orders-of-magnitude greater than the linear damping, which seems to suggest that the mooring lines were the main source of the damping. Additionally the viscous drag damping was 2 orders-of-magnitude greater in heave compared to sway. Large viscous damping can be partially explained by the small natural period of the heave mode (4.45 s), which – compared to the natural period of sway (39 s) – will result in large viscous damping as it is proportional to the square of the floater velocity.

The rotational DsoF (roll, pitch and yaw) are coupled to other modes of motion by hydrodynamic and gyroscopic effects. Roll is the only DoF of the 3 that does not give rise to any gyroscopic moments as the rotor's plane of rotation does not change, but it is still cross-coupled to the sway DoF. This effect of cross-coupling made extracting damping coefficients for rotational DsoF more difficult. Withee [99] showed that linear damping is an

order-of-magnitude larger than the quadratic damping in the coupled roll-sway mode. The roll linear damping coefficient was shown to be 25% of the pitch coefficient. The linear damping effects in the pitch DoF are the greatest of all DsoF, as in the pitch DoF the rotor experiences the largest changes in the out-of-plane velocity. On the other hand, the viscous drag coefficient is identical to that in the roll DoF since the floater is symmetrical and it is 2 orders-of-magnitude smaller than the linear damping from the wind turbine. Cross-coupling between pitch and surge was also observed. Finally, the yaw DoF damping is dominated by the linear damping from the wind turbine; however the OC3-Hywind would also see some damping coming from the mooring lines.

The wind turbine rotor was found to provide the majority of the system's damping in the pitch and yaw DsoF, whilst the viscous drag was the major damping mechanisms in the translational modes.

## 3.2. Fully-unsteady aerodynamics

Being an aero-elastic structural code, FAST simulations include flexible structures (tower and blades), a controller that was specifically designed for spar-type floating wind turbines, and coupled aerodynamic and hydrodynamic effects.

Initially, each DoF was simulated separately by disabling other DsoF by setting acceleration to zero and keeping the initial velocities constant for each disabled DoF. This allowed the responses of the system in each of the DsoF to be compared for the quasi-steady and unsteady aerodynamics assumptions. However, the author noticed that disabling DsoF of the spar shifted the natural frequencies in the roll and pitch DsoF (as described in 3.1.3.6). Therefore, all subsequent simulations were carried out with all DsoF active.

AeroDyn [15] is used in FAST to calculate aerodynamic loading. Two different setting sets were used – quasi-steady and fully-unsteady. Similarities and differences between these aerodynamic modelling techniques are summarised in Table 11.

A simplified flowchart of AeroDyn, as seen by the author, is shown in Figure 110.

Different combinations of sea states were used. These included regular waves of 1 to 6 meters in height and eight different periods in range from 5 to 25 seconds. A MATLAB code was written to generate the primary and platform files, as each run involved 96 simulations (48 for each aerodynamic setting).

**Table 11 – Similarities and differences between the quasi-steady and unsteady aerodynamic settings in FAST**

EQUIL + STEADY	DYNIN + BEDDOES
<b><i>Similar</i></b>	
Large aero-elastic deflections or significant coning of the blades will not represent aerodynamic loading precisely (both theories based on a flat disc assumption).	
SWRIL/WAKE/NONE option for induction factor calculation (flags).	
All input files for FAST are the same except for two lines in AeroDyn input file.	
<b><i>Different</i></b>	
Quasi-steady aerofoil characteristics – look-up tables (STEADY)	Dynamic aerofoil characteristics – Beddoes-Leishman model (BEDDOES)
“Quasi-steady” or equilibrium wake (EQUIL) <ul style="list-style-type: none"> <li>• No time lag (no dynamic inflow).</li> <li>• Glauert’s model for heavily loaded rotors.</li> <li>• Prandtl’s hub/tip loss model or GTECH model for tip losses.</li> </ul>	Dynamic wake (DYNIN or GDW) <ul style="list-style-type: none"> <li>• Time lag (dynamic inflow).</li> <li>• Unstable at low wind speed (&lt; 8m/s) /highly loaded (switches to BEM).</li> <li>• Inherent modelling of the dynamic wake effects, tip losses and skewed wake aerodynamics.</li> <li>• Does not account for wake rotation (uses BEM theory equations for <math>\alpha'</math>).</li> </ul>

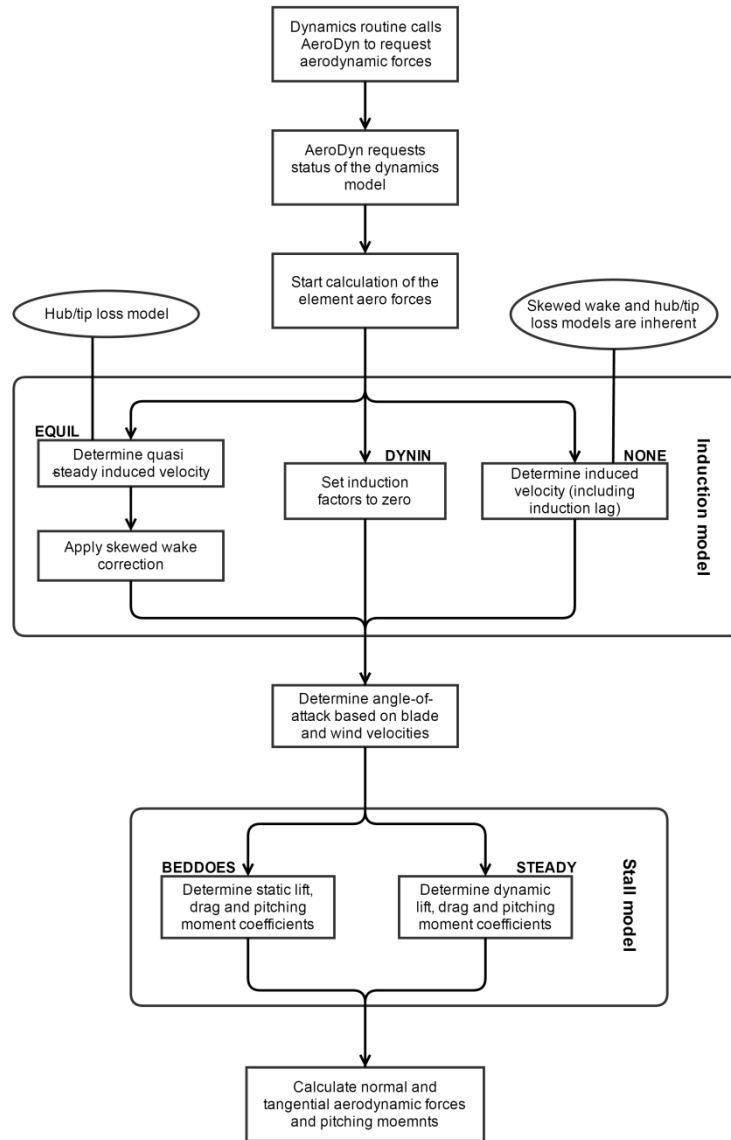


Figure 110 – Flowchart of AeroDyn

### 3.2.1. Unsteady aerodynamic effects

In the previous chapter fully-attached unsteady aerodynamics were compared to quasi-steady aerodynamics for a fully-rigid NREL 5MW in the absence of a controller. With all the multiple simplifications that were made, some useful results were obtained. These showed that there is a difference between both cases (quasi-steady and fully-unsteady), which revealed themselves as a slight change in the mean and amplitude of loading, and a phase shift. The author came to the conclusion that for environmental conditions that diverge

from the quasi-steady case, such as large amplitudes and small periods of wave motion, the unsteady aerodynamic effects need to be taken into account when trying to quantify dynamic loading effects and even when performing the initial design of a wind turbine. This is particularly true due to high influence that the wake effects (such as the 'memory-effect') have on the rotor and hence the tower and blade loads.

In this section of the thesis, a further investigation is performed into the unsteady aerodynamics of a floating offshore wind turbine. A much more realistic case is used, where parts of the turbine (tower and blades) are modelled as flexible and the control algorithm used is one that has been designed to avoid introducing negative aerodynamic damping in pitch motion, a phenomenon that has long been recognised [81].

Whilst many simulations were carried out in FAST, discussion will concentrate on the case of regular waves of 5 m height and 10 s period, and a uniform 10 m/s wind. This represents a relatively unsteady environment. Wind and wave inputs were aligned in all simulations.

The fully-unsteady aerodynamics produces almost identical amplitude and larger mean displacement in surge compared to the quasi-steady simulations (Figure 111). The same applies to pitch displacement which shows a higher mean in the unsteady case (compared to quasi-steady), but a smaller amplitude. Responses in other DoF are not shown as they are at least an order-of-magnitude smaller than in surge. Because surge and thrust are directly interlinked (platform motion leads to a change in thrust and vice-versa), the thrust response on the rotor follows a very similar response as in the surge DoF (see Figure 111 and Figure 112). However, while the mean values are higher in the unsteady case, the relative size of the amplitude differs between surge and thrust response. This is due to the increased aerodynamic damping in the unsteady case (see 3.1.5.1).

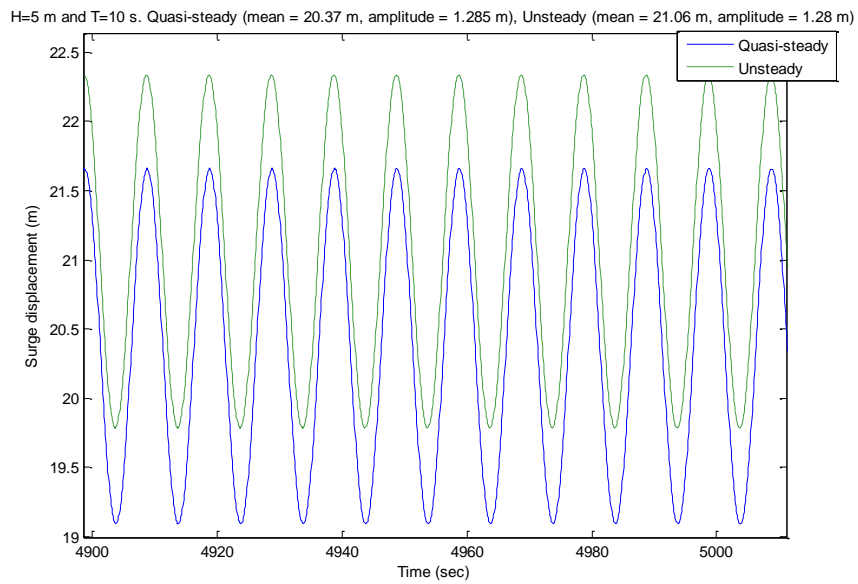


Figure 111 – Surge displacement

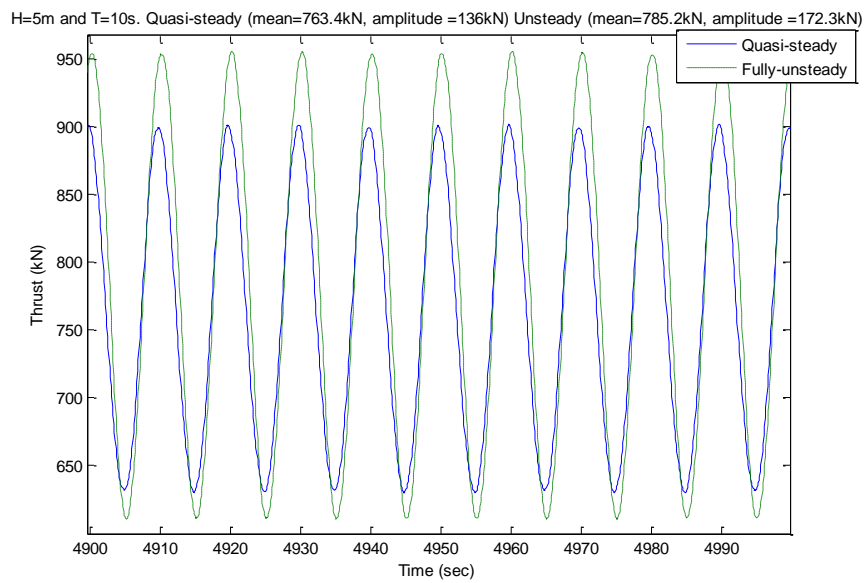


Figure 112 – Thrust force on the rotor

Also evident is a phase shift between the quasi-steady and unsteady cases, where the fully-unsteady results lag behind the quasi-steady as they did in the fully-attached results and as the theories suggest they should.

Next, torque response was analysed. Figure 113 shows significant deviation between the quasi-steady and unsteady aerodynamic runs, with the unsteady aerodynamic simulations

displaying the presence of some high frequency components. These were identified, using the FFT, as being the wave harmonics (Figure 114). The very large peak-to-trough range of torque values can be explained by the highly non-linear response of the system to induction lag<sup>6</sup> [100, 101]. The following figures (Figure 114, Figure 116 and Figure 119) confirm this with the presence of either wave harmonics and/or sum- and difference-frequencies of rotation and wave in the single-sided amplitude spectrums. Also clearly seen from these figures is that the fundamental frequency (wave frequency) is of much larger amplitude in the unsteady case (roughly triple that of the quasi-steady). Use of the GDW for modelling aerodynamics (dynamic wake) will result in significant power overshoots whenever blades experience any change in the angle of oncoming wind (for example due to surging motion of the system), as the wake behind the rotor takes time to develop and adjust to new conditions. However, because floating offshore wind turbines are always surging or undergoing some other motion, they are also always experiencing varying oncoming wind, and the wake never reaches an equilibrium condition with the rotor thrust.

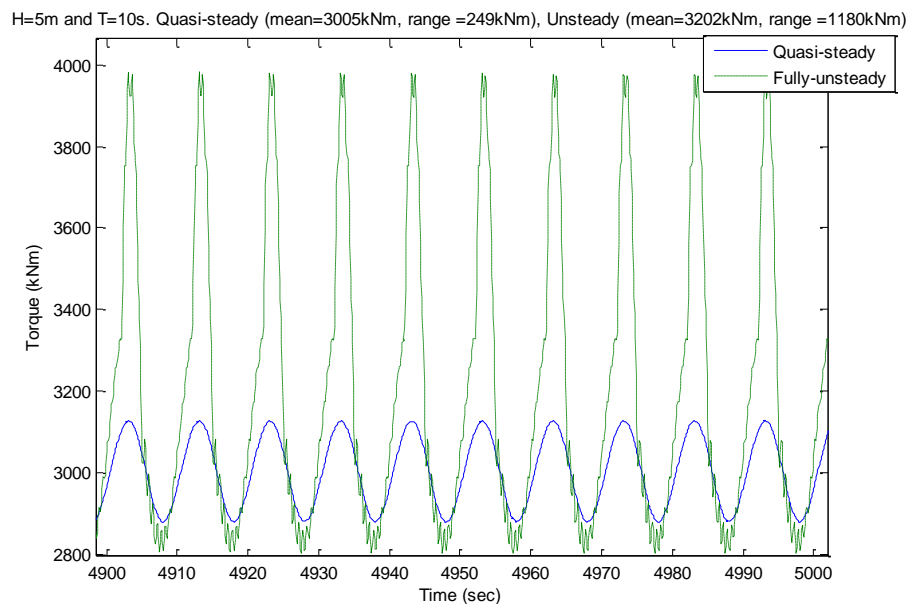


Figure 113 – Torque response

---

<sup>6</sup> Induction lag (also known as dynamic inflow) is a time lag in the induced velocities created by vorticity being shed from the blades and convected downstream which results in blade moment and torque overshoots compared to standard quasi-steady calculations.

Compared to the results presented in Chapter 2, Figure 113 and Figure 114 show much greater difference between the quasi-steady and fully-unsteady aerodynamic representations. This is believed to be a direct result of the unsteady effects, such as induction lag – which were not considered and accounted for – and other simplifications made in Chapter 2. Additionally, the results presented in Figure 113 are for relatively severe waves, which could potentially lead to some contribution to results from the dynamic stall model employed in the fully-unsteady case. All results presented in this chapter include damping, which was completely ignored in Chapter 2. However, there is very little damping in the side-to-side direction of WTs and hence this should have no significant effect on the torque response. There is a possibility of obtaining negative damping in spar-type FOWTs [82]. However, this would have been apparent in Figure 112 with the presence of large thrust forces due to excessive motion in the pitch DoF, which is not the case for the results presented.

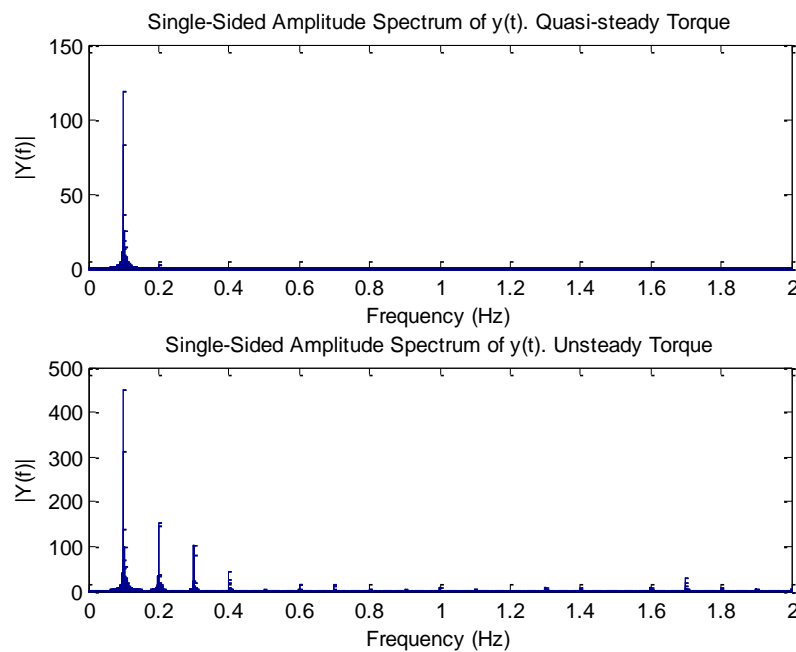


Figure 114 – Amplitude spectrum for torque response

As the tower side-to-side (SS) bending moment is mainly excited by the variation in torque (it could also be excited by misaligning the wind and wave oncoming directions), the torque and tower base SS moment responses are very similar (Figure 113 and Figure 115).

H=5m and T=10s. Quasi-steady (mean=3301kNm, range=856kNm), Unsteady (mean=3843kNm, range=2360kNm)

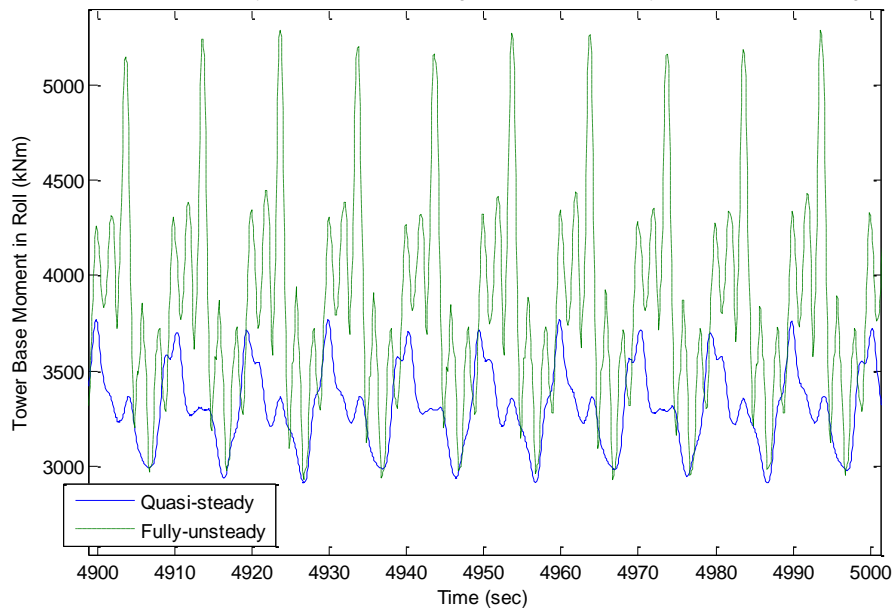


Figure 115 – Tower base SS moment

Figure 116 shows exactly why the unsteady aerodynamic effects have to be taken into account, when designing WTs. The large range of the SS moments in Figure 115 in the unsteady case is the result of interaction between wave harmonics and the 1<sup>st</sup> natural frequency of the tower. If this were not taken into account when designing the system, it could well lead to fatigue failure significantly before design life of the turbine. Also evident in the unsteady aerodynamics response, whilst very small, is the collective blade edgewise mode at 1.7 Hz. It is only present in the unsteady aerodynamics response as it coincides with and responds to one of the wave harmonics (which are only present due to the non-linearity of the unsteady aerodynamics).

Tower base fore-aft moment (FA) comes from surge motion and thrust force and hence is a pure sine wave with a slightly higher mean loading and amplitude in the unsteady case (Figure 117).

Blade root edgewise moment is in the same plane as the torque and tower SS moment. However, because it is dominated by the gravitational loads that reverse as the blade is making a full rotation, the response is a pure sine wave with no visible evidence of the 'noise' that is present in the torque (Figure 113) and tower base SS moment (Figure 115). On the other hand, blade root flap moment (Figure 118) is not a pure sine wave and

contains a mixture of multiple frequency components (wave frequency and rotational frequency). Also, because the wind turbine is a highly non-linear system, blade flap moments have a response at the sum- and difference-frequencies of the wave and rotation frequencies. Furthermore, wave harmonics, whilst very small in size, are also present in the amplitude spectrum (Figure 119). As expected, the dominant peak of the blade flapwise moment is at the wave frequency. In the case of unsteady aerodynamics it is roughly twice the size of the quasi-steady case (resulting from response overshoot due to the induction-lag effect). However, the second peak is smaller in the unsteady case due to greater aerodynamic damping (see 3.1.5.1). The collective blade flap frequency is not present in the response as it is located quite far from the exciting frequencies and is also heavily damped.

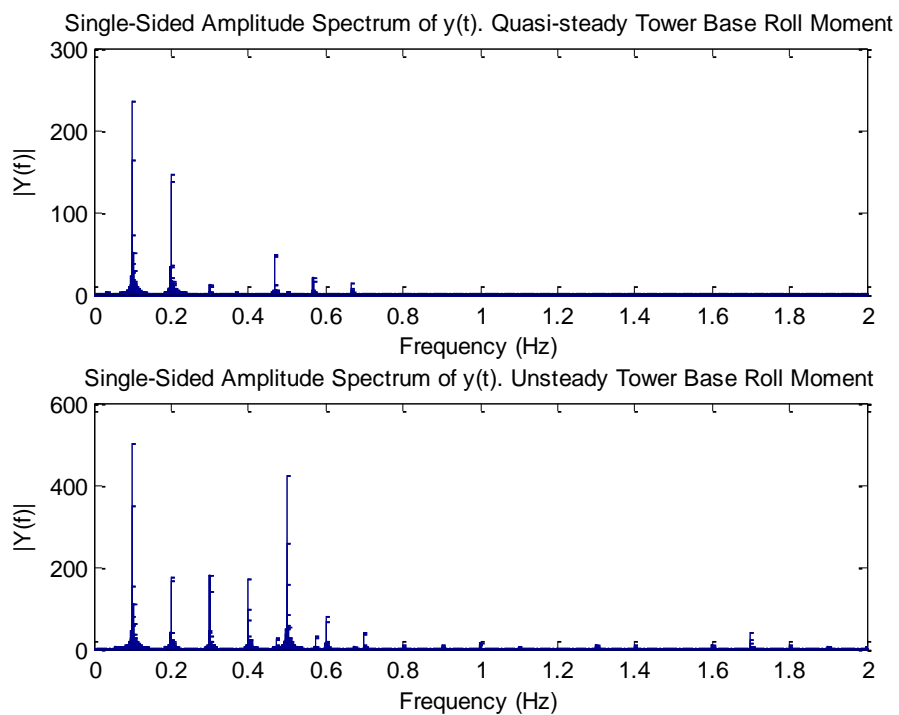


Figure 116 – FFT of tower base side-to-side moment

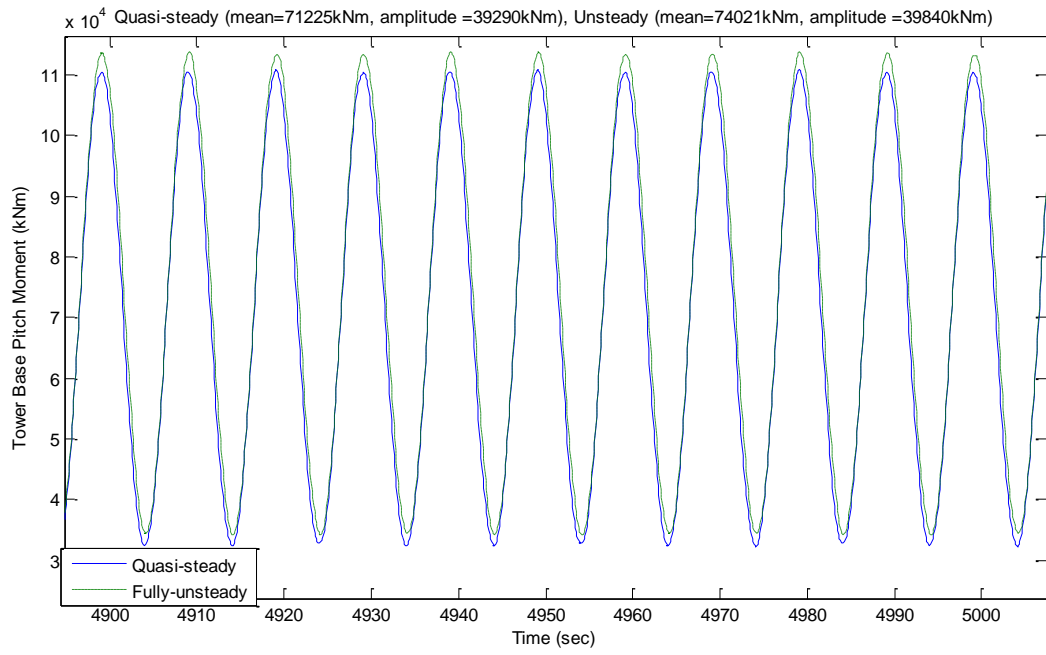


Figure 117 – Tower base fore-aft moment

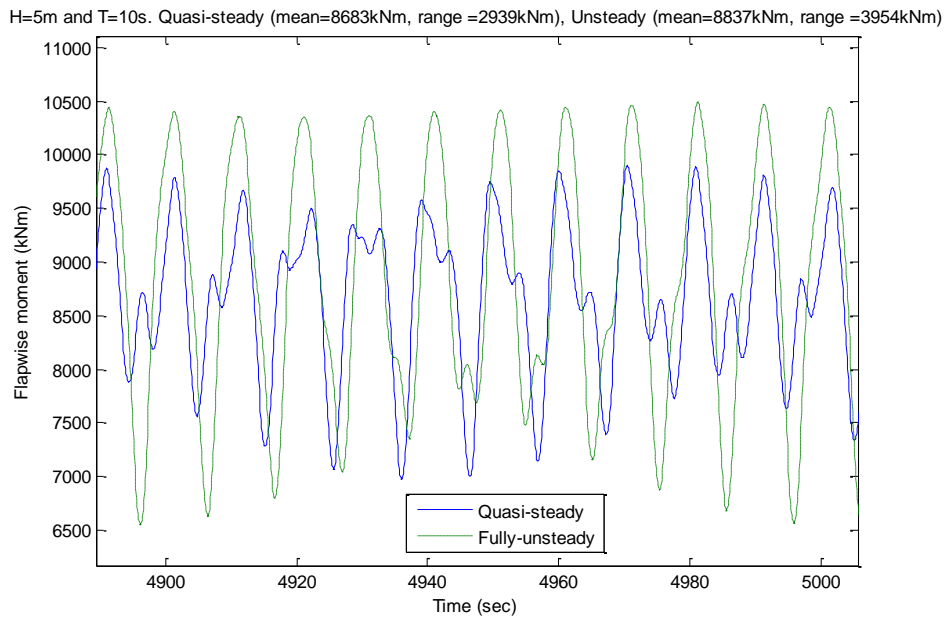


Figure 118 – Flapwise moment response

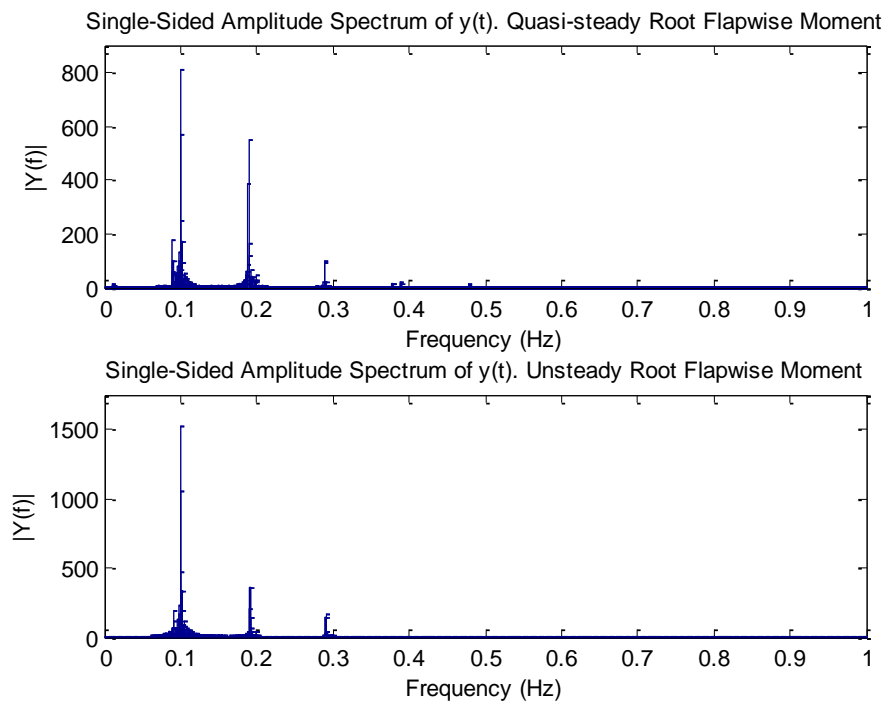


Figure 119 – FFT of blade root flapwise moment

Compared to small differences between the fully-attached and the quasi-steady results in Chapter 2, the fully-unsteady aerodynamics (in particular induction lag), as investigated in this chapter, introduce significant effects not seen in models where only blade aerodynamics are looked at. This furthermore highlights the necessity to include unsteady aerodynamic loads when designing new turbines.

### 3.2.2. Most detrimental degree-of-freedom

Sebastian in his published works [51, 91-93] identifies surge, pitch and yaw DsoF as the most aerodynamically significant DsoF. Motion in these DsoF influences the resultant velocity (by modifying the effective free-stream velocity) at every blade station, whilst the other 3 DsoF (sway, heave and roll) do not alter the free-stream velocity and can be viewed as a sinusoidally yawing turbine. The latter can be modelled as a skewed wake, which, while introducing another harmonic component (rotational) into the response of the system, has very little influence on the change in thrust force on the rotor and power generated by the turbine. Small changes in thrust will lead to very small varying loads on the system, as the majority of the fatigue in tower and blades comes from changes in the thrust load on the

rotor and these are much more susceptible to changes in the free-stream velocity (changes in wind conditions or motions in surge, pitch or yaw DsoF).

As the spar is symmetrical about its vertical axis, any modifications to the spar should have almost identical effects on surge and sway natural frequencies and also almost identical effects on pitch and roll frequencies (modifications in heave DoF can be easily achieved by installing some damping plates or skirts on the bottom of the spar), sway, heave and roll DsoF were disregarded as potentially the most detrimental to the system. Because the OC3-Hywind spar is symmetrical, it is almost impossible to excite it in the yaw DoF. There is also much hydrodynamic damping in the yaw DoF from the mooring system [46] and the only significant excitation is from gyroscopic coupling between pitch and yaw DsoF. Thus the yaw DoF can also largely be disregarded in terms of long term damage. This leaves surge and pitch motion as potentially the most damaging.

Due to the great distance of 200m between the blade tip at top-dead-centre and the CoG of the system, it takes only a small inclination of the system to produce significant displacements of the tip. Thus relatively small pitch motion angular amplitudes can produce large velocities. It may therefore be expected that pitch motion might be the most detrimental DoF, but this needs to be investigated further.

#### *3.2.2.1. Surge and pitch*

Because disabling DsoF of the spar is not an option that can be trusted in FAST simulations (see 3.1.3.6), it is hard separately to identify the damage caused by motion in each individual DoF. To be able to concentrate on comparing surge and pitch DsoF, wind and wave inputs were aligned. This allowed the sway and roll DsoF to be disregarded, as they will not be excited or their excitation would be so small as to be negligible. Heave was also shown before to have no significant influence on fatigue, and the excitation in yaw and its influence on fatigue was also reasoned to be negligible (see reasoning above). The methodology used was to take the wave-excitation force vector, which is obtained from WAMIT and used in FAST as an input, and to scale it separately in the surge and pitch DsoF until the response in either surge or pitch DoF matched the original response (as shown in Figure 120). Whichever DoF was not matched then has a different response from the

original and these can be compared in order to identify which DoF causes the more damage, surge or pitch.

To use this method, multiple assumptions and simplifications had to be made, the most important of them being that the whole approach can be assumed to be linear. Secondly, simple regular waves and uniform wind across the rotor were used in order to have as few frequency components as possible in the response. Thirdly, the results are only strictly valid for the specific wind and wave conditions used.

Next, a step-by-step approach and example is shown in calculating the surge and pitch effects on the system's overall fatigue in below-rated operating conditions.

#### *3.2.2.2. Below-rated*

To simulate below-rated conditions, 2 m, 13 s regular waves were used together with a 6 m/s wind. Wind and wave inputs were aligned, as the author was interested in exciting the system in surge and pitch only. The wave-excitation force-vector was scaled using 8 different scaling factors to obtain 9 different points (0.25, 1/3, 0.5, 2/3, 1, 1.5, 2, 3 and 4), as shown in Figure 120. The peak-to-trough ranges of the surge and pitch response displacements are given in Figure 121 as functions of the wave-excitation force-vector scaling factor.

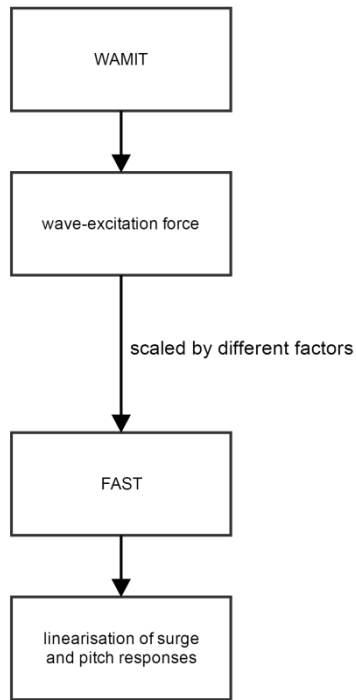


Figure 120 – Flow diagram of approach used to compare the pitch and surge DsoF

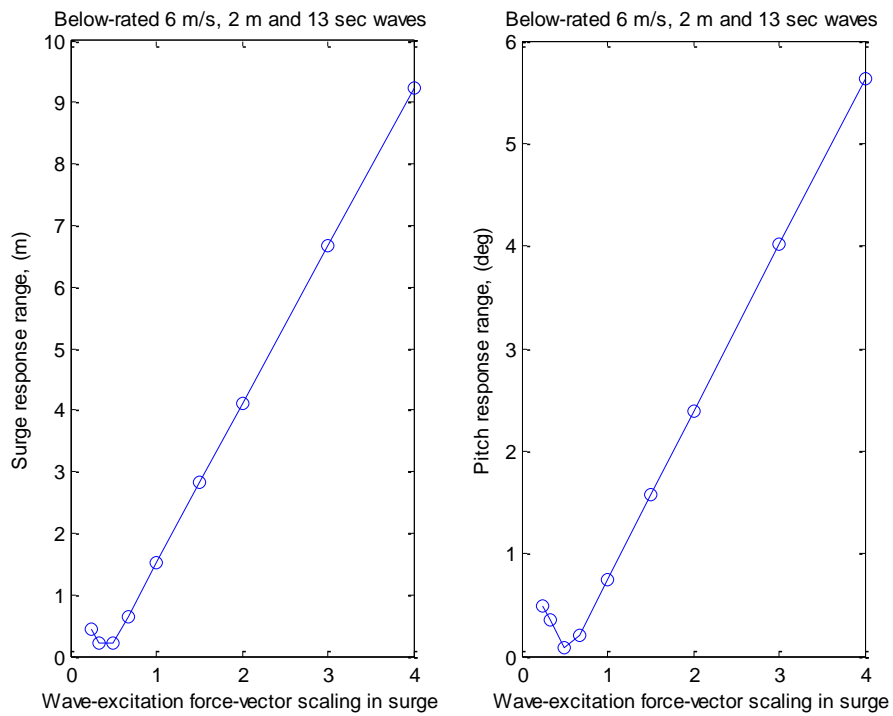
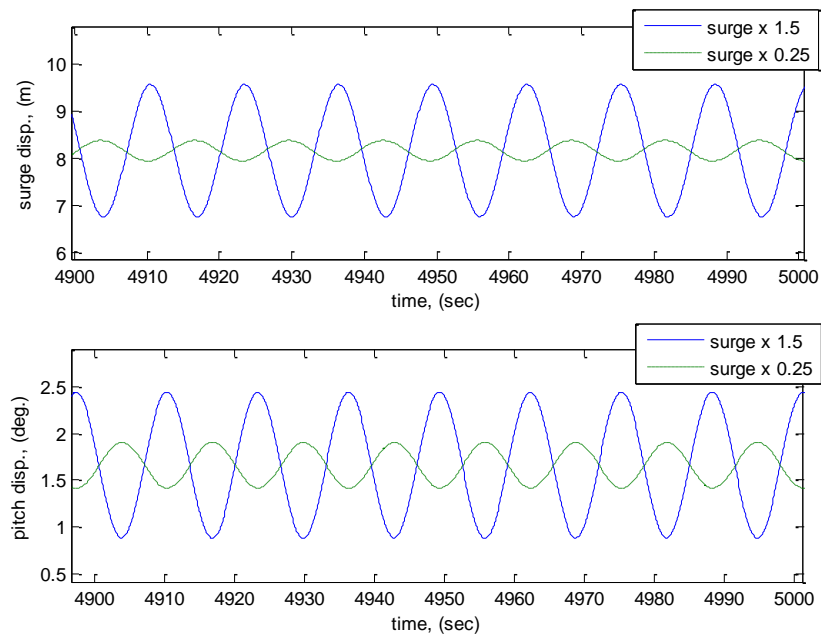


Figure 121 – Wave-excitation force-vector scaled in the surge DoF

For most of the scaling factors (from 2/3 to 4) the response is linear in Figure 121. The pitch response follows the surge response, as would be expected, as there is a very strong coupling between the two DsoF. However, at very small scaling factors (0.25 to 0.5) the responses in both surge and pitch DsoF flatten out and even increase with decreasing scaling factors. Also, for the same scaling factors (0.25 to 0.5) there is a phase shift which is not seen in the base case of no scaling or in any of the greater scaling factors. This effect can be seen in Figure 122.

Initially, the non-linear effects at small scaling factors were thought to be the result of the control influence on the system, as it is highly non-linear. However, identical simulations with no wind or aerodynamic loads (air density set to 0) showed very little difference in the results. Similarly, phase shift and non-linearities were present in the response of the system, when the pitch wave-excitation force-vector was scaled (Figure 123 and Figure 124).



**Figure 122 – Surge and pitch response (scaled surge wave-excitation force-vector)**

Contrary to the wave-excitation force-vector scaling in surge, scaling in pitch results in a ‘V’ shaped response amplitude curve with the linear part ranging between scale factors of 0.25

and 1.5. The phase shift is present for results from scaling factors 2 to 4, as demonstrated in Figure 124.

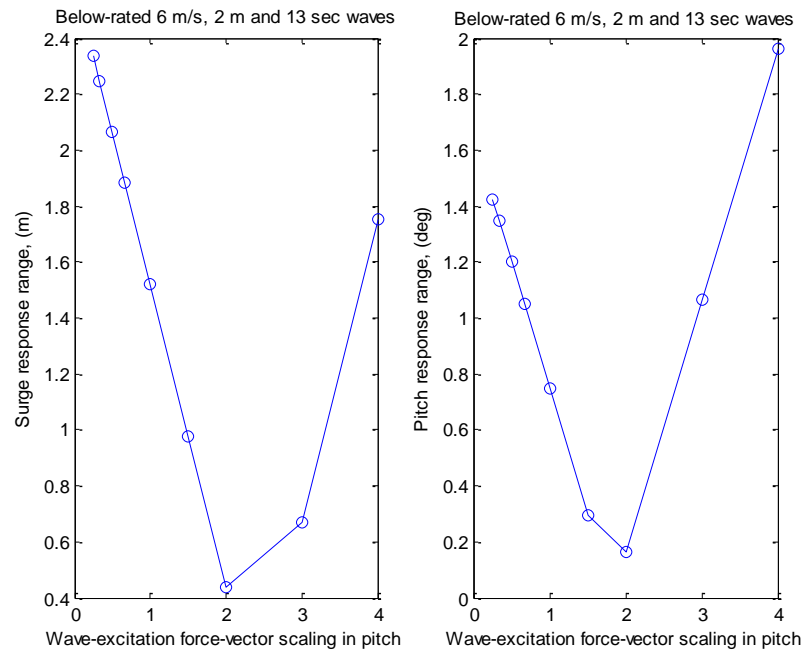


Figure 123 – Wave-excitation force-vector scaled in the pitch DoF

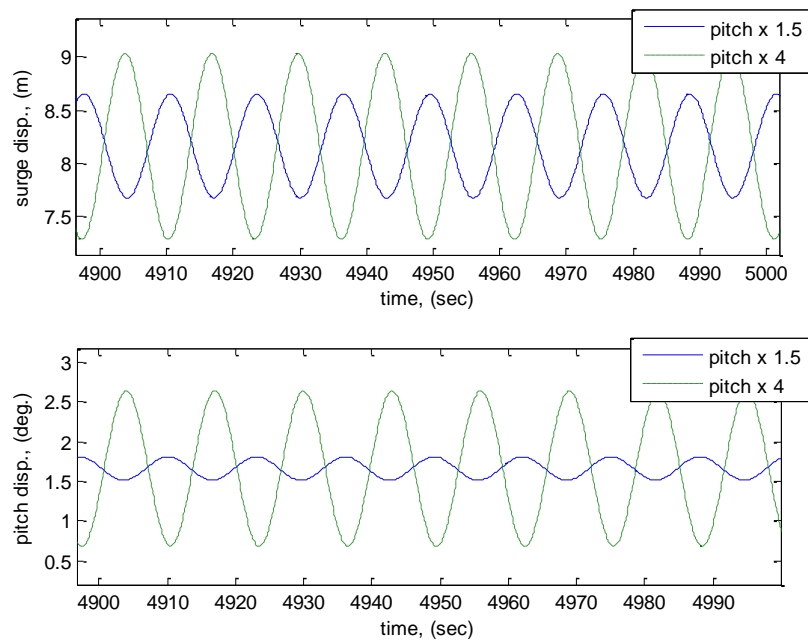


Figure 124 – Surge and pitch response (scaled pitch wave-excitation force-vector)

Just as in the case of scaling the surge component of the forcing vector, the author does not have a definitive explanation for the non-linearities in the response and phase shift when pitch wave-excitation is scaled. However, the most likely source of this is the coupling effects between different DsoF that are not taken into account when scaling the wave-excitation force vector, with no changes to off-diagonal terms. The overall transfer function is non-linear, as there are multiple non-linearities in the system associated with the mooring lines, controller, etc. There is also a possibility that the author is doing something that FAST was not really designed to be used for or physical, similar to disabling different DsoF of the spar.

Two different approaches of the same method were used to compare surge and pitch DsoF:

In the first approach, the original response (no scaling or scale factor of 1) of the OC3-Hywind loads was compared to one that was initially scaled in pitch by 1.5 and then in surge by 1.273. The original run had surge and pitch displacement ranges of 1.522 m and 0.747 deg. The matched pitch run produced a surge range of 1.689 m and pitch range of 0.746 deg. Almost identical responses in pitch allows differences in tower and blade loads to be attributed to differences in the surge displacement response.

The second approach involved linearising the surge and/or the pitch response. Using this approach the surge force-vector was scaled by 1.28 to match pitch x 1/3 response in surge (2.247 m and 1.349 deg. for pitch x 1/3, and 2.25 m and 1.207 deg. for surge x 1.28). The difference in the tower and blade loads was then related to the difference in pitch response between the two simulations.

### 3.2.2.3. Example

In this example the former approach is used. The original below-rated run with 2 m, 13 s waves and 6 m/s wind was compared to one where surge and pitch wave-excitation force-vectors had been scaled. Both responses are shown in Figure 125.

Table 12 – Surge and pitch displacement for two different wave-excitation force-vectors

	Surge range (m)	Pitch range (deg.)
<b>Original</b>	1.522	0.747
<b>Pitch x 1.5 and surge x 1.273</b>	1.689	0.746

The difference in pitch range is negligible. However, the difference in the surge range is 0.167 m. The mean surge and pitch displacements are identical in both simulations, as would be expected as these are due to wind and not wave input.

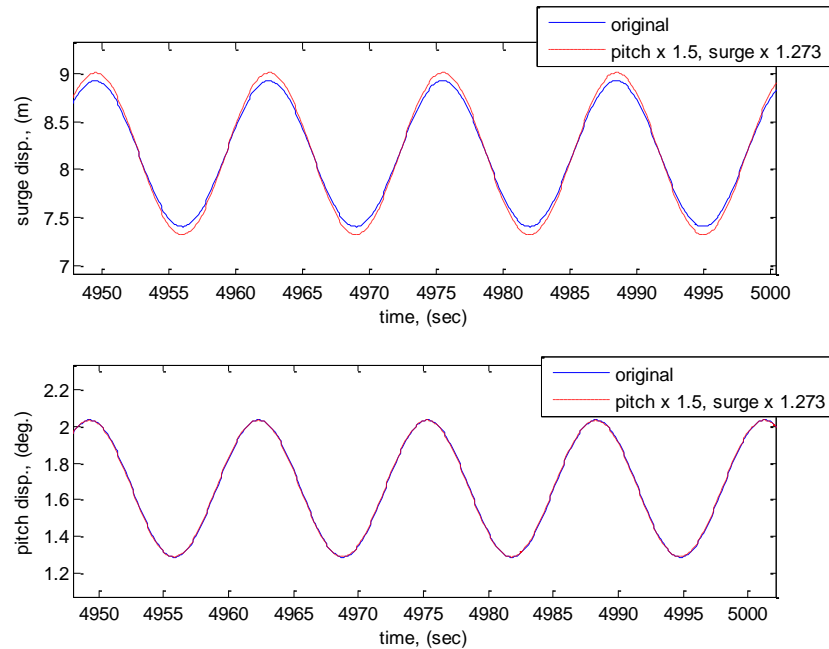


**Figure 125 – Surge and pitch displacement response**

With identical responses in pitch, any difference in the tower and blade loads, if present, can be attributed to the difference in surge displacement.

First, the tower loads are investigated. The tower base fore-aft moment is shown in Figure 126. The original simulation displays smaller loading at the tower base compared to the scaled wave-excitation force vector run. This is consistent with Figure 125, where larger surge displacement is demonstrated by the scaled simulation. The original simulation produces a tower loading range of 28,840 kNm, whilst the modified run 30,320 kNm. The difference between the both runs is 1,480 kNm (an increase of 5%) and can be attributed to the extra 0.167 m displacement in surge in the modified simulation (an increase of 11%). Assuming that the load response is linear with respect to displacement, the tower base fore-aft load due to the total displacement in the surge DoF for both runs can now be calculated.

$$1.522 \text{ m surge} \xrightarrow{\text{yields}} 1.522 \div 0.167 \times 1,480 = 13,488.4 \text{ kNm}$$

$$1.689 \text{ m surge} \xrightarrow{\text{yields}} 1.689 \div 0.167 \times 1,480 = 14,968.3 \text{ kNm}$$

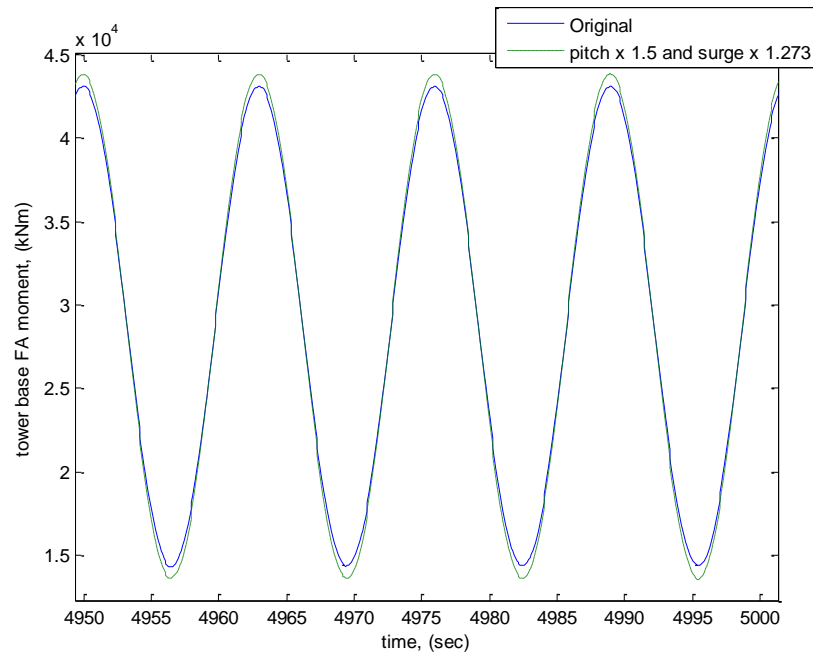


Figure 126 – Tower base FA moment

Now, the moment at the tower base in the FA direction due to motion in the pitch DoF can be calculated by subtracting the load due to motion in the surge DoF from the total load at the tower base.

$$0.747^\circ \text{ pitch} \xrightarrow{\text{yields}} 28,810 - 13,488.4 = 15,351.6 \text{ kNm}$$

$$0.746^\circ \text{ pitch} \xrightarrow{\text{yields}} 30,320 - 14,968.4 = 15,351.6 \text{ kNm}$$

Again assuming linearity, the load components due to 1 m displacement in surge and 1 deg. displacement in pitch can be calculated as 8,862 kNm and 20,551 kNm, respectively.

The tower FA bending moment at 9.7 m above the base is shown in Figure 127. This point was identified as the most likely place where the tower could fail (see A1.11.1) even though the bending moment here is smaller than at the tower base (Figure 126). An identical approach was used to calculate the influence of both surge and pitch displacements on the FA bending moment at this location as the one used for calculating the load at the tower base (the same assumption of linearity was used). This time the load components due to 1

m displacement in surge and 1 deg. displacement in pitch at 9.7 m above the tower base were calculated as 7,485 kNm and 17,855 kNm, respectively. However, for a fairer comparison these values should be multiplied by the response amplitudes expected in below-rated conditions, yielding 11,329 kNm for 1.522 m motion in surge and 13,338 kNm for 0.747 deg. in pitch for the specific below-rated conditions given above.

At different locations along the tower, the ratios of tower loads due to motions in surge and pitch are very similar. At the tower base, loading due to motion in surge is 42% of the loading due to pitch and 43% at 9.7 m along the tower length. Similarly, the ratio of surge and pitch loading at 9.7 m location and base is 0.85% and 0.87%.

It is a common practise to measure blade root moments. However, just as with the tower, simplified calculations were made to identify the weakest points on the blade. As well as at the blade root, strain gauge sensors were set at 6.83 m and 43.05 m from the blade root in the simulations (see A1.11.2 for derivation).

Only flapwise moments were investigated, as edgewise moments are dominated by the gravitational loads and would still be present even if there were no wave input. The flapwise moment at the blade root is shown in Figure 128. Compared to the tower moments (Figure 126 and Figure 127), the response clearly contains more than one frequency component. A single-sided amplitude spectrum shown in Figure 129 confirms that there are 4 frequency components present. These were identified as:

- 0.0565 Hz (17.7 s) – difference between rotational and wave frequencies
- 0.0769 Hz (13 s) – wave frequency
- 0.134 Hz (7.46 s) – rotational frequency
- 0.21 Hz (4.76 s) – sum of wave and rotational frequencies

Two of these frequencies (wave and rotational) can be thought of as the ‘fundamental’ frequencies and display higher peaks in Figure 129, while the other two are the non-linear 2<sup>nd</sup> order effects that come about due to the fact that the wind turbine’s aerodynamics is highly non-linear.

The presence of multiple frequency components prevents the use of the same approach that was used in the tower load calculations. Instead the fatigue equivalent load cycle method [102] was used together with a rainflow cycling algorithm initially developed by

[103] and later improved by [104, 105]. Linear Miner's rule [106] was used to combine cycles of different load ranges.

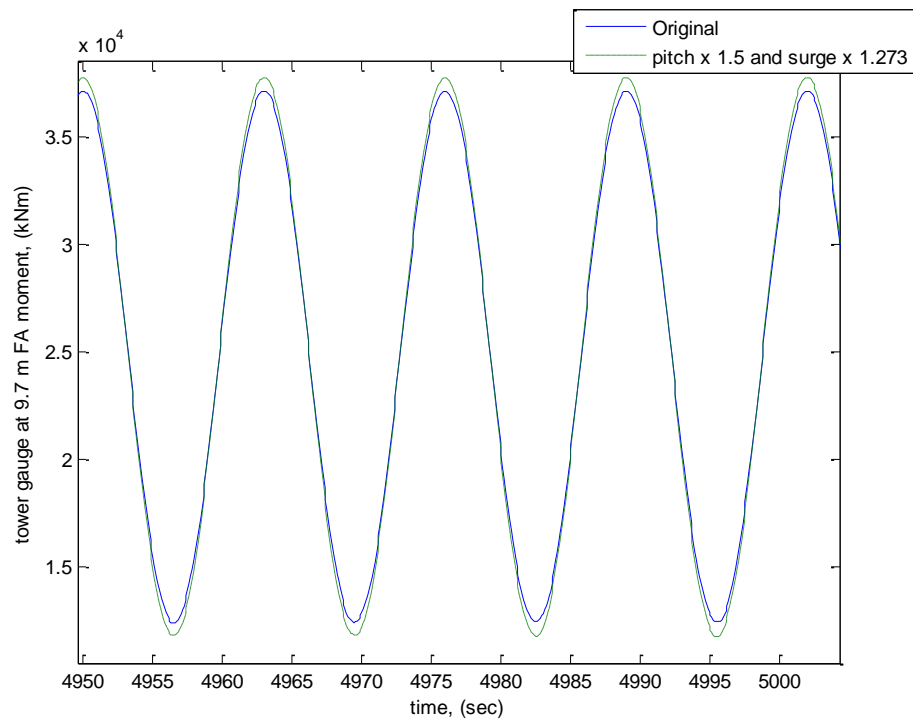


Figure 127 – Tower FA bending moment at 9.7 m from the base

Damage-equivalent loads (DELs) were calculated for the last 1000 seconds of each simulation run to make sure that all transients have dissipated and a steady-state reached. No corrections for mean stress or load were applied in these calculations, such as Goodman's [107] or Walker's [108], as it is the relative magnitude of each load and not the absolute value that is of interest.

The slope in the Wohler diagram (S-N diagram) was chosen as 12 for the composite blades used in the NREL 5 MW wind turbine, which is consistent with other works published [109].

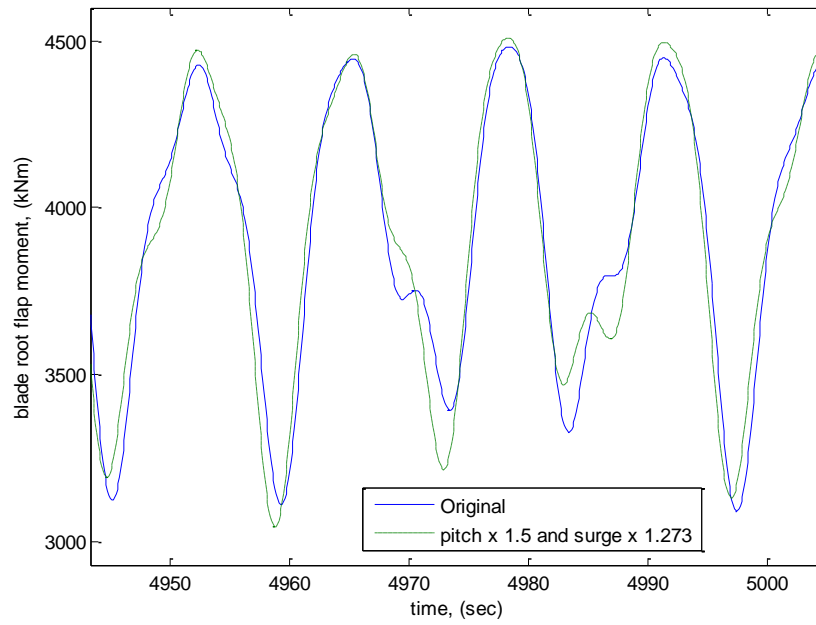


Figure 128 – Blade root flapwise moment

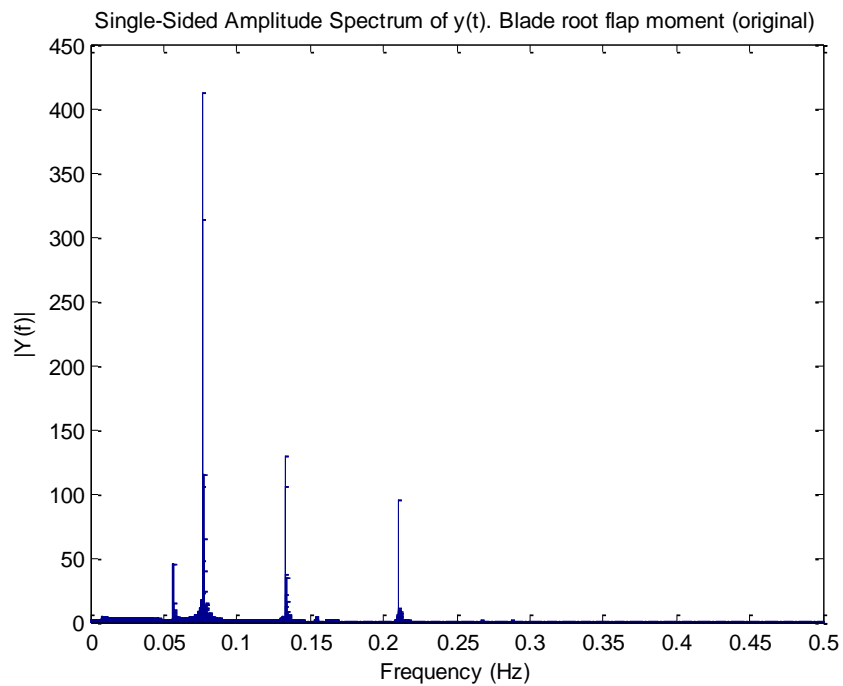


Figure 129 – Amplitude spectrum for blade root flapwise moment

Damage-equivalent loads for 1 Hz loading for the original and modified wave-excitation force-vector simulations were calculated to be 1,035.8 kNm and 1084.7 kNm. This gives a

difference of 48.9 kNm (an increase of 4.7%) in damage-equivalent load due to 0.167 m motion in surge. Because the damage-equivalent load method is linear, the total damage-equivalent loads for the total motion in surge can be calculated.

$$1.522 \text{ m surge} \xrightarrow{\text{yields}} 445.66 \text{ kNm DEL}$$

$$1.689 \text{ m surge} \xrightarrow{\text{yields}} 494.56 \text{ kNm DEL}$$

Now, the DEL due to 0.747 ° and 0.746 ° pitch motion can be calculated as the difference between the total and surge motion DEL:

$$0.747^\circ \text{ pitch} \xrightarrow{\text{yields}} 1,035.8 - 445.66 = 590.14 \text{ kNm DEL}$$

$$0.746^\circ \text{ pitch} \xrightarrow{\text{yields}} 1,084.7 - 494.56 = 590.14 \text{ kNm DEL}$$

This gives DEL due to 1 m motion in surge and 1 deg. pitch of 292.8 and 790 kNm.

Figure 130 shows blade flap moments at 6.83 m and 43.05 m from the blade root. An identical approach to blade root moment calculations was used for comparing loads from surge and pitch DsoF at 6.83 and 43.05 m along the blade length. The results for these locations along the blade span are summarised in Table 13.

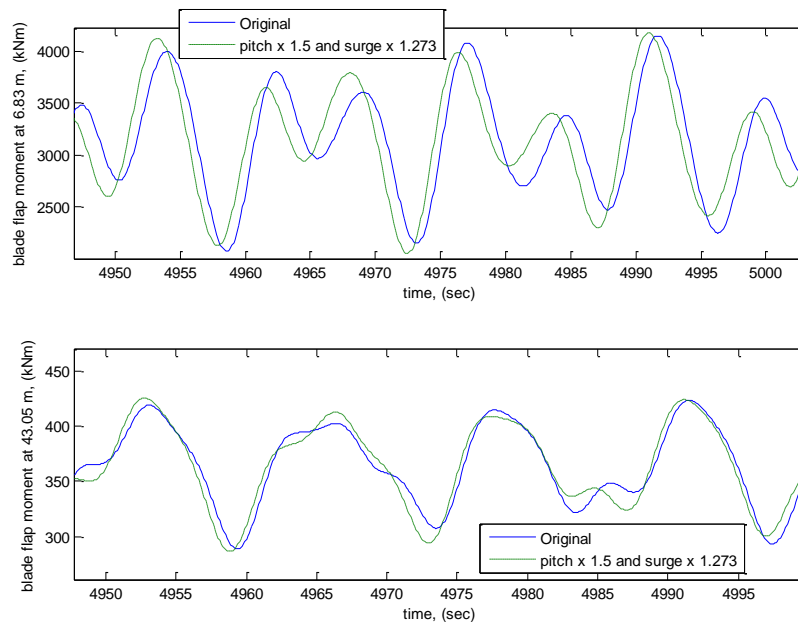


Figure 130 – Blade flapwise moments at 2 difference locations along the blade length

**Table 13 – Blade DELs in surge and pitch DsoF in below-rated conditions**

	Surge		Pitch	
	per 1 m	per 1.522 m	per 1 deg.	per 0.747 deg.
<b>Blade 6.83 m</b>	55.69 kNm	84.76 kNm	1,923.09 kNm	1,436.55 kNm
<b>Blade 43.05 m</b>	33.53 kNm	51.03 kNm	61.19 kNm	45.71 kNm

The results for the location 6.83 m along the blade span show that almost all damage comes from pitch motion. While these results drastically differ from those at the blade root and 43.05 m along the blade length, it is the relative value that is important and not the absolute. However, for a fairer comparison of like with like Table 14 should be consulted, as it compares two responses with the wave-excitation force-vector modified in each, whereas the results presented above compared an unmodified wave-excitation force vector simulation with a scaled one.

The results obtained using the second approach of comparing scaled pitch and surge (pitch x 1/3 and surge x 1.28) wave-excitation force vectors are shown in Table 14. These results agree very well with the ones presented above, with an exception of blade DELs at 6.83 m along the blade length. While they show that pitch is still more detrimental, at least per 1m or 1 deg. displacements, the difference between loads for the expected response amplitudes in below-rated conditions in surge and pitch is quite small, making both DsoF comparable.

**Table 14 – Loads and DELs for tower and blade in surge and pitch DsoF in below-rated conditions**

	Surge		Pitch	
	per 1 m	per 1.522 m	per 1 deg.	per 0.747 deg.
<b>Tower base</b>	9,278.6 kNm	14,122 kNm	19,795.5 kNm	14,787.2 kNm
<b>Tower at 9.7 m</b>	7,895.5 kNm	12,017 kNm	17,108.6 kNm	12,780.1 kNm
<b>Blade root</b>	377.2 kNm	574.1 kNm	598.7 kNm	447.2 kNm
<b>Blade at 6.83 m</b>	531.9 kNm	809.6 kNm	554.3 kNm	414.1 kNm
<b>Blade at 43.05</b>	37.4 kNm	56.8 kNm	51.3 kNm	38.4 kNm

The results for the rated (11.4 m/s wind, and 3 m and 15 s regular waves) and above-rated conditions (18 m/s wind and 5 m and 17 s regular waves) are very similar to the ones shown above. These are presented in A1.12.1 and A1.12.2.

### 3.2.3. Correlational approach

In the following few pages a statistical approach was used to analyse connections between different modes of motion, and tower and blade loads. Three different operational conditions of the OC3-Hywind were simulated in FAST (see Table 15), and 2-D correlation coefficients were used to compare signals.

Unsteady aerodynamic settings were used in all simulations, as there was almost no difference between the quasi-steady and unsteady correlation coefficients, and unsteady aerodynamics were shown to be very crucial in the offshore floating wind turbine design (3.2.1). Any results that showed correlation of less than 0.5% ( $-0.05 < x < 0.05$ ) were assigned a zero value.

While in the majority of cases FOWTs would experience aligned wind and wave inputs, wind and wave inputs were also misaligned by 90 degrees to excite turbine in the side-to-side direction.

Table 15 – Environmental conditions used

	Wind speed, $U_{\infty}$ (m/s)	Significant wave height, $H_s$ (m)	Peak spectral period of waves, $T_P$ (s)
<b>Below-rated</b>	6	1.83	12.72
<b>Rated</b>	11.4	2.54	13.35
<b>Above-rated</b>	18	4.09	15.33

These environmental conditions were used to model the wave spectrum, which was calculated in FAST using the IEC 61400-3 standard [110]. Because for all 3 cases  $T_P / \sqrt{H_s} > 5$ , the peak enhancement factor gamma,  $\gamma$ , came out as 1, matching the JONSWAP spectrum with the Pierson–Moskowitz spectrum. The corresponding surge and pitch displacements, together with the initial transients, are shown in Figure 131. It shows that

the highest displacement in both DsoF is at the rated conditions, as would be expected at the point of the highest thrust. It is then followed by the above-rated and below-rated runs.

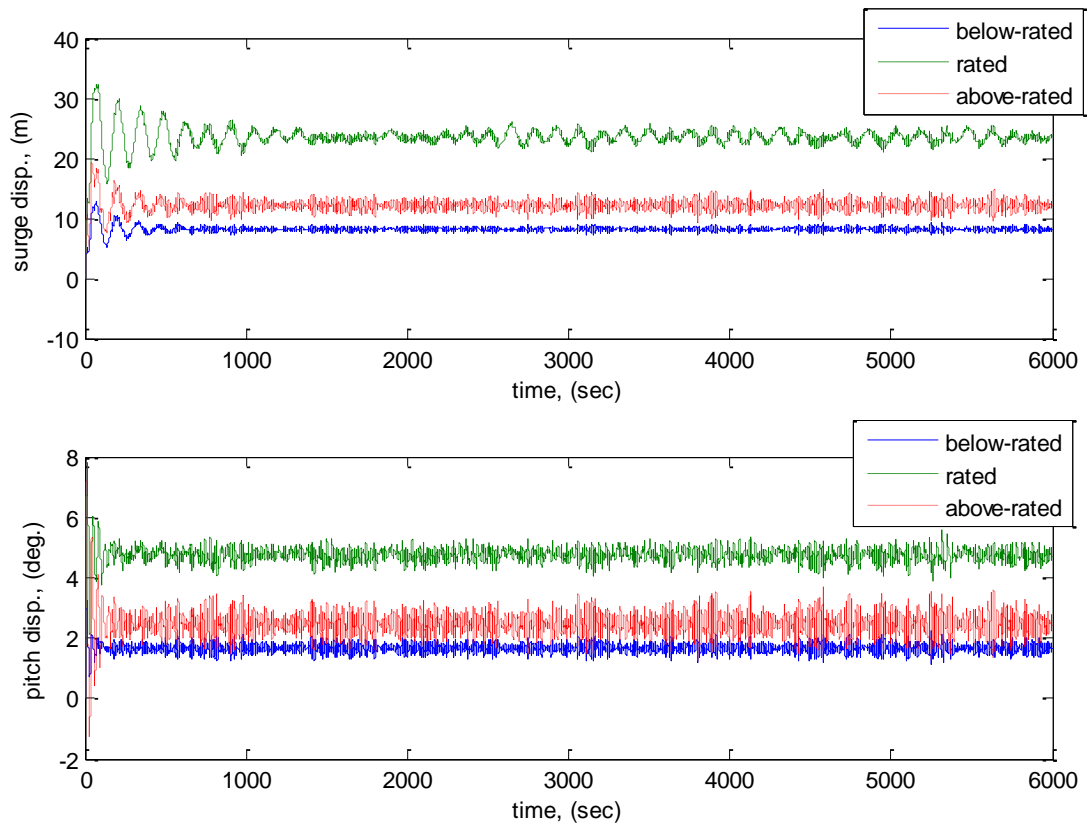


Figure 131 – The OC3-Hywind response in surge and pitch DsoF

Table 16 and Table 17 illustrate the correlations matrix for the OC3-Hywind tower loads in the below-rated conditions, when wind and wave inputs are, first, aligned and then, misaligned. Displacements and velocities of all 6 DsoF are correlated with the tower base fore-aft (TwrBsMy) and side-to-side (TwrBsMx) moments. Also analysed is the point above the base, where the tower is most likely to fail (see A1.11.1). This point applies to both fore-aft (TwHt1My) and side-to-side (TwHt1Mx) moments.

**Table 16 – Correlation matrix for tower loads for below-rated, aligned wind and waves**

	Surge disp.	Sway disp.	Heave disp.	Roll disp.	Pitch disp.	Yaw disp.	Surge vel.	Sway vel.	Heave vel.	Roll vel.	Pitch vel.	Yaw vel.	TwrBsMx	TwrBsMy	TwHtIMx	TwHtIMy
Surge disp.	1	-0.1604	-0.0346	0.1215	0.4783	0.3746	-0.0553	0.2906	-0.4726	-0.3037	-0.0677	-0.0463	-0.2008	0.4337	-0.2336	0.4323
Sway disp.	-0.1604	1	-0.2446	-0.8655	-0.4538	-0.2723	-0.2105	-0.0281	0.1675	-0.0588	-0.2577	-0.1237	-0.0747	-0.1738	-0.0465	-0.171
Heave disp.	-0.0346	-0.2446	1	0.2859	0.1053	0.2493	0.9136	-0.3307	0	0.4829	0.8811	0.6011	-0.2238	-0.1614	-0.2495	-0.1687
Roll disp.	0.1215	-0.8655	0.2859	1	0.5889	0.4403	0.2734	0.1477	-0.3082	-0.0392	0.2415	0.1143	0.0403	0.3118	0	0.3085
Pitch disp.	0.4783	-0.4538	0.1053	0.5889	1	0.7295	0.043	0.5414	-0.8563	-0.4246	-0.0167	-0.0391	-0.1865	0.8229	-0.2383	0.8202
Yaw disp.	0.3746	-0.2723	0.2493	0.4403	0.7295	1	0.1165	0.2956	-0.7609	-0.2177	0.0526	0	-0.221	0.762	-0.2697	0.7596
Surge vel.	-0.0553	-0.2105	0.9136	0.2734	0.043	0.1165	1	-0.4112	0.0232	0.5897	0.9785	0.7368	-0.2295	-0.2093	-0.2513	-0.2173
Sway vel.	0.2906	-0.0281	-0.3307	0.1477	0.5414	0.2956	-0.4112	1	-0.4992	-0.945	-0.4904	-0.3883	-0.0519	0.5166	-0.0723	0.5181
Heave vel.	-0.4726	0.1675	0	-0.3082	-0.8563	-0.7609	0.0232	-0.4992	1	0.4163	0.0887	0.0868	0.2567	-0.8833	0.303	-0.8813
Roll vel.	-0.3037	-0.0588	0.4829	-0.0392	-0.4246	-0.2177	0.5897	-0.945	0.4163	1	0.6635	0.6493	-0.0111	-0.4184	0	-0.4218
Pitch vel.	-0.0677	-0.2577	0.8811	0.2415	-0.0167	0.0526	0.9785	-0.4904	0.0887	0.6635	1	0.7567	-0.2093	-0.2664	-0.2263	-0.2743
Yaw vel.	-0.0463	-0.1237	0.6011	0.1143	-0.0391	0	0.7368	-0.3883	0.0868	0.6493	0.7567	1	-0.1831	-0.05	-0.1936	-0.056
TwrBsMx	-0.2008	-0.0747	-0.2238	0.0403	-0.1865	-0.221	-0.2295	-0.0519	0.2567	-0.0111	-0.2093	-0.1831	1	-0.1669	0.9972	-0.1636
TwrBsMy	0.4337	-0.1738	-0.1614	0.3118	0.8229	0.762	-0.2093	0.5166	-0.8833	-0.4184	-0.2664	-0.05	-0.1669	1	-0.2083	1
TwHtIMx	-0.2336	-0.0465	-0.2495	0	-0.2383	-0.2697	-0.2513	-0.0723	0.303	0	-0.2263	-0.1936	0.9972	-0.2083	1	-0.2047
TwHtIMy	0.4323	-0.171	-0.1687	0.3085	0.8202	0.7596	-0.2173	0.5181	-0.8813	-0.4218	-0.2743	-0.056	-0.1636	1	-0.2047	1

**Table 17 – Correlation matrix for tower loads for below-rated, misaligned wind and waves**

	Surge disp.	Sway disp.	Heave disp.	Roll disp.	Pitch disp.	Yaw disp.	Surge vel.	Sway vel.	Heave vel.	Roll vel.	Pitch vel.	Yaw vel.	TwrBsMx	TwrBsMy	TwHtIMx	TwHtIMy
Surge disp.	1	0.1252	-0.0681	-0.01	0.1289	0	-0.3202	0.012	0.0052	0	-0.1889	0	0	0.1106	0	0.1074
Sway disp.	0.1252	1	0.0133	-0.9791	0.0265	-0.7493	-0.094	0	-0.9734	0.0075	0.0312	-0.5323	-0.8784	0.0285	-0.8777	0.0324
Heave disp.	-0.0681	0.0133	1	-0.0326	-0.0418	0.5159	0.0254	0.9357	0	-0.9173	0.0205	-0.7368	-0.0163	-0.134	-0.0159	-0.1363
Roll disp.	-0.01	-0.9791	-0.0326	1	-0.0259	0.7532	0	-0.0079	0.9919	0	0	0.5537	0.9116	-0.0269	0.9109	-0.0311
Pitch disp.	0.1289	0.0265	-0.0418	-0.0259	1	-0.0171	-0.2207	-0.0123	0	0	-0.1735	0	-0.0094	0.8986	-0.0095	0.8907
Yaw disp.	0	-0.7493	0.5159	0.7532	-0.0171	1	-0.0057	0.5325	0.767	-0.5329	-0.0051	0	0.6074	-0.076	0.6068	-0.0811
Surge vel.	-0.3202	-0.094	0.0254	0	-0.2207	-0.0057	1	0.0173	-0.0504	-0.0126	0.6085	-0.0277	-0.0228	-0.1964	-0.0228	-0.1973
Sway vel.	0.012	0	0.9357	-0.0079	-0.0123	0.5325	0.0173	1	0.0136	-0.9983	0.0148	-0.6917	0	-0.1231	0	-0.127
Heave vel.	0.0052	-0.9734	0	0.9919	0	0.767	-0.0504	0.0136	1	-0.02	-0.0763	0.5433	0.9097	0	0.909	0
Roll vel.	0	0.0075	-0.9173	0	0	-0.5329	-0.0126	-0.9983	-0.02	1	-0.0185	0.6771	0	0.112	0	0.1161
Pitch vel.	-0.1889	0.0312	0.0205	0	-0.1735	-0.0051	0.6085	0.0148	-0.0763	-0.0185	1	-0.0459	-0.0415	-0.1707	-0.0414	-0.1725
Yaw vel.	0	-0.5323	-0.7368	0.5537	0	-0.0277	-0.6917	0.5433	0.6771	-0.0459	1	0.4839	0.069	0.4831	0.0681	0.0681
TwrBsMx	0	-0.8784	-0.0163	0.9116	-0.0094	0.6074	-0.0228	0	0.9097	0	-0.0415	0.4839	1	-0.0074	1	-0.0107
TwrBsMy	0.1106	0.0285	-0.134	-0.0269	0.8986	-0.076	-0.1964	-0.1231	0	0.112	-0.1707	0.069	-0.0074	1	-0.0075	0.9998
TwHtIMx	0	-0.8777	-0.0159	0.9109	-0.0095	0.6068	-0.0228	0	0.909	0	-0.0414	0.4831	1	-0.0075	1	-0.0108
TwHtIMy	0.1074	0.0324	-0.1363	-0.0311	0.8907	-0.0811	-0.1973	-0.127	0	0.1161	-0.1725	0.0681	-0.0107	0.9998	-0.0108	1

Correlations results show significant coupling between different DsoF. Some of these are expected according to common-sense; surge–pitch coupling in the aligned case, through the line-of-action of loads being displaced from the centre of mass, and similarly, sway and roll displacements in the misaligned case. Yaw and pitch are coupled through gyroscopic effects in the aligned case. However, the results also show some coupling between yaw and sway displacements, and yaw and roll displacements in the misaligned wind and wave input. This is unexpected, as there is no gyroscopic coupling between yaw and roll, and yaw DsoF. A probable explanation is that sway introduces cyclic loading as blades experience cyclic variation in in-plane wind. This gives rise to sway-pitch coupling and then yaw coupling through gyroscopic effects. Similarly, the coupling between roll and yaw arises due to rotational stiffness between the wind rotor and the electric machine’s stator. As almost all motions come about from wave excitation, it is not unexpected that heave velocity correlates well with sway, roll and yaw displacements in the misaligned case and

surge, pitch and yaw displacements in the aligned case. Yaw velocity produces very high correlations coefficients with heave displacement, and surge, roll and pitch velocities in the aligned case. In the misaligned wind and wave input case, yaw velocities correlate with sway, heave and roll displacements, and sway, heave and roll velocities.

The tower loads show a very predictable outcome of correlating very well between base and strain gauge locations moments. Correlation is also present between surge, pitch, and hence yaw displacements as it is coupled to pitch, and tower fore-aft moment in the aligned case and sway, roll and yaw displacements with tower side-to-side moments in the misaligned case.

Next, the blade loads are analysed for the same simulation conditions (Table 18 and Table 19). RootMEdg and RootMFlp are blade edgewise and flapwise moments at the blade root. Spn1Mx, Spn2Mx, and Spn1My, Spn2My are blade local edgewise and flapwise moments at span stations 3.83 m and 43.05 m from the blade root. These were shown to be the most likely places for the blade to fail (see A1.11.2).

**Table 18 – Correlation matrix for blade loads for below-rated, aligned wind and wave**

	Surge disp.	Sway disp.	Heave disp.	Roll disp.	Pitch disp.	Yaw disp.	Surge vel.	Sway vel.	Heave vel.	Roll vel.	Pitch vel.	Yaw vel.	RootMEdg	RootMFlp	Spn1Mx	Spn2Mx	Spn1My	Spn2My
Surge disp.	1	-0.1604	-0.0346	0.1215	0.4783	0.3746	-0.0553	0.2906	-0.4726	-0.3037	-0.0677	-0.0463	0	0.0376	-0.0059	-0.0069	0	-0.0519
Sway disp.	-0.1604	1	-0.2446	-0.8655	-0.4538	-0.2723	-0.2105	-0.0281	0.1675	-0.0588	-0.2577	-0.1237	0	0.1574	0	0	0.0773	0.1951
Heave disp.	-0.0346	-0.2446	1	0.2859	0.1053	0.2493	0.9136	-0.3307	0	0.4829	0.8811	0.6011	-0.0058	-0.7467	0.0152	0	-0.336	-0.7458
Roll disp.	0.1215	-0.8655	0.2859	1	0.5889	0.4403	0.2734	0.1477	-0.3082	-0.0392	0.2415	0.1143	-0.0054	-0.1524	0	0	-0.0781	-0.2123
Pitch disp.	0.4783	-0.4538	0.1053	0.5889	1	0.7295	0.043	0.5414	-0.8563	-0.4246	-0.0167	-0.0391	0	0.1001	-0.0056	-0.0052	0.028	-0.0461
Yaw disp.	0.3746	-0.2723	0.2493	0.4403	0.7295	1	0.1165	0.2956	-0.7609	-0.2177	0.0526	0	0	0.0631	0	0	0.0152	-0.0814
Surge vel.	-0.0553	-0.2105	0.9136	0.2734	0.043	0.1165	1	-0.4112	0.0232	0.5897	0.9785	0.7368	-0.0071	-0.8245	0.0161	0	-0.3707	-0.8119
Sway vel.	0.2906	-0.0281	-0.3307	0.1477	0.5414	0.2956	-0.4112	1	-0.4992	-0.945	-0.4904	-0.3883	0	0.4022	-0.0109	0	0.171	0.3161
Heave vel.	-0.4726	0.1675	0	-0.3082	-0.8563	-0.7609	0.0232	-0.4992	1	0.4163	0.0887	0.0868	0	-0.1796	0.0052	0	-0.0648	-0.0254
Roll vel.	-0.3037	-0.0588	0.4829	-0.0392	-0.4246	-0.2177	0.5897	-0.945	0.4163	1	0.6635	0.6493	0	-0.5378	0.0179	0.0081	-0.2307	-0.4783
Pitch vel.	-0.0677	-0.2577	0.8811	0.2415	-0.0167	0.0526	0.9785	-0.4904	0.0887	0.6635	1	0.7567	-0.0071	-0.8332	0.0164	0	-0.3737	-0.8116
Yaw vel.	-0.0463	-0.1237	0.6011	0.1143	-0.0391	0	0.7368	-0.3883	0.0868	0.6493	0.7567	1	0.0113	-0.6374	0.0294	0.0161	-0.2747	-0.6618
RootMEdg	0	0	-0.0058	-0.0054	0	0	-0.0071	0	0	0	-0.0071	0.0113	1	0.09	0.9996	0.9998	0.9034	0.3085
RootMFlp	0.0376	0.1574	-0.7467	-0.1524	0.1001	0.0631	-0.8245	0.4022	-0.1796	-0.5378	-0.8332	-0.6374	0.09	1	0.063	0.0891	0.5075	0.9503
Spn1Mx	-0.0059	0	0.0152	0	-0.0056	0	0.0161	-0.0109	0.0052	0.0179	0.0164	0.0294	0.9996	0.063	1	0.9995	0.8915	0.2831
Spn2Mx	-0.0069	0	0	0	-0.0052	0	0	0	0	0.0081	0	0.0161	0.9998	0.0891	0.9995	1	0.9027	0.3073
Spn1My	0	0.0773	-0.336	-0.0781	0.028	0.0152	-0.3707	0.171	-0.0648	-0.2307	-0.3737	-0.2747	0.9034	0.5075	0.8915	0.9027	1	0.68
Spn2My	-0.0519	0.1951	-0.7458	-0.2123	-0.0461	-0.0814	-0.8119	0.3161	-0.0254	-0.4783	-0.8116	-0.6618	0.3085	0.9503	0.2831	0.3073	0.68	1

Table 19 – Correlations matrix for blade loads for below-rated, misaligned wind and waves

	Surge disp.	Sway disp.	Heave disp.	Roll disp.	Pitch disp.	Yaw disp.	Surge vel.	Sway vel.	Heave vel.	Roll vel.	Pitch vel.	Yaw vel.	RtMEdg	RtMFlp	Spn1Mx	Spn2Mx	Spn1My	Spn2My
Surge disp.	1	0.1252	-0.0681	-0.01	0.1289	0	-0.3202	0.012	0.0052	0	-0.1889	0	-0.0057	-0.0832	0	-0.0066	-0.0266	-0.1123
Sway disp.	0.1252	1	0.0133	-0.9791	0.0265	-0.7493	-0.094	0	-0.9734	0.0075	0.0312	-0.5323	-0.0084	-0.0487	-0.0078	-0.0088	-0.0199	-0.0592
Heave disp.	-0.0681	0.0133	1	-0.0326	-0.0418	0.5159	0.0254	0.9357	0	-0.9173	0.0205	-0.7368	0	-0.0082	0	0	0	0
Roll disp.	-0.01	-0.9791	-0.0326	1	-0.0259	0.7532	0	-0.0079	0.9919	0	0	0.5537	0.0092	0.0484	0.0087	0.0096	0.0205	0.0557
Pitch disp.	0.1289	0.0265	-0.0418	-0.0259	1	-0.0171	-0.2207	-0.0123	0	0	-0.1735	0	-0.0065	0.0475	-0.0072	-0.0071	0	0.009
Yaw disp.	0	-0.7493	0.5159	0.7532	-0.0171	1	-0.0057	0.5325	0.767	-0.5329	-0.0051	0	0.0054	0.0233	0.0052	0.0061	0.0112	0.0311
Surge vel.	-0.3202	-0.094	0.0254	0	-0.2207	-0.0057	1	0.0173	-0.0504	-0.0126	0.6085	-0.0277	0	-0.06	0	0	-0.013	0.0069
Sway vel.	0.012	0	0.9357	-0.0079	-0.0123	0.5325	0.0173	1	0.0136	-0.9983	0.0148	-0.6917	0	-0.0178	0	0	-0.0085	-0.0177
Heave vel.	0.0052	-0.9734	0	0.9919	0	0.767	-0.0504	0.0136	1	-0.02	-0.0763	0.5433	0.0093	0.0576	0.0085	0.0095	0.0227	0.0613
Roll vel.	0	0.0075	-0.9173	0	0	-0.5329	-0.0126	-0.9983	-0.02	1	-0.0185	0.6771	0.005	0.0141	0	0	0.0081	0.0149
Pitch vel.	-0.1889	0.0312	0.0205	0	-0.1735	-0.0051	0.6085	0.0148	-0.0763	-0.0185	1	-0.0459	0	-0.0604	0	0	-0.013	-0.0075
Yaw vel.	0	-0.5323	-0.7368	0.5537	0	0	-0.0277	-0.6917	0.5433	0.6771	-0.0459	1	-0.0059	0.0334	-0.0065	-0.0065	0	0.0289
RtMEdg	-0.0057	-0.0084	0	0.0092	-0.0065	0.0054	0	0	0.0093	0.005	0	-0.0059	1	0.1672	0.9999	0.9999	0.9761	0.5725
RtMFlp	-0.0832	-0.0487	-0.0082	0.0484	0.0475	0.0233	-0.06	-0.0178	0.0576	0.0141	-0.0604	0.0334	0.1672	1	0.1552	0.1778	0.3771	0.8788
Spn1Mx	0	-0.0078	0	0.0087	-0.0072	0.0052	0	0	0.0085	0	0	-0.0065	0.9999	0.1552	1	0.9997	0.9734	0.5627
Spn2Mx	-0.0066	-0.0088	0	0.0096	-0.0071	0.0061	0	0	0.0095	0	0	-0.0065	0.9999	0.1778	0.9997	1	0.9782	0.5807
Spn1My	-0.0266	-0.0199	0	0.0205	0	0.0112	-0.013	-0.0085	0.0227	0.0081	-0.013	0	0.9761	0.3771	0.9734	0.9782	1	0.7335
Spn2My	-0.1123	-0.0592	0	0.0557	0.009	0.0311	0.0069	-0.0177	0.0613	0.0149	-0.0075	0.0289	0.5725	0.8788	0.5627	0.5807	0.7335	1

Compared to the tower loads, the blade loads are much less correlated to displacements and velocities in all 6 DsoF. While aligned wind and wave inputs show moderate correlations between heave displacement, surge, roll, pitch and yaw velocities with blade flap moments, misaligned wave and wind inputs show no correlation to any of the DsoF or associated velocities. This is expected as the flap loads are very small in the misaligned case and edgewise loads dominate the response. Moreover, the edgewise loads are dominated by the gravitational loads (rotational frequency). On the other hand, in the aligned case the flapwise loads can be of a significant size. Because wind turbines are designed to obtain some side-to-side aerodynamic damping by coupling edgewise and flapwise modes, the results show significant coupling between all edgewise and flapwise loads, in particularly in the misaligned wind and wave input cases.

In this section only the below-rated result were discussed. The results for the rated and above-rated runs are provided in A1.13. Overall, the results for the rated and above-rated cases are very similar to the ones analysed above. However, the rated response shows much stronger correlation of the tower and blade loads as the turbine is experiencing the highest thrust and hence the largest displacements and velocities in different DsoF (see Figure 131).

### 3.3. Conclusions

All simulations performed in this chapter were completed in FAST. Whilst FAST has its limitations and simplifications, in particular in the hydrodynamics and mooring system, it was judged to be sufficiently comprehensive to perform the intended tasks of comparing the quasi-steady and unsteady loads, identifying which DoF is the most detrimental and performing a simple statistical analysis between different modes of motion, and tower and blade loads.

The fully-unsteady simulations performed in FAST incorporated some aspects of the fully-attached Theodorsen and Van der Wall and Leishman theories [53, 63]. The inherent structure of AeroDyn, which is partially based on Leishman's model, results in some similarities between aerodynamic codes, FAST and the fully-attached code written and described in Chapter 2.

The mean loading is almost always higher in the unsteady case in both fully-attached and fully-unsteady aerodynamics code simulations, though these differences never exceed a few per cent. Conversely, when considering the dynamic load ranges, the results differ greatly between the fully-attached and fully-unsteady aerodynamics, and between different DsoF. The fully-attached codes of Theodorsen and Van der Wall and Leishman show larger amplitudes of forces in the quasi-steady case for surge, pitch and yaw (DsoF modelled as changes in the free-stream velocity), whilst the fully-unsteady results of FAST show larger peak-to-trough ranges of force in the unsteady results over the quasi-steady for the same DsoF (except yaw – no results).

The side-to-side DsoF (sway and roll) were excited by misaligning the wind and wave inputs by 90 degrees. Similar magnitudes of surge and pitch displacements (due to wave motion) were obtained, but the variation in thrust was much smaller. This can be explained in two different ways. In 6 m and 25 s waves, sway displacement amplitude is 2.27 m. The maximum velocity of sway motion is 0.57 m/s. The majority of thrust is generated at blade locations that are furthest away from the hub. However, the rotational velocity at these locations is relatively high and addition or subtraction of 0.57 m/s will not make as large a difference as it would close to the hub.

Another way of looking at it is to see a sway velocity as having a similar effect as a yaw error, with a resulting skewed wake. For a skewed wake, the thrust coefficient is expressed as:

$$C_{T_{skewed}} = 4a[\cos(\varphi) - a] \quad 3.7$$

where  $\varphi$  is the yaw angle. Using a moderate yaw error of 15 deg.,  $C_{T_{skewed}}$  is 0.97 which leads to 0.03 difference compared to the aligned free-stream case given below.

$$C_T = 4a(1 - a) \quad 3.8$$

Additionally, sway motion or yaw error introduces cyclic 1P component in in-plane wind velocities seen by the blades, causing cyclic 1P loads. These would transfer to tower as 3P tower loads.

Heave DoF produced almost identical results to sway and roll.

No yaw DoF results were obtained, as it is nearly impossible to excite the OC3-Hywind purely in this DoF. The only way to excite the system in yaw is through gyroscopic coupling between pitch and yaw. Any excitation in yaw is opposed by a net moment about the vertical axis in a direction which will try to restore the rotor axis to a position aligned with the wind and by large damping and stiffness from the mooring system. Theoretically, disabling or modifying the controller could allow some results in the yaw DoF to be obtained.

The quasi-steady and fully-unsteady aerodynamic comparison was performed by including the Beddoes-Leishman dynamic stall model and induction-lag in the unsteady aerodynamic simulations. Several differences between these cases were observed.

The first major difference observed was a small but significant phase difference in the results between the two aerodynamic assumptions. This is consistent both with theory and with the results in Chapter 2, which suggests that for small reduced frequencies the unsteady aerodynamic results will lag behind the quasi-steady. Secondly, unsteady aerodynamics seems to produce significantly larger aerodynamic damping. The results showed 2.3% and 3.7% aerodynamic damping in the quasi-steady and unsteady aerodynamics in 10 m/s wind, and 6 m and 18 s regular waves. The reason behind the

significantly larger aerodynamic damping in the unsteady case is due to the effect that induction-lag has on thrust. In the presence of an induction-lag model (dynamic wake) any change in the angle-of-attack of the blades will result in an overshoot in thrust. Aerodynamic damping is directly proportional to the rate of change of thrust with respect to velocity and this is greater in the unsteady case, hence the increase in the aerodynamic damping.

Secondly, the highly non-linear nature of wind turbines, and particularly induction-lag, leads to the appearance of wave harmonics in the unsteady simulations. These were shown to be very detrimental to the system, in particular when coinciding with other natural frequencies of the system, such as the tower FA and SS modes. Thirdly, the unsteady aerodynamics always predicts much higher loads. Again, this can be attributed to induction lag and the same explanation as for the increase in the aerodynamic damping can be used.

Surge and pitch DsoF were compared to identify which one is the most detrimental to the system in terms of fatigue. The work concentrated only on these two DsoF as the others were reasoned to be of a lesser importance. In particular, sway, roll and heave were shown to be of a very little importance as the motion in these DsoF is in the plane of the rotor rotation. The yaw degree-of-freedom was also disregarded, as the spar is symmetric and it is almost impossible to excite the system in yaw DoF through hydrodynamic loads. The only way yaw would be excited is through gyroscopic coupling with pitch DoF. Because pitch DoF was identified as the most detrimental to the system, any modification to dampen out or minimise motion in pitch DoF would also result in smaller displacements in yaw and roll DsoF.

Surge and pitch DsoF were compared by modifying the wave-excitation force vector by scaling the load magnitude by different factors. Different runs were then compared that had an identical displacement in one DoF, but a different one in another. The difference in the displacement was then used as the explanation for the variation in the tower and blade loads. Because blade loads contained multiple frequency components (wave, rotational, and their sum- and difference-frequencies), damage equivalent loads (DELs) had to be used to compare loads in surge and pitch DsoF. Linearity was assumed in all of these calculations. Tower loads were calculated at the base and at the most vulnerable height above the base.

Blade loads were investigated at the blade root and at 2 strain gauge locations, as these, together with another tower strain gauge location, were identified as the most likely points of failure for the tower and blade. All loads and DELs per 1 m and deg. of displacement showed that pitch is much more detrimental to the system than surge. This was expected, as there is a significant distance between blades and the overall CoG of the system, and any motion in pitch would result in significant variation in the free-stream velocities seen by each blade element. However when tower loads and blade DELs were calculated for the actual responses in the surge and pitch DsoF in below-rated, rated and above-rated conditions, the results showed that both DsoF are of similar importance, with each load case being of a similar size between both DsoF.

Lastly, a very simple statistical analysis was performed on the FAST results. Different operating conditions (below-, rated and above-rated) with full-spectrum irregular waves were used and displacements and velocities in different DsoF were correlated with the tower and blade loads. To excite the turbine in the side-to-side direction, waves were aligned with the y-axis (90 degrees misaligned with wind). Overall, 12 correlation matrices were produced to account for tower and blade loads, aligned and misaligned cases, and 3 different operating conditions. Only unsteady aerodynamics was used. These results confirmed what was already known or expected. For example, there is strong coupling between surge and pitch, and sway and roll. Coupling exists between flap-wise and edge-wise blade loads (to obtain extra aerodynamic damping in side-to-side direction). The impact of surge, pitch and yaw motions on tower FA and blade flapwise loads and sway, heave and roll motions on tower SS loads were recognised. However, some new connections were also identified such as correlations between sway and yaw DsoF.

# Chapter 4: Alternative spar designs

---

As previously mentioned, the OC3-Hywind is limited to very deep water depths. The original Hywind design for a 2.3 MW wind turbine had 100 m draft, which limited it to 120+ m water depths. Why was not a shorter spar used, thus allowing it also to be installed in medium depth waters? This question is discussed in this chapter, as well as several others, such as; what are the main trade-offs, how do they influence each other and how do the natural frequencies vary with shortening of the spar length?

## 4.1. Excel spread sheet

A relatively simple, but very insightful, Excel spreadsheet was built to reverse engineer the OC3-Hywind using the data provided in [46]. In a number of ways, not enough specific data was given in [46] to allow variations in the design to be explored. For example, the ballast density was not provided, only the overall mass, the CM (centre of mass) was only given for the spar together with its ballast, not separately, and many other instances. Consequently, some informed guesses had to be made. A very realistic hull structure and weight distribution was borrowed from a group project in Texas A&M University [111], which had communicated with Technip and obtained some design details of the OC3-Hywind.

A high-level flowchart showing how the Excel spreadsheet works is given in Figure 132. This spreadsheet was used, firstly, to reverse engineer the OC3-Hywind, secondly, to perform a

parametric study, and thirdly, to suggest alternative designs of shortened spar for medium-to-high depth waters.

A step-by-step run through the flowchart is as follows:

- Spar geometry was used to calculate the total displacement. Because the vessel is floating, the weight had to be balanced by the buoyancy force.
- Approximate steel thickness. Whereas in reality the steel thickness would vary along the spar's length, a simplified approach was used, whereby one steel thickness was used for the top cylinder and conical section, and a greater thickness for the bottom cylinder (see Figure 135).
- Using the spar geometry and steel thickness data, the weight of the hull could be approximated. By slightly adjusting steel thickness, it was made to match the result of 1,493,830 kg given in [111].
- Hull CoG was then calculated by splitting the hull into 5 sections (sections 1-5 in Figure 135).
- The weight of ballast could be approximated by subtracting the wind turbine, the hull and the mooring system weight from the total weight of the system, which equalled the buoyancy force. Alternatively it could be calculated by subtracting the hull weight from the total spar weight given in [46] (this applied only to reverse engineering the OC3-Hywind).
- The volume of ballast and its CoG could be calculated by providing the ballast density as an input variable. Ballast density was calculated as  $1,900 \text{ kg/m}^3$  for the OC3-Hywind to match the CoG of spar given in [46].
- The total CoG was calculated by combining the CoG of wind turbine, spar and ballast. The mooring system was ignored in these calculations, as it is relatively light compared to the other parts of the system.
- Metacentric height, GM, was then calculated by subtracting KB (centre of buoyancy measured from the keel) from KG (centre of gravity measured from the keel). KB was calculated from the spar geometry (see 4.1.2.8).
- Inertias in the roll/pitch and yaw DsoF were calculated by using different simplifications (see 4.1.2.2).
- The thrust on the rotor could be calculated either using some simple formulae or by simulating the OC3-Hywind in FAST. While the max and min values of the thrust would vary with different spar designs, the mean thrust should be the same, as the same NREL 5MW turbine [47] was used in all calculations.
- The static heel angle (at max thrust on the rotor), and the roll and pitch natural frequencies could then be calculated (4.1.2.4 and A1.9.3).

In Figure 132, a colour scheme is used to differentiate between different block types, where red stands for parameters that can be changed/adjusted, blue for fixed parameters, white

for operations/calculations and yellow for the final objectives, which have been identified as the static heel angle and the pitch natural frequency.

The built-in Solver function in Excel was used to perform a parametric study and put forward some preliminary potential shortened spar designs that could be used in shallower waters than the current Hywind and OC3-Hywind designs.

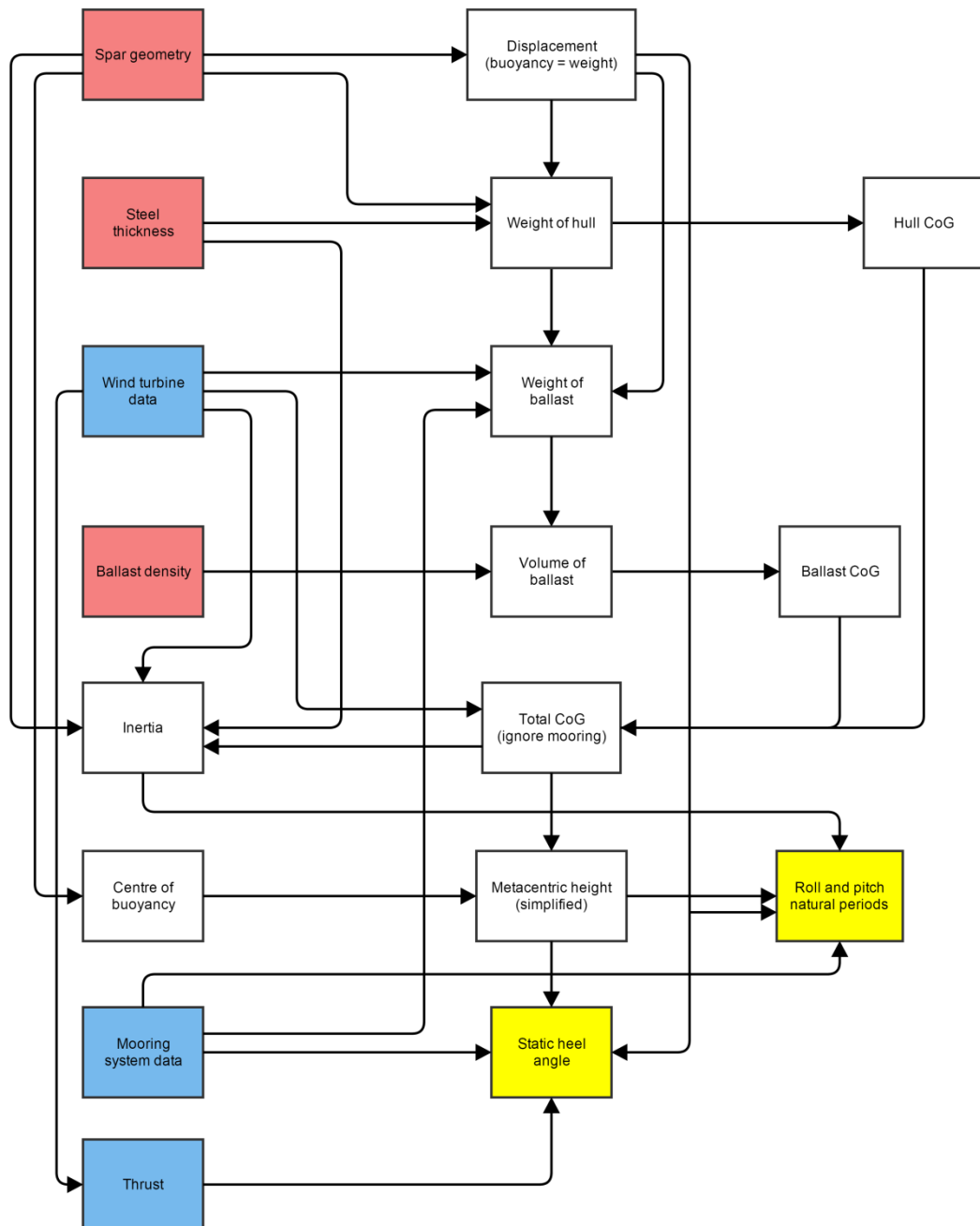


Figure 132 – Flowchart of Excel spreadsheet

The leading design parameters for shortened spar designs were identified as the static heel angle (had to be limited to below a specific value), the natural frequency in pitch (kept as high as possible to keep away from the predominant wave frequencies) and the metacentric height (had to be positive to make sure that the design does not capsize). The importance of these parameters is clearly seen in Figure 132, where the static heel angle and roll and pitch natural periods are the final calculation blocks and objectives of the spreadsheet. Additionally, the metacentric height is the penultimate calculation that then feeds into static heel and pitch period calculations.

#### 4.1.1. OC3-Hywind

In this section the derived OC3-Hywind variables, used in the Excel model to reverse engineer the original OC3-Hywind described in [46], are given and discussed. Some of these were kept constant when shortening the spar's draft, others changed.

The same NREL 5MW wind turbine with the modified tower was used in all spar designs, so that values given by the NREL or derived in Excel did not need to be adjusted for each design. The majority of the wind turbine data, except for inertias and the overall CM, was taken from [46]. The main values are summarised and given in the table below.

Table 20 – The OC3-Hywind wind turbine data

<b>Tower mass (kg)</b>	249,718
<b>CM of tower from SWL (m)</b>	43.3
<b>Tower <math>I_{xx}</math> and <math>I_{yy}</math> (<math>\text{kgm}^2</math>)</b>	2,161,570
<b>Tower <math>I_{zz}</math> (<math>\text{kgm}^2</math>)</b>	1,816,870
<b>Nacelle <math>I_{zz}</math> (<math>\text{kgm}^2</math>)</b>	2,607,890
<b>Rotor <math>I_{zz}</math> (<math>\text{kgm}^2</math>)</b>	33.3E+06
<b>Turbine <math>I_{zz}</math> (<math>\text{kgm}^2</math>)</b>	37.7E+06
<b>Rotor mass (kg)</b>	110,000
<b>Nacelle mass (kg)</b>	240,000
<b>Hub height above SWL (m)</b>	90
<b>Turbine CM from SWL (m)</b>	70

The turbine's inertia about the z-axis was calculated by summing up the individual inertias for the rotor, nacelle and tower. The rotor provided the majority of the inertia. The nacelle's yaw inertia was given in [47], whilst the tower's and rotor's inertias were calculated in the Excel spreadsheet. The tower's inertia about the centreline was calculated by splitting the tower into shorter sections. These were simplified as thick-walled tubes with the effective density of the steel increased to 8,500 kg/m<sup>3</sup> to account for paint, bolts, welds and stiffeners otherwise not accounted for in the tower thickness data. The radius and thickness of the tower wall were assumed to be linearly tapered. The distribution of the tower's properties was given in [46]. The rotor's inertia about the z-axis was calculated by ignoring the hub's inertia about its own centre of mass.

The rotor's and nacelle's inertias about the x- and y-axes were not given in Table 20, as their inertia about their own CM were very small compared to the inertia about the overall CM of the system.

As the hull dimensions were given, this allowed the overall mass of the hull to be calculated by adding up the mass of each section. Overall, 5 sections were included (see Figure 135). However, to calculate the mass of the each section, the steel thickness had to be calculated first. To simplify calculations the hull was assumed to have two different steel thicknesses, one for the top cylinder and conical section (sections 1-3), and one for the bottom cylinder (sections 4 and 5). These steel thicknesses were chosen in such a way as to match the combined hull and ballast CM given in [46], while at the same time trying to match the individual hull CM taken from [111]. The priority was given to the former, which was matched to within 3.5 cm. This meant that the hull CM would not be matched perfectly (mainly due to the simplified steel thickness distribution along the spar's length), and it was out by about 1.5 m. The mass of the ballast was estimated by subtracting the mass of the hull (taken from [111]), mooring system and wind turbine (both given in [46], except for rotor and nacelle [47]) from the mass of the total water displaced by the spar. Again, ballast density was calculated to match the CM of the combined hull and ballast.

**Table 21 – The OC3-Hywind spar data**

<b>Steel thickness for top cylinder and conical section (m)</b>	0.02
---	------

<b>Steel thickness for the bottom cylinder (m)</b>	0.051
<b>Mass of hull (kg)</b>	1,493,137
<b>Hull CM from SWL (m)</b>	-62.18
<b>Hull and ballast CM from SWL (m)</b>	-89.88
<b>Mass of mooring lines (kg)</b>	163,806
<b>Total displacement (m<sup>3</sup>)</b>	8,029.21
<b>Mass of ballast (kg)</b>	5,970,470
<b>Ballast density (kg/m<sup>3</sup>)</b>	1,900
<b>Ballast CM from SWL (m)</b>	-96.81
<b>Overall CM of system (m)</b>	-78

The static heel angle of the system was calculated using equation 4.3. Compared to simulations of the OC3-Hywind in FAST (Figure 131), the result had an error of approximately 12% (4.74 deg. in FAST and 5.3 in Excel). While one might argue that this is a relatively high error, the aim was not to design a new spar, but merely to ascertain whether or not it would be possible to have a shorter spar without breaching limits, and to explore the influence such design changes would have on the system's dynamics. In addition, having a slightly greater static heel angle than obtained in FAST means that, for the shortened spar designs, calculations of the static heel angle would possibly be on the conservative side. Similarly, the yaw inertia of the system was under-calculated by almost 60% for the spar with ballast calculations (given in [46]). This resulted in under predicting the yaw natural period by around 1.3 s. Due to relatively simple and crude inertia calculations about the x- and y-axis, the roll and pitch natural frequency had an error of approximately 6% (calculated as 27.4 and given as 29.3 s). However, just as with the static heel angle, this meant that all subsequent calculations would possibly give conservative figures for roll and pitch periods. Surge, sway and heave natural periods matched those published in [95].

**Table 22 – The OC3-Hywind static heel angle, inertia and natural periods**

	<b>Calculated</b>	<b>FAST</b>
<b>Max static heel angle (deg.)</b>	5.3	4.74
<b>Total I<sub>zz</sub> (kgm<sup>2</sup>)</b>	135,104,202	191,573,000
<b>Total I<sub>xx</sub> and I<sub>yy</sub> (kgm<sup>2</sup>)</b>	30,318,198,505	-

<b>Natural period of surge/sway (s)</b>	125.6	125
<b>Natural period of heave (s)</b>	31	30.86
<b>Natural period of roll/pitch (s)</b>	27.4	29.24/29.15
<b>Natural period of yaw (s)</b>	7	8.26

#### *4.1.2. Design parameters*

The flowchart described in 4.1 and shown in Figure 132 contains an algorithm that is dependent on multiple parameters. Some of these parameters are fixed, such as the seawater density, the wind turbine data, the mooring system data etc., but some are not. Those that are not are either chosen by the Solver algorithm to match a specific value, or are just a by-product of achieving a set goal. Some of these variables are briefly described next to give an idea of the complexity of designing a spar-type floating offshore wind turbine.

##### *4.1.2.1. Steel thickness*

In a real design, the steel thickness would be most likely to vary with distance along the spar length, with sections farther from the SWL being thicker and having more stiffeners (as shown in Figure 133 [111]).

In the Excel spreadsheet, two different values for steel thickness were used to represent the OC3-Hywind design. For sections 1, 2 and 3 steel was prescribed 0.02 m thickness, but for sections 4 and 5 0.051 m (sections are shown in Figure 135). Only 2 varying steel thicknesses were used compared to 6 in Figure 133 to simplify the overall calculations. The two values given have been equated to represent both plate thickness and stiffeners. The two specific values were chosen to match the mass of hull given in [111] exactly, and to match the CoG as closely as possible (error approx. 1.5 m).

Diameter (m)	Section length (m)	Plate thickness (m)	Inner diameter (m)	Stiffener	Stiffener area (m <sup>2</sup> )	# of stiffeners	Adjusted inner diameter (m)
9.4	17.81	0.045	9.31	WT15X117.5	0.022	12	9.29
9.4	25.99	0.042	9.32	WT15X117.5	0.022	17	9.29
9.4	25.99	0.039	9.32	WT15X117.5	0.022	9	9.31
9.4	25.99	0.039	9.32	WT15X117.5	0.022	9	9.31
9.4	12.19	0.032	9.34	WT15X117.5	0.022	4	9.33
7.95	8.00	0.029	7.89	WT15X117.5	0.022	2	7.89
6.5	13.99	0.026	6.45	WT15X117.5	0.022	3	6.44

Figure 133 – The OC3-Hywind hull structural properties [111]

In a simple sensitivity study, it was found that the hull steel thicknesses (over quite a wide range from 0.03 to 0.065 m) had little influence on the static heel angle and roll/pitch natural periods, as shown in Figure 134. In subsequent calculations, the steel thicknesses were kept constant.

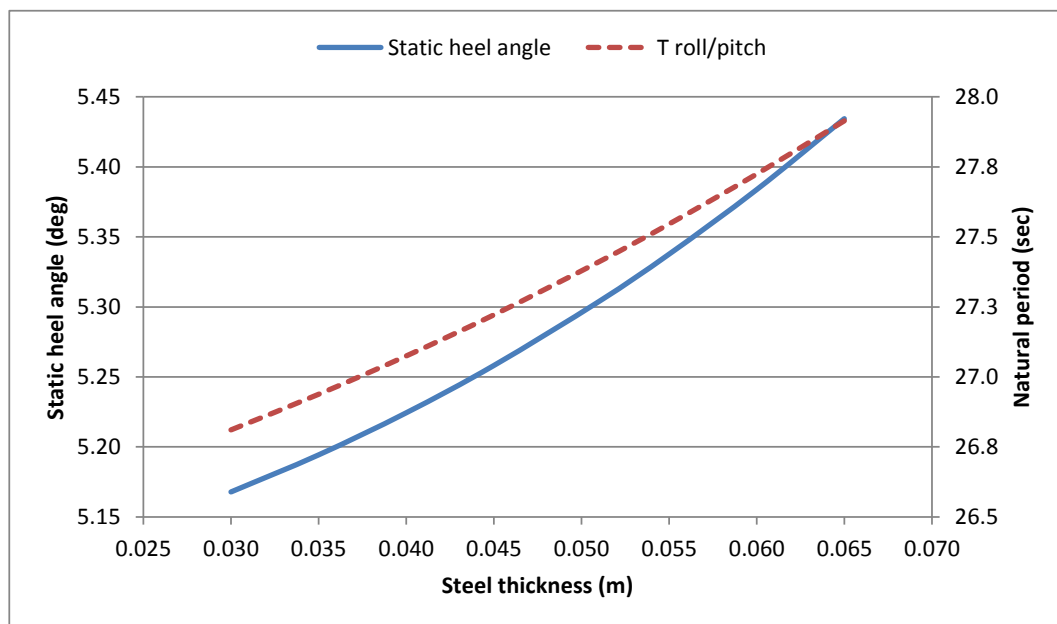


Figure 134 – Static heel angle, and roll and pitch natural period variation with varying steel thickness

#### 4.1.2.2. Inertia

The inertia of the spar was calculated by separating the hull into 6 sections as shown in Figure 135. Sections 1, 5 and 6, and 2, 3 and 4 used the same formulae.

Top and bottom lids (sections 1 and 5) and ballast (section 6) inertias were calculated by approximating each section as a solid cylinder.

$$I_{xx,yy} = \frac{1}{12}m(3r^2 + h^2) \quad 4.1$$

$$I_{zz} = \frac{mr^2}{2}$$

where  $m$  is the mass of each section,  $r$  is the radius and  $h$  is the section height.

Equations 4.1 and 4.2 give inertia with respect to each section's own CM. To calculate the total inertia about the overall CoG of the system, the parallel axis theorem (also known as Huygens-Steiner theorem) was used.

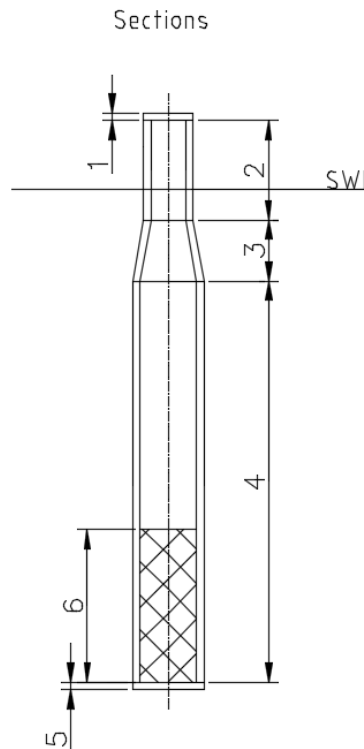


Figure 135 – Sections of spar-type floating offshore wind turbine's hull

Sections 2, 3 and 4 were assumed to be thick-walled cylindrical tubes with open ends.

$$I_{xx,yy} = \frac{1}{12}m[3(r_2^2 + r_1^2) + h^2] \quad 4.2$$

$$I_{zz} = \frac{1}{2}m(r_2^2 + r_1^2)$$

where  $r_1$  is the inner- and  $r_2$  is the outer-radius.

The conical section was approximated as a thick-walled cylindrical tube by taking the average diameter. The wind turbine's inertia was calculated by splitting the whole structure into 3 parts: rotor, nacelle and tower. The rotor and nacelle inertias around the x- and y-axes were simplified. It was assumed that their own inertia about their own CoG was very small compared to the inertia about the overall CoG, as it is located quite far away, and hence was ignored. The mooring system inertia was ignored in these calculations.

#### 4.1.2.3. Added inertia

The added inertias about the x- and y-axes were calculated for 3 sections (top cylinder section below the SWL, conical section and bottom cylinder). These were approximated as solid cylinders of waters.

Due to the complete circular symmetry of the spar there is no added inertia about the z-axis.

Added mass or inertia for the section above the SWL was ignored, due to the low density of air compared to seawater.

#### 4.1.2.4. Static heel angle

The static heel angle is a measure of how far the system heels under mean aerodynamic load. This is an important measure in FOWTs, as wind turbines experience high thrust loads on the rotor and are currently designed in such a way that they cannot heel more than 6 degrees without damaging the drive-train [112].

Static heel angle was approximated as:

$$\text{static heel angle} = \frac{\text{Thrust} \times l}{\overline{GM} * m * g + k} \quad 4.3$$

where  $l$  is the distance from the hub to the CoG (assuming that the mooring system is attached at the CoG),  $\overline{GM}$  is the metacentric height,  $m$  is the overall mass,  $g$  is gravitational acceleration and  $k$  is the restoring stiffness in roll and pitch exerted by the mooring system [46].

Equation 4.3 assumes that the only forcing comes from the thrust on the rotor, which is approximated as a point load at the hub. Additionally, the mooring system was assumed to

be attached to the spar at the CoG of the system allowing subsequent calculations to be simplified. In the OC3-Hywind and Hywind this is not the case (8 m difference for the OC3-Hywind). However, for very simplified calculations performed in this chapter, this simplification was judged to be appropriate.

#### 4.1.2.5. Roll and pitch natural period

Roll and pitch natural periods are considered in A1.9.3.

#### 4.1.2.6. Ballast

The original Hywind design uses olivine as ballast. Olivine is a magnesium iron silicate,  $(Mg, Fe)_2SiO_4$ . It is a commonly occurring mineral in the Earth's crust. It has also been found on the Moon, Mars and meteorites. Around 90% of it is used as a slag conditioner in metallurgy; but it has many other uses such as sauna stoves, refractory products, etc. Olivine is most commonly sourced from Norway (see Table 23), where exports to the U.S. alone make around 150,000 – 200,000 metric tons annually. In 2010, the average price of ground olivine was \$25 per metric ton.

Due to its high density, 3,200 – 4,500 kg/m<sup>3</sup> depending on the magnesium and iron content, and its common occurrence in Norway, it was chosen as ballast for the Hywind design. For the same reason and its relatively low price, it was also considered, together with haematite and magnetite, for the shortened spar designs discussed in this chapter.

**Table 23 – Olivine production by country in thousand metric tons for year 1995 and 1999**

	<b>1995</b>	<b>1999</b>
<b>Norway</b>	5,850	6,300
<b>Japan</b>	900	900
<b>Spain</b>	500	500
<b>the U.S.</b>	90	90
<b>Italy</b>	50	50
<b>Others</b>	40	65

Spar buoys depend for their stability on lowering the CoG of the system with a ballast of high density. Together with seawater, olivine produces a highly dense slurry, which is capable of serving this purpose. Different concentrations of solids in the slurry can be used to achieve the necessary ballast density. These can be calculated using equation 4.4.

$$\rho_{sl} = \frac{100}{\left[ \frac{\varphi_{sl}}{\rho_s} + \frac{(100 - \varphi_{sl})}{\rho_l} \right]} \quad 4.4$$

where  $\rho_{sl}$  is density of slurry in  $\text{kg/m}^3$ ,  $\varphi_{sl}$  is concentration of solid in the slurry in %,  $\rho_s$  and  $\rho_l$  is density of solids and liquid in  $\text{kg/m}^3$ .

In the calculations, the seawater and olivine densities were taken as  $1,025 \text{ kg/m}^3$  and  $3,320 \text{ kg/m}^3$ .

**Table 24 – Different types of olivine and seawater slurries**

<b>Concentration of olivine (%)</b>	50	60	70	80	90
<b>Concentration of sea water (%)</b>	50	40	30	20	10
<b>Density of slurry (<math>\text{kg/m}^3</math>)</b>	1,566.39	1,751.42	1,985.99	2,293.13	2,712.64

While Table 24 looks at solid concentrations of up to 90%, in reality it would not exceed roughly 70%. This is because the maximum packing density of spheres is  $\pi/\sqrt{18}$  or approx. 0.74. Potentially, this could be surpassed, if different sizes of spheres were used and packed to a specific arrangement. However, this would be quite challenging. In addition, it is important to consider any issues that might arise, if one tries to pump ballast, which is too viscous, into the spar (there might be some maximum pumping viscosity).

Using data published in [46], the density of the ballast was approximated as around  $1,900 \text{ kg/m}^3$  for the OC3-Hywind, giving 65% concentration of olivine solids. Assuming that the OC3-Hywind design would also use olivine and seawater slurry, and that olivine would cost \$25 per metric ton, one would need 6 million kg of ballast for the system to stabilise, which would cost around \$97,500 (assuming the price of olivine not to have changed).

Other minerals, such as haematite and magnetite, were also considered for use in the ballast. These minerals offer superior relative densities compared to olivine (5.26 and 5.17), which would be beneficial as the spar is shortened.

**Table 25 – Different types of haematite and seawater slurries**

<b>Concentration of iron ore (%)</b>	50	55	60	65	70
<b>Concentration of seawater (%)</b>	50	45	40	35	30
<b>Density of slurry (kg/m<sup>3</sup>)</b>	1,715.7	1,839.6	1,982.9	2,150.4	2,345.7

If haematite was used instead, the same slurry density could be achieved at approximately 10% lesser solid concentration, compared to olivine. This would allow the maximum slurry density to be increased from just below 2,000 kg/m<sup>3</sup> to almost 2,350 kg/m<sup>3</sup> (for 70% solid concentration).

#### 4.1.2.7. Spar dimensions

Spar length and diameter are very important design parameters. These are discussed in detail in 4.2.

#### 4.1.2.8. Metacentric height

The metacentric height is a direct measure of a floating vessel’s static stability. It is measured as the distance between the centre of gravity of the vessel and its metacentre. Large metacentric heights provide superior static stability against heel and increased stiffness in roll and pitch, leading to higher natural frequencies (as shown in equation A.44).

When a spar-type floating offshore wind turbine heels, its centre of gravity stays in the same position relative to the structure, but its centre of buoyancy moves laterally (only applicable for small angles of heel). The metacentre is the point at which a vertical line through the new, heeled centre of buoyancy crosses the line through the original centre of buoyancy. For small angles of heel, the metacentre is always above the centre of buoyancy.

The metacentre, measured from the keel, can be calculated as:

$$\overline{KM} = \overline{KB} + \overline{BM} \quad 4.5$$

where  $\overline{KB}$  is the centre of buoyancy and  $\overline{BM}$  is the metacentric radius.

The metacentric radius can be calculated using:

$$\overline{BM} = \frac{I}{V} \quad 4.6$$

where  $I$  is the second moment of area of the waterplane and  $V$  is the total displacement [113].

The metacentric height can now be expressed as:

$$\overline{GM} = \overline{KB} - \overline{KG} + \overline{BM} \quad 4.7$$

where  $\overline{KG}$  is the centre of gravity in m, measured from the keel.

However, the metacentric radius is very small for long, slender spar-type designs, such as that used in OC3-Hywind. With the total displacement of 8,026 m<sup>3</sup> and spar diameter of 6.5 m at the SWL, the metacentric radius is only 0.011 m. Compared to a distance of approximately 16 m between the centres of buoyancy and gravity, the contribution of the metacentric radius in calculating the metacentric height for the OC3-Hwyind is negligible and can be ignored.

Similarly, the metacentric radius could be ignored even for shortened designs of the OC3-Hywind spar, where the top cylinder is kept the same and the bottom cylinder is shortened. The metacentric radius with varying draft is shown in Figure 136. Even for as extreme a case as a draft of 50 m, the metacentric radius would be less than 3 cm. In reality, this number would be even smaller as the diameter of the spar has to increase with decreasing draft (assuming that the waterplane area is kept constant and the total displacement increased).

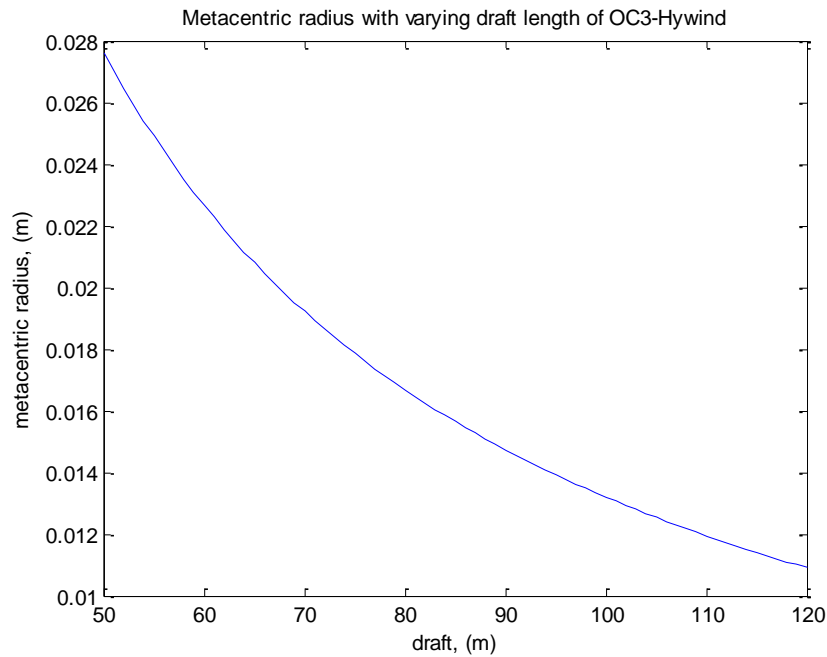


Figure 136 – Metacentric radius distribution for varying draft of the OC3-Hywind

This means that the metacentric height for small angles of heel (0 – 15 deg.) can now be approximated as:

$$\overline{GM} \approx \overline{KB} - \overline{KG} \quad 4.8$$

This simplification is used in all the subsequent calculations.

Additionally, equations 4.5 – 4.8 assume that the system is freely floating with no constraints, hence completely ignoring the mooring system. This could potentially lead to some errors in the subsequent calculations. However, as the whole system is significantly simplified and the mooring system ignored to a large extent as it is beyond the scope of this study, the assumption of a freely floating system was judged reasonable for performing preliminary study and calculations.

## 4.2. Parametric study

In the previous section, a brief introduction was given to various parameters that needed to be considered when designing a spar-type FOWT. In this section, parametric studies were performed in greater detail, firstly, on a theoretical uniform spar and secondly, on the OC3-Hywind.

Whilst the mooring system and wind turbine were kept the same (including the control algorithm); the following parameters of the floater were varied to modify the current design of the OC3-Hywind spar and also to alleviate loads on the system:

- Spar diameter
- Spar length
- Ballast density
- Steel thickness

Any significant increase in steel thickness would greatly increase the overall cost of the system. Ideally, steel use should be minimised as its price as a commodity is both relatively high and volatile<sup>7</sup> [114, 115]. Further costs associated with thicker steel sections are an increase in welding costs, and difficulty in rolling to form cylinders.

Changing the spar diameter, length and/or ballast density can potentially result in shifting the natural frequencies of the OC3-Hywind into the high spectral energy range associated with waves (wave periods between 5 sec and 20 sec). For these reasons, these variables are analysed next, by first looking at an idealised uniform spar and then at the OC3-Hywind.

#### *4.2.1. Uniform spar*

##### *4.2.1.1. Spar diameter*

Assuming that all other parameters are kept constant (mooring system, ballast density, mass, etc.), changing the spar diameter for a uniform spar would change the cross-sectional area along the spar length. This would cause the added mass to change in proportion to the volume in all modes except for yaw (as no water is displaced in this mode). This would also change the restoring coefficients in pitch, roll and especially heave, as the restoring stiffness in heave arises almost entirely from the change in buoyancy due to changes in water displaced with heave motion. A small proportion of restoring in heave also comes from the mooring lines.

---

<sup>7</sup> Iron-ore price (US\$ for metric ton) from 1985 to 2010 has increased from around \$25 to \$180 [100], or more recently from \$190 in 02/2011 to \$100 in 09/2012 [101].

Increasing the diameter of a uniform cylinder spar would cause the surge and sway natural periods to increase (assuming that the mooring stiffness is kept the same), due to an increase in the added mass, which can be approximated as the amount of water displaced by the spar. The heave natural period is a function of both reserve buoyancy and added-mass (assuming that the mass of the system is kept constant). Increasing the spar diameter would increase both the added-mass and the reserve buoyancy in heave. The direction of the change in the natural period of heave would depend on the spar radius. For  $r < 14.715$  m an increase in the reserve buoyancy would be larger than the increase in the added mass, so the natural period of heave would decrease. For  $r > 14.715$  m the added mass would take over and the period would increase.

The yaw natural period would increase, as it is a function of the mooring system's restoring stiffness, which would be kept constant, and inertia, which would increase with the radius (assuming that the system's mass is kept constant). Pitch and roll natural periods are functions of multiple variables: the distance between the centre of mass and the centre of buoyancy, the mass and the inertia of the system. Assuming that all were kept constant and only the spar diameter were enlarged, the natural period of both pitch and roll would increase due to the increase in inertia. However, in practice an increase in the diameter of the spar would be met with a decrease in the length of the spar. In addition, the distance between the centre of mass and centre of buoyancy would also change (decrease).

Increasing the cross-sectional area of the spar at the SWL would make the system begin to resemble a barge-type floater and would increase its sensitivity to wave input. This is the main reason why the Hywind and OC3-Hywind have a much smaller diameter at the SWL compared to the keel. For the same reason, the radius at the SWL was not altered when shortening the OC3-Hywind spar.

#### 4.2.1.2. Spar length

Changing the spar length would not change the first natural period in heave, as long as the overall mass of the system and the mooring system were kept constant (as the natural period in heave should be expressed as  $f_{Hz} = \frac{1}{2\pi} \sqrt{\frac{k_{buoyancy} + k_{mooring}}{m + m'}}$  and not  $f_{Hz} = \frac{1}{2\pi} \sqrt{\frac{g}{h}}$ ). However, it would change the added-mass in surge and sway, but not in heave, as the

added-mass in heave can be approximated as a half-sphere of water beneath the spar. Compared with a change in the spar diameter, the buoyancy of a spar would change linearly with spar length. Assuming that other parameters of the system were kept constant, surge and sway natural periods would increase with increasing length of the system as the result of an increase in the added-mass.

The natural period in yaw is a function of the mooring restoring stiffness and the inertia about the centre-line of the spar and is not a function of the spar length. This means that the natural period in yaw would also not change, if the mass of the system and mooring system were kept constant, as the spar length were changed. However, if the spar were to be extended and its mass were increased, then the natural period in yaw would also increase due to the change in inertia. Similarly, pitch and roll natural periods would increase, if the length of a spar were increased. However, compared to yaw, the natural periods in pitch and roll are also a function of the spar length, so whether the mass of the system were increased or not with an increase in the length of the spar, the natural periods in pitch and roll would increase.

Both, an increase in the spar diameter and a decrease in the spar length, would have very similar, almost identical, effects on the natural periods of a uniform spar. The surge and sway natural periods would increase, and so would the yaw, and roll and pitch natural periods. The only exception is in the heave natural period, which does not change with the spar length, but changes with the spar diameter.

#### *4.2.2. OC3-Hywind*

The OC3-Hywind is not a uniform spar, and while it makes calculations slightly more complicated, it has two advantages. Firstly, a smaller diameter at the SWL makes the whole system less sensitive to wave input. Secondly, having a larger diameter at the keel allows the overall CoG of the system to be lowered, hence improving the static stability.

The OC3-Hywind spar dimensions as given in [46] are shown in Figure 137.

When performing some simplistic back-of-the-envelope calculations, the whole spar was split into sections, as shown in Figure 135. When carrying out the parametric study, only the bottom section of 108 m length was modified (in either diameter or length). This of

course meant that the conical section would also change. However, the top cylinder was kept the same, to maintain low excitation from wave input.

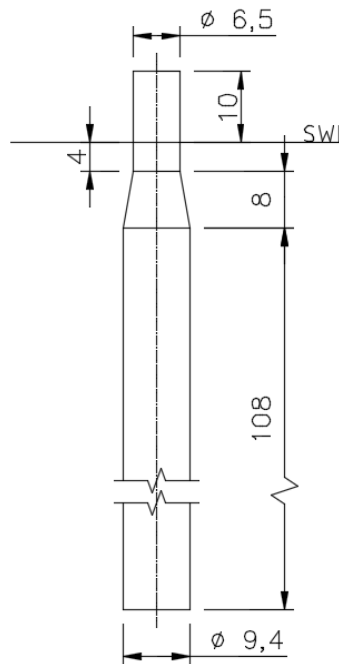


Figure 137 – Dimensions of the OC3-Hywind spar in meters [46]

#### 4.2.2.1. Draft

The draft of the OC3-Hywind was varied from the original 120 m to 50 m to allow for deployment of the spar in water depths of 60+ m. To vary the draft, the bottom cylinder of the spar (section 4 in Figure 135), was shortened from 108 m to 38 m in 10 m steps starting at 68 m. As this is a very simple parametric study, all other parameters were kept constant (ballast density, steel thickness and spar diameter) while varying the draft.

A simple diagram showing the influence of shortening the draft has on the other parameters is given in Figure 138. The mass includes both hull and ballast mass,  $\overline{GM}$  is the metacentric height, *Inertia* is inertia about the x- and y-axes, *T* stands for natural period and  $\theta_{heel}$  is the static heel angle.

The mass of the system changes linearly, as expected and shown in Figure 139. As the wind turbine was kept the same, only the mass of the hull and ballast changed. The mass of the

hull decreases with shorter spar, and ballast also decreases to balance the equation of the total buoyancy versus total weight.

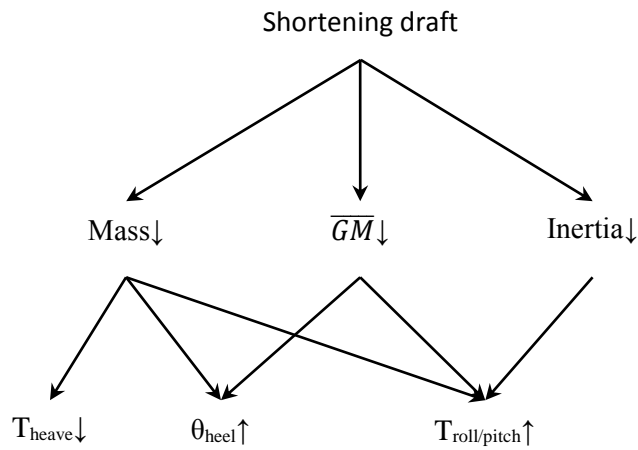


Figure 138 – Influence diagram of shortening the draft of the OC3-Hywind

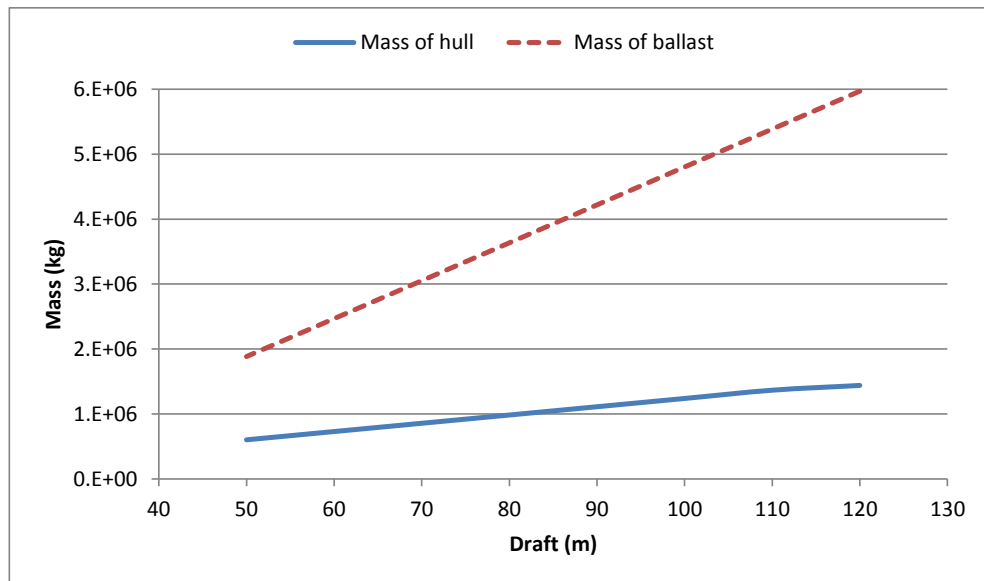


Figure 139 – Change of mass for varying draft

The metacentric height also contracts with shortened spar length. As the spar length decreases, the CoB and CoG tend towards the SWL, but CoG does so at a higher rate. This can lead to the CoG being closer to the SWL than the CoB, making the spar intrinsically

unstable. To ensure that this does not happen, it is necessary to lower the overall CoG by increasing the ballast density, by increasing the spar diameter or by some other means. For this reason, the current design of the OC3-Hywind cannot be shortened below 70 m whilst keeping the other variables constant.

The inertias of the system about the x- and y-axes also diminished with shortening of the spar. This is shown in Figure 138 and Figure 140. This can also be confirmed by looking at equations 4.1 and 4.2, which depend on section mass and/or length (diameter is kept constant).

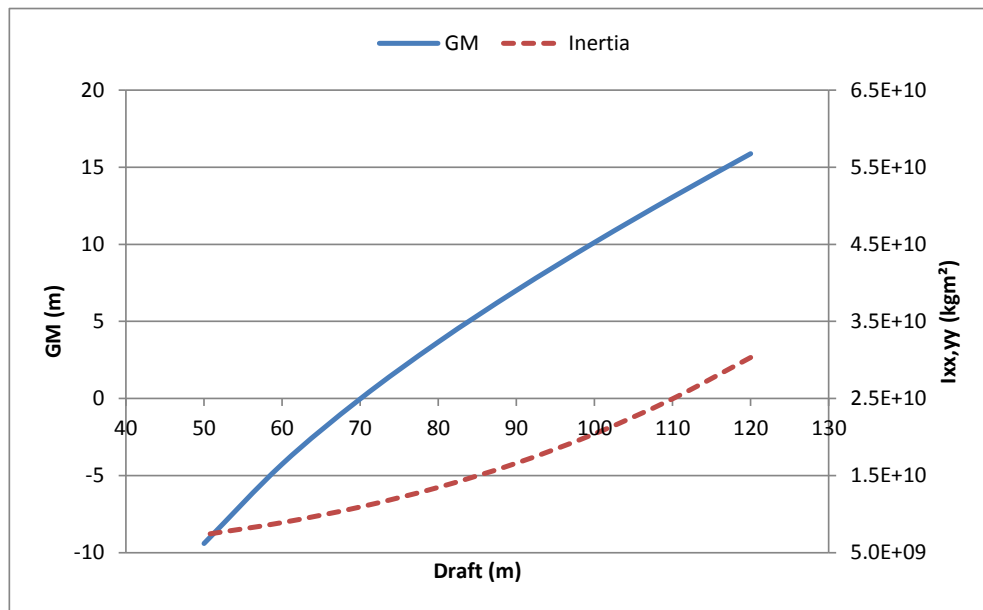


Figure 140 – Metacentric height and inertia about the x- and y-axis for varying draft

As the mooring system (no change in the restoring force) and spar diameter at the keel and SWL (no change in the added mass and restoring) were not modified, the heave natural period varied in proportion to the system’s total mass.

The static heel angle is a function of many variables (see 4.1.2.4). Some of these were not changed in the course of this study, such as the mooring system stiffness and the thrust on the rotor. On the other hand, the static heel angle did change with changes explored in the mass, metacentric height, and distance from the rotor to the CoG. The static heel angle varies with the spar length in a non-linear manner, as shown in Figure 141. In this figure, the static heel angle is shown only down to 60 m draft, at which point it is already 40.7

degrees. For 50 m draft, metacentric height is negative. The heel angle is calculated as 485 degrees, according to the simplified formulae employed here, but this just serves to illustrate the shortcomings of the method of calculation for large deflections as it is only applicable for small angles of heel, and this result is not shown in the figure.

The pitch DoF was identified as the most detrimental DoF to the system (along with surge) in the previous chapter. The only difference between the roll and pitch natural frequencies results from the wind turbine inertia. Because the difference is very small and the total inertia is anyway dominated by the spar inertia (which is equal in both DoF due to the symmetry of the spar), both natural frequencies are assumed to be identical.

Figure 138 and Figure 141 show that, as the spar draft was reduced, the natural periods in roll and pitch increased as the result of decreasing metacentric height, total mass and inertia. A decrease in the inertia should have resulted in a decrease in the natural period, but because the response is dominated by the change in the metacentric height, and hence stiffness, the opposite effect was achieved.

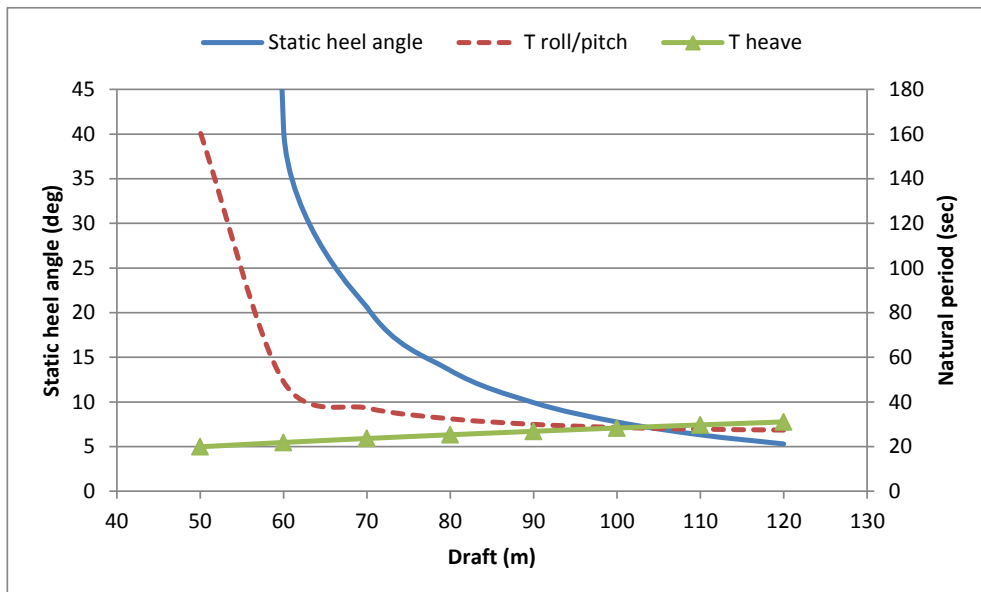


Figure 141 – Static heel angle and natural periods for varying draft

It should be noted that while the metacentric height, GM, is negative for drafts shorter than 70 m (Figure 140), heave, roll and pitch natural frequencies were still calculated and are displayed in Figure 141. This can be explained by looking at equations A.54 and A.55, where the stiffness for calculating the natural frequencies in heave, pitch and roll were provided

not only by the hydrostatic restoring but also by the stiffness of the mooring system. Nevertheless, these types of design are not stable and are shown here to highlight the importance of the mooring system.

#### 4.2.2.2. Ballast density

Eight different ballast densities were compared from 1,900 kg/m<sup>3</sup> to 2,950 kg/m<sup>3</sup>. Although the upper limit is somewhat excessive (see 4.1.2.6), the range was extended to such high numbers in order to fully explore the influence of increasing the ballast density on the OC3-Hywind system parameters, as shown in Figure 142.

Many parameters did not change at all with changes in the ballast density, such as the heave natural period, total displacement and mass of the system. Intuitively, increasing the ballast density should result in an increase in the mass of the system (increase in the ballast mass). However, as the buoyancy force is equal to the total weight of the system, any increase in the ballast density is counteracted by a decrease in the total ballast volume.

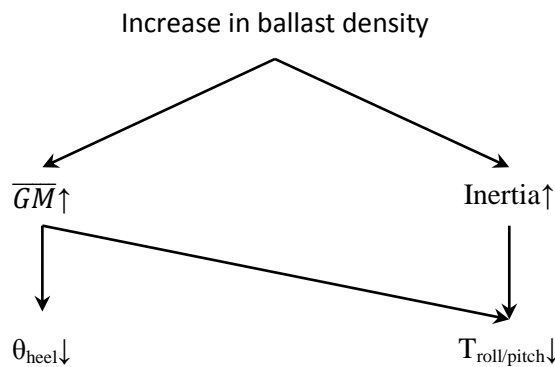


Figure 142 – Influence diagram of increasing ballast density

Two parameters that do change are the metacentric height and the inertia about the x- and y-axis. Whilst the change in the inertia is very small (just over 10% between the two density extremes), the change in the metacentric height is more pronounced (almost 40%), as compared to the OC3-Hywind and shown in Figure 143.

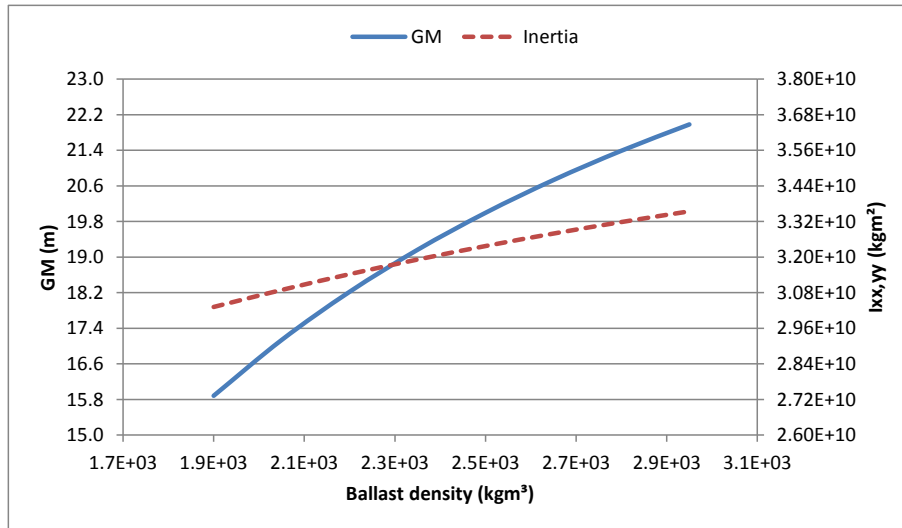


Figure 143 – Metacentric height and inertia variation with ballast density

Any increase in the metacentric height would have a positive effect on the static stability of the floater, as the static heel angle would decrease. On the other hand, such a significant increase in the metacentric height and the associated marginal increase in the inertia would result in the natural roll and pitch periods being lowered, hence bringing them closer to the predominant wave input periods (5 to 20 seconds). Both these trends are shown in the figure below.

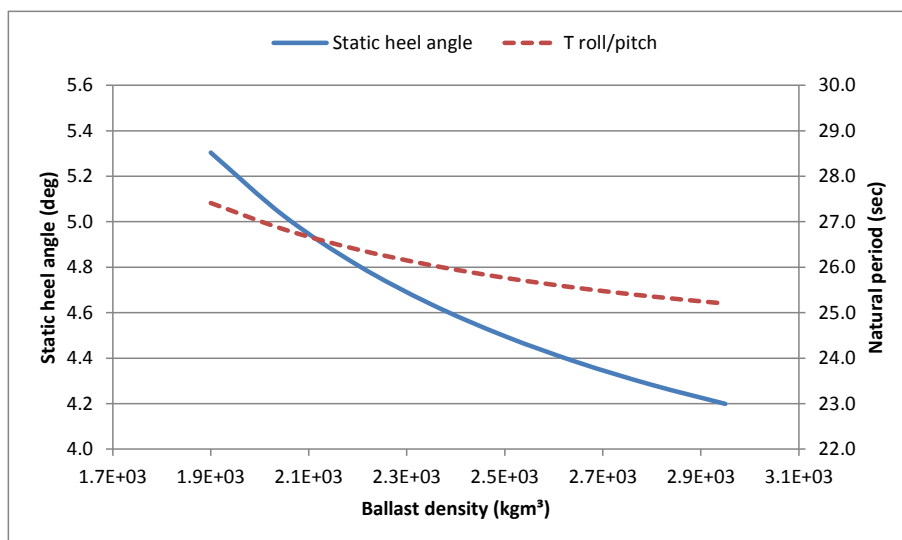


Figure 144 – Static heel angle and natural period variation with ballast density

#### 4.2.2.3. Steel thickness

In order to minimise costs, it would be desirable to minimise the mass of steel used as long as structural integrity is not compromised. The influence of steel thickness on the most important properties of the system was explored, over a range of steel thickness for the bottom cylinder 0.03 m to 0.065 m with a step size of 0.005 m.

Increasing the steel thickness increases the hull mass, which must then be compensated by an equal drop in the ballast mass. Both responses are linear, as shown in Figure 145.

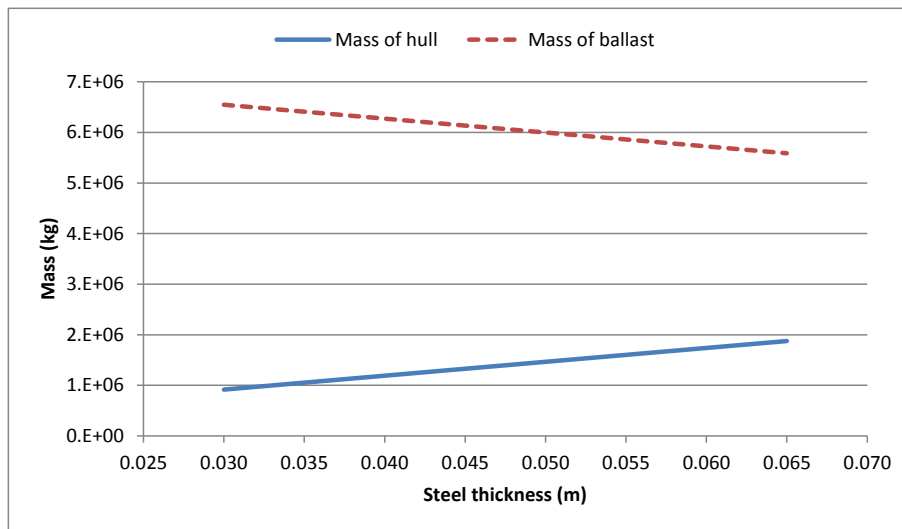


Figure 145 – Mass variation with varying steel thickness

Both the metacentric height and inertia about the x- and y-axis change very little with increasing steel thickness, as shown in Figure 146. There is around a 2% increase in the inertia and a 7% decrease in the metacentric height. There is a slight loss of static stability (leading to an increase in the static heel angle) and an improvement in the roll and pitch natural periods (shifting them farther away from the dominant wave periods). This is displayed in Figure 147. These changes result from change in the metacentric height being greater than the change in inertia.

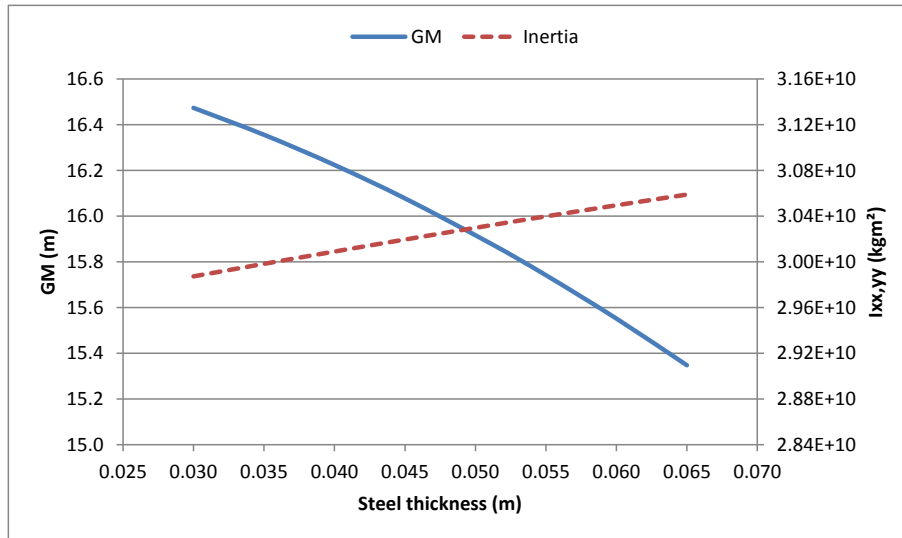


Figure 146 – Metacentric height and inertia variation with varying steel thickness

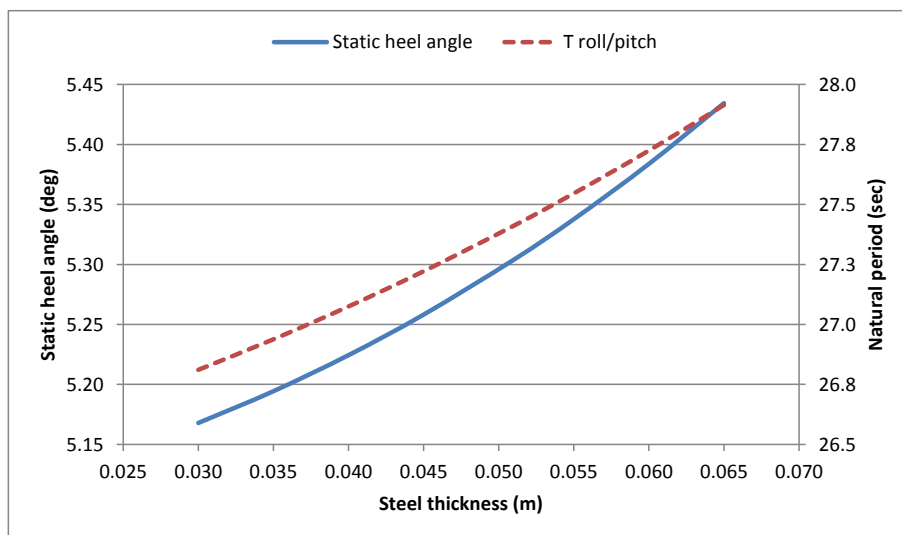


Figure 147 – Static heel angle and natural period variation with varying steel thickness

Due to the very small influence that the steel thickness has on any of the other properties, it was kept constant for all subsequent designs.

#### 4.2.2.4. Draft diameter

The spar diameter is the last variable to be explored that can be changed to modify the OC3-Hywind. Compared to changing the spar length, the opposite effect is achieved on all the spar parameters. Changing the spar length had a proportional effect on the mass; however changing the spar diameter has quadratic effect on the mass, as shown in Figure

148. As mentioned before, only the bottom cylinder's diameter was changed, while leaving the top cylinder the same.

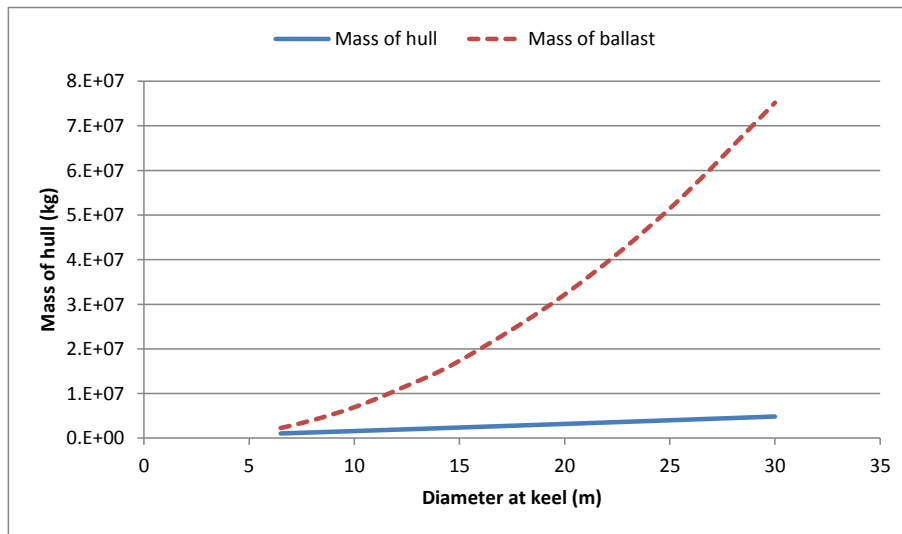


Figure 148 – Mass of hull change with increasing spar diameter

The effect of changing the spar diameter on the other OC3-Hywind properties is shown in Figure 149 below. Compared to Figure 138, Figure 149 shows that the increasing spar diameter has the opposite effect of spar length on the relevant system properties.

The heave natural period is dependent on the spar diameter through increases in both the system mass (hull and ballast) and the added mass (which is approximated as a half-sphere of water below the spar). As the mooring system and top cylinder were not changed (leading to no change in the restoring forces), the heave natural period would increase with increasing diameter (see Figure 151).

Increasing the spar's diameter increased its inertia through an increase in the mass and radius, and the metacentric height increased through a lowering of the overall CoG. Both these trends are clearly shown in Figure 150. Whilst the inertia kept increasing with diameter, the metacentric height levelled off above 20 m diameter.

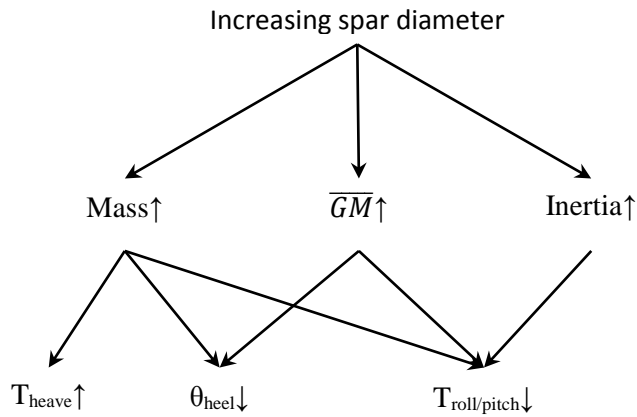


Figure 149 – Influence diagram of increasing spar diameter

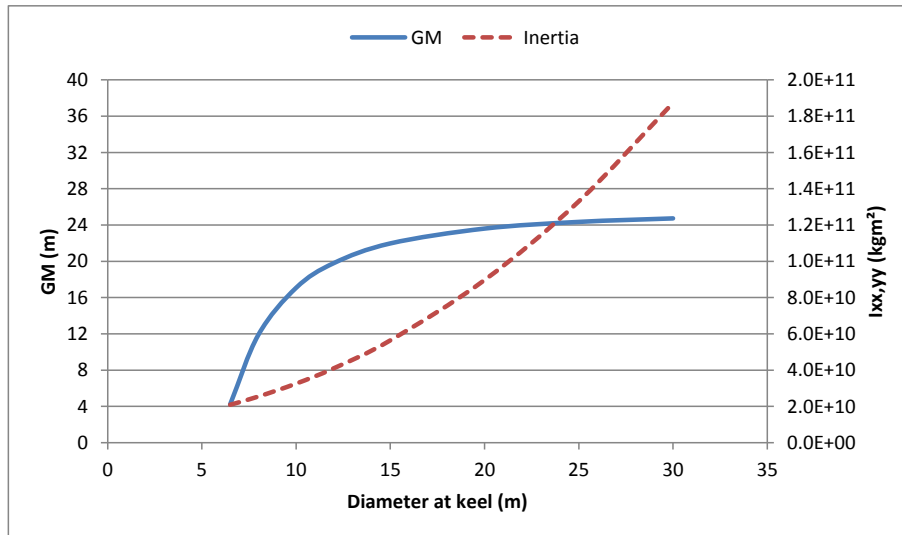


Figure 150 – Metacentric height and inertia variation for varying spar diameter

Increases in the metacentric height and in inertias about the x- and y-axes would result in a decrease in the static heel angle, and decreases in roll and pitch natural periods. While the former would result in increased static stability of the system, decreasing the natural periods of roll and pitch could bring these too close to the predominant wave excitation frequencies (0.05-0.2 Hz), resulting in potentially large, damaging response amplitudes.

As the static heel angle, and roll and pitch natural frequency are highly dependent on the metacentric height, both experience a marked levelling off of their variation with diameter above 20 m, just as with the metacentric height in Figure 150.

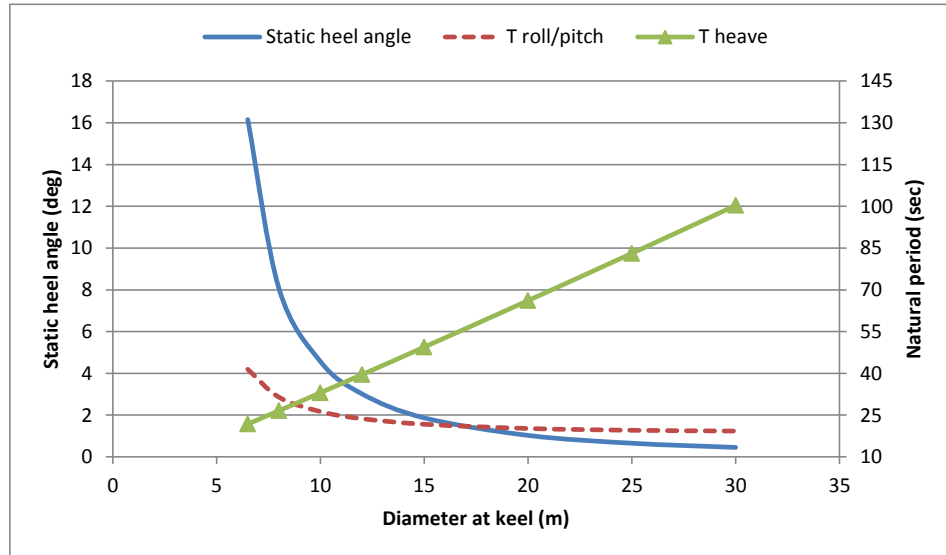


Figure 151 – Static heel angle and natural period variations for varying spar diameter

Compared to the results for the uniform spar, the OC3-Hywind natural periods display somewhat different dependencies on modifications in the spar diameter and length. For example, the heave natural period decreases with shortening of the draft, while the opposite is true for the roll and pitch natural period.

#### 4.2.3. Design limits

Multiple design limits exist when talking about floating offshore wind turbines. Some of these are structural, others cost related. The main ones identified by the author are:

- Static stability
- Maximum ballast density
- Steel thickness
- Static heel angle
- Spar diameter
- Others

Static stability in spar-type floating offshore wind turbines can be measured by the metacentric height. The greater the metacentric height, the more stable the system. An

intrinsic requirement of an OC3-Hywind type system is to have the total CoG located below the CoB. In addition, because floating wind turbines may be located in very harsh environments (strong winds and large waves), it is important not just to have  $\overline{GM} > 0$ , but for it to be sufficiently large to produce large enough restoring moments during extreme events throughout the system's life.

One of the easiest ways to lower the overall CoG and improve the static stability is to use high-density ballast. However, multiple constraints of the maximum ballast density, with different reasoning for each, exist. Quite often the denser the material, the more expensive, scarce or safe it is to use. For example, tungsten has a specific gravity of 19.5; however it is very expensive, making it infeasible for using as the ballast. Similarly, lead has density of around 13,350 kg/m<sup>3</sup>; however it is also expensive (approx. \$1,800 per metric ton). The materials that were considered for use as the ballast were olivine (due to previous use in Hywind), haematite and magnetite. Like any other mineral, in the form of nodules, there are limits to packing density, hence lowering the overall ballast density. Last, but not least, one needs to make sure that the ballast can be pumped into the hull, as there might exist some physical limits to maximum pumping viscosity.

Steel is an expensive material and one would want to use as little of it as possible in the design of floating offshore wind turbines. Using thinner steel sheets would save on the material costs, and maybe even lower the CoG of the system; however, it could also compromise the structural integrity of the system. There would also seem to be an upper limit on steel thickness, above which welding costs increase dramatically, as the standard approach for welding cannot be used anymore.

Similarly, there must be some spar diameter size above which the welding costs are just too high to make FOWTs feasible. This is due to large welding costs associated with stiffeners that have to be welded around the circumference of the spar.

Heel angle is another limit that is present due to the specific design of the current wind turbines. Because the offshore industry effectively uses wind turbines largely based on onshore designs that have been 'marinised' for use offshore, there is a maximum heel angle above which parts of the drivetrain are not lubricated sufficiently. From conversation with the industry and [112], the current wind turbine designs are limited to a maximum 6

degrees of heel angle. For the same reason, until redesigned, floating spar-type WTs could not be towed out using cradle vessels.

Other limits include mooring systems, installation and decommissioning, O&M, etc. None of these have been considered as they are beyond the scope of the thesis.

#### *4.2.4. Trade-offs*

Many trade-offs exist in designing a 'perfect' system. In floating spar-type offshore wind turbines, the following trade-offs were identified and look at:

- Spar diameter vs. spar length
- Spar diameter vs. ballast density
- Static heel angle vs. roll/pitch natural period

Another trade-off is between steel thickness and structural integrity but since structural analysis is beyond the scope of this thesis, it has not been considered. Similarly, mooring system design changes are also beyond the scope of the thesis.

While no specific values are attached to the steel thickness vs. structural integrity analysis, one would want any structure to use as little steel as possible to save on costs, but at the same time maintain strong structural soundness.

The trade-off between the ballast density and the spar diameter at the keel for the 80 m draft design is shown below. The Excel Solver function was used to solve for maximum roll and pitch natural period by changing the diameter at the keel and ballast density. Constraints were placed on the maximum static heel angle, as shown by the 6, 5.5 and 5-degree data series in Figure 152. Due to the inherent functioning of the Solver, the static heel angle would always tend to its maximum allowable value, while maintaining the minimum possible ballast density.

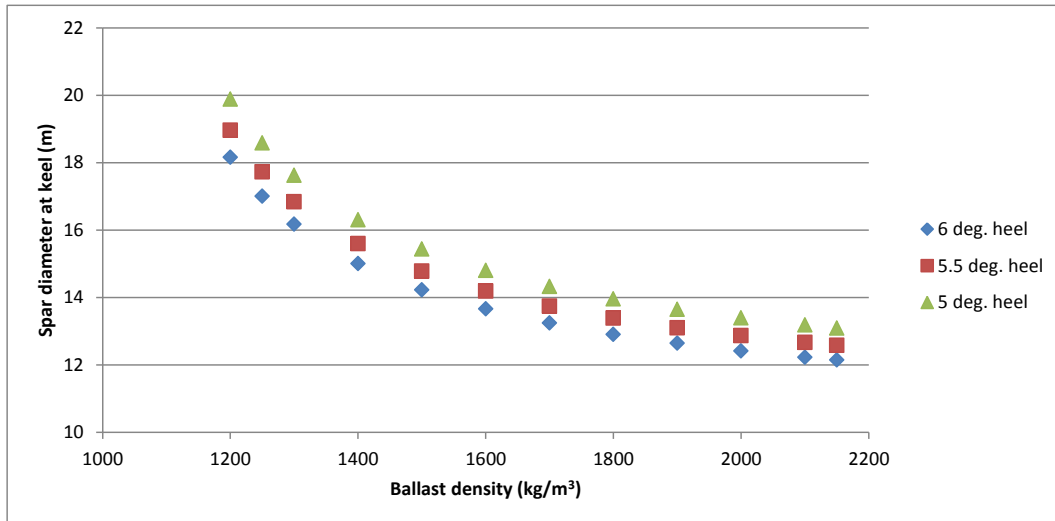


Figure 152 – Trade-off between ballast density and spar diameter for 80 m draft design

Figure 152 clearly shows variation in the gradient at different points along the x-axis. Levelling of the spar diameter at high ballast densities means that while one might find a material that can give higher ballast densities, the overall gain in the spar diameter would be very small. At the same time, quite often denser minerals are the more expensive ones, and any gain in steel savings would be opposed by ballast overheads.

As profit margins are much smaller in the wind energy industry than the oil and gas industry, an ‘ideal’ design should use as little steel as possible to save on cost. There is no reason why 2,000 kg/m<sup>3</sup> or higher densities of ballast of haematite slurry could not be used/achieved, so the best designs from Figure 152 are those in the bottom right corner. These designs, at very little cost of increasing haematite concentration in the slurry, would potentially produce significant savings in steel costs by reducing the diameter.

Another trade-off displayed in Figure 152 is between the spar diameter and static heel angle. For all ballast densities, having a smaller static heel angle would mean having a larger spar diameter. However, the difference in spar diameter for different static heel angles decreases with increasing ballast densities. In a similar manner to the ballast density and spar diameter trade-off, it makes more sense to use higher ballast densities to achieve smaller static heel angles.

Figure 153 shows the trade-off between the ballast density and roll and pitch natural periods for the same spar diameters as in Figure 152. Compared to Figure 152, where small

spar diameter values were favourable, in this case larger natural periods are preferred in order to shift these away from the most likely wave input periods (5-20 s). In a similar manner to Figure 152, the results level off at greater ballast densities. Comparing both figures, there are no significant gains or losses from going to even greater ballast densities, except for a slight increase in static stability (increase in the metacentric height) and an increase in the ballast material costs. At very high ballast densities this becomes a trade-off between increased ballast costs and static stability.

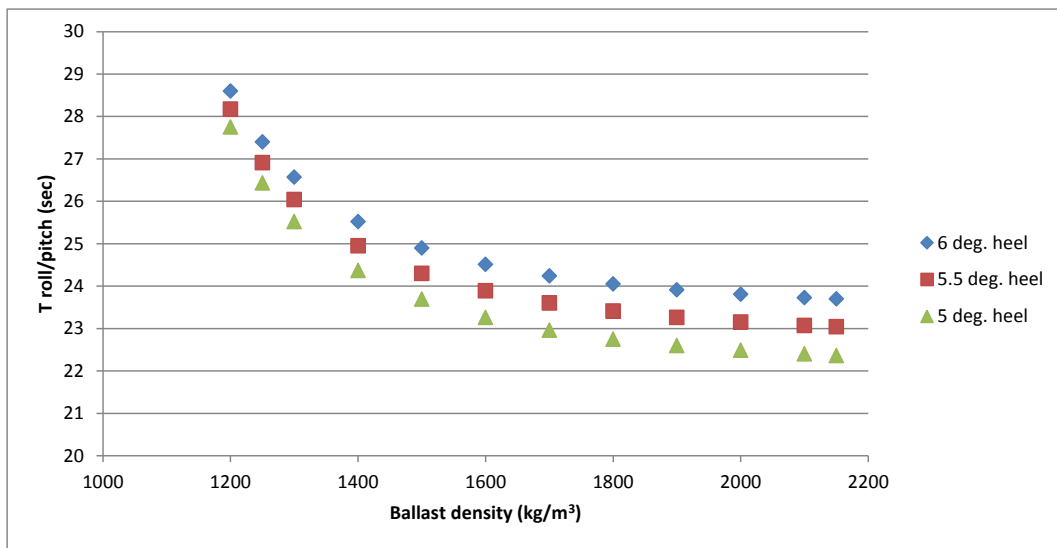


Figure 153 – Trade-off between ballast density and natural period in roll and pitch DsoF for 80 m draft design

Alternatively, this can be analysed using Figure 154. For the same conditions as before, any decrease in the static heel angle will be met with a decrease in the natural period of roll and pitch. This is consistent with Figure 142. Identically, any decrease in the spar diameter for the same static heel value will result in a decrease in the natural period. At this point, one should ask how much should be sacrificed in the roll and pitch natural periods to improve the static stability (static heel angle) and to reduce material costs through a decrease in spar diameter?

As current wind turbines are not designed to tolerate heel angles greater than 6 degrees (see [112]), the static heel angle is something that cannot be compromised on, at least until new wind turbine drivetrain designs are developed. This means that some compromise will have to be made between the static stability and the natural period of roll and pitch DsoF, by bringing them closer to the most likely wave input periods. However, while no solution is

currently available for large heel angles, roll and pitch excitation can be mitigated by providing more damping in these DsoF. One solution could be using fins and damping plates, which will increase the added mass of the system and also provide extra damping (see 4.7).

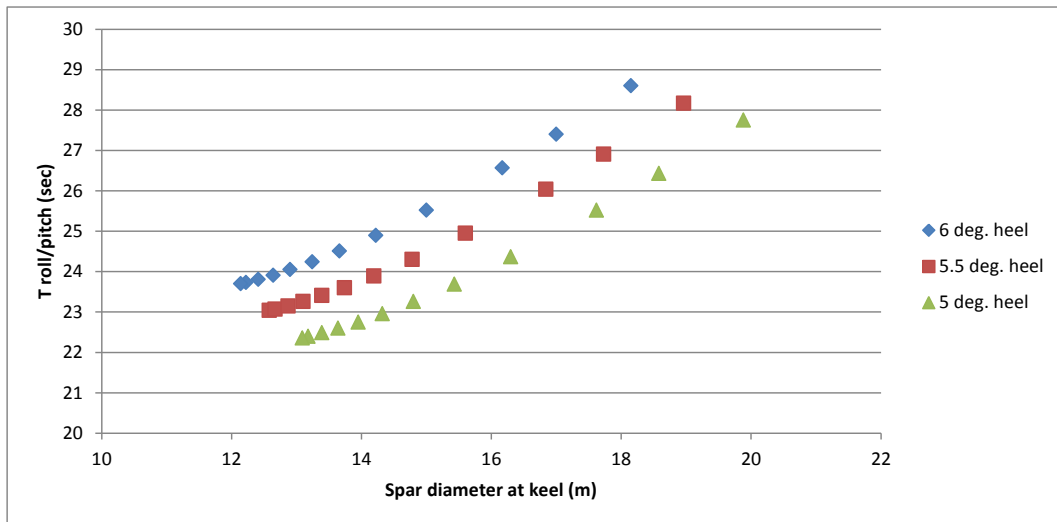


Figure 154 – Trade-off between spar diameter and natural period in roll and pitch DoF for 80 m draft design

Similar results were obtained for the 70, 60 and 50 m draft designs, which are shown in Figure 155 - Figure 160. Identical trends are present across all draft designs. However, the ranges in diameter and its maximum and minimum allowable values all increase with a decrease in the draft. For 80 m draft, the spar diameter at the keel was 12.1 - 19.9 m, while for 50 m draft it was 19.2 - 33.5 m. On the other hand, the roll and pitch natural periods decrease (both max and min values) with decreasing spar length. However, the range in periods increase with a decrease in the draft, yet by a much smaller percentage compared to its dependence on spar diameter values.

For the different static heel angles considered in this study, the  $T_{roll/pitch}$  values are much more concentrated at low ballast densities and dispersed for large. The opposite is true for the ballast density versus the spar diameter results. This is clearly shown in Figure 152 – Figure 160 (except for Figure 154).

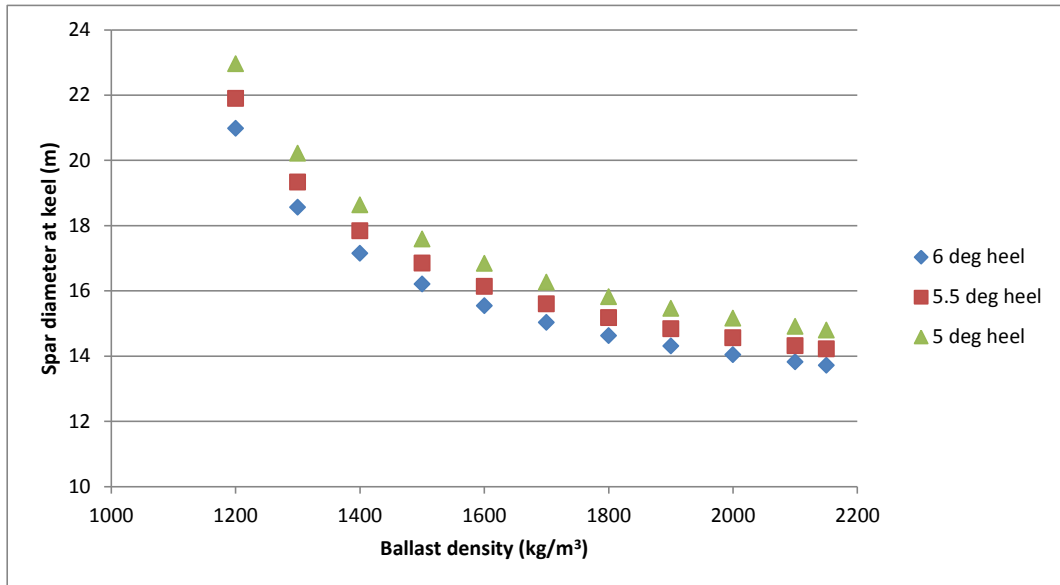


Figure 155 – Trade-off between ballast density and spar diameter for 70 m draft design

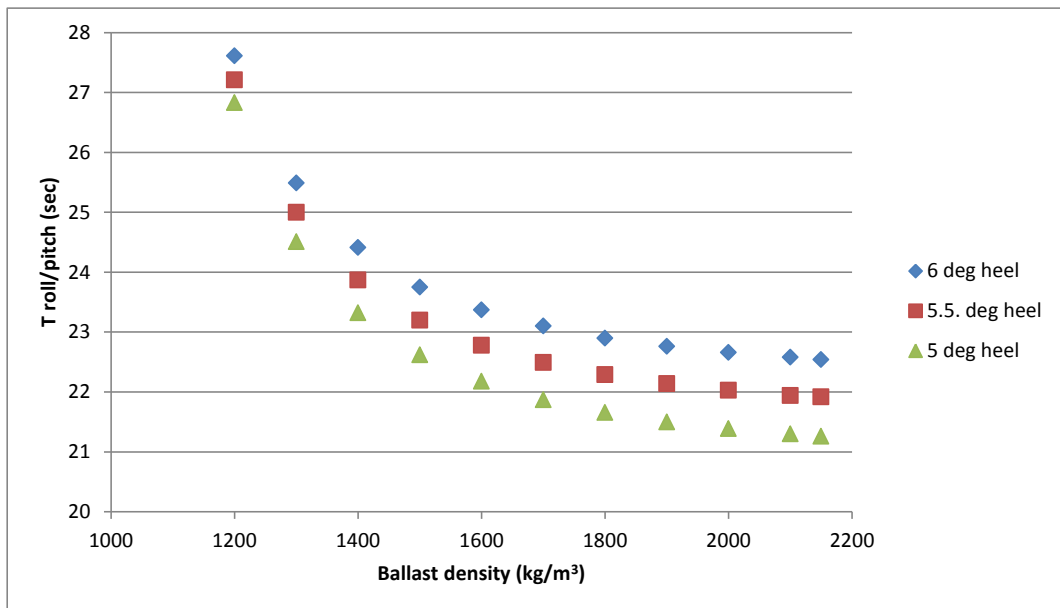


Figure 156 – Trade-off between ballast density and roll and pitch natural period for 70 m draft design

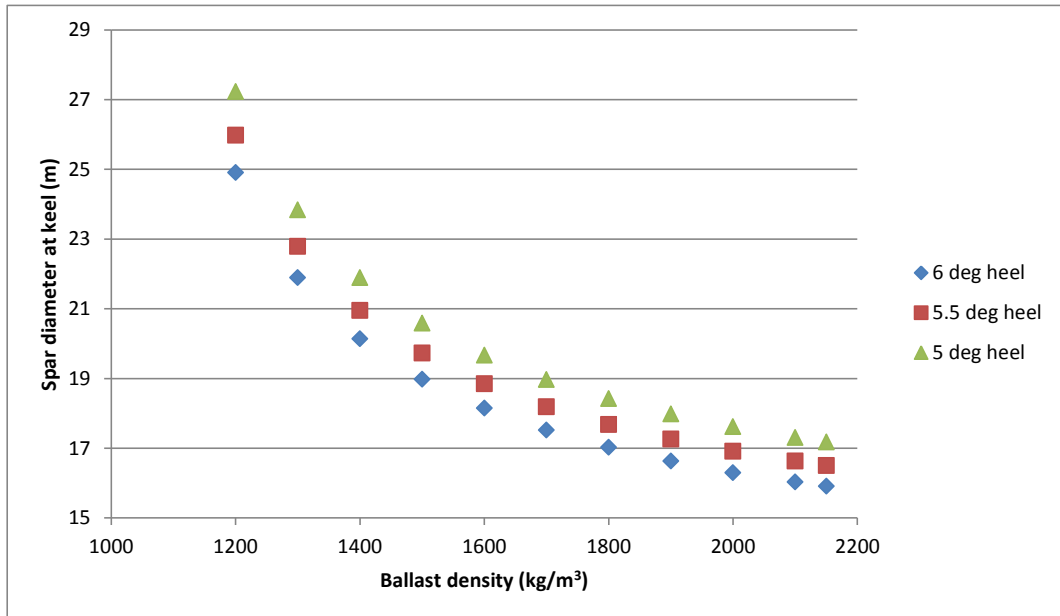


Figure 157 – Trade-off between ballast density and spar diameter for 60 m draft design

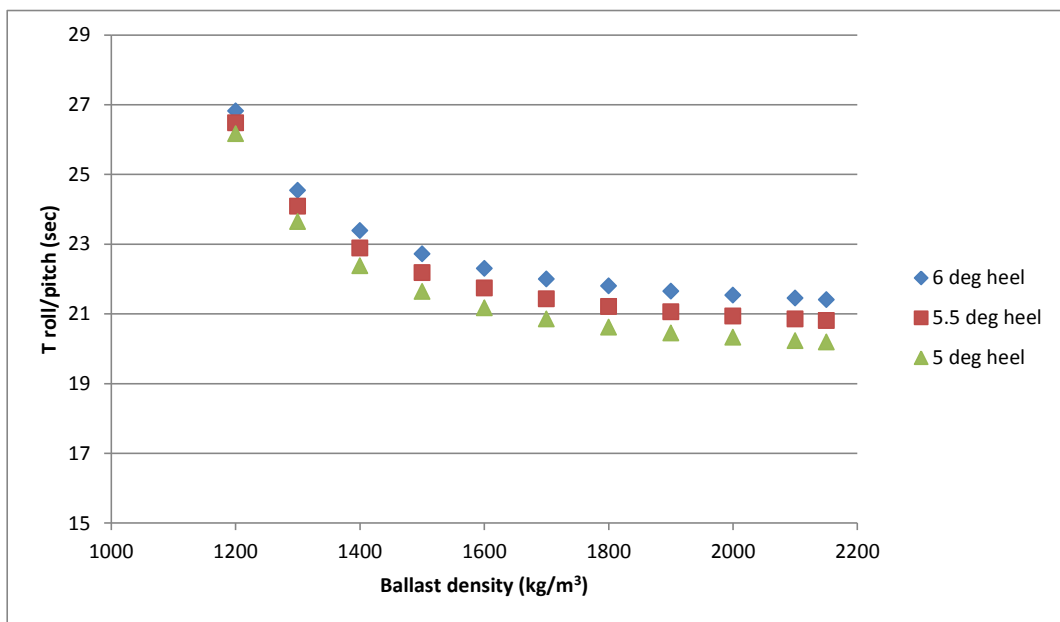


Figure 158 – Trade-off between ballast density, and roll and pitch natural period for 60 m draft design

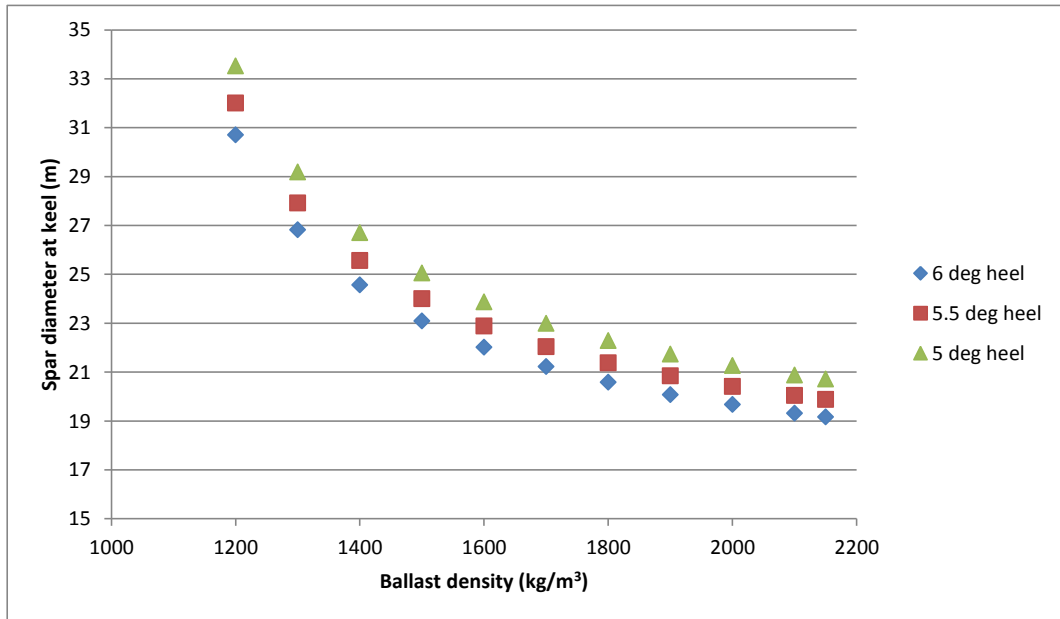


Figure 159 – Trade-off between ballast density and spar diameter for 50 m draft design

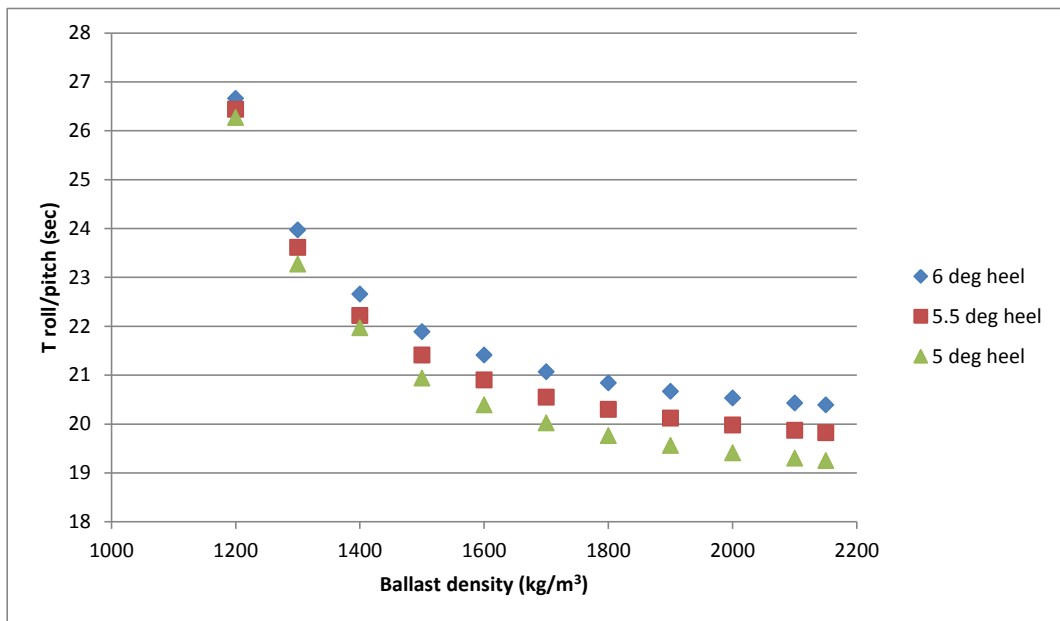


Figure 160 – Trade-off between ballast density, and roll and pitch natural period for 50 m draft design

### 4.3. Spar for medium-deep waters

The current OC3-Hywind design, due to its very long spar (120 m draft), is only applicable to water depths of 130+ m. This leaves a significant gap between the conventional fixed-bottom foundations, such as monopile, jacket, tripod, etc., that are economical up to 50 m [2], and floating wind turbines that employ a spar-type floater. The OC3-Hywind's spar was shortened and four alternative hypothetical designs were considered with 50, 60, 70 and 80 m long draft (Table 26). It should be noted that none of these design is probably the best possible choice for each specific draft, as even such big constraints as cost and structural integrity were not considered in detail. This is merely an exercise to show and prove that it is possible to have a shortened spar with acceptable and achievable characteristics for medium depth waters.

Table 26 – Three alternative designs of the OC3-Hywind with a shortened spar obtain using Excel Solver

	Draft (m)			
	80	70	60	50
<b>Ballast density (kg/m<sup>3</sup>)</b>	2,150	2,150	2,150	2,150
<b>Static heel angle (deg.)</b>	5	5	5	5
<b>Water displaced (m<sup>3</sup>)</b>	9,910.6	10,863.0	12,200.0	14,200.0
<b>Mass of hull (t)</b>	1,361.8	1,339.3	1,324.8	1,327.1
<b>Mass of ballast (t)</b>	8,029.6	9,028.0	10,412.5	12,458.4
<b>CoG from SWL(m)</b>	-54.57	-48.22	-41.85	-35.46
<b>GM (m)</b>	11.47	9.88	8.28	6.66
<b>Diameter at the keel (m)</b>	13.09	14.80	17.18	20.71
<b>I<sub>xx,yy</sub> (kgm<sup>2</sup>)</b>	18,423.7E+06	15,918.4E+06	13,696.8E+06	11,847.5E+06
<b>T<sub>surge/sway</sub> (s)</b>	140	146	155	167
<b>T<sub>heave</sub> (s)</b>	35	37	40	44
<b>T<sub>roll/pitch</sub> (s)</b>	22.4	21.3	20.2	19.3
<b>T<sub>yaw</sub> (s)</b>	9.7	11.3	13.5	17.3

Table 26 was produced by modifying the OC3-Hywind design in Excel using the Solver function to obtain as large as possible natural periods in roll and pitch, whilst limiting the maximum ballast density and heel angle. Multiple simplifications and assumptions were made for these crude, initial designs:

- Ballast is assumed to be denser than the one used in the Hywind design (2,150 vs. approximately 1,900 kg/m<sup>3</sup>)
- While normal steel density is between 7,750 and 8,050 kg/m<sup>3</sup>, a value of 8,500 kg/m<sup>3</sup> was used to account for paint, bolts, etc.
- The mooring system was not modified.
- Two averaged steel thicknesses were used, which represented hull and stiffeners.
- The top cylinder's dimensions and the conical section's length (section 2 and 3 in Figure 135) were not changed.
- Simplified centre of buoyancy calculations.
- Simplified metacentric height calculations (as shown in 4.1.2.8).

A comparison between the OC3-Hywind and the proposed shortened spar designs is shown in Figure 161.

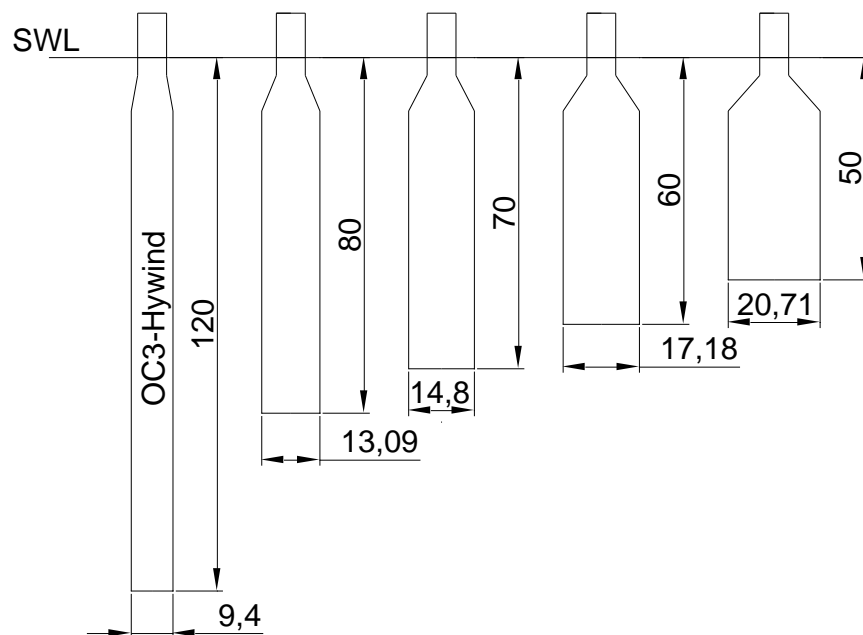


Figure 161 – OC3-Hywind and shortened spar platform dimensions

Comparing the different draft designs, the mass of the hull does not change significantly, as shown in Figure 162. This is partly a consequence of keeping the steel thickness the same across all designs and partially because any decrease in the hull mass due to a decrease in draft is compensated by an increase in the hull mass due to an increase in the spar diameter. The overall trend is a slight decrease in the hull mass as far as 58 m draft, at which point there will be a slight increase in the hull mass, as it is a function of multiple variables. The mass of the ballast increases significantly with decreasing spar draft and increasing spar diameter at the keel, which is shown in Figure 163. This is to maintain static stability, which is highly dependent on the metacentric height.

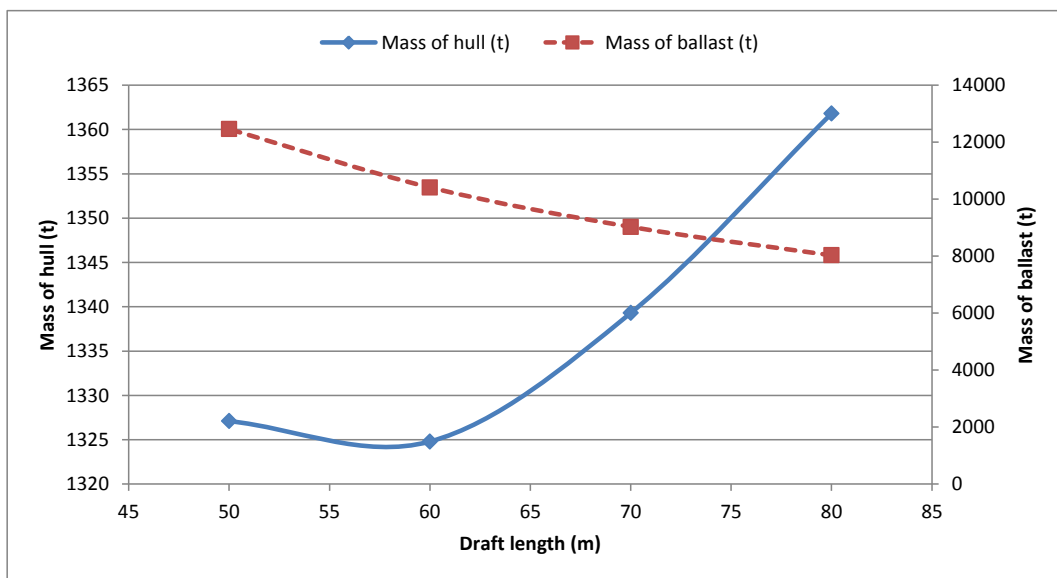


Figure 162 – Mass of hull and ballast change with draft

The centre of gravity in Figure 163 is taken as an absolute value measured from the SWL. The diameter at the keel has to increase to maintain the required response of the shortened system, as it is an important trade-off with spar length (see 4.2.4). The metacentric height decreases with shortening of the spar, as the distance between the centre of mass and buoyancy decreases.

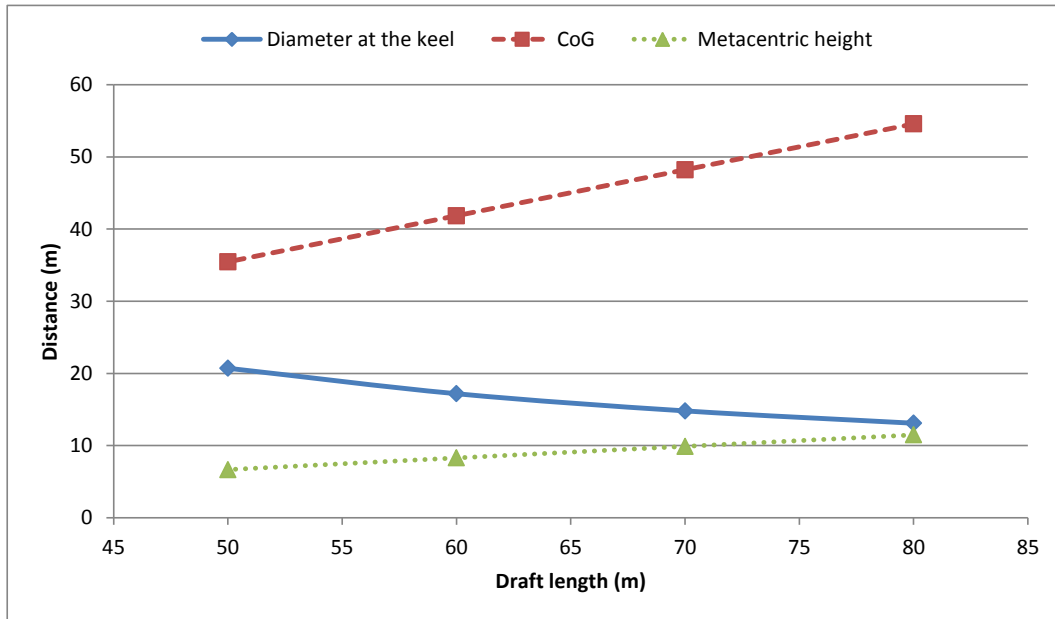


Figure 163 – Diameter at the keel, CoG and metacentric height variation with draft

### 4.3.1. Natural frequencies

#### 4.3.1.1. Surge and sway

The OC3-Hywind surge and sway natural period is 125 s. For the designs presented in this thesis the natural period varied from 140 s at 80 m draft to 167 s at 50 m draft. As the mooring system was not changed, the difference in the natural period with draft was purely due to the change in the total mass of the system (solid and liquid). The natural frequency in surge and sway of the modified systems was well separated from the most likely wave frequencies and, whilst resonance is not expected, damping in the surge and sway DsoF should be considered very carefully, as these DsoF are highly coupled to the pitch and roll DsoF. In particular, this applies to surge and pitch, which both were identified as the most detrimental DsoF in the previous chapter.

The response of the system could also be modified to meet any requirements by adjusting the mooring system properties.

#### 4.3.1.2. Heave

The added mass in the heave DoF can be approximated as a half-sphere of water at the bottom of the spar (equation 4.9). It is a function of the hull diameter at the keel and

density of the water. Because floating offshore wind turbines will be installed, predominantly, in seawater (the only potential exception being the Great Lakes in the U.S. and Canada), density is almost constant, and hence the added mass can be thought of purely as being a function of the hull diameter at the keel.

$$\text{added mass (AM)} = \frac{\frac{4}{3}\pi r_{keel}^3 \times \rho_{water}}{2} \quad 4.9$$

where  $r_{keel}$  is the radius of the hull at the keel in metres and  $\rho_{water}$  is the water density in kg/m<sup>3</sup>.

Using the same assumption of water density being constant, the restoring force in heave per 1 m of displacement becomes a function of the spar diameter at the SWL.

$$\text{Restoring (extra buoyancy)} = \pi r_{SWL}^2 \times \rho_{water} \times g \quad 4.10$$

The other variable, which can influence the natural frequency in heave, is the total mass of the system, which is much higher for shortened spar designs due to significant increases in the ballast mass. Whilst the results in Figure 164 show some variation in the heave natural period, neither of the shortened spar designs place the heave natural frequency anywhere close to the most likely wave input forcing periods of 5 to 20 s. Hence, shortening the OC3-Hywind spar should not bring about any resonance in heave. The only thing that designers need to consider are the second-order effects, such as the difference-frequency excitation, and the Mathieu instability (see 4.4), which could be a particular worry for the 50 and 60 m designs as the heave natural period is almost twice the roll and pitch natural period. These calculations do not include any contributions from the mooring system, as it is very small in these modes.

#### 4.3.1.3. Roll and Pitch

The natural frequencies in roll and pitch are almost identical for spar-type floating offshore wind turbines. The difference is very small and comes from the different geometry at the rotor and nacelle. The rest of the structure (tower and spar) is symmetrical in both x- and y-axis.

Compared to the original OC3-Hywind design, only the gravitational acceleration and mooring system are the same in calculating the natural frequency of roll and pitch DsoF (equation A.44). The mass of the system for all designs in Table 26 is higher than for the original OC3-Hywind. This would result in some increase in the natural frequency and decrease in natural period in roll and pitch DsoF. This could potentially be very damaging to the system, as it could shift the natural frequency in roll and pitch from 29 s for the OC3-Hywind closer to the most common wave periods.

For all designs without exception, the distance between the centre of mass and the centre of buoyancy has been shortened, as would be expected from a shorter spar, as the whole point of long spars is to lower the CoG. In the proposed designs, the metacentric height varies between 7.5 and 12.5 m. In some cases, it is less than half of the original metacentric height for the OC3-Hywind (15.9 m). This could lead to a significant increase in the natural frequency in pitch and roll DsoF. Just as for the other DsoF, the mooring system was not modified and assumed to hold the same properties as for the original OC3-Hywind design.

As the pitch DoF along with surge was identified as the most detrimental DoF in terms of fatigue for the wind turbine, it is important to consider using fins and helical strakes to improve damping and reduce vortex induced motion due to underwater currents. These add-ons are discussed in 4.7. Last but not least, the phenomenon of Mathieu instability needs to be taken into account when designing spar and choosing where to place the pitch natural frequency, as it was shown to be a potential issue in 4.3.1.2.

#### *4.3.1.4. Yaw*

Because the mooring system was not changed, changes in the natural frequency in the yaw DoF were analysed by looking at how the total inertia about the z-axis changed with shortening of the spar. As the same wind turbine was used in the OC3-Hywind and modified draft designs of Table 26, there was no change in the inertia of the WT about the centreline. However, because the overall design and properties of the spar had been changed, the inertia of the spar had also changed.

The natural period in the yaw DoF of the OC3-Hywind is 8.26 s, which is in the middle of most likely wave input periods. At the same time, it is very hard to excite the system in the

yaw degree-of-freedom, as the spar is completely symmetrical. The most likely cause of excitation would come from gyroscopic coupling with the pitch DoF. While there is very little hydrodynamic damping in the yaw DoF, because it is coupled to pitch and pitch is highly damped due to aerodynamic damping, excitation in the yaw DoF should not be too detrimental to the system. Furthermore, the natural period in yaw can be adjusted by modifying the mooring system and the delta (crow-foot) connection of the mooring system to the spar. This is the main source of stiffness in yaw. This could allow the yaw natural frequency to be shifted outside the predominant wave input frequencies, if required.

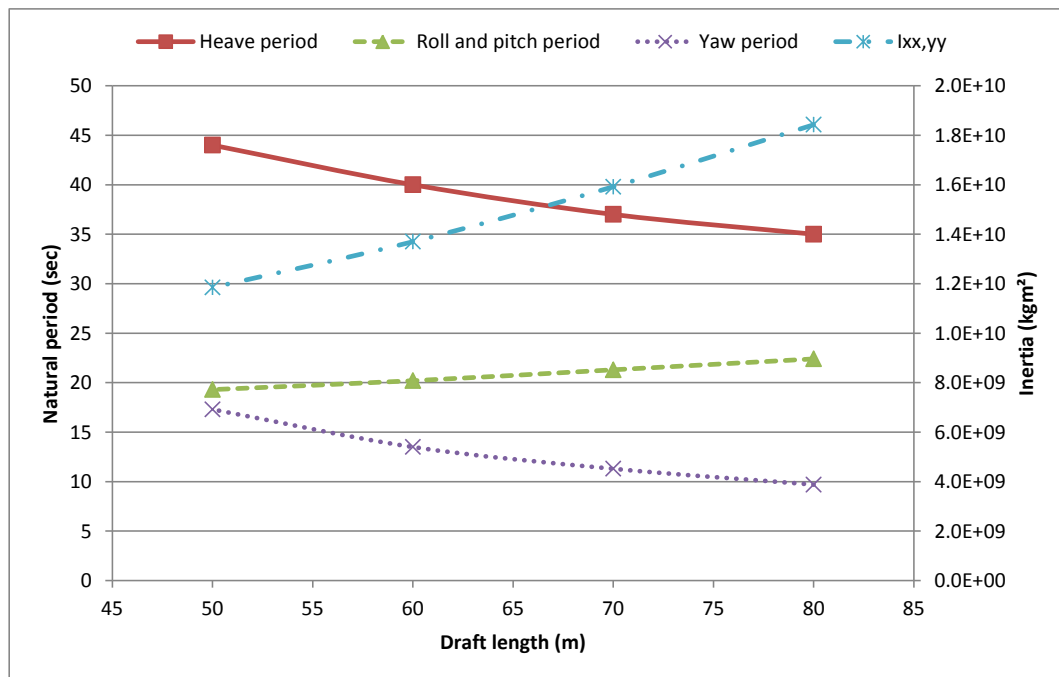


Figure 164 – Natural periods and roll/pitch inertia variation with draft

From the results discussed and presented, the author does not see any reason why shortened spar-type offshore floating wind turbines could not be feasible in the future. However, a very important aspect, such as the cost of the system, has largely been ignored in this thesis.

The conclusion is consistent with the proposed FOWTs by Statoil to be installed in Scotland [49], which will have a draft of 70-85 m.

## 4.4. Mathieu instability

When designing any floating system, one should be careful not to design it in such a way that heave and pitch natural frequencies form a ratio of 0.5, 1, 1.5, 2, etc. On spar-type structures the phenomenon of significant heave and pitch coupling is known as the Mathieu instability [116]. If the heave natural period is half of the pitch natural period (or any other multiple or sub-multiple), any motion in the heave DoF will couple into the pitch DoF and can lead to large oscillating loads on the wind turbine components. Haslum and Faltinsen [117] showed that the largest Mathieu instability occurs when the ratio of pitch over heave natural frequency is 0.5 and 1, and that with increasing ratio the possibility of instability reduces.

This needs to be taken into account when shortening the spar of the OC3-Hywind, as both heave and pitch natural periods will undergo some changes compared to the original OC3-Hywind values. This is particularly relevant for the 50 and 60 m draft designs discussed above.

## 4.5. Spar modification

The main objective in design of a floating offshore wind turbine is to avoid resonance of the system with any probable periodic excitation force, such as aerodynamic 1P and 3P frequencies and hydrodynamic wave excitations between 0.04 Hz and 1 Hz (with the majority of excitation in the 0.05 – 0.2 Hz range).

Two different strategies can be used to alleviate loads in DsoF subject to excessive forcing. These are:

- Shift the natural frequency by modifying the mass and/or the stiffness.
- Reduce the forced response by increasing damping.

Increasing damping of the system will lead to a lower peak in the system's response (as shown in an idealised manner by the red arrow in Figure 165 and in Figure 166). By decreasing the area under the curve, loads on the system are also reduced. On the other

hand, modifying the mass and/or stiffness of the system (shown by the black arrows) can allow natural frequencies of the system to be shifted to make sure that these are not placed at the predominant wave input frequencies, hence reducing the forced response of the system.

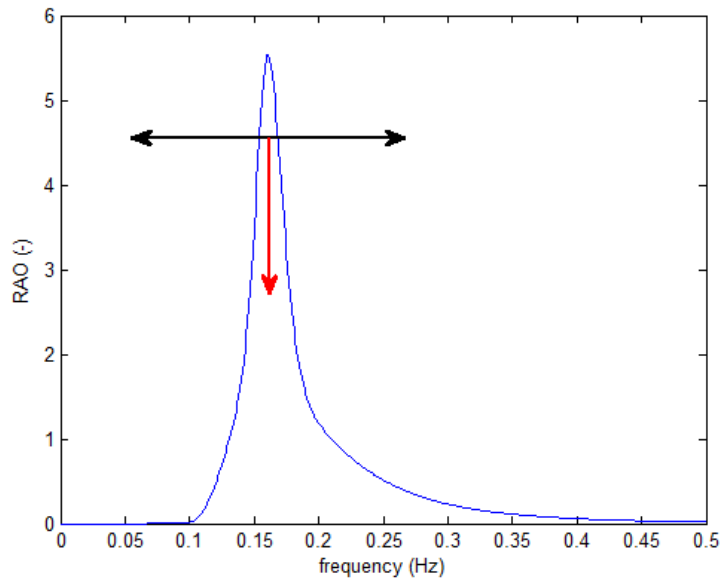


Figure 165 – Strategies for reducing response of a system

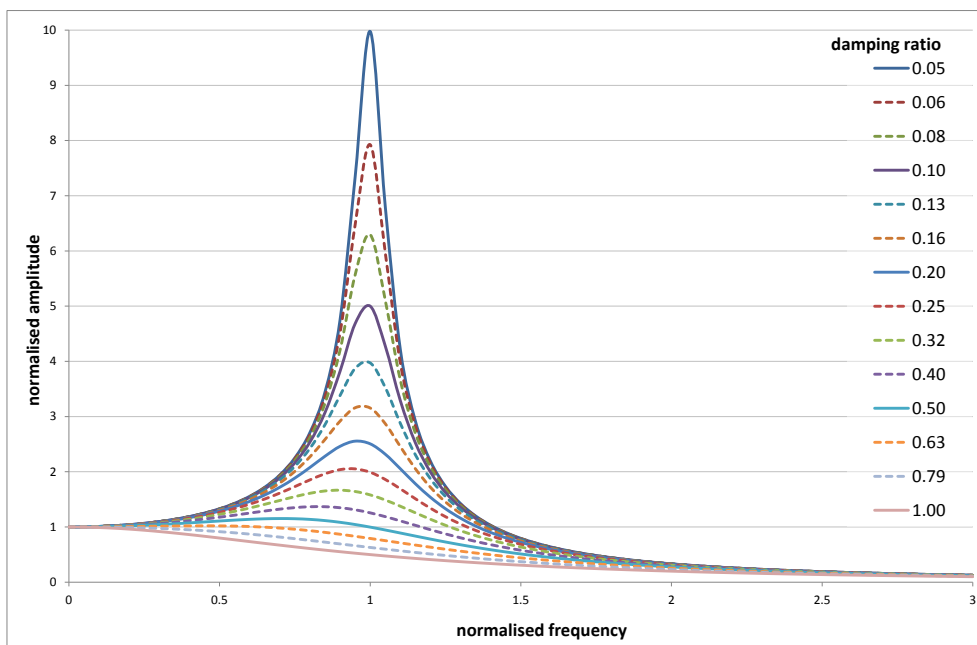


Figure 166 – Damped vibration of a system

## 4.6. Second-order hydrodynamics

In the previous chapter, under ‘disadvantages of FAST hydrodynamics modelling’ (3.1.3.2), it was explained that, essentially, FAST uses linear hydrodynamics with a slight modification using the Morison’s equation to account for those cases when the flow is to be assumed separated. However, no information was given on how significant these second-order hydrodynamics effects, such as mean- and slow-drift forces, and sum- and difference-frequencies forces are.

A report by Roald et al. [118] gives a very good comparison between the first- and second-order hydrodynamics and the relative importance of the second-order hydrodynamics compared to the aerodynamics of floating offshore wind turbines, in particular the OC3-Hywind. The main results from [118] are summarised next.

A tweaked methodology of the one used in the oil and gas industry, together with FAST and WAMIT, was used to calculate the first- and second-order hydrodynamics. Of particular interest were the sum- and difference-frequencies of the incident waves, as these can coincide with eigenfrequencies of the structure. Using WAMIT resulted in some simplifications to the model: ignored structure flexibility (structures outside of the water in WAMIT are assumed to be rigid) and absence of viscous effects (these would most likely damp out some of the 2<sup>nd</sup> order motion response).

A comparison of the 1<sup>st</sup> and 2<sup>nd</sup> order hydrodynamic forces for the OC3-Hywind in a specific sea state (Pierson-Moscowitz wave spectrum with  $H_s = 3.66$  m and  $T_p = 9.7$  s) showed that the second-order hydrodynamic forces are very small compared to the first-order hydrodynamic forces, and the only DoF, where the 2<sup>nd</sup> order difference-frequency response was of any significance, was heave.

For all the operational wind speeds of the OC3-Hywind (3-25 m/s), the mean-drift hydrodynamic force was shown to be less than 1% of the rotor thrust. In the example given above, in cut-out conditions this increased to 10-15%. These calculations completely ignored the wind drag on the tower, yet were still shown to be small enough to allow the mean-drift force to be ignored.

A comparison of the OC3-Hywind motion response due to excitation from the second-order hydrodynamic and aerodynamic forces showed that the aerodynamic forces dominate the response of the OC3-Hywind in the low-frequency domain and are several orders-of-magnitude greater than the response due to the second-order hydrodynamic effects.

The second-order hydrodynamics forces were shown to be of significant size in the UMaine TLP [119] case. As only one specific sea-state was used in the comparison of the first and second order hydrodynamic forces in [118], it is important to consider the second-order hydrodynamic effects once any design changes have been applied to the original OC3-Hywind and/or the environmental conditions are known for the site of installation. This is further confirmed in Figure 167, where in a similar manner to Figure 94, and using periodic sea states from Table 9, the diameter to wavelength ratios for a 50 m draft spar design are shown. Flow separation will occur in 4 different sea states compared to only 2 for the OC3-Hywind (Figure 94), making modelling and accounting for the 2<sup>nd</sup> order hydrodynamic effects more essential for the shortened spar designs.

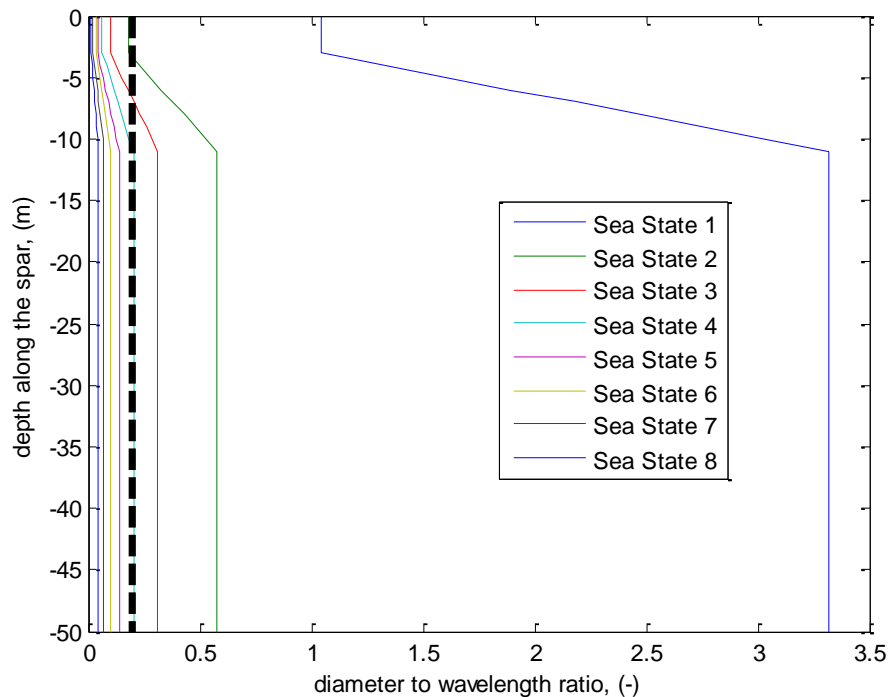


Figure 167 – Diameter to wavelength ratio for 50 m draft spar

## 4.7. Strakes and damping plates

In this thesis only the WT fatigue (blades and tower) has been considered. However, vortex induced vibration (VIV) and vortex induced motion (VIM) can be significant sources of fatigue on FOWT, both on the spar and the WT. VIV and VIM are caused by exciting forces produced by vortex shedding on the hull of a bluff body, such as a spar. The main difference between the two phenomena is the length of the period of motion, with VIV having small periods and VIM large periods. Also, VIM applies to rigid bodies and to bodies that can be treated as rigid as the flexure is small compared to whole-body motion, while VIV is applicable to flexible bodies where flexure is a greater part of the motion than whole-body motion.

In term of spar type floating offshore wind turbines, VIM is a much more likely cause of significant fatigue damage, as vortex shedding frequency can coincide with any of the 6 natural DsoF of the spar, leading to resonant response.

In places where there are strong currents, it is normal practise to install helical strakes on the spar to counter VIM and VIV.

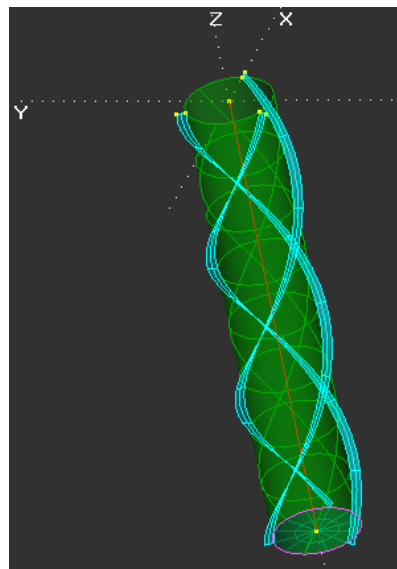


Figure 168 – Helical strakes on a spar

Damping plates can also be installed on a spar to increase added mass and damping in different DsoF (widely used for heave in the oil and gas spars). This could be particularly

beneficial in the pitch DoF, as while installing fins or cross plates would increase the mass of the system (both solid and added-mass) and hence lower the natural period of pitch, it would also provide extra damping in pitch and roll DoF.

## 4.8. Conclusion

In this chapter, different parameters that make up the spar of a spar-type FOWT were reviewed using an Excel spreadsheet. These parameters were analysed by performing simplified parametric studies on a uniform spar and on the OC3-Hywind by varying the spar diameter, spar length, ballast density and steel thickness. Through this process, the main design limits and trade-offs were identified. These were then taken into account when suggesting four hypothetical spar-type FOWT designs of 50 to 80 m draft that could be used in medium or medium-deep waters. Lastly, some thoughts for future work were suggested, such as the second-order hydrodynamics, Mathieu instability and modifications to the spar, in terms of strakes and damping plates, which might give spar superior performance.

An Excel spreadsheet was built based on the data from [46, 111] and Archimedes' principle to reverse engineer the OC3-Hywind. The same Excel spreadsheet was then used to identify which are the main design parameters that govern the response of a spar-type FOWT and, in particular, the pitch and surge  $D_{soF}$ , as they were identified as the most detrimental  $D_{soF}$  in the previous chapter. Controlled design dimensions included steel thickness, ballast, spar draft and diameter, and resulting properties that were determined by these dimensions included inertia, static heel angle, the natural spar periods and the metacentric height. Additionally, this included identifying any potential minerals, other than the olivine used in the Hywind, which could be used as ballast in the shortened-spar OC3-Hywind designs.

Five main variables were identified that can be used to modify the OC3-Hwyind system. These were the spar length, diameter, ballast density, steel thickness and the mooring system stiffness. All except for the mooring system were analysed using a simplified parametric study. The mooring system was not looked at as it was beyond the scope of this thesis.

Firstly, a uniform spar was analysed in terms of its diameter and length. Both increasing the spar diameter and decreasing the length of the spar showed almost identical trends in terms of increase or decrease in the natural frequencies. However, because the OC3-Hywind is not a uniform spar, in that the spar diameter is smaller at the SWL mainly in

order to lower the overall CoG and to make the spar less sensitive to wave excitation, a separate parametric study was performed on the reverse engineered OC3-Hywind data. Steel thickness was shown to have very little effect on the main design criteria (the static heel angle and pitch natural frequency). For this reason, it was decided to keep it at a fixed value in all subsequent shortened spar designs. The ballast density was shown to have a limited influence on the spar's properties. Only the static heel, and roll and pitch natural periods were shown to decrease with increase in the ballast density, which is very beneficial in terms of the static stability, but less so in terms of fatigue. This led to the identification of the static heel angle, and the roll and pitch natural periods as the main design trade-off for a shortened spar. A parametric study on the OC3-Hywind spar length and diameter showed some disagreement with the previous results obtained assuming a uniform spar. For example, the opposite effect of increasing the spar diameter was seen on the roll and pitch natural periods. Similarly, the heave natural period decreased with shortening of the OC3-Hywind spar. This led to the conclusion that while a uniform spar can give some useful insight into the problem, a much more realistic and complex representation of the OC3-Hywind in the Excel should be used for more accurate results.

While looking at the different parameters of the spar and performing a parametric study, the main design limits and trade-offs were identified. The design limits included the static stability (having CoG below CoB), the maximum achievable ballast density (packing density), the steel thickness (cost and welding), the static heel angle (lubrication of the drive-train), the spar diameter (excessive welding costs at large diameters) and others. At the same time 3 different trade-offs were analysed. These included the spar diameter against the spar length, the spar diameter against the ballast density and the static heel angle against the natural periods in roll and pitch. This final trade-off is the main design driver, as no compromises can be made on the static heel angle for the currently WT designs. Other trade-offs involving cost, structural integrity and mooring system were not analysed as they were beyond the scope of this study.

Using the trade-off analysis and the data obtained using the Solver function in Excel, four different hypothetical shortened spar designs of 50 to 80 m were proposed. All four designs involved using the smallest possible static heel angle analysed, 5 degrees, and the densest ballast,  $2,150 \text{ kgm}^{-3}$ . All four shortened spar designs (Table 26) were deemed feasible.

However, no cost analyses were performed. The natural frequencies of the proposed spar designs showed very good results in the surge and sway, and heave modes, with all being sufficiently far away from the main wave input frequencies. The yaw mode was assumed to be of a relatively minor importance as the spar is rotationally symmetrical, making it very hard to excite the system in the yaw DoF. It was predicted that the main yaw excitation would come from the gyroscopic coupling between the pitch and yaw DoF. However, as the pitch DoF is heavily damped, this should result in very little fatigue damage arising from motion in the yaw mode. The pitch and roll natural periods were shown to approach the predominant wave input periods as the spar is shortened. The 50 and 60 m designs were also shown to be susceptible to the Mathieu instability, as the pitch natural frequency was roughly twice the size of the heave frequency.

The potential benefits of spar modifications by installing strakes and fins along the spar length were identified, with fins being particularly beneficial in the pitch DoF to provide more damping. The second-order hydrodynamic effects were shown to be of little importance for the original OC3-Hywind design, but this might not be the case for the shortened spar designs, suggesting some future work in this area.

# Chapter 5: Summary

---

The work presented in this thesis has established some very simple guidelines that can be used to review which areas of the system can be simplified and which not, when designing new FOWTs. The work was based on using a spar-type offshore floating wind turbine as the base case. Nevertheless, many conclusions are applicable to other FOWT substructure types, such as semi-sub, barge and TLP. Areas reviewed include the importance of fully-attached and fully-unsteady aerodynamics compared to quasi-steady aerodynamics, and identifying what effect motion in each DoF has on the WT loads. The most detrimental DsoF for spar-type FOWTs were also identified. Additionally, an analysis was performed on the possibility of using shortened spar-type FOWTs in medium-depth waters.

The chapter starts by giving an overall review for each chapter. This is followed by providing recommendations in order to be able to confidently design floating wind turbines. The chapter finishes by giving some examples of future work that have been identified and could be performed as either a continuation of this thesis or independently.

## 5.1. Review of conclusions

In Chapter 1 a brief introduction to the argument between the onshore and offshore wind was given, showing that the offshore wind is on average 1 m/s stronger, when 10 km offshore, compared to onshore, and that it has very little or no visual impact depending on how far offshore a wind farm is placed. This was followed by identifying 3 potential offshore markets (Europe, Japan and the U.S.), and performing a wind resource assessment for each. A bathymetry analysis was then performed for each of the identified markets. This

led to the identification of those parts of each region to be only suitable for very deep offshore wind, where fixed-bottom offshore installations are not feasible. These areas were: all of Japan, Hawaii, the West Coast and the Great Lakes of the U.S.A., and Norway, the Mediterranean Sea and around the Iberian Peninsula.

Different substructures were presented that could be used at different water depths, before a general classification of FOWT substructures was given. It was recognised that there are three main physical principles by which static stability of a FOWT can be achieved, buoyancy moment (barge), mooring system (TLP) and ballast (spar), and that the majority of the currently proposed FOWTs are hybrid systems, which borrow the best from each principle. This was followed by compiling a list of different vertical- and horizontal-axis FOWTs, which were then compared. Due to the immaturity of VAWT technology, only horizontal-axis FOWTs were considered, eventually leading to Hywind being chosen as the focus of this study. This decision was significantly influenced by the fact that Hywind was the only existing full-scale FOWT at the start of this study, which has been operational for years. The choice was further confirmed by identifying semi-sub and spar having the smallest life-cycle costs, with the spar having a superior dynamic response due to its small area at the SWL.

Because Hywind employs a 2.3 MW WT and it was shown that the foundation contributes a large proportion of the overall capital costs, it was decided to use the OC3-Hywind, which uses the 5 MW NREL reference WT, for all future work.

The work in Chapter 2 concentrated on modelling fully-attached flow, as unsteady aerodynamic effects are present even in the fully-attached flow. These reveal themselves as moderate changes in amplitude and phase compared to the quasi-steady loads. Reduced frequency analysis showed that unsteady effects are most likely to be experienced close to the blade root and at low wind speeds.

Theodorsen's theory was used to model blade plunging and pitching, which is equivalent of FOWT surge and pitch motions. As predicted by the theory, a reduction in the lift amplitude

and a lag in phase were present in the fully-attached unsteady results when compared to the quasi-steady aerodynamic loads.

Because Theodorsen's theory is only strictly applicable to a fixed free-stream velocity and can only really model 2 DsoF of a typical FOWT, Van der Wall and Leishman's theory was used next. Van der Wall and Leishman's theory, together with Wagner's function, was discretised in the time-domain allowing all 6 DsoF of any FOWT to be simulated. To validate the code, it was run against previous work by Leishman, giving very good agreement. Each DoF was prescribed sinusoidal motion of multiple amplitude (1-5 m or deg.) and period (5-25 s) combinations, which was then expressed as a change in the free-stream and/or rotational velocity. Only the lift components and loads at the rotor were looked at. These included thrust and torque on the rotor, and out-of-plane and in-plane bending moments at the blade root. Just as for the Theodorsen theory solution, circulatory and non-circulatory effects were both present. However, in the Van der Wall and Leishman results these were separated and the non-circulatory effects (added-mass) shown to be of very little significance for conditions typical for WTs.

The simulations were performed for 10 m/s uniform wind (no wind shear, tower shadow, turbulence). The thin aerofoil theory and NREL 5MW WT look-up table approaches for obtaining lift force were used, assuming that the rotor is rigid and without any control action. Surge, pitch and yaw DsoF were modelled as changes in the free-stream velocity, while sway, heave and roll were modelled as azimuth angle dependent periodic changes in the rotational velocity of the rotor. The main findings were: firstly, the mean loading values do not differ greatly between the quasi-steady and fully-attached unsteady results. Secondly, for those DsoF that were modelled as a change in the free-stream velocity, the periodic components of the thrust and out-of-plane bending moments were smaller for the unsteady case. Thirdly, the same periodic loads for sway, heave and roll were larger in the unsteady treatment. Fourthly, the in-plane forces and bending moments were always smaller in the unsteady calculations. All these findings were consistent across the thin aerofoil theory and look-up data method.

It was shown that the fully-attached unsteady aerodynamic loads have to be accounted for when performing even the initial design. Failure to do so can potentially result in adverse

fatigue effects on the turbine, if the lag effect is not accounted for when designing the controller.

In Chapter 3 FAST was used to simulate the OC3-Hywind. Compared to the previous chapter, where multiple simplifications were made and only the rotor modelled, this time the whole structure, including the mooring and control system, was included. In addition, not only were the fully-attached unsteady aerodynamic results included in modelling the OC3-Hywind, but the whole spectrum of the unsteady effects (attached-, separated-flow and dynamic stall). Whilst this represented a much more realistic scenario, FAST has its own shortcomings in terms of simplified hydrodynamics and mooring system modelling, and inability to account for vortex ring states. Furthermore, when trying to model motion in each DoF separately by disabling spar DsoF, a flaw was discovered, as in doing so the natural frequencies of the spar shifted (this was noticed particularly in pitch and roll DsoF).

A detailed comparison of the fully-unsteady and quasi-steady aerodynamic simulation results highlighted that there is much more aerodynamic damping in the fully-unsteady case. This was found by carrying out a logarithmic decrement analysis on the tower top fore-aft displacement in response to an impulse. This explained why there is the same amplitude displacement in surge for both quasi-steady and unsteady cases, but much larger amplitude of loading in thrust in the unsteady aerodynamic runs. In addition, the unsteady aerodynamic simulations showed the presence of wave harmonics in the torque response which were not present in the quasi-steady case. These also appeared in the tower side-to-side response, further stressing the importance of choosing the correct aerodynamic modelling settings when designing a new wind turbine, as these wave harmonics were shown to coincide with the 1<sup>st</sup> tower side-to-side mode.

As disabling spar DsoF and simulating each DoF one at-a-time was not an option, an alternative method was devised of isolating the effects of the different DsoF. This was achieved by scaling the wave-excitation force-vector obtained from WAMIT. Only the surge and pitch DsoF were compared, as sway, heave and roll were shown to be of little significance in fatigue as no change in the free-stream velocity is experienced in these DsoF. Yaw was ruled out on the basis that the spar is rotationally symmetrical and thus very hard

to excite. Yaw is highly coupled to the pitch DoF through gyroscopic coupling, but the pitch DoF contains the highest degree of aerodynamic damping. Surge and pitch DsoF were compared by looking at the tower base and blade root moments together with the previously identified maximum stress points (9.7 m from the tower base, 6.83 and 43.05 m from the blade root). For all 3 operational conditions (below-rated, rated and above-rated), surge and pitch DsoF were identified as having a very comparable detrimental effect on the OC3-Hywind system. Lastly, for the same locations along the tower and blade span, correlations matrices were established to identify any unidentified links and couplings between different DsoF and loads.

Chapter 4 looked at how the OC3-Hywind could be shortened, so that it could be used in shallower waters. To do so, the OC3-Hywind was reverse engineered in Excel using some simplifications, and its parameters studied. Four main design variables were identified that could be adjusted to obtain the required design. These were: steel thickness, ballast density, spar length and diameter. A parametric study was then performed on the identified variables by firstly using a theoretical uniform diameter spar and then the OC3-Hywind. Due to the very limited influence of the steel thickness on the static heel angle and the roll/pitch natural period, it was decided to keep the steel thickness the same across all subsequent designs. Three different ballast materials were considered: olivine (used in Hywind), haematite and magnetite. In the end, haematite was chosen due to its superior specific gravity and abundance around the world.

Through the process of performing a parametric study on the OC3-Hywind, multiple design limits and trade-offs were identified. Some of the design limits identified were: static stability (the CoG has to be located below the CoB), the maximum ballast density (limited by the maximum packing density), steel thickness (high cost of steel and welding), static heel angle (limited by drive-train lubrication system), spar diameter (high cost of steel and welding), etc. Multiple different trade-offs were identified, but not all of these were investigated. The main trade-off that had to be taken into account when shortening the spar was found to be between spar diameter and length. To maintain reasonable static stability, any change in the spar length (decrease) had to be countered by a change in the

spar diameter (increase) to maintain a low CoG. However, some savings can be achieved in the spar diameter and hence steel costs by increasing the ballast density. A very important trade-off for a spar-type FOWT, in terms of its operational dynamics, is between the static heel angle and the roll and pitch natural frequency. Almost no compromises can be made in the static heel angle which is limited to max 6 deg. for current WTs. This will inevitably mean placing the roll/pitch natural frequency close to the predominant wave input frequencies. Other trade-offs identified, but not looked at included the steel thickness against the structural integrity, and others concerning the mooring system and costs which were beyond the scope of this thesis.

Using the trade-offs identified, 4 different hypothetical shortened spar FOWTs were proposed of 50, 60, 70 and 80 m draft. All these used the maximum ballast density of seawater and haematite slurry of  $2,150 \text{ kgm}^{-3}$  (65% solid concentration) and a static heel angle of 5 degrees. The decrease in the spar length resulted in increases in all natural periods apart from roll and pitch, with surge and sway, and heave being placed outside the most commonly occurring wave periods. The yaw period increased from 9.7 s at 80 m draft to 17.3 s at 50 m draft. However, the roll and pitch periods decreased from 22.4 s to 19.3 s, compared to approx. 29 s for the original OC3-Hywind, bringing them very close to the most probable wave input periods. The Mathieu instability was identified as a potential issue in the 50 and 60 m draft designs, as the heave to pitch natural period ratios were very close to 2:1. It was suggested that fins (cross-plates) be installed along the spar length to provide extra damping and added-mass. This would prevent the Mathieu instability by decreasing the period in the pitch DoF and by providing extra damping in all but the heave DoF. This would be particularly beneficial in surge and pitch as they were identified as the most detrimental DsoF to the system in Chapter 3.

## 5.2. Recommendations

This study has clearly demonstrated that there is still plenty of scope for further improvements in the field of FOWT modelling. FOWTs operate in a very adverse environment, which, if not modelled correctly, can lead to inadequate design and early

failure of FOWTs. However, to date no official guidelines have been released for the design of FOWTs. In this section the author provides some recommendations which he has drawn from his research and findings in this study. These can be used to help design floating wind turbines.

The following guidelines are suggested for use in designing future FOWTs:

- The mean and amplitude of fully-attached unsteady loads are comparable to quasi-steady and hence can be ignored in the preliminary design of FOWTs.
- The phase lag between the fully-attached unsteady and quasi-steady aerodynamic representations has to be accounted for when designing the controller of a FOWT.
- The mean and amplitude of fully-unsteady loads significantly differs from those of quasi-steady. The main reason for this was shown to be dynamic inflow or induction lag. This effect has to be taken into account even in the preliminary design of FOWTs.
- There is a significant phase difference between aerodynamic loads when calculated using fully-unsteady and quasi-steady aerodynamic representations. This is consistent with point two and further highlights the importance of the phase lag between both representations. This is particularly true for spar-type FOWTs as these can experience negative damping if the controller is not designed to accommodate for the delay.
- A large proportion of the total damping in FOWTs is provided by the aerodynamic damping generated by the rotor. In this study it was shown that magnitude of aerodynamic damping depends on the aerodynamic representation used (see 3.1.5.1). When using quasi-steady aerodynamics the aerodynamic damping due to dynamic wake (induction lag) is ignored. However, because aerodynamic damping can be used to reduce FOWT's motion in the pitch DoF – which was identified as particularly detrimental to the system (see 3.2.2) – it is important to use fully-unsteady aerodynamic representation when performing dynamic analysis of FOWTs.
- Motion in surge and pitch was identified as the most detrimental to the system. This means that particular care has to be shown when choosing where to place the surge and pitch natural frequencies of FOWTs as these can trigger resonance if

placed near the predominant wave spectrum frequencies. The yaw DoF can also potentially be very detrimental to the system as, just like surge and pitch, it experiences change in the free-stream velocity. If the natural frequencies cannot be placed far enough from the predominant wave frequencies then additional damping must be provided.

- The second order hydrodynamic effects of sum- and difference- frequency, and mean drift force on the OC3-Hywind were shown to be very small [118]. However, whilst this was true for the OC3-Hywind, the same paper showed that the second-order hydrodynamic effects are significant for TLPs. This leads to the suggestion that second-order hydrodynamic effects should be considered even in the initial design of FOWTs and might be particularly relevant for FOWTs with a large cross-sectional area at water level.
- It is important to perform some basic calculations to make sure that the Mathieu instability will not occur. This is particularly important for FOWTs as motion in the pitch DoF was shown to be very detrimental to the system.
- For the current designs of WTs available on the market, it is essential that the static heel angle of FOWTs is kept low (below 5-6 deg.) to make certain not to damage the drive-train by limiting its lubrication.
- Mooring systems are intrinsically highly non-linear. However, in FOWT simulation packages these are quite often modelled as purely quasi-static and completely ignore any dynamic effects. Whilst this might be applicable for the preliminary design of FOWTs (static analysis), dynamic analysis of FOWTs should use dedicated mooring codes that can account at least for some of the more pronounced and important dynamic mooring effects.

Provided above are some basic guidelines that engineers may find useful in designing new FOWTs. Additionally, the author is of the opinion that significant effort has to be put into the design of improved software packages for modelling FOWTs. Very often existing packages have been adopted from the onshore wind turbine and the oil and gas sectors, leading to questions about their accuracy in modelling FOWTs. This could be helped by developing a fully integrated aero-hydro-servo-elastic code that would use a free-wake model to account for aerodynamics and a fully non-linear

hydrodynamics model that could account for 1<sup>st</sup>, 2<sup>nd</sup> and higher order hydrodynamic and mooring effects.

### 5.3. Future work

Multiple extensions and future work areas exist that could be made as either in-depth investigations of the areas that were simplified or as a continuation of the work already performed in this thesis. Next, the future work already identified by the author is listed in order by chapter.

Many simplifications were made in Chapter 2 when comparing fully-attached unsteady loads with quasi-steady. One of these simplification involved assuming that the rotor was rigid. Any interaction of the rotor with other parts of the system, such as the tower, control and spar were also ignored. For more precise calculations a full servo-hydro-aero-elastic code should be used. Theodorsen, Van der Wall and Leishman approaches only account for the unsteady lift and not drag. Accounting for the drag in calculating the in-plane forces can be very important, if the right conditions are met (large inflow angles or angles-of-attack). In modelling motion in 6 DoF using the Van der Wall and Leishman approach, the motions in side-to-side direction (sway, heave and roll) were modelled as increases and decreases in the rotational velocity of the blade. Alternatively, this could be modelled as yawing motion. However, it is important to account for the rotor inertia (particularly in the roll DoF), which requires some substantial changes to be made to the code or some already written software, such as FAST or Bladed, to be modified in order to look only at the fully-attached unsteady loads.

In Chapter 3 FAST version 7 was used to simulate the OC3-Hywind turbine. Since then a new version of FAST (version 8) has been released which is much more advanced. Firstly, it is now highly modular, allowing individual modules to be modified for specific purposes and substituted. Secondly, it includes tower drag, 2<sup>nd</sup> order hydrodynamic effects, marine

growth, mooring dynamics and much more<sup>8</sup>, that were not modelled in version 7, or only to a limited degree. FAST version 8 could be used to simulate a much more realistic representation of the highly complex operating environment of FOWTs. This could be taken one step further by linking FAST to a free wake model, such as that of Sebastian [120] to account for the vortex ring state.

The work in Chapter 4 concentrated at looking at the possibility of shortening the OC3-Hywind spar, so that it could be installed in water depths starting from 60 m. The steel thickness of the spar was kept the same for 50-80 m draft designs. However, in reality each design would be optimised and steel thickness would vary between each design, optimised for structural integrity. This could then be tied into a cost study, as steel drives costs and can incur high fabrication costs (steel rolling and welding). The mooring system for the shortened spar designs was borrowed from the OC3-Hywind, but should also be optimised for each specific design. Modifying the mooring system could improve the overall response of the system, as it directly influences several properties of the spar, in particular pitch natural frequency and static heel angle.

From the results shown in Chapter 4 there seems to be no reason why a shortened spar should not be viable. However, all the calculations performed so far completely ignored the costs associated with building, installing and maintaining such FOWTs. Hence it is important that a detailed cost analysis (including construction, material, installation, O&M, etc.) be performed to ensure that these designs are feasible and economical. Also, no dynamic simulations were performed on the designs, as only the static properties and natural frequencies were considered. These could be then taken further by installing fins (cross-plates) and helical strakes along the spar length to see how the response changes. Additionally, a simple design rule-of-thumb representing damping as a function of design variables could be developed.

---

<sup>8</sup> A full comparison of version 7 and 8 is given in *NWTC Information Portal (FAST v8)* <https://nwtc.nrel.gov/FAST8>. Last modified 06-October-2014 ; Accessed 27-November-2014

# References

- [1] T. Burton, N. Jenkins, D. Sharpe, and E. Bossanyi, *Wind energy handbook*, 2 ed.: John Wiley & Sons, 2011.
- [2] EWEA, "Deep Water: The next step for offshore wind energy," 2013.
- [3] EEA, "Europe's onshore and offshore wind energy potential," 2009.
- [4] Risø. (20/09/2014). *European wind resources over open sea*. Available: <http://www.windatlas.dk/europe/oceanmap.html>
- [5] EWEA, "The European offshore wind industry - key trends and statistics 2013," EWEA.
- [6] S. Lindenberg, *20% Wind Energy By 2030: Increasing Wind Energy's Contribution to US Electricity Supply*: DIANE Publishing, 2009.
- [7] EIA. (06/05/2014). *State Electricity Sales Spreadsheet*. Available: [www.eia.gov/electricity/sales\\_revenue\\_price/xls/table5\\_a.xls](http://www.eia.gov/electricity/sales_revenue_price/xls/table5_a.xls)
- [8] M. Schwartz, D. Heimiller, S. Haymes, and W. Musial, "Assessment of Offshore Wind Energy Resources for the United States," National Renewable Energy Laboratory (NREL), Golden, CO.2010.
- [9] S. Butterfield, W. Musial, J. Jonkman, and P. Sclavounos, "Engineering Challenges for Floating Offshore Wind Turbines," National Renewable Energy Laboratory (NREL), Golden, CO.2007.
- [10] C. Arakawa, "Status and plans for offshore wind in Japan," in *9th Deep Sea Offshore Wind R&D Seminar*, Trondheim, Norway, 2012.
- [11] P. Sclavounos, "Floating offshore wind turbines," *Marine Technology Society Journal*, vol. 42, pp. 39-43, 2008.
- [12] H. Sorenson, L. Hansen, and K. Hammarlund, "Social acceptance, environmental impact and politics," *Final report WP2. 5 Concerted Action on Offshore Wind Energy in Europe*, 2001.
- [13] I. D. Bishop and D. R. Miller, "Visual assessment of off-shore wind turbines: the influence of distance, contrast, movement and social variables," *Renewable Energy*, vol. 32, pp. 814-831, 2007.
- [14] J. Ladenburg, "Visual impact assessment of offshore wind farms and prior experience," *Applied Energy*, vol. 86, pp. 380-387, 2009.

- [15] D. Van Hertem and M. Ghandhari, "Multi-terminal VSC HVDC for the European supergrid: Obstacles," *Renewable and sustainable energy reviews*, vol. 14, pp. 3156-3163, 2010.
- [16] ENTSOE, "Offshore Transmission Technology," 2011.
- [17] K. Veum, L. Cameron, D. Huertas, and M. Korpaas, "Roadmap to the deployment of offshore wind energy in the Central and Southern North Sea (2020-2030)," *Final report (D6. 4), IEE WINDSPEED project*, 2011.
- [18] A. Czyzewski. (06/05/2015). Wind energy gets serial. *the ENGINEER*. Available: <http://www.theengineer.co.uk/in-depth/the-big-story/wind-energy-gets-serial/1012449.article>
- [19] W. Musial, S. Butterfield, and A. Boone, "Feasibility of floating platform systems for wind turbines," in *23rd ASME Wind Energy Symposium, Reno, NV, 2004*.
- [20] M. Cahay, E. Luquiau, C. Smadja, and F. Silvert, "Use of a vertical wind turbine in an offshore floating wind farm," in *Offshore technology conference*, 2011, pp. 2-5.
- [21] L. Vita, F. Zhale, U. S. Paulsen, T. F. Pedersen, H. A. Madsen, and F. Rasmussen, "A novel concept for floating offshore wind turbines: recent developments in the concept and investigation on fluid interaction with the rotating foundation," in *ASME 2010 29th International Conference on Ocean, Offshore and Arctic Engineering*, 2010, pp. 389-396.
- [22] L. Vita, U. Schmidt Paulsen, T. Friis Pedersen, H. Aagaard Madsen, and F. Rasmussen, "A novel floating offshore wind turbine concept," in *2009 European Wind Energy Conference and Exhibition*.
- [23] L. Vita, U. Schmidt Paulsen, and T. Friis Pedersen, "A novel floating offshore wind turbine concept: new developments," in *2010 European Wind Energy Conference and Exhibition*.
- [24] T. Nakamura, K. Mizumukai, H. Akimoto, Y. Hara, and T. Kawamura, "Floating Axis Wind and Water Turbine for High Utilization of Sea Surface Area: Design of Sub-Megawatt Prototype Turbine," in *ASME 2013 32nd International Conference on Ocean, Offshore and Arctic Engineering*, 2013.
- [25] Gwind. (19/05/2014). *Gwind*. Available: <http://www.gwind.no/>
- [26] H. Stiesdal, "Hywind: The world's first floating MW-scale wind turbine," *Wind directions, Dec*, pp. 52-53, 2009.
- [27] NauticaWindpower. (19/05/2014). *Nautica*. Available: <http://www.nauticawindpower.com/>
- [28] Sway. (19/05/2014). *Sway*. Available: <http://www.sway.no/>

- [29] D. Roddier, C. Cermelli, A. Aubault, and A. Weinstein, "WindFloat: A floating foundation for offshore wind turbines," *Journal of Renewable and Sustainable Energy*, vol. 2, 2010.
- [30] FOWC. (28/05/2014). *Fukushima Offshore Wind Consortium*. Available: <http://www.fukushima-forward.jp/english/index.html>
- [31] WindSea. (19/05/2014). *WindSea*. Available: <http://www.windsea.com/>
- [32] Blue-H. (19/05/2014). *Blue-H concept*. Available: <http://www.bluehgroup.com/>
- [33] Éole. (19/05/2014). *Éole*. Available: <http://www.eolecapchat.com/>
- [34] D. Quarton, "FLOAT - Technical and economic feasibility of a floating wind turbine," ed, 1993.
- [35] C. Kost, J. N. Mayer, and J. Thomsen, "Levelized Cost of Electricity - Renewable Energy Technologies," Fraunhofer ISE, 2013.
- [36] IRENA, "Renewable Energy Technologies: Cost Analysis Series," 2012.
- [37] "Offshore Wind Cost Reduction," The Crown Estate, 2012.
- [38] M. I. Blanco, "The economics of wind energy," *Renewable and sustainable energy reviews*, vol. 13, pp. 1372-1382, 2009.
- [39] EWEA, *The economics of wind energy*: EWEA, 2009.
- [40] E. t. Horst. (06/05/2015). *GL Garrad Hassan - Cost of Energy of Floating Wind* [Presentation]. Available: [http://www.gl-garradhassan.com/assets/downloads/Cost\\_of\\_energy\\_of\\_floating\\_wind.pdf](http://www.gl-garradhassan.com/assets/downloads/Cost_of_energy_of_floating_wind.pdf)
- [41] I. Dinwoodie, D. McMillan, M. Revie, I. Lazakis, and Y. Dalgic, "Development of a Combined Operational and Strategic Decision Support Model for Offshore Wind," *Energy Procedia*, vol. 35, pp. 157-166, 2013.
- [42] P. Tavner, *Offshore wind turbines: reliability, availability and maintenance*: Institution of Engineering and Technology, 2012.
- [43] C. S. Laura and D. C. Vicente, "Life-cycle cost analysis of floating offshore wind farms," *Renewable Energy*, vol. 66, pp. 41-48, 2014.
- [44] P. Patel, "Floating Wind Turbines to Be Tested," ed: IEEE Spectrum, 2009.
- [45] Nielsen. (06/05/2015). *Statoil wants Hywind in Japan*. Available: <http://www.tu.no/industri/2011/04/04/onsker-hywind-til-japan>
- [46] J. M. Jonkman, "Definition of the Floating System for Phase IV of OC3," National Renewable Energy Laboratory (NREL), Golden, CO, USA NREL/TP-500-47535, 2010.

- [47] J. M. Jonkman, S. Butterfield, W. Musial, and G. Scott, "Definition of a 5-MW reference wind turbine for offshore system development," National Renewable Energy Laboratory (NREL), Golden, CO, USA, NREL/TP-500-38060, 2009.
- [48] H. Kooijman, C. Lindenburg, D. Winkelaar, and E. van der Hooft, "DOWEC 6 MW pre-design," *Energy Research Center of the Netherlands (ECN)*, 2003.
- [49] Xodus, "Hywind Scotland Pilot Park Project - EIA Scoping Report," Edinburgh, 2013.
- [50] J. Jonkman. (06/05/2015). *NWTC Computer-Aided Engineering Tools (FAST)*. Available: <http://wind.nrel.gov/designcodes/simulators/fast/>
- [51] T. Sebastian and M. Lackner, "Analysis of the induction and wake evolution of an offshore floating wind turbine," *Energies*, vol. 5, pp. 968-1000, 2012.
- [52] J. M. Jonkman and M. L. Buhl Jr, "FAST user's guide," *Golden, CO: National Renewable Energy Laboratory*, 2005.
- [53] T. Theodorsen, "General Theory of Aerodynamic Instability and the Mechanism of Flutter," NACA 496, 1935.
- [54] T. v. Karman and W. R. Sears, "Airfoil theory for non-uniform motion," *Journal of the Aeronautical Sciences (Institute of the Aeronautical Sciences)*, vol. 5, pp. 379-390, 1938.
- [55] R. L. Bisplinghoff, H. Ashley, and R. L. Halfman, *Aeroelasticity*: Courier Corporation, 2013.
- [56] J. Leishman, "Challenges in modelling the unsteady aerodynamics of wind turbines," *Wind Energy*, vol. 5, pp. 85-132, 2002.
- [57] H. Wagner, "Über die Entstehung des dynamischen Auftriebes von Tragflügeln," *ZAMM-Journal of Applied Mathematics and Mechanics/Zeitschrift für Angewandte Mathematik und Mechanik*, vol. 5, pp. 17-35, 1925.
- [58] R. T. Jones, "The unsteady lift of a wing of finite aspect ratio," National Advisory Committee for Aeronautics 681, 1940.
- [59] W. P. Jones, *Aerodynamic forces on wings in non-uniform motion*,: HM Stationery Office, 1945.
- [60] I. E. Garrick, "On some reciprocal relations in the theory of nonstationary flows," NACA 629, 1938.
- [61] J. G. Leishman, *Principles of helicopter aerodynamics*, 2 ed.: Cambridge University Press, 2006.
- [62] J. W. Miles, "The aerodynamic force on an airfoil in a moving gust," *Journal of the Aeronautical Sciences (Institute of the Aeronautical Sciences)*, vol. 23, pp. 1044-1050, 1956.

- [63] B. G. Van Der Wall and J. Leishman, "On the influence of time-varying flow velocity on unsteady aerodynamics," *Journal of the American Helicopter Society*, vol. 39, pp. 25-36, 1994.
- [64] R. Isaacs, "Airfoil theory for flows of variable velocity," *Journal of the Aeronautical Sciences*, vol. 12, pp. 113-117, 1945.
- [65] R. Isaacs, "Airfoil theory for rotary wing aircraft," *Journal of the Aeronautical Sciences*, vol. 13, pp. 218-220, 1946.
- [66] J. M. Greenberg, *Airfoil in sinusoidal motion in a pulsating stream*: National Advisory Committee for Aeronautics, 1947.
- [67] S. B. Kottapalli, "Unsteady aerodynamics of oscillating airfoils with inplane motions," *Journal of the American Helicopter Society*, vol. 30, pp. 62-63, 1985.
- [68] W. Johnson, *Helicopter theory*: Princeton University Press, Princeton, NJ, 1980.
- [69] J. Leishman and T. Beddoes, "A semi-empirical model for dynamic stall," *Journal of the American Helicopter Society*, vol. 34, pp. 3-17, 1989.
- [70] P. J. Moriarty and A. C. Hansen, *AeroDyn theory manual*: National Renewable Energy Laboratory (NREL), Golden, Colorado, 2005.
- [71] C. H. Lee, *WAMIT theory manual*: Massachusetts Institute of Technology, Department of Ocean Engineering, 1995.
- [72] J. M. Jonkman, *Dynamics modeling and loads analysis of an offshore floating wind turbine*: ProQuest, 2007.
- [73] G. B. Airy, "Tides and waves," 1841.
- [74] J. Wheeler, "Method for calculating forces produced by irregular waves," *Journal of Petroleum Technology*, vol. 22, pp. 359-367, 1970.
- [75] J. Morison, J. Johnson, and S. Schaaf, "The force exerted by surface waves on piles," *Journal of Petroleum Technology*, vol. 2, pp. 149-154, 1950.
- [76] R. G. Dean, "Stream function wave theory; Validity and application," 1965.
- [77] T. Sarpkaya, "Force on a circular cylinder in viscous oscillatory flow at low Keulegan—Carpenter numbers," *Journal of Fluid Mechanics*, vol. 165, pp. 61-71, 1986.
- [78] G. H. Keulegan and L. H. Carpenter, *Forces on cylinders and plates in an oscillating fluid*: US Department of Commerce, National Bureau of Standards, 1956.
- [79] T. Sarpkaya, "In-Line And Transverse Forces On Cylinders In Oscillatory Flow At High Reynolds Numbers," in *Offshore Technology Conference*, 1976.

- [80] F. G. Nielsen, T. D. Hanson, and B. Skaare, "Integrated dynamic analysis of floating offshore wind turbines," in *25th International Conference on Offshore Mechanics and Arctic Engineering*, 2006, pp. 671-679.
- [81] T. J. Larsen and T. D. Hanson, "A method to avoid negative damped low frequent tower vibrations for a floating, pitch controlled wind turbine," in *Journal of Physics: Conference Series*, 2007, p. 012073.
- [82] J. M. Jonkman, *Influence of control on the pitch damping of a floating wind turbine*: National Renewable Energy Laboratory (NREL), Golden, CO., 2008.
- [83] H. Namik and K. Stol, "Individual blade pitch control of floating offshore wind turbines," *Wind Energy*, vol. 13, pp. 74-85, 2010.
- [84] P. Bearman, M. Downie, J. Graham, and E. Obasaju, "Forces on cylinders in viscous oscillatory flow at low Keulegan-Carpenter numbers," *Journal of Fluid Mechanics*, vol. 154, pp. 337-356, 1985.
- [85] O. Faltinsen, *Sea loads on ships and offshore structures*. vol. 1: Cambridge university press, 1993.
- [86] J. Browning, J. Jonkman, A. Robertson, and A. Goupee, "Calibration and validation of a spar-type floating offshore wind turbine model using the FAST dynamic simulation tool," *Proceedings of the Science of Making Torque From Wind, Oldenburg, Germany*, 2012.
- [87] J. Jonkman, "The New Modularization Framework for the FAST Wind Turbine CAE Tool," in *51st AIAA Aerospace Sciences Meeting and 31st ASME Wind Energy Symposium, Grapevine, Texas*, 2013.
- [88] M. D. Masciola, "Instructional and Theory Guide to the Mooring Analysis Program," National Renewable Energy Laboratory (NREL), 2014.
- [89] J. Jonkman, *Dynamics Modeling and Loads Analysis of an Offshore Floating Wind Turbine*: ProQuest, 2007.
- [90] C. Chen, "Development of a simplified inflow model for a helicopter rotor in descent flight," Georgia Institute of Technology, 2006.
- [91] T. Sebastian, "The aerodynamics and near wake of an offshore floating horizontal axis wind turbine," University of Massachusetts Amherst, 2012.
- [92] T. Sebastian and M. Lackner, "Characterization of the unsteady aerodynamics of offshore floating wind turbines," *Wind Energy*, vol. 16, pp. 339-352, 2013.
- [93] T. Sebastian and M. Lackner, "Offshore Floating Wind Turbines-An Aerodynamic Perspective," in *49th AIAA Aerospace Sciences Meeting, Orlando, Florida*, 2011.
- [94] J. Jonkman, T. J. Larsen, A. M. Hansen, T. Nygaard, K. Maus, M. Karimirad, Z. Gao, T. Moan, I. Fylling, and J. Nichols, "Offshore code comparison collaboration within IEA

Wind Task 23: Phase IV results regarding floating wind turbine modeling," in *2010 European Wind Energy Conference and Exhibition*, 2010.

- [95] D. Matha, "Model Development and Loads Analysis of an Offshore Wind Turbine on a Tension Leg Platform with a Comparison to Other Floating Turbine Concepts: April 2009," National Renewable Energy Laboratory (NREL), Golden, CO.2010.
- [96] M. H. Hansen, K. Thomsen, P. Fuglsang, and T. Knudsen, "Two methods for estimating aeroelastic damping of operational wind turbine modes from experiments," *Wind Energy*, vol. 9, pp. 179-191, 2006.
- [97] D. Salzmänn and J. Van der Tempel, "Aerodynamic damping in the design of support structures for offshore wind turbines," in *Paper of the Copenhagen Offshore Conference*, 2005.
- [98] J. van der Tempel, "Lifetime Fatigue of an Offshore wind Turbine Support Structure," Delft University of Technology, 2000.
- [99] J. E. Withee, "Fully coupled dynamic analysis of a floating wind turbine system," Monterey, California. Naval Postgraduate School, 2004.
- [100] H. Snel and J. Schepers, "Engineering models for dynamic inflow phenomena," *Journal of Wind Engineering and Industrial Aerodynamics*, vol. 39, pp. 267-281, 1992.
- [101] S. Øye, "Unsteady wake effects caused by pitch-angle changes," in *IEA R&D WECS Joint Action on Aerodynamics of Wind Turbines, 1st Symposium*, 1986, pp. 58-79.
- [102] H. Hendriks and B. Bulder, "Fatigue Equivalent Load Cycle Method," *ECN, The Netherlands, Tech. Rep. ECN-C-95-074*, 1995.
- [103] M. Matsuishi and T. Endo, "Fatigue of metals subjected to varying stress," *Japan Society of Mechanical Engineers, Fukuoka, Japan*, pp. 37-40, 1968.
- [104] F. Richards, N. LaPointe, and R. Wetzel, "A cycle counting algorithm for fatigue damage analysis," SAE Technical Paper, 1974.
- [105] S. D. Downing and D. Socie, "Simple rainflow counting algorithms," *International Journal of Fatigue*, vol. 4, pp. 31-40, 1982.
- [106] M. A. Miner, "Cumulative damage in fatigue," *Journal of applied mechanics*, vol. 12, pp. 159-164, 1945.
- [107] J. Goodman, *Mechanics applied to engineering*: Longmans, Green & Company, 1919.
- [108] K. Walker, "The effect of stress ratio during crack propagation and fatigue for 2024-T3 and 7075-T6 aluminum," *Effects of environment and complex load history on fatigue life, ASTM STP*, vol. 462, pp. 1-14, 1970.

- [109] P. Brøndsted, H. Lilholt, and A. Lystrup, "Composite materials for wind power turbine blades," *Annu. Rev. Mater. Res.*, vol. 35, pp. 505-538, 2005.
- [110] IEC, "IEC 61400-3," *Wind Turbines—Part 3: Design Requirements for Offshore Wind Turbines*, 2009.
- [111] F. K. Blackburn M, Gibson A, Parker C, Ryan C, Stevenson K, "Offshore floating wind turbine," Texas A&M University, 2011.
- [112] P. S. De Ugarte Sevilla and J. M. Z. ZABALA, "Oil level maintenance system," US Patent US8820479 B2, 2014.
- [113] J. F. Kemp, P. Young, and C. Barrass, *Ship Stability Notes & Examples*: Stanford Maritime, 1971.
- [114] W. Plaizier and B. Nachtergaele, "Steel's Challenge - Living with higher and more volatile iron-ore prices," A. T. Kearney, 2010.
- [115] M. Elliott, A. Agrawal, C. Assis, B. Stall, P. Mangers, and A. Beifus, "Global steel 2013 - A new world, a new strategy," Ernst and Young, 2013.
- [116] B. Koo, M. Kim, and R. Randall, "Mathieu instability of a spar platform with mooring and risers," *Ocean engineering*, vol. 31, pp. 2175-2208, 2004.
- [117] H. Haslum and O. Faltinsen, "Alternative shape of spar platforms for use in hostile areas," in *Offshore technology conference*, 1999.
- [118] L. Roald, J. Jonkman, A. Robertson, and N. Chokani, "The Effect of Second-order Hydrodynamics on Floating Offshore Wind Turbines," *Energy Procedia*, vol. 35, pp. 253-264, 2013.
- [119] A. J. Goupee, B. J. Koo, R. W. Kimball, K. F. Lambrakos, and H. J. Dagher, "Experimental comparison of three floating wind turbine concepts," *Journal of offshore mechanics and Arctic engineering*, vol. 136, p. 020906, 2014.
- [120] T. Sebastian and M. Lackner, "Development of a free vortex wake method code for offshore floating wind turbines," *Renewable Energy*, vol. 46, pp. 269-275, 2012.
- [121] A. R. Bramwell, D. Balmford, and G. Done, *Bramwell's helicopter dynamics*: Butterworth-Heinemann, 2001.

# Appendix

## A1.1. UK Round 1, 2 and 3 wind farms

The following two tables give the water depth and distance to shore for various projects in Round 1 and 2, and Round 3, respectively.

**Table 27 – UK Round 1 and 2 wind farms and the corresponding water depths and distances to shore**

<b>Name</b>	<b>Water depth (m)</b>	<b>Distance to shore (km)</b>	<b>State of development</b>
Barrow	15 - 20	7.5	operational
Blyth	5	-	operational
Burbo Bank	2 - 8	6.4	operational
Docking Shoal	3 - 14	-	refused consent
Dudgeon East	20 - 25	> 32	in construction
Greater Gabbard	4 - 37	36	operational
Gunfleet Sands 1 & 2	0 - 13	7	operational
Gwynt Y Mor	12 - 33	13	in construction
Humber Gateway	11 - 18	8	in construction
Inner Dowsing	6 - 8	5	operational
Kentish Flats	5	10	operational
Lincs	7 - 12	8	operational
London Array	0 - 23	20	operational
Lynn	7 - 11	5	operational
North Hoyle	7 - 11	7	operational
Ormonde	17 - 21	9.5	operational
Race Bank	4 - 23	27	consented
Rhyl Flats	4 - 11	8	operational
Robin Rigg East & West	0 - 12	11	operational
Scroby Sands	0 - 8	2.3	operational
Sheringham Shoal	14 - 23	17-23	operational
Teesside	6 - 18	1.5	operational
Thanet	20 - 25	12	operational
Triton Knoll	8 - 28	33	consented
Walney	19 - 30	14.4 - 25.8	operational
West Duddon	17 - 21	15	operational
Westermost Rough	12 - 22	8	in construction

**Table 28 – UK Round 3 wind farm zones and the corresponding water depths and distances to shore**

<b>Name</b>	<b>Water depth (m)</b>	<b>Distance to shore (km)</b>	<b>State of development</b>
Moray Firth	30 - 57	-	consented
Firth of Forth	30 - 80	22 – 80	consented
Dogger Bank	18 - 63	125 – 195	consented
Hornsea	30 - 40, max 70	34 – 190	consented
East Anglia	5 - 71	≈ 55.5	consented
Rampion	19 - 62	13 – 26	consented
Navitus Bay	27.8 - 56.3	< 32	planned
Atlantic Array	19.5 - 60.9	≈ 24.4	cancelled
Celtic Array	28 - 78	> 15	cancelled

## A1.2. Comparison of different floating HAWTs

Given below is the assessment criteria used in choosing one specific floating offshore wind turbine concept. Each design is given a score of 0-10 with 10 being the best. Each criterion is also given a weight, as not all criteria are of the same importance. The design with the highest total score was assumed to be the best and consequently used in this thesis.

Table 29 – Floating HAWT assessment criteria

<b>Cost</b>	Weight	Hywind	Blue-H	WindFloat	Nautica	Sway	WindSea
Buoyancy tank material	9	2	6	6	8	4	6
Buoyancy tank fabrication	5	5	4	3	6	6	3
Mooring line system	4	6	2	5	6	6	5
Anchor	5	8	1	7	3	2	7
Float out	4	8	6	6	3	3	6
Onsite installation	6	3	2	8	6	6	8
Decommissioning	5	5	1	6	4	4	6
Power cable connection	2	8	8	8	2	2	2
Buoyancy tank complexity	6	6	5	4	5	6	4
Maintainability	8	5	6	4	4	4	4
<b>Motion</b>							
Wave sensitivity	10	7	9	4	7	7	4
Corrosion and fatigue	6	8	8	4	7	7	4
Heel (pitch) angle	7	7	9	6	4	4	5
Yaw & Roll motion	5	7	10	5	8	8	4
Heave/Surge/Sway	3	5	4	5	4	4	4
Impact on power production	8	6	9	4	7	7	4
<b>Other</b>							
Sensitivity to soil	8	7	2	7	4	4	7
Footprint	1	3	7	3	9	9	3
CO <sub>2</sub> footprint	1	2	6	6	8	4	6
Technology's maturity	9	9	6	7	2	5	3
Depth reliance < 100 m	4	0	7	8	4	4	8
Depth reliance > 100 m	4	8	2	5	6	6	5
<b>Total</b>	<b>713</b>	<b>676</b>	<b>656</b>	<b>630</b>	<b>618</b>	<b>593</b>	

### A1.3. Approximations to Theodorsen's function

Table 30 – Approximations to generalised Theodorsen's function

$$\frac{0.5s^2 + 0.2808s + 0.01365}{s^2 + 0.3455s + 0.01365}$$

R.T. Jones

$$\frac{s^4 + 0.761s^3 + 0.1021s^2 + 2.551e^{-3}s + 9.557e^{-6}}{2s^4 + 1.064s^3 + 0.1134s^2 + 2.617e^{-3}s + 9.557e^{-6}}$$

Vepa

$$\frac{0.5(s + 0.088)(s + 0.37)(s + 0.922)}{(s + 0.072)(s + 0.261)(s + 0.8)}$$

Venkatesan &  
Friedman

$$\frac{0.5177s^2 + 0.2752s + 0.01576}{s^2 + 0.3414s + 0.01582}$$

Breuker et al.

## A1.4. Van der Wall and Leishman - Discretisation

Per personal communication with Prof Shan Huang.

Leishman showed that for time-varying incident velocity, where shed wake is convected at a non-uniform velocity; the circulatory part of the lift coefficient can be shown to be:

$$C_L^c(s) = \frac{2\pi}{V(s)} \left[ V(s_0)\alpha(s_0)\phi(s) + \int_{s_0}^s \frac{d(V\alpha)}{d\sigma} \phi(s - \sigma) d\sigma \right] \quad \text{A.1}$$

where

$$s = s(t) = \frac{2}{c} \int_0^t V(t) dt \quad \text{A.2}$$

where  $s$ , non-dimensional time, represents the distance travelled by an aerofoil (blade element) in terms of its semi-chords. Equation A.2 leads to one-to-one mapping between  $s$  and  $t$ .

Looking at the second term of equation A.1 for  $s = s_n$ :

$$\int_0^{s_n} \frac{d(V\alpha)}{d\sigma} \phi(s_n - \sigma) d\sigma = \sum_{i=1}^n \int_{s_{i-1}}^{s_i} \frac{d(V\alpha)}{d\sigma} \phi(s_n - \sigma) d\sigma \quad \text{A.3}$$

An approximation for Wagner's function is given as:

$$\phi(s) \approx \frac{s + 2}{s + 4} \quad \text{A.4}$$

Inserting the approximation to Wagner's function (equation A.4) into equation A.3 and looking at one interval between  $s_{i-1}$  and  $s_i$ :

$$\int_{s_{i-1}}^{s_i} \frac{d(V\alpha)}{d\sigma} \frac{s_n - \sigma + 2}{s_n - \sigma + 4} d\sigma \quad \text{A.5}$$

If we now make interval between  $s_{i-1}$  and  $s_i$  small enough, equation A.5 can be rewritten as:

$$\left[ \frac{d(V\alpha)}{ds} \right]_{s=s_{i-1}}^{s_i} \int_{s_{i-1}}^{s_i} \frac{s_n - \sigma + 2}{s_n - \sigma + 4} d\sigma \quad \text{A.6}$$

Using equation A.2, the derivative part of equation A.6 can be rewritten into:

$$\frac{d(V\alpha)}{ds} = \frac{d(V\alpha)}{dt} \div \frac{ds}{dt} = \frac{d(V\alpha)}{dt} \div \frac{2U(t)}{c} = \frac{c}{2U(t)} \frac{d(V\alpha)}{dt} \quad \text{A.7}$$

Likewise the integral part of equation A.6 can be rewritten in form:

$$\int_{s_{i-1}}^{s_i} \frac{s_n - \sigma + 2}{s_n - \sigma + 4} d\sigma = \int_{s_{i-1}}^{s_i} \frac{\sigma}{\sigma - (s_n + 4)} d\sigma + \int_{s_{i-1}}^{s_i} \frac{-(s_n + 2)}{\sigma - (s_n + 4)} d\sigma \quad \text{A.8}$$

Using tables of standard integrals:

$$\int \frac{c}{ax + b} dx = \frac{c}{a} \ln(ax + b) \quad \text{A.9}$$

$$\int \frac{x}{ax + b} dx = \frac{x}{a} - \frac{b}{a^2} \ln(ax + b)$$

Equation A.8 can now be simplified to:

$$\begin{aligned} & \{ \sigma + (s_n + 4) \ln[\sigma - (s_n + 4)] - (s_n + 2) \ln[\sigma - (s_n + 4)] \}_{s_{i-1}}^{s_i} \\ & = \{ \sigma + 2 \ln[\sigma - (s_n + 4)] \}_{s_{i-1}}^{s_i} \end{aligned} \quad \text{A.10}$$

By applying limits to equation A.10, the integral part of equation A.5 can be rewritten as:

$$\int_{s_{i-1}}^{s_i} \frac{s_n - \sigma + 2}{s_n - \sigma + 4} d\sigma = s_i - s_{i-1} + 2 \ln \left[ \frac{s_i - (s_n + 4)}{s_{i-1} - (s_n + 4)} \right] \quad \text{A.11}$$

Using equation A.11, equation A.5 can be rewritten as:

$$\begin{aligned}
& \left[ \frac{d(V\alpha)}{ds} \right]_{s=s_i} \left\{ s_i - s_{i-1} + 2 \ln \left[ \frac{s_i - (s_n + 4)}{s_{i-1} - (s_n + 4)} \right] \right\} \\
& = [(V\alpha)_{s_i} - (V\alpha)_{s_{i-1}}] \\
& + 2 \left[ \frac{d(V\alpha)}{ds} \right]_{s=s_i} \ln \left[ \frac{s_i - (s_n + 4)}{s_{i-1} - (s_n + 4)} \right]
\end{aligned} \tag{A.12}$$

Now equation A.3 becomes:

$$\begin{aligned}
& \int_0^{s_n} \frac{d(V\alpha)}{d\sigma} \phi(s_n - \sigma) d\sigma = \sum_{i=1}^n \int_{s_{i-1}}^{s_i} \frac{d(V\alpha)}{d\sigma} \phi(s_n - \sigma) d\sigma \\
& = \sum_{i=1}^n [(V\alpha)_{s_i} - (V\alpha)_{s_{i-1}}] + \sum_{i=1}^n 2 \left[ \frac{d(V\alpha)}{ds} \right]_{s=s_i} \ln \left[ \frac{s_i - (s_n + 4)}{s_{i-1} - (s_n + 4)} \right] \\
& = V(s_n)\alpha(s_n) - V(s_0)\alpha(s_0) \\
& + \sum_{i=1}^n \left\{ 2 \left[ \frac{d(V\alpha)}{ds} \right]_{s=s_i} \ln \left[ \frac{s_i - (s_n + 4)}{s_{i-1} - (s_n + 4)} \right] \right\}
\end{aligned} \tag{A.13}$$

Using equation A.13 for  $s = s_n$ , the circulatory lift coefficient of equation A.1 is now in the form of:

$$\begin{aligned}
C_L^c(s_n) &= \frac{2\pi}{V(s_n)} \left| V(s_0)\alpha(s_0)\phi(s_n) + V(s_n)\alpha(s_n) - V(s_0)\alpha(s_0) \right. \\
& \quad \left. + \sum_{i=1}^n \left\{ 2 \left[ \frac{d(V\alpha)}{ds} \right]_{s=s_i} \ln \left[ \frac{s_i - (s_n + 4)}{s_{i-1} - (s_n + 4)} \right] \right\} \right|
\end{aligned} \tag{A.14}$$

However,  $\phi(s) \rightarrow 1$  as  $s \rightarrow \infty$ :

$$C_L^c(s_n) = \frac{2\pi}{V(s_n)} \left| V(s_n)\alpha(s_n) + \sum_{i=1}^n \left\{ 2 \left[ \frac{d(V\alpha)}{ds} \right]_{s=s_i} \ln \left[ \frac{s_i - (s_n + 4)}{s_{i-1} - (s_n + 4)} \right] \right\} \right| \tag{A.15}$$

Equation A.15 now represents the circulatory part of the lift coefficient as a summation of the quasi-steady and memory-effect components.

The effective angle of attack can now be expressed as:

$$\alpha_e(s_n) = \frac{1}{V(s_n)} \left| V(s_n) \alpha(s_n) + \sum_{i=1}^n \left\{ 2 \left[ \frac{d(V\alpha)}{ds} \right]_{s=s_i} \ln \left[ \frac{s_i - (s_n + 4)}{s_{i-1} - (s_n + 4)} \right] \right\} \right| \quad \text{A.16}$$

## A1.5. 6 DsoF

### A1.5.1. Sway

Sway is a translational degree-of-freedom, which resembles side-to-side motion of a wind turbine (Figure 169).

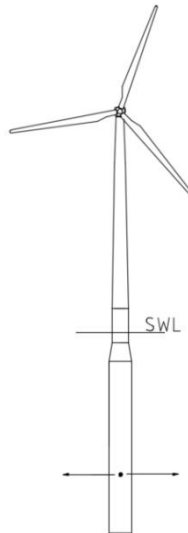


Figure 169 – Sway motion

Compared to the surge DoF, the azimuth angle has to be accounted for. Azimuth angle dependence can be imagined by splitting the rotor into two equal parts by drawing a horizontal line through the centre. Depending on the relative motion of the blade and swaying motion, one half of the rotor disc will see an overall increase in the in-plane velocity and a decrease in the other.

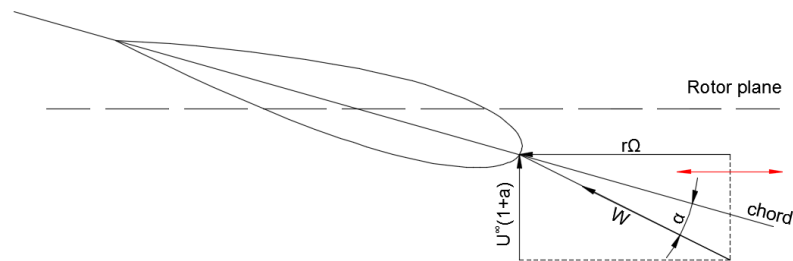


Figure 170 – Sway influence on the in-plane velocity seen by a blade element

Similarly as in surge, sway motion induced velocity can be added to the blade element triangle by superimposing it on top of the in-plane velocity as shown in Figure 170.

Defining sway motion as  $A \sin(\omega t)$  and sway velocity as  $\omega A \cos(\omega t)$ , it can be shown that:

$$W(t) = \sqrt{[r\Omega + \omega A \cos(\omega t) \cos(\Omega t)]^2 + [U_\infty(1 - a)]^2} \quad \text{A.17}$$

$$\alpha(t) = \tan^{-1} \left[ \frac{U_\infty(1 - a)}{r\Omega + \omega A \cos(\omega t) \cos(\Omega t)} \right] - \beta \quad \text{A.18}$$

It is important to get the correct sign in the denominator of Equation A.18. It depends on the initial assumption of the rotor and sway motion directions. In this report, it is assumed that initially the blade is at 0 azimuth angle (straight upright) and that the rotor is rotating clock-wise, and sway motion is initially to the left.

While in this report the sway DoF is represented as an increase or a decrease in the in-plane velocity of blade elements, it could have also been modelled as a yawing turbine.

### A1.5.2. Heave

Heave is the last translational DoF. Very much like sway, simplified, heave motion can be represented as variation in the in-plane velocity at each blade element.

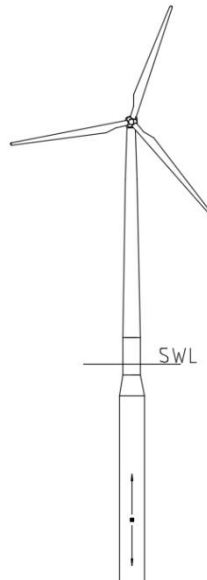


Figure 171 – Heave motion

Similarities can be drawn between heave and sway dependence on the azimuth angle of the blade. In sway a horizontal line was drawn through the centre of the rotor disc, now, a vertical one needs to be drawn to see how one side will see an increase and the other a decrease in the total in-plane velocity as seen by the blade elements.

Using the same assumptions as in surge (clock-wise blade rotation, initial 0 azimuth angle and opposing initial heave and blade motion directions) and defining heave velocity as  $\omega A \cos(\omega t)$ , one can see from Figure 172 how the angle-of-attack can be expressed in a very similar format as before in sway.

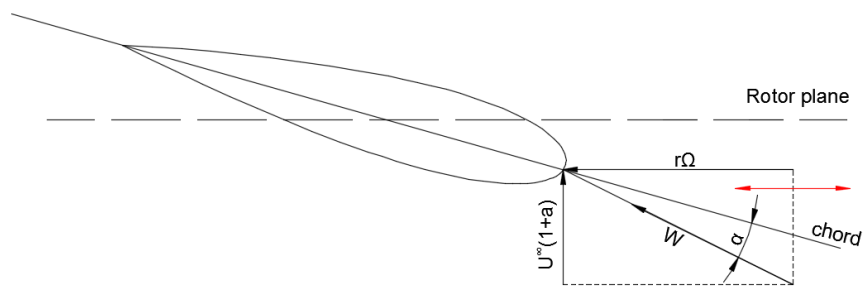


Figure 172 – Heave influence on the in-plane velocity seen by blade element

$$W(t) = \sqrt{[r\Omega - \omega A \cos(\omega t) \sin(\Omega t)]^2 + [U_\infty(1 - a)]^2} \quad \text{A.19}$$

$$\alpha(t) = \tan^{-1} \left[ \frac{U_\infty(1 - a)}{r\Omega - \omega A \cos(\omega t) \sin(\Omega t)} \right] - \beta \quad \text{A.20}$$

### A1.5.3. Roll

The roll DoF, besides pitch and yaw, is one of the three rotational DsoF. It exhibits a side-to-side rocking motion (Figure 173). Potentially, it is one of the most destructive DsoF, as it offers very little aerodynamic damping compared to the pitch or yaw DsoF.

The rotational roll DoF can be simplified into the translational sway DoF (which has already been derived) – representing motion as a change in the rotational velocity for each blade element.

Given that:

$$\text{Roll} = \theta = A \sin(\omega t) \quad \text{A.21}$$

$$\text{Roll velocity} = \dot{\theta} = \omega A \cos(\omega t) \quad \text{A.22}$$

Sway displacement can be approximated by adding together the hub and blade element displacement:

$$\text{hub displacement} = l * \sin(\theta) \approx l * A \sin(\omega t) \quad \text{A.23}$$

$$\text{blade element displacement} = r * \cos(\Omega t) * A \sin(\omega t) \quad \text{A.24}$$

where  $\cos(\Omega t)$  presents dependence to the azimuth angle. Combining both displacements together, the total sway velocity can be expressed as:

$$\text{Total sway displacement} = (l + r \cos(\Omega t)) * A \sin(\omega t) \quad \text{A.25}$$

$$\text{Total sway velocity} = (l + r \cos(\Omega t)) * \omega A \cos(\omega t) \quad \text{A.26}$$

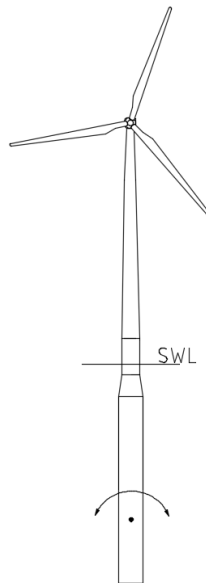


Figure 173 – Roll motion

If modelled very precisely, the roll DoF is a combination of the sway and heave DsoF. However, as a first approximation, roll can be modelled by only using sway (completely ignoring heave). It can be shown using simple trigonometry, that for 5 degree displacement

in roll, only  $\approx 0.57$  m displacement in heave will be seen by the hub of the 5MW NREL spar-type wind turbine. This increases to  $\approx 0.8$  m at the blade tip at  $0^\circ$  azimuthal angle with 210 m distance to the centre of mass of the system.

The apparent wind velocity and angle-of-attack can be expressed as:

$$W(t) = \sqrt{\left\{ r \left[ \Omega + \left( \frac{l}{r} + \cos(\Omega t) \right) \omega A \cos(\omega t) \right] \right\}^2 + [U_\infty(1-a)]^2} \quad \text{A.27}$$

$$\alpha(t) = \tan^{-1} \left\{ \frac{U_\infty(1-a)}{r \left[ \Omega + \left( \frac{l}{r} + \cos(\Omega t) \right) \omega A \cos(\omega t) \right]} \right\} - \beta \quad \text{A.28}$$

#### A1.5.4. Pitch

The pitch DoF should not be confused with pitching of the rotor blades. Figure 174 shows a typical rotational movement of a floating wind turbine in pitching around its centre of mass.

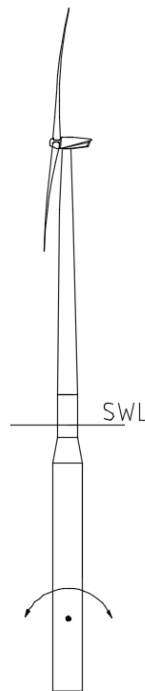


Figure 174 – Pitch DoF

Pitching of a floating wind turbine can be modelled as surging of blade elements by different amounts depending on the blade elements' distance from the centre of mass and azimuth angle.

Representing pitching as  $\theta = A \sin(\omega t)$  and pitching velocity as  $\dot{\theta} = \omega A \cos(\omega t)$ , the whole floating system can be simplified as shown in Figure 175.

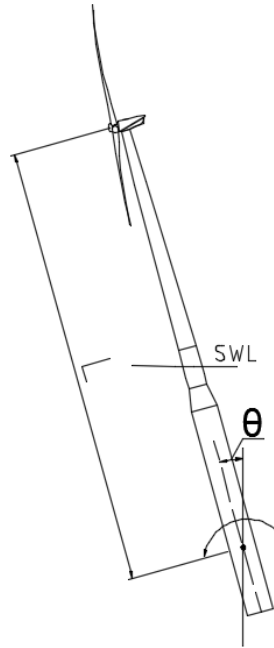


Figure 175 – Simplified pitch DoF

From Figure 175:

$$\text{surge displacement} = (l + r \cos(\Omega t)) \sin(\theta) \quad \text{A.29}$$

Using small-angle approximation (assuming that turbine is not pitching more than 5 deg.):

$$\text{surge velocity} = (l + r \cos(\Omega t)) * \omega A \cos(\omega t) \quad \text{A.30}$$

Now, pitching of wind turbine can be represented as a change in the free-stream velocity – just like in surge.

$$W(t) = \sqrt{(r\Omega)^2 + \{U_\infty(1 - a) + [l + r \cos(\Omega t)] * \omega A \cos(\omega t)\}^2} \quad \text{A.31}$$

$$\alpha(t) = \tan^{-1} \left\{ \frac{U_{\infty}(1 - a) + [l + r \cos(\Omega t)] * \omega A \cos(\omega t)}{r\Omega} \right\} - \beta \quad \text{A.32}$$

The pitch DoF of a floating platform is a combination of the surge and heave DsoF. In this model heave contribution was ignored.

#### A1.5.5. Yaw

The yaw DoF is probably one of the most common DsoF in real wind turbine environment, as very often turbines are not aligned with the free-stream velocity and are actually operating in a slight yaw. In floating wind turbines this DoF is further amplified by coupling between different DsoF and misalignment between the wave and wind inputs to the system.

Very much like all other rotational DsoF, yaw can be represented using one of the translational DsoF - surge.

Two different degree-of-complexity representations of the yaw DoF were used. Both represented yaw using surge, however, one included a modification to the free-stream and in-plane velocity due to the skewed flow, while the other did not. Both representations are given below.

The simplest way to represent yaw is by surging of blade element by different amounts.

$$\text{Yaw angle} = \theta = A \sin(\omega t) \quad \text{A.33}$$

$$\text{Yaw velocity} = \dot{\theta} = \omega A \cos(\omega t) \quad \text{A.34}$$

When yawing, blade elements will see opposite effects on the left and right side of the rotor. One side of the rotor will see an increase in the free-stream velocity and vice versa on the other. This variation, which depends on the azimuthal angle, can be represented using a sine function (assuming blade is upright at  $t = 0$ ).

$$\text{surge displacement} = rA * \sin(\omega t) * \sin(\Omega t) \quad \text{A.35}$$

The incident velocity and the angle-of-attack can be expressed as:

$$W(t) = \sqrt{(r\Omega)^2 + [U_\infty(1 - a) + r\omega A \cos(\omega t) \sin(\Omega t)]^2} \quad \text{A.36}$$

$$\alpha(t) = \tan^{-1} \left[ \frac{U_\infty(1 - a) + r\omega A \cos(\omega t) \sin(\Omega t)}{r\Omega} \right] - \beta \quad \text{A.37}$$

For a slightly more realistic representation of the yaw DoF, one needs to modify the free-stream and the in-plane velocity by the circulatory component seen by each blade element.

The free stream velocity becomes:

$$U_\infty(1 - a) * \cos(\theta) \approx U_\infty(1 - a) * \left(1 - \frac{\theta}{2}\right) \quad \text{A.38}$$

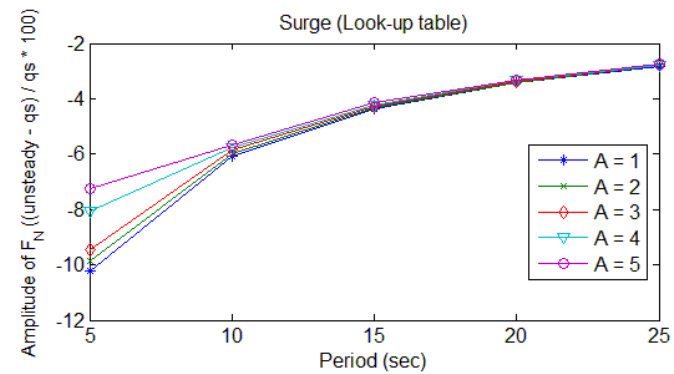
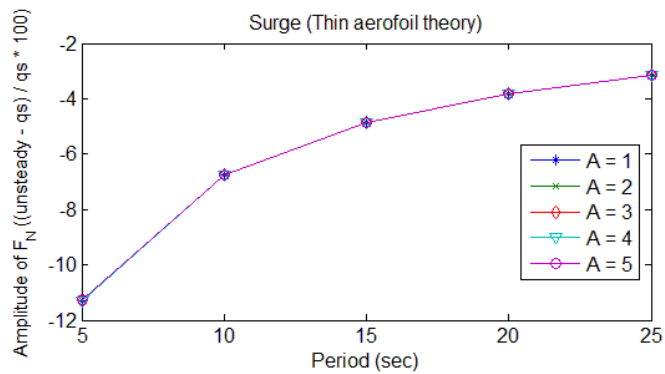
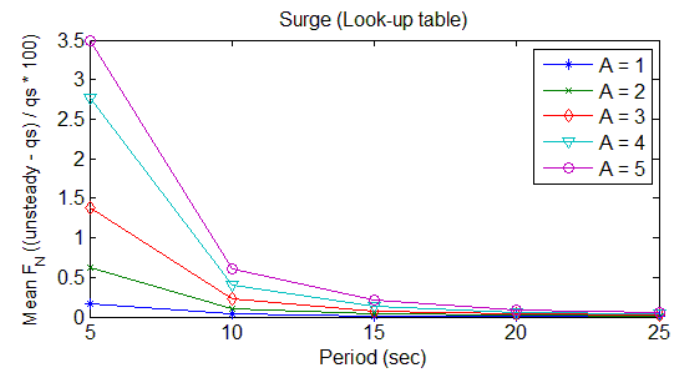
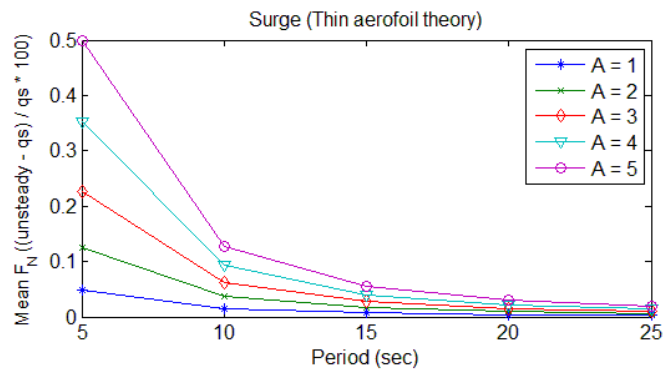
and the adjusted in-plane component:

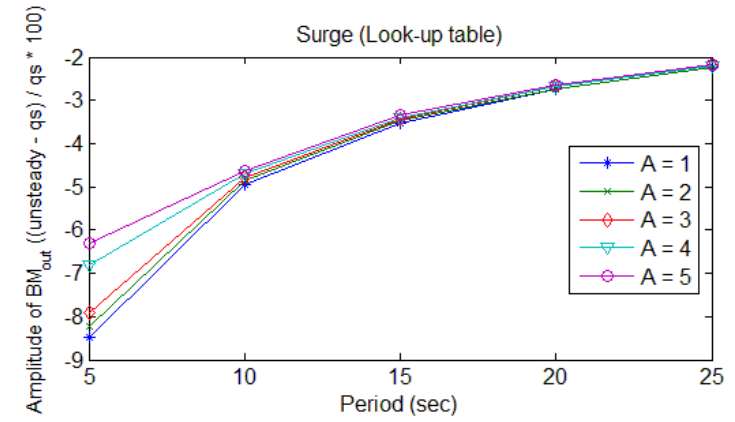
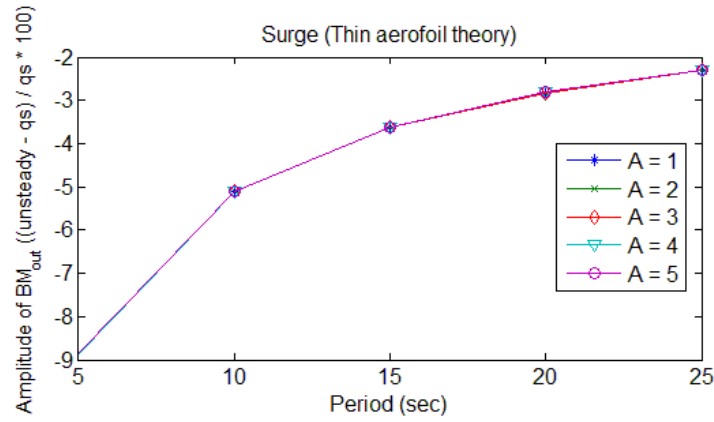
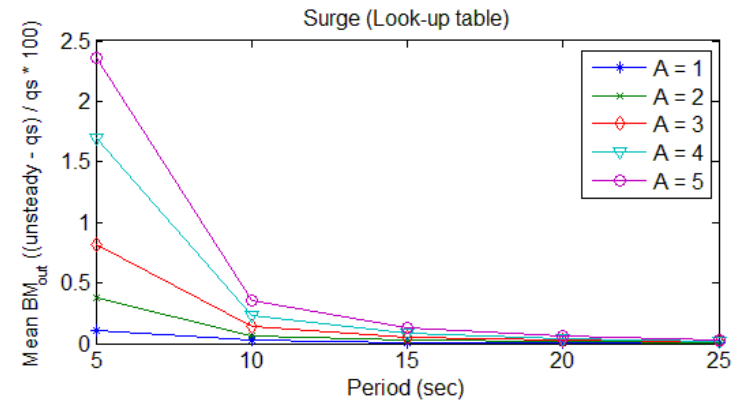
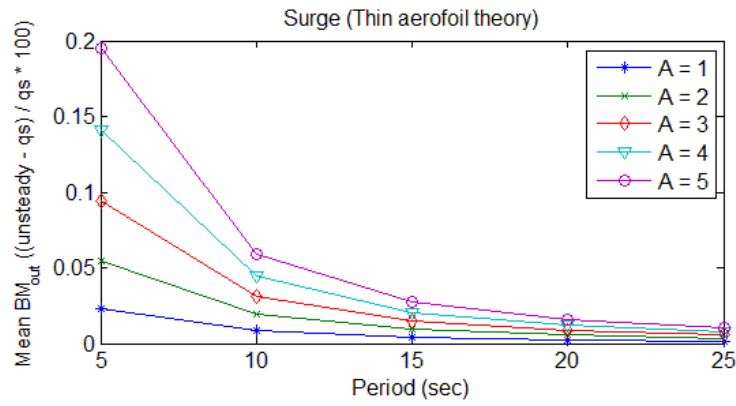
$$r\Omega + U_\infty(1 - a) * \sin(\theta) * \cos(\Omega t) \quad \text{A.39}$$

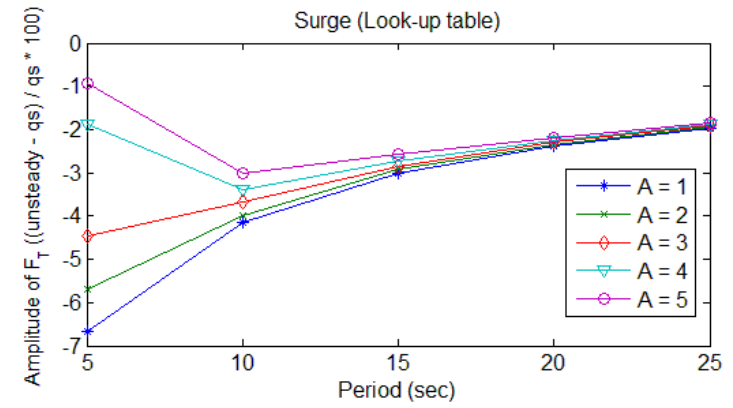
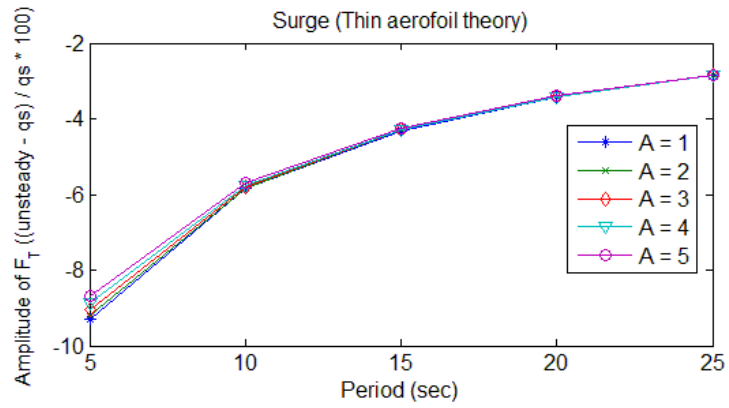
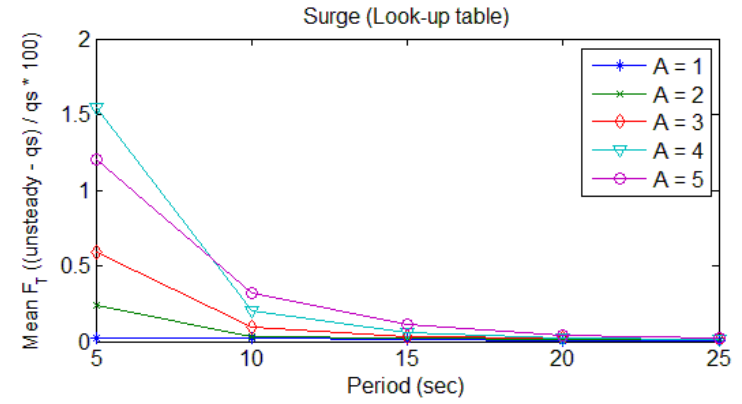
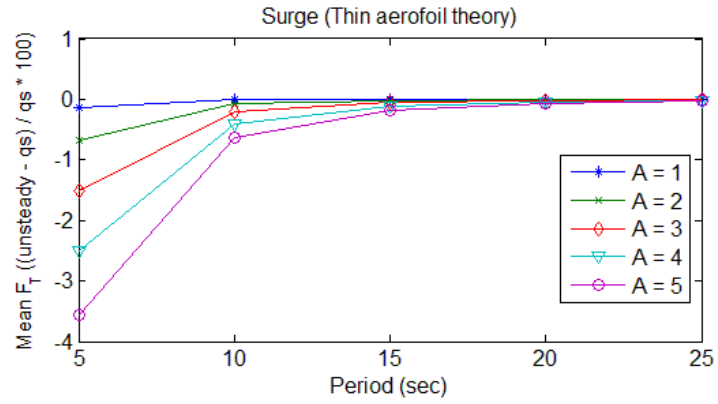
The difference between including and not including the cyclic component modification to the free-stream and in-plane velocity could change the angle-of-attack from 0 deg. at the blade tip to approx. 5 deg. at the blade root.

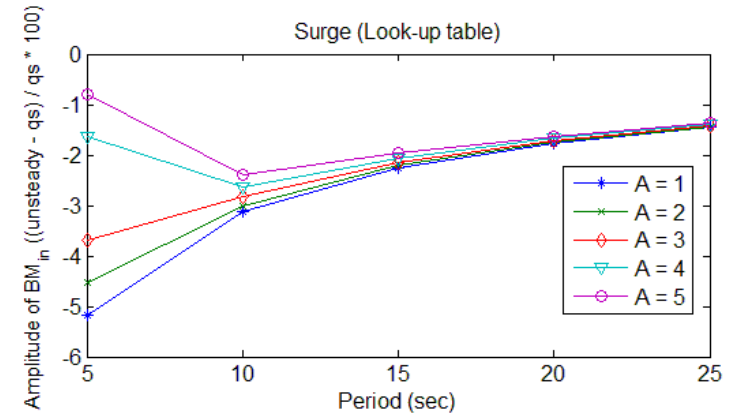
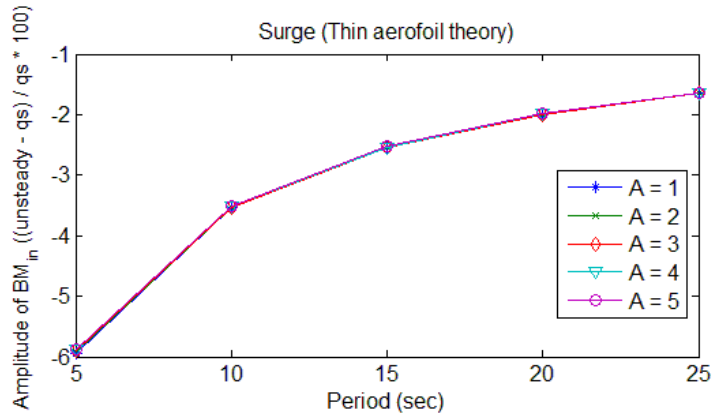
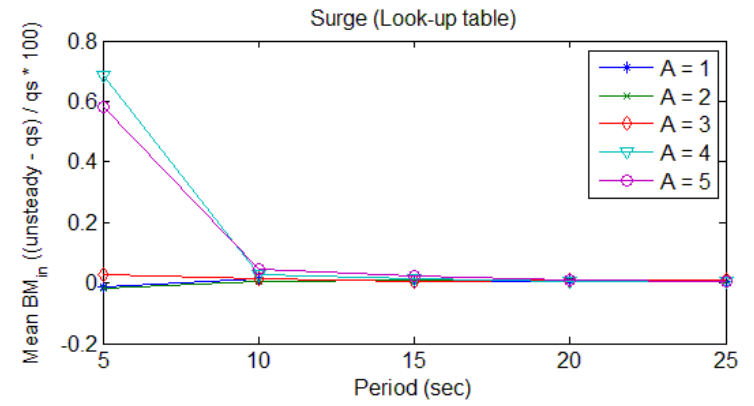
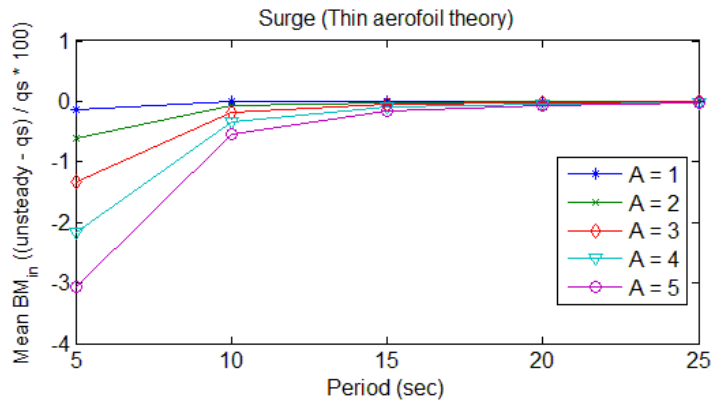
## A1.6. Van der Wall and Leishman - Results

### A1.6.1. Surge

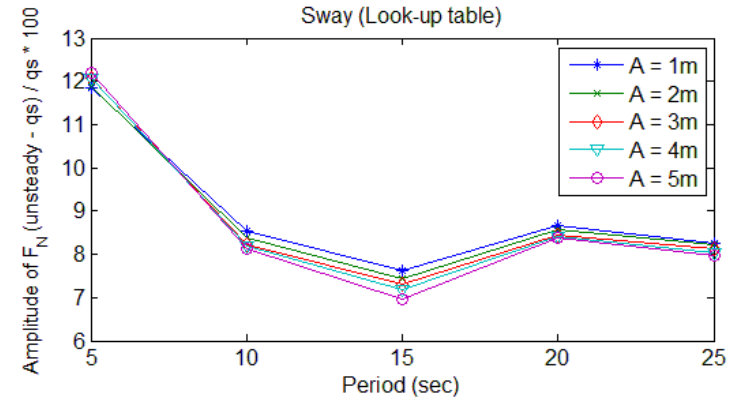
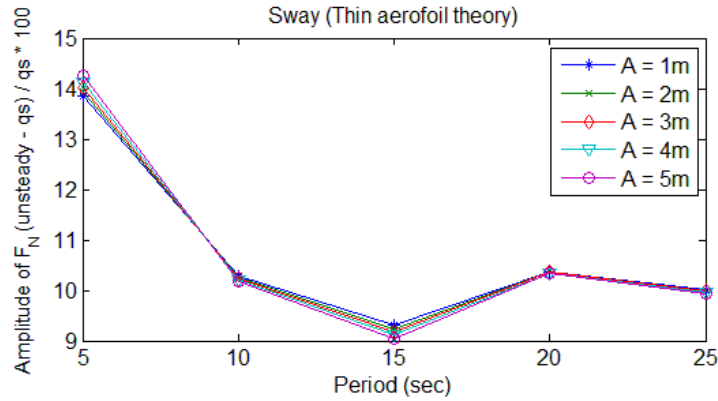
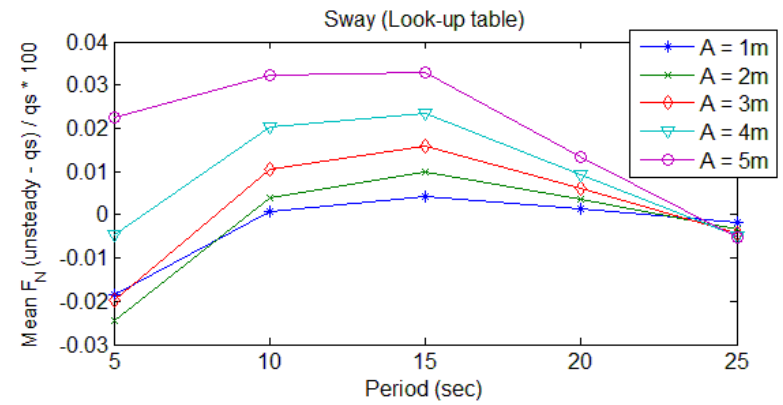
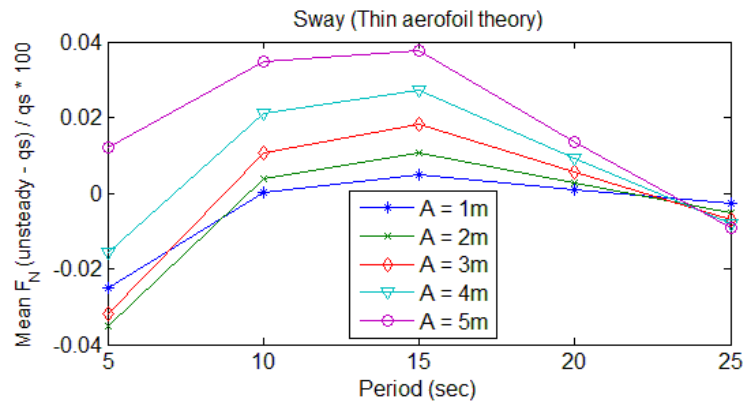


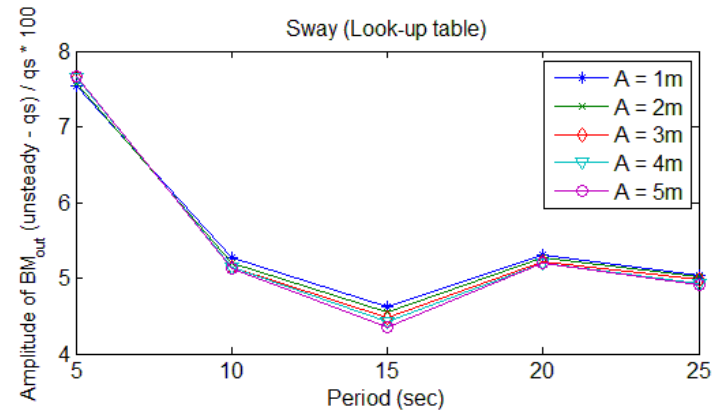
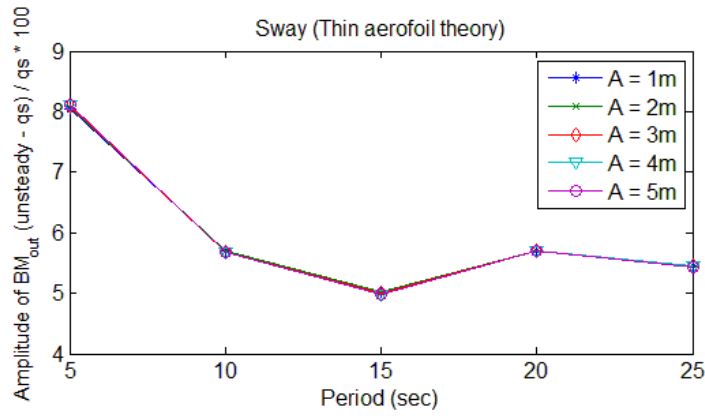
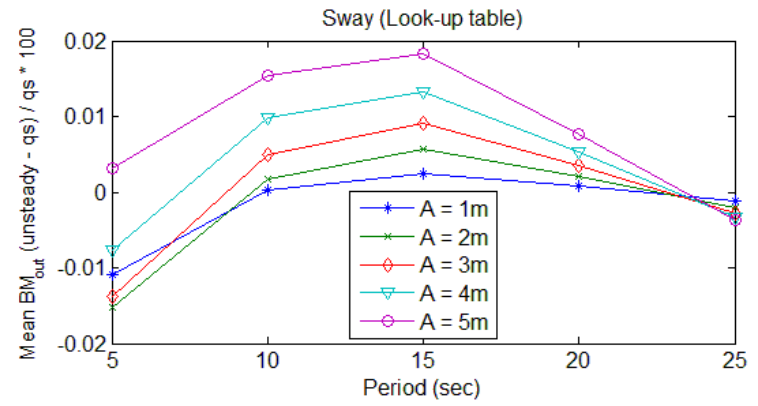
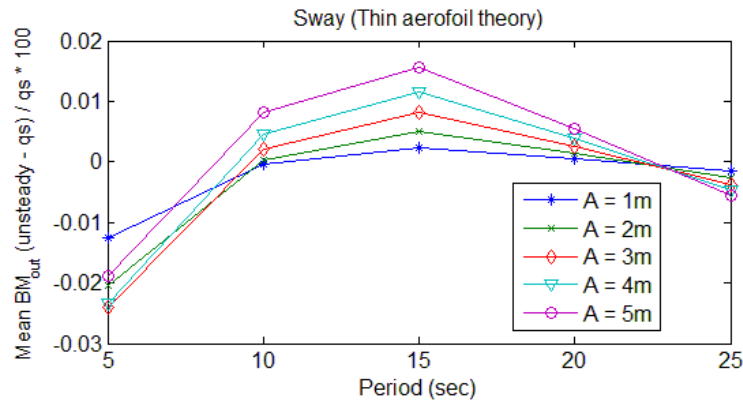


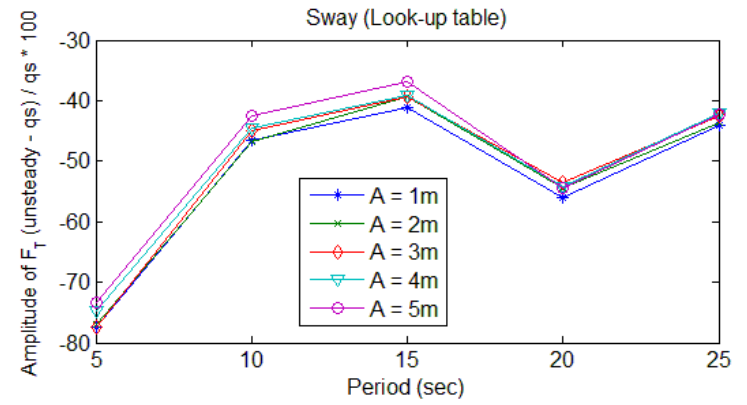
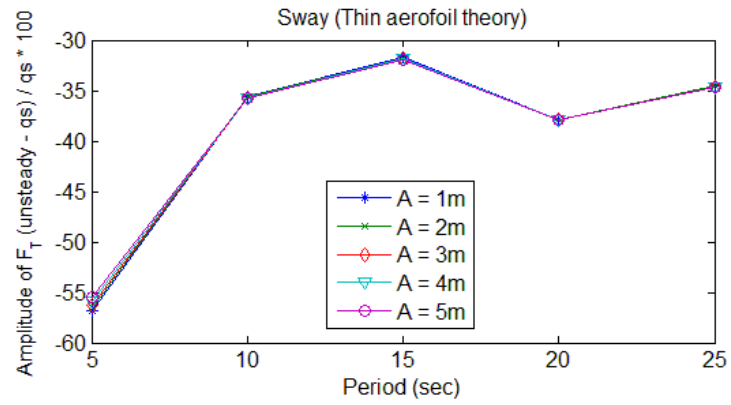
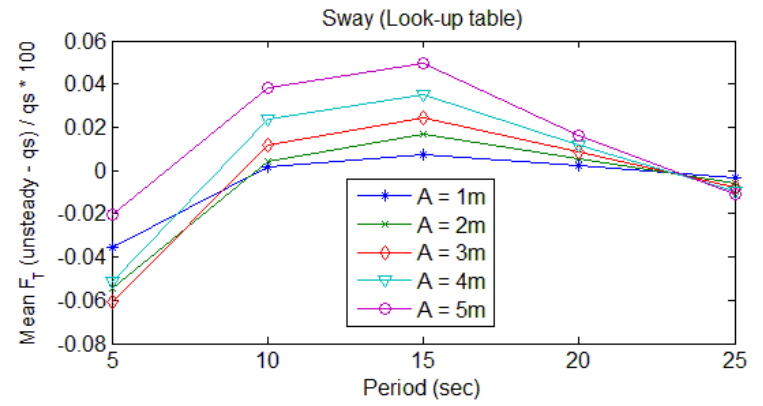
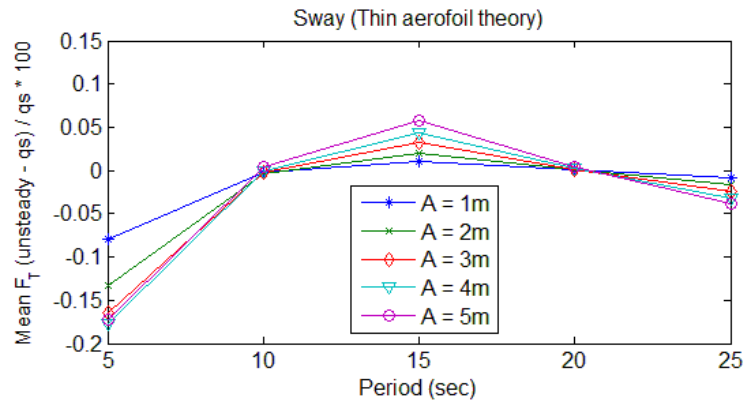


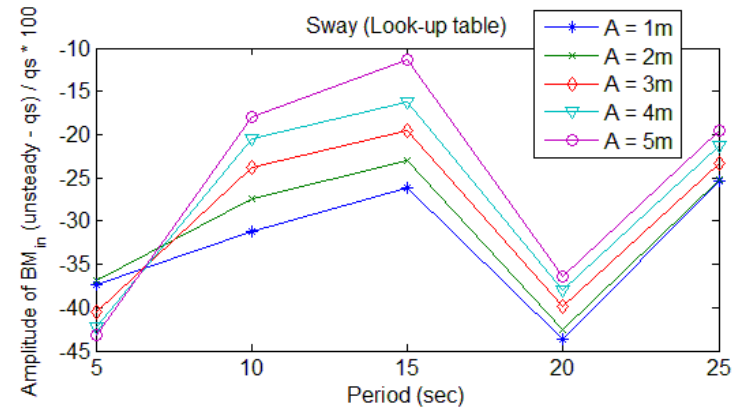
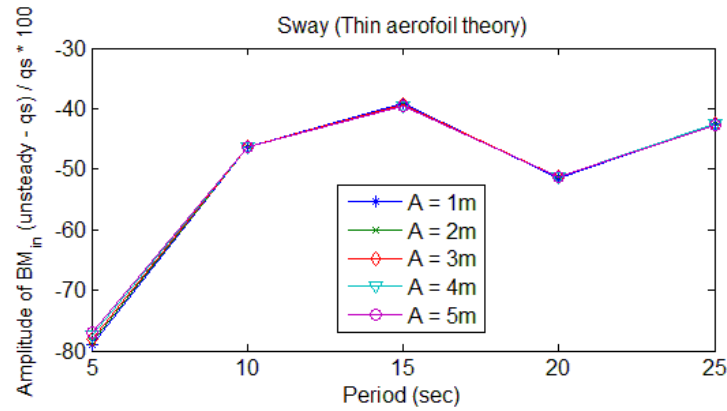
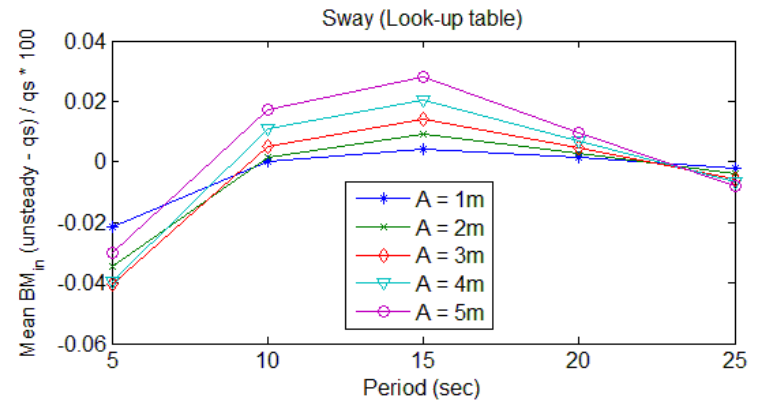
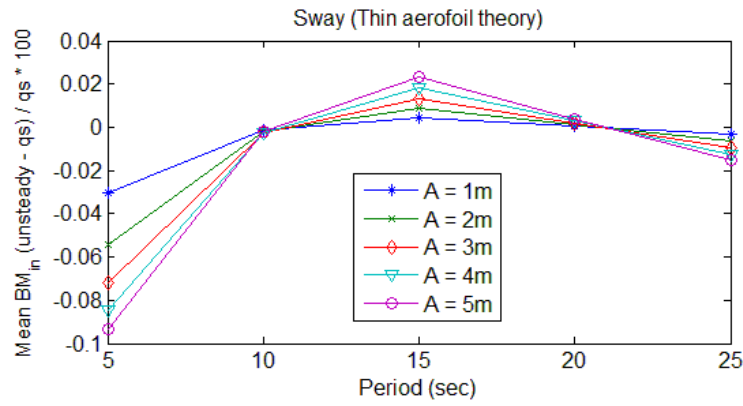


### A1.6.2. Sway

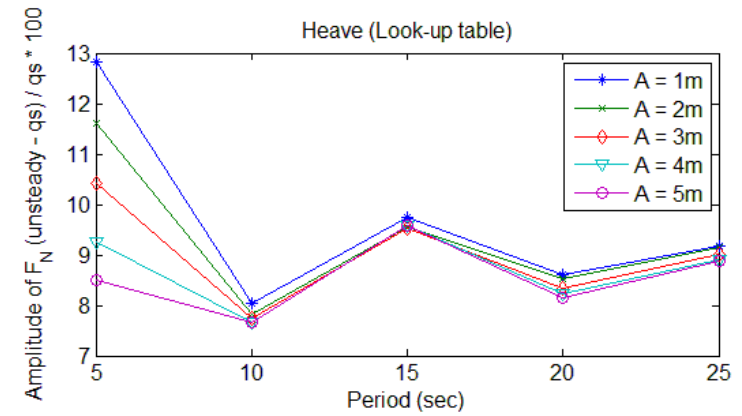
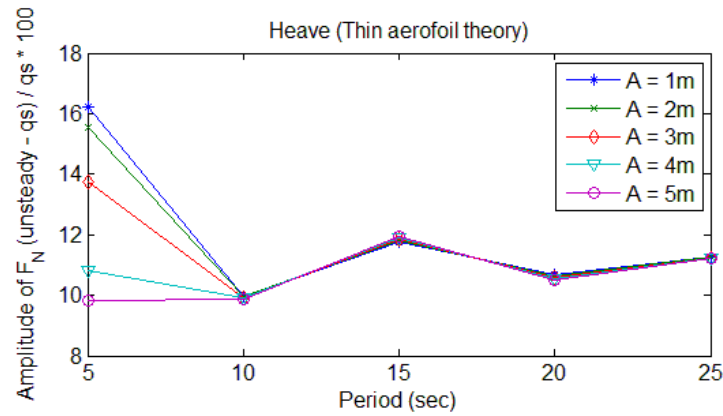
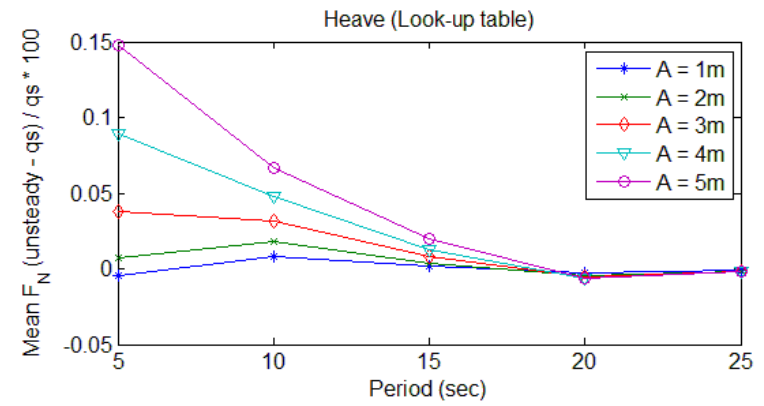
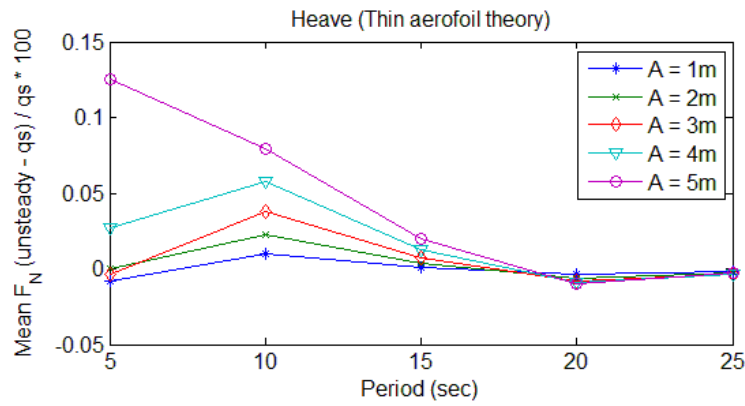


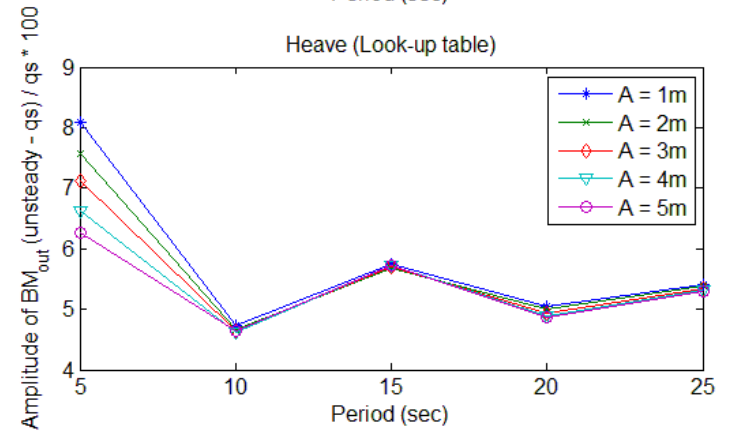
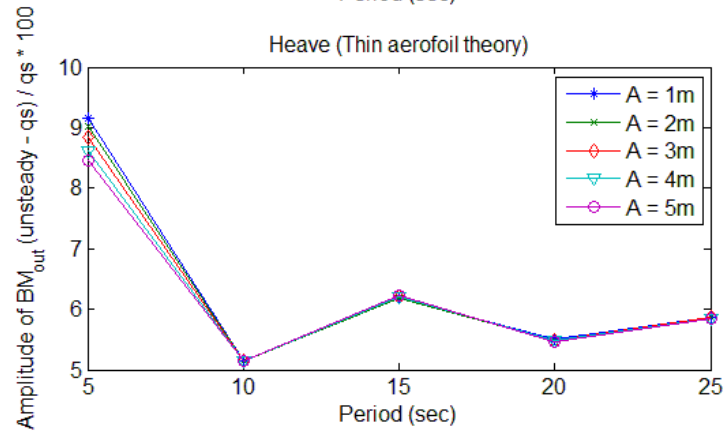
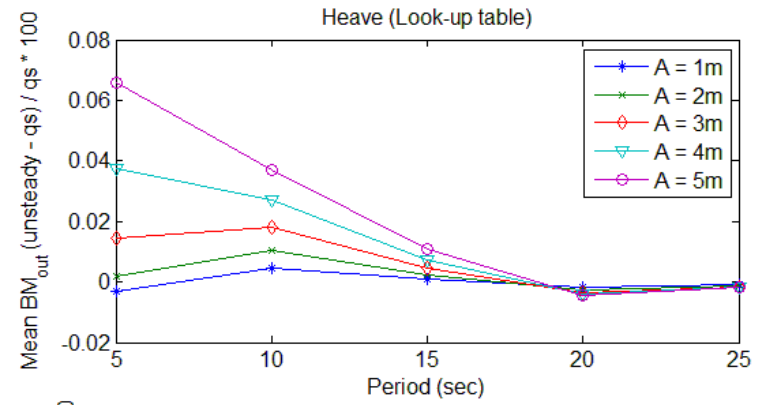
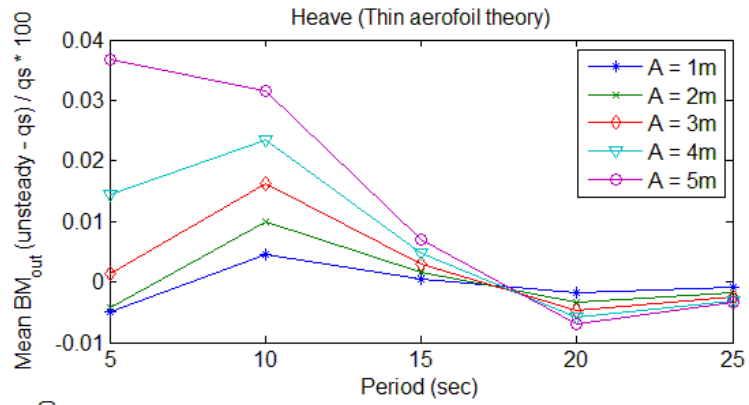


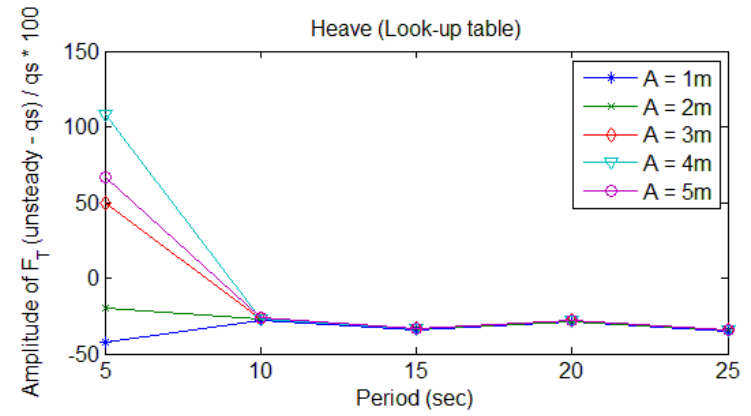
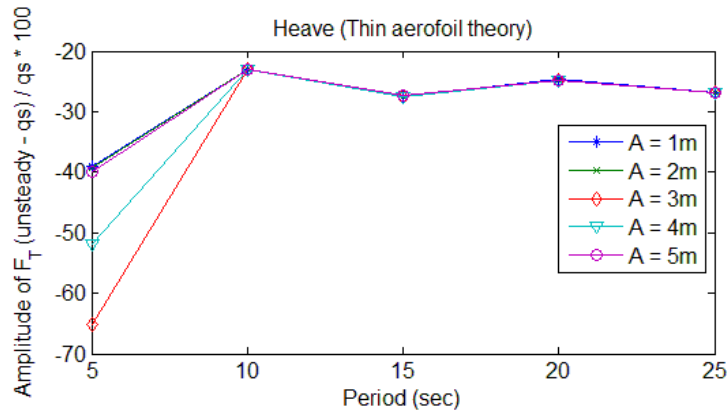
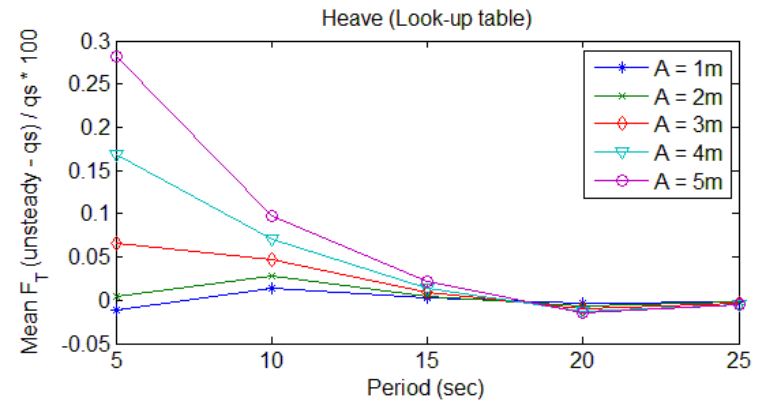
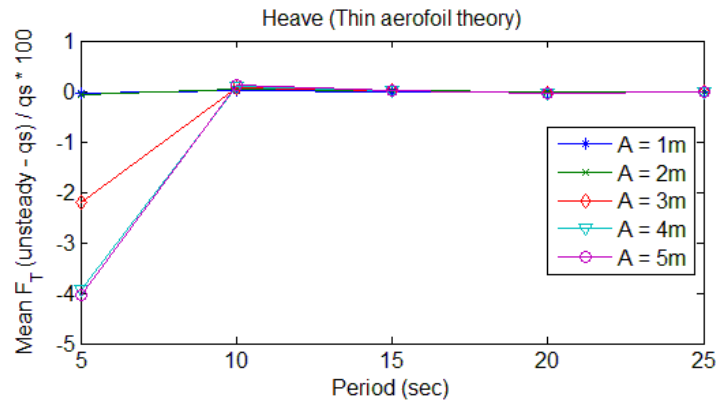


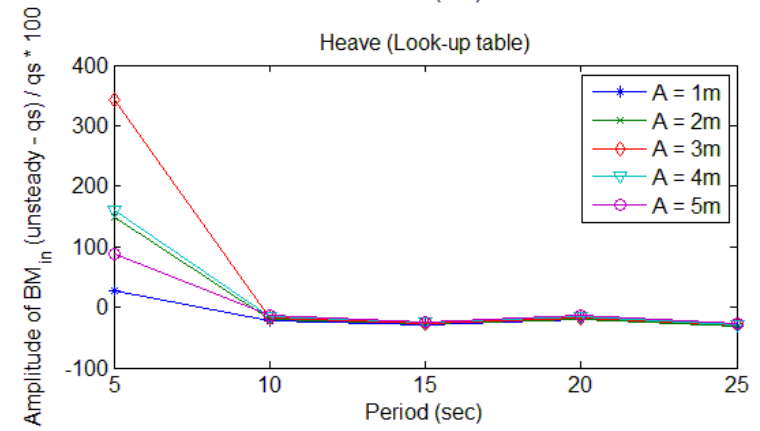
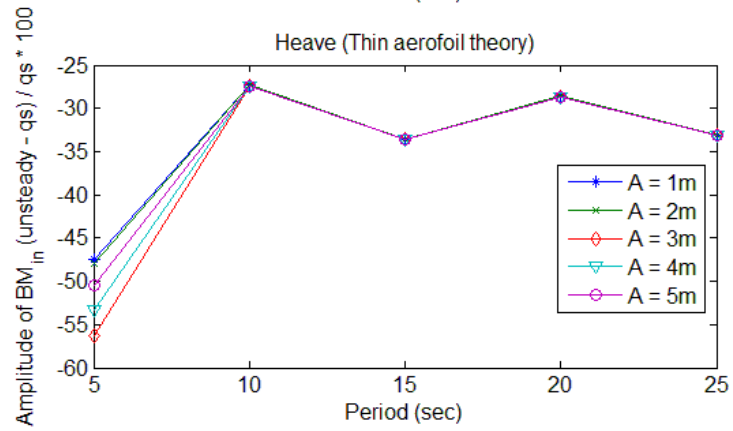
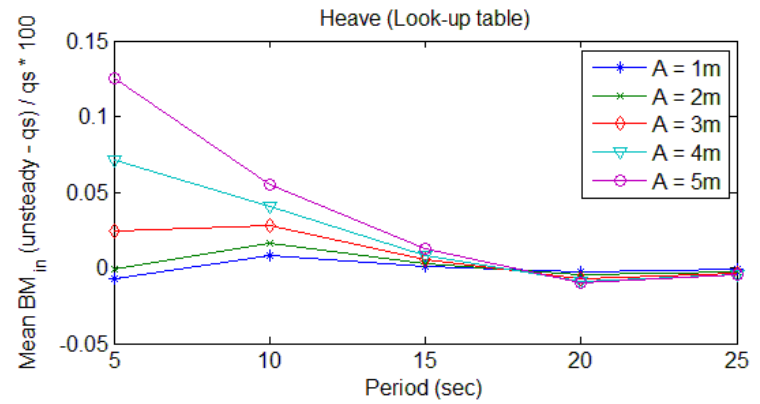
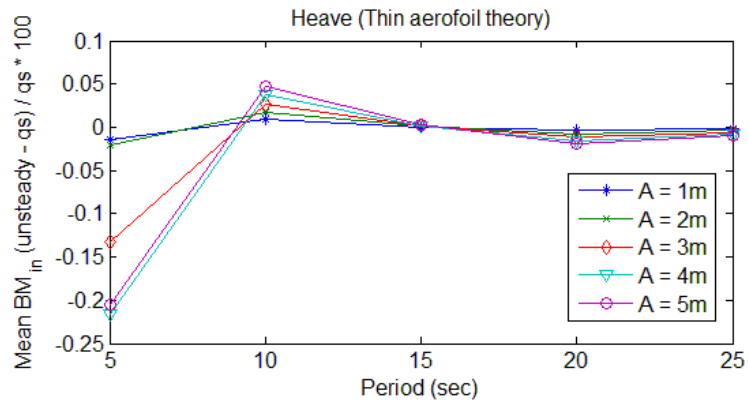


### A1.6.3. Heave

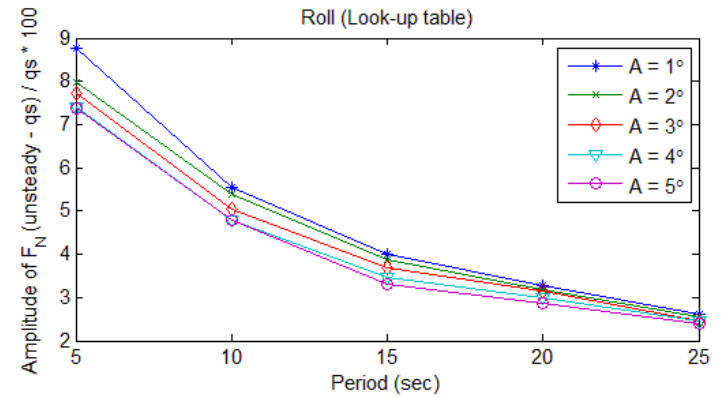
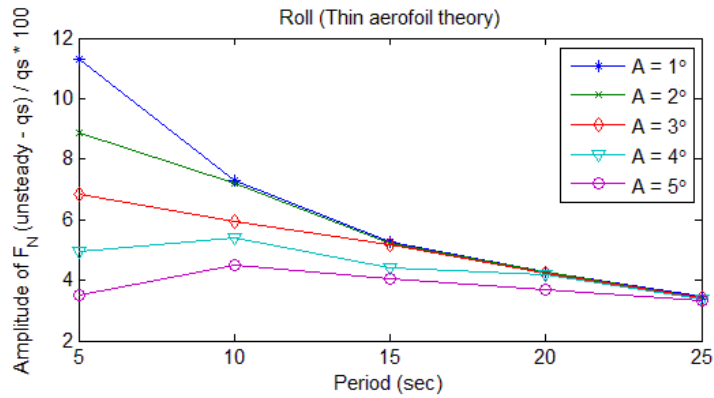
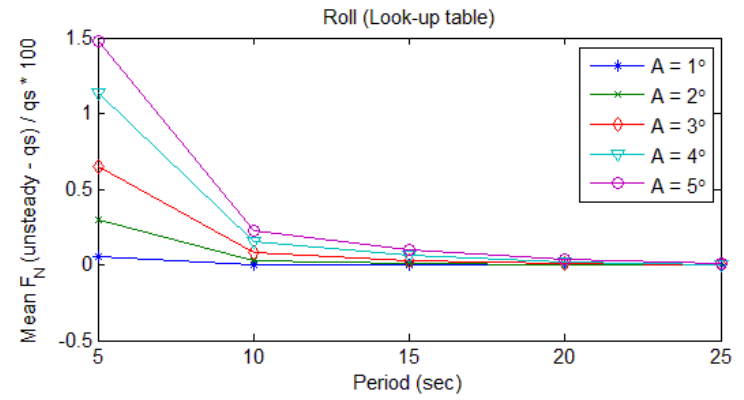
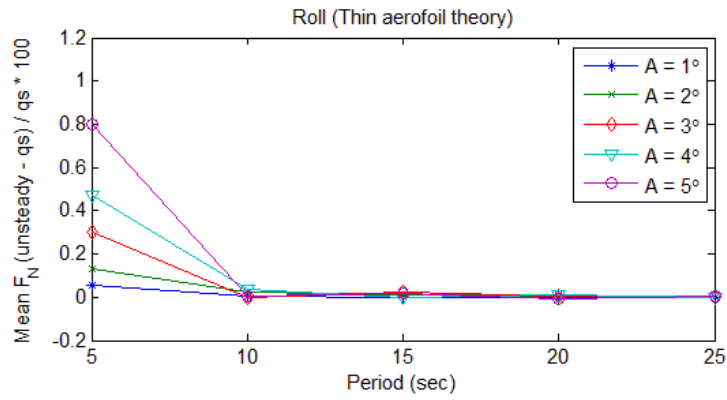


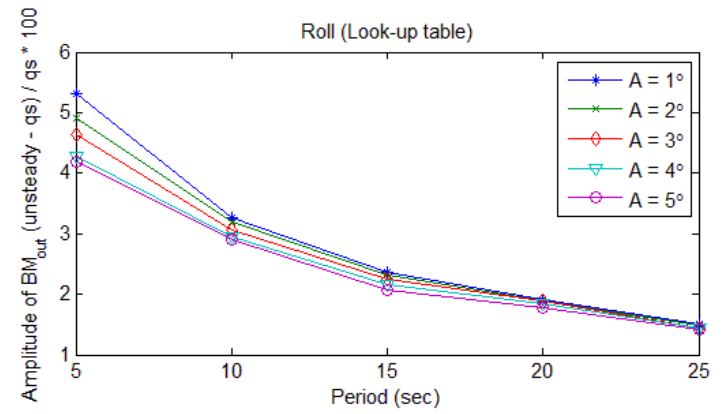
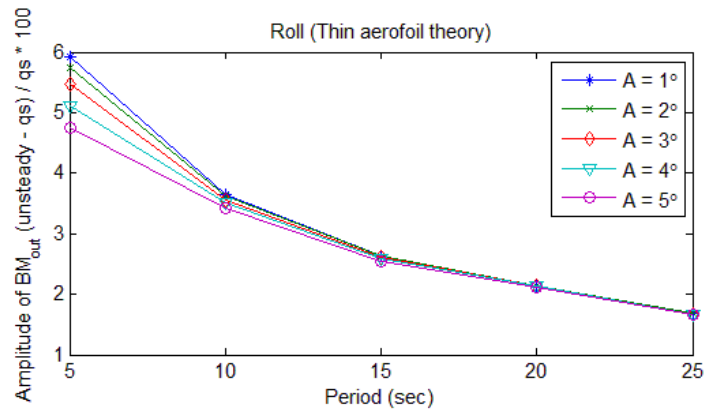
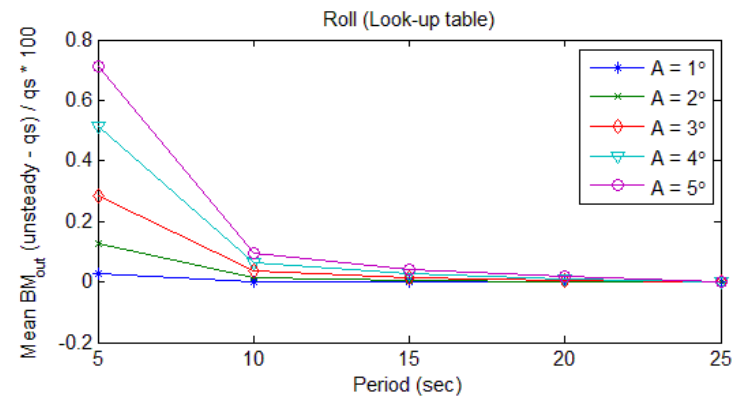
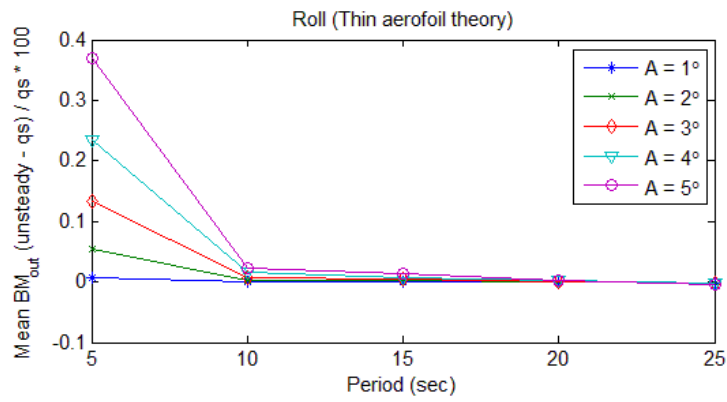


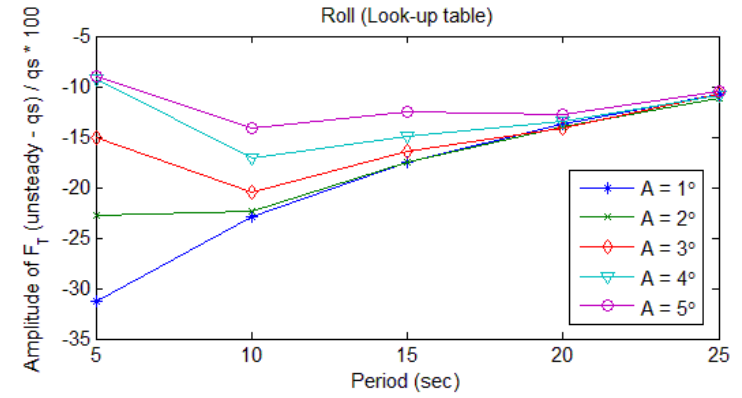
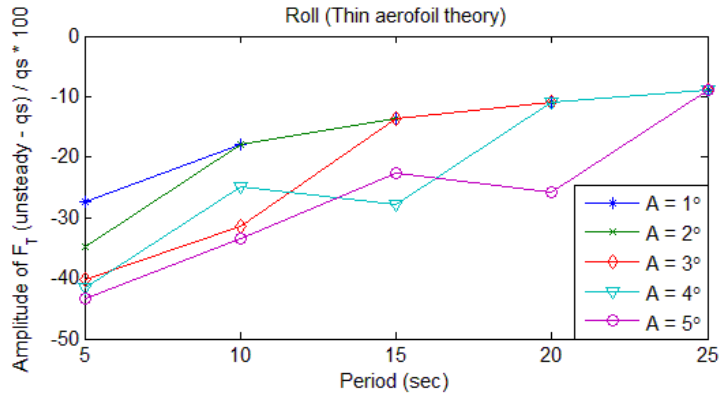
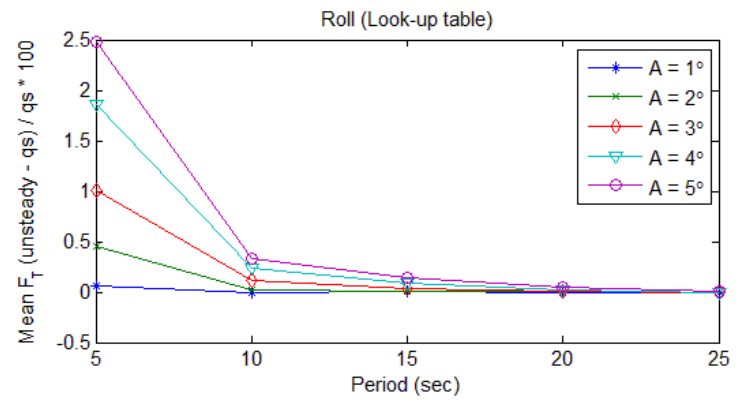
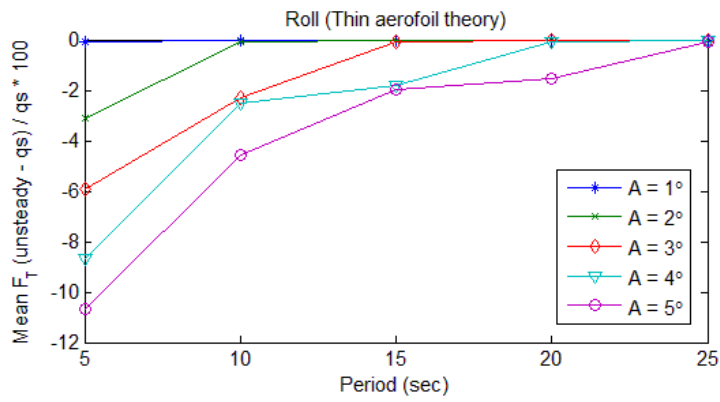


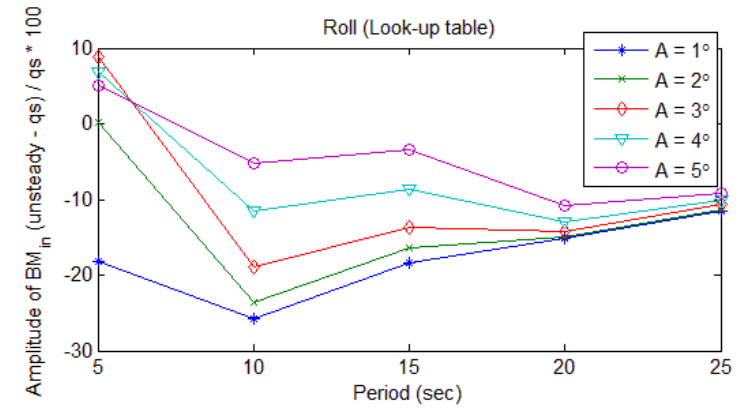
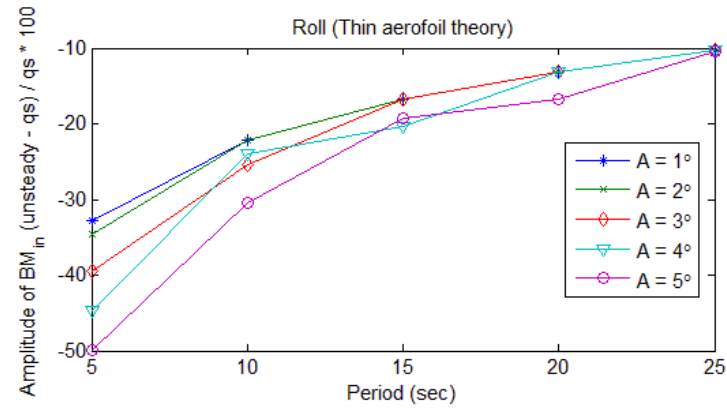
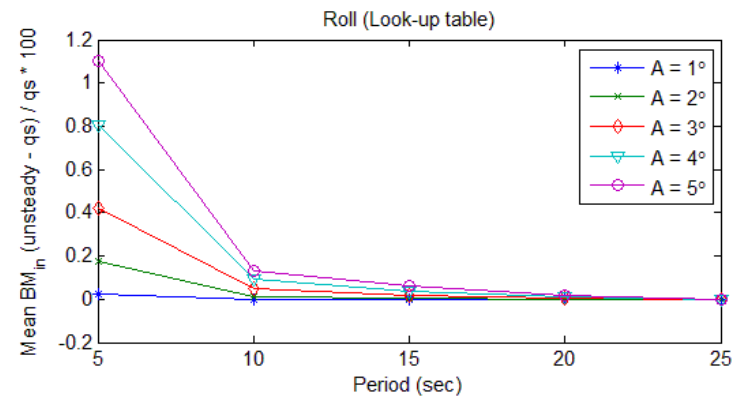
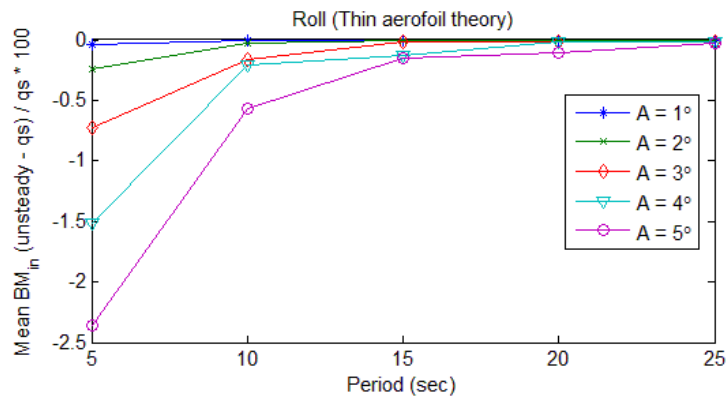


### A1.6.4. Roll

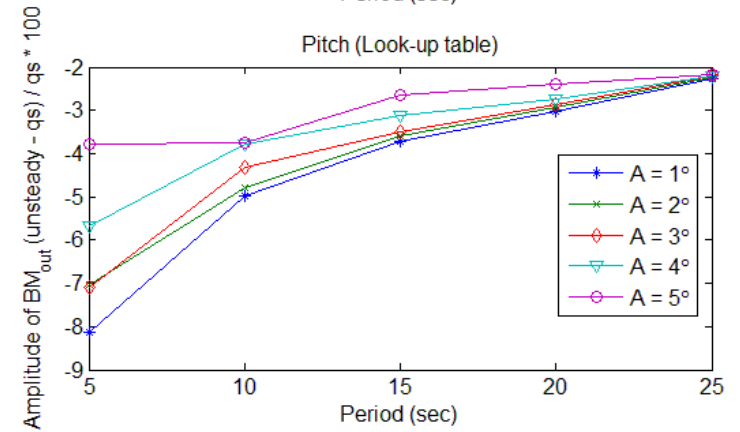
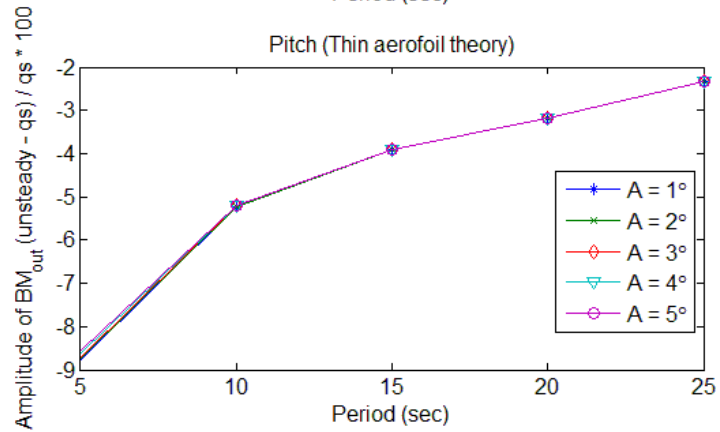
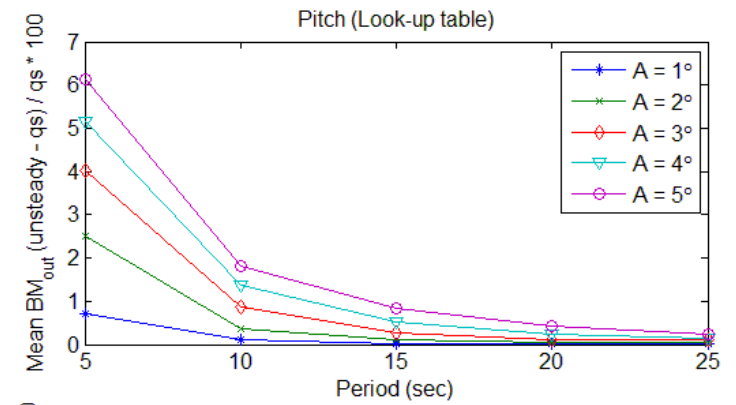
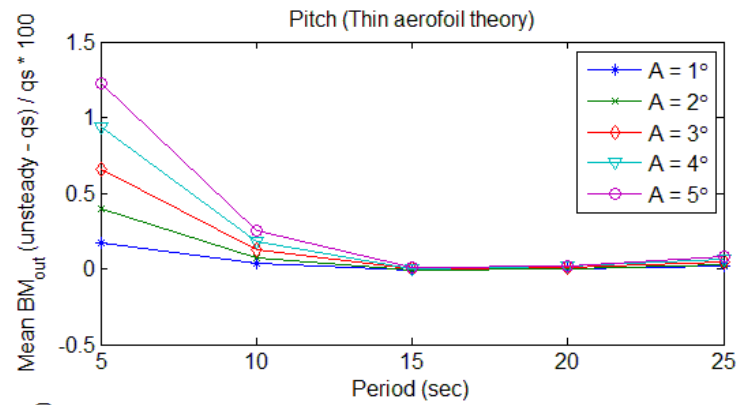


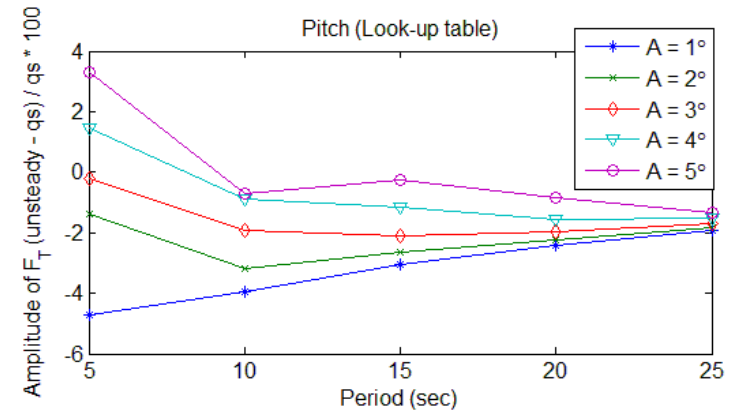
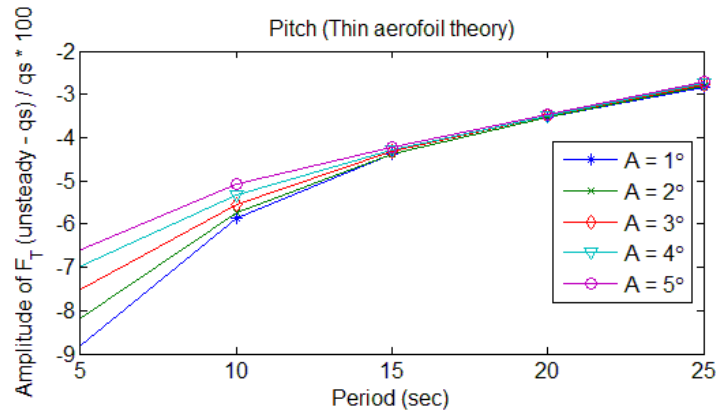
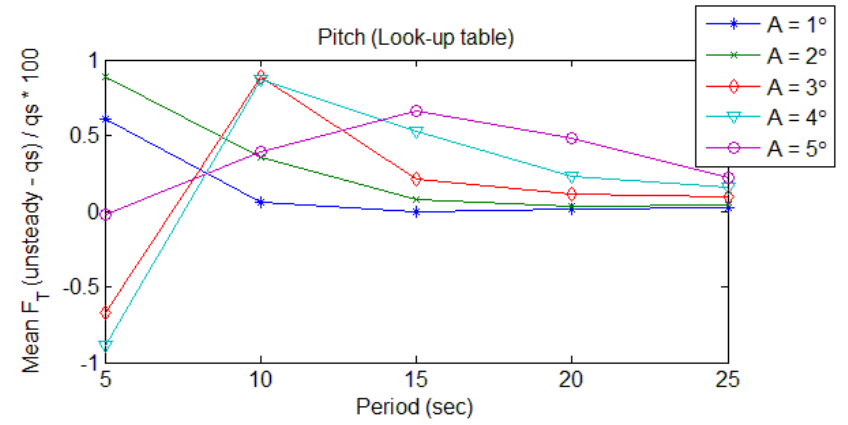
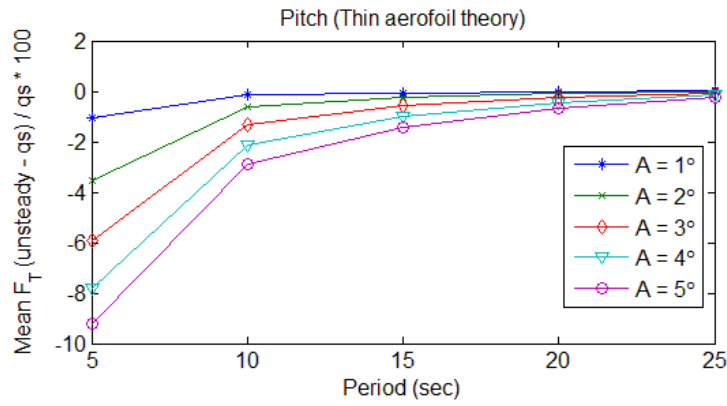


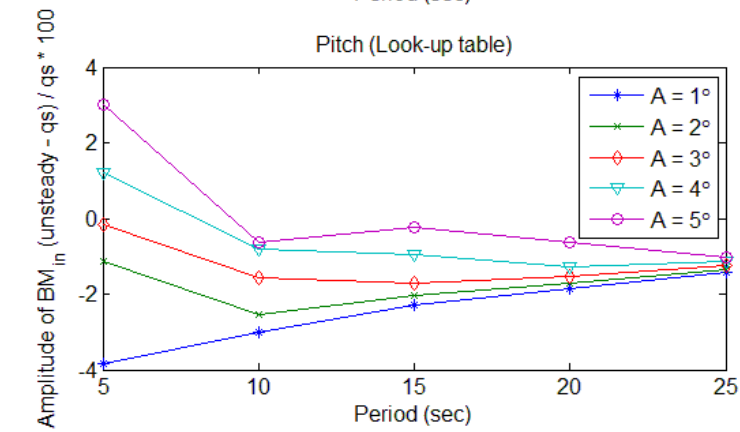
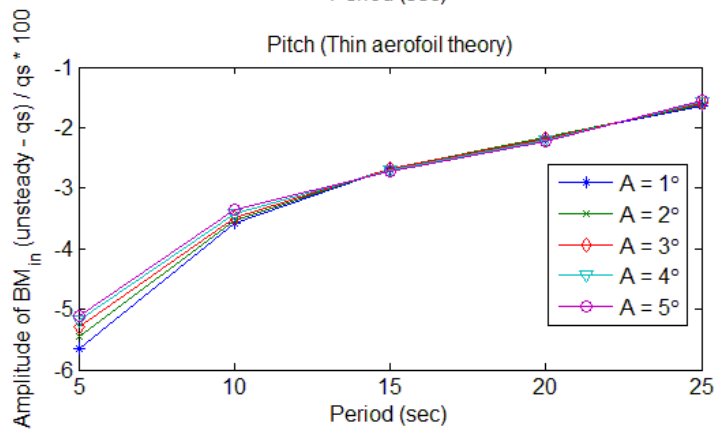
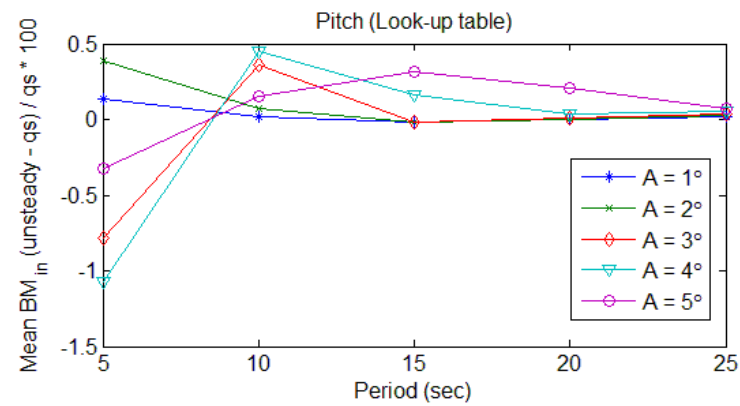
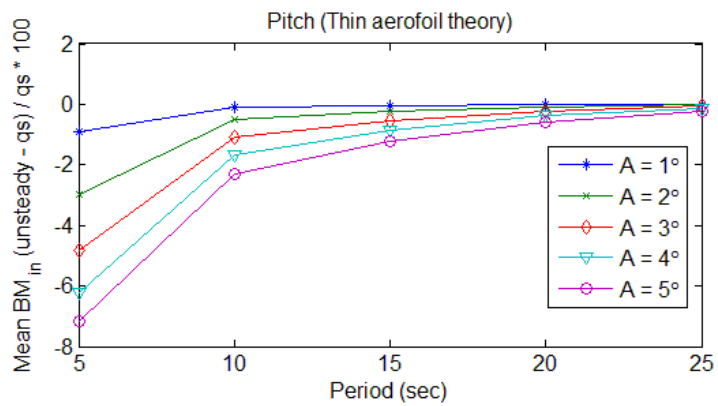




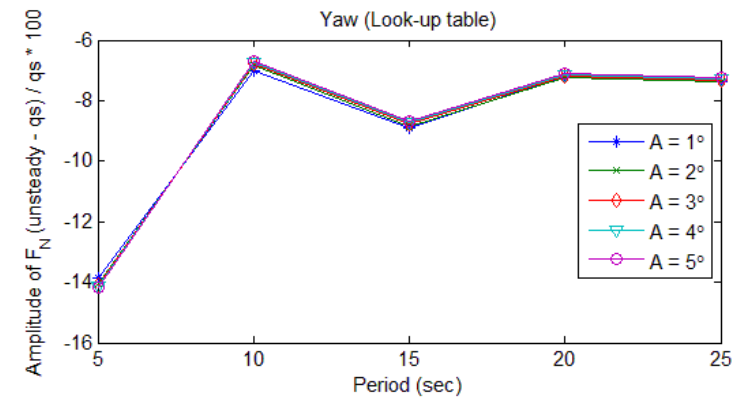
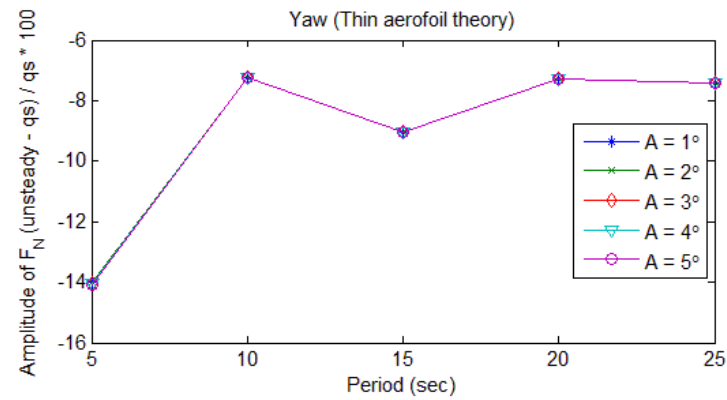
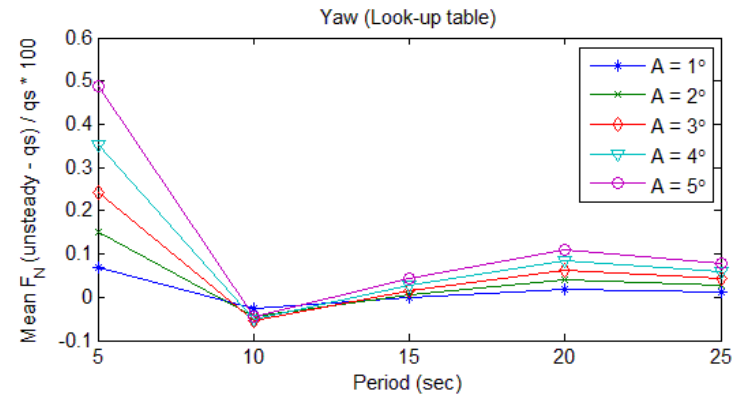
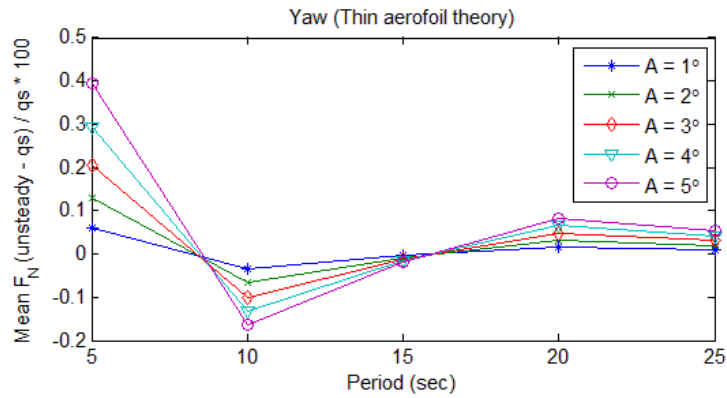
### A1.6.5. Pitch

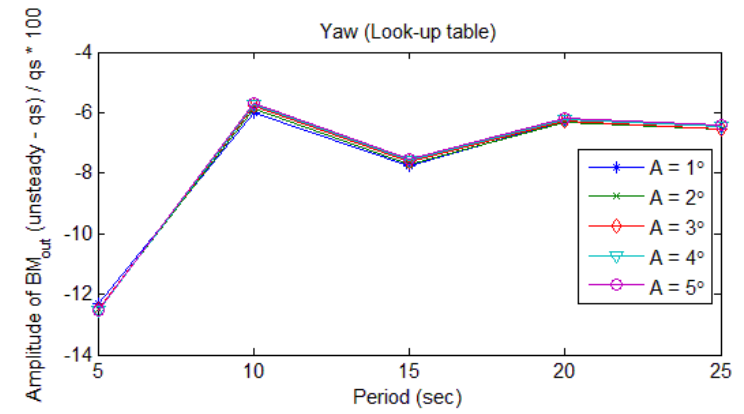
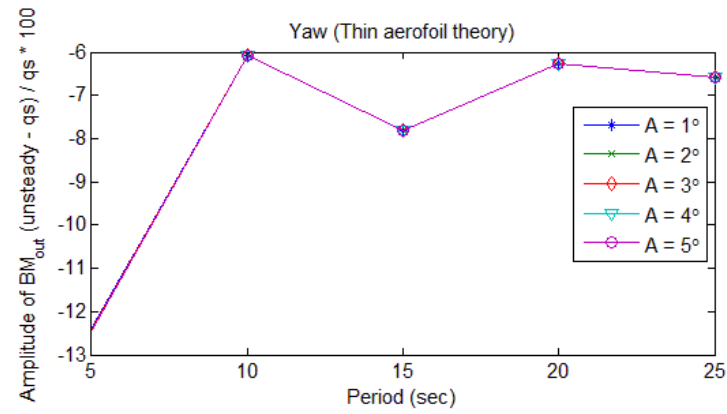
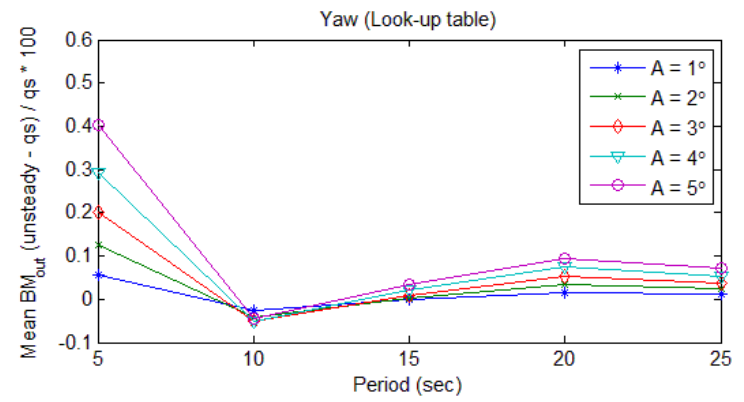
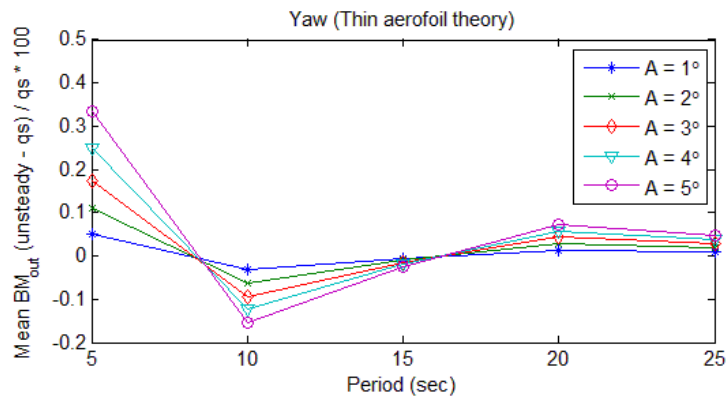


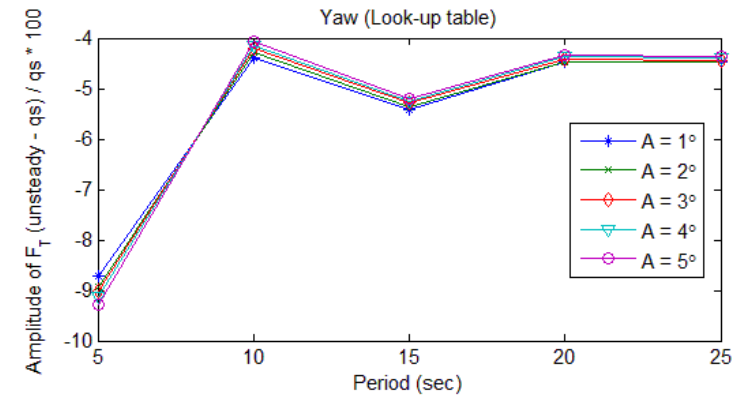
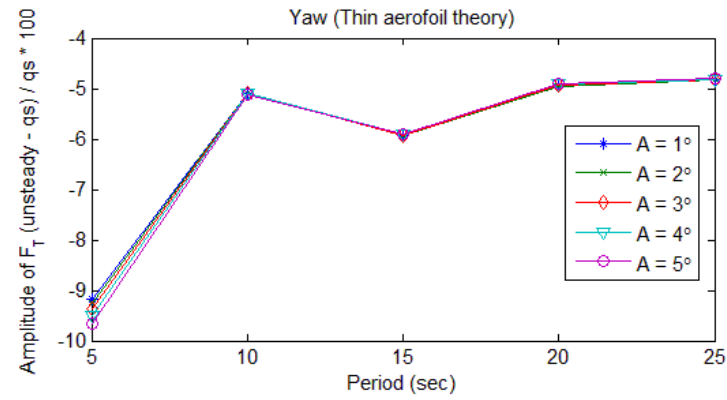
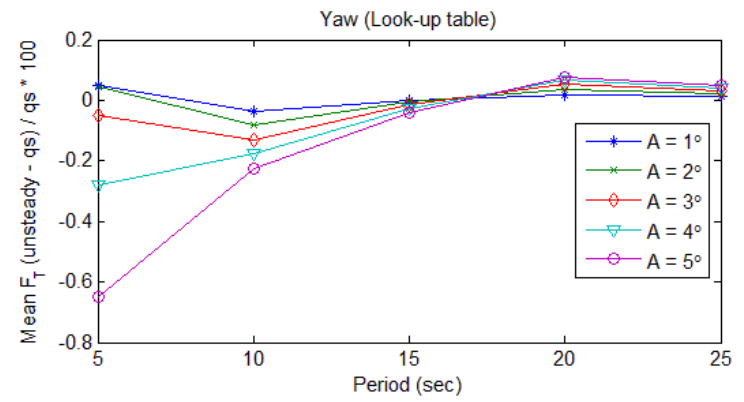
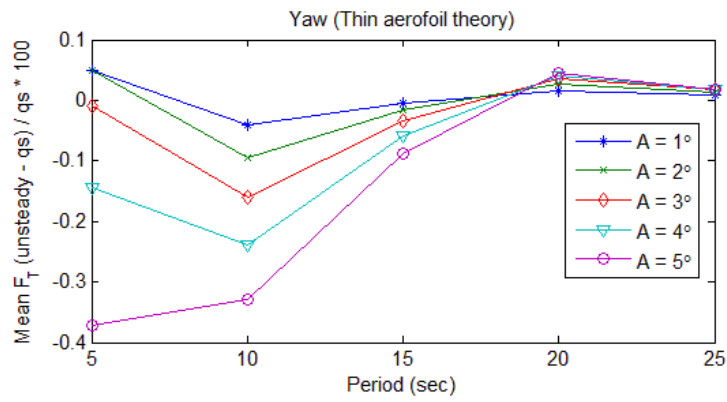


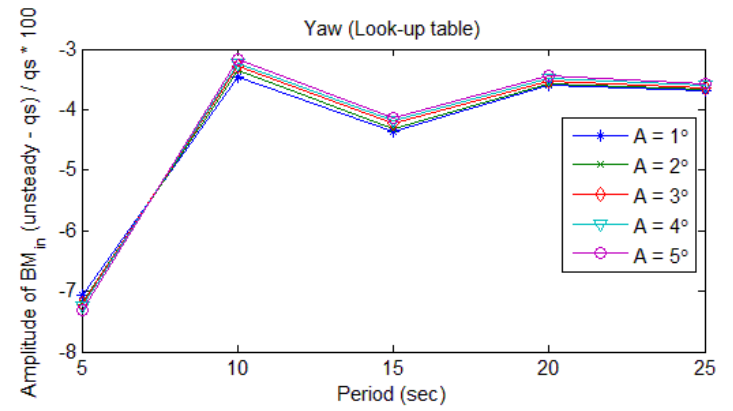
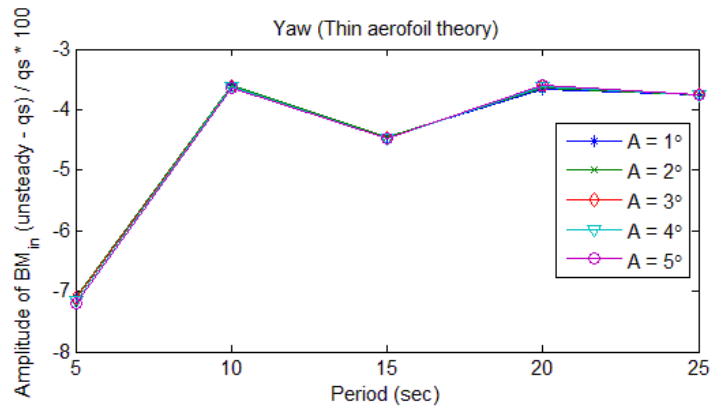
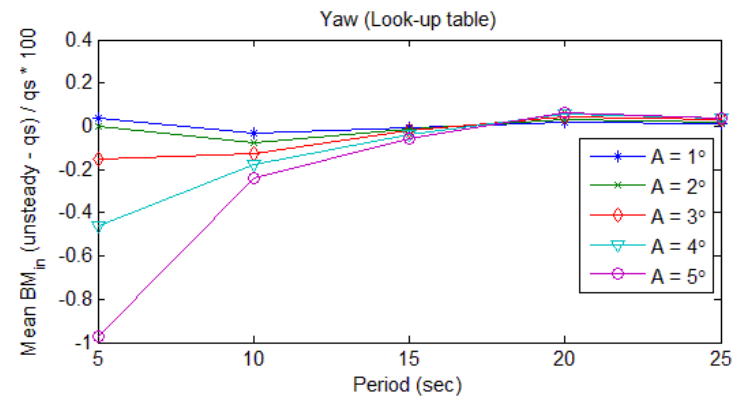
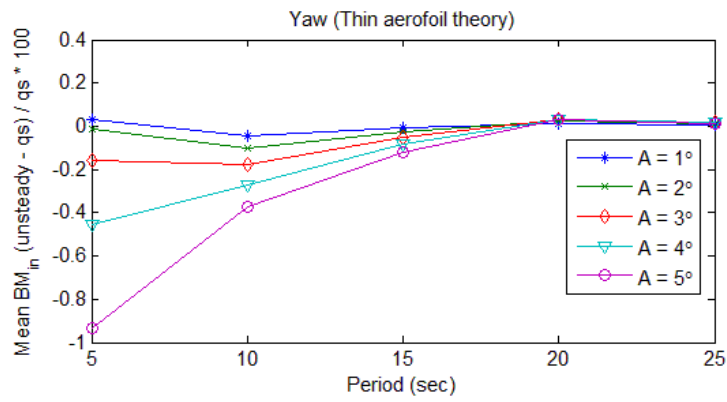


### A1.6.6. Yaw









## A1.7. Changes in axial force

Per personal communication with Dr Julian Feuchtwang.

According to blade-element theory, the axial force on a rotor blade is given by:

$$F_N = \frac{1}{2} \rho c W^2 [C_L(\alpha) \cos(\varphi) + C_D(\alpha) \sin(\varphi)] \quad \text{A.40}$$

where  $\rho$  is air density,  $c$  is the local blade chord-width,  $W$  is the resultant wind speed,  $\alpha$  is the angle-of-attack relative to the aerofoil chord-line,  $\varphi$  is the flow angle relative to the plane of rotation and  $\alpha = \varphi - \beta$ , where  $\beta$  is the pitch angle of the aerofoil relative to the plane of rotation.

Using the local speed ratio,  $\lambda = \frac{r\Omega}{U_\infty}$ , the resultant wind speed can be expressed as:

$$\begin{aligned} W^2 &= U_\infty^2 (1 - a)^2 + r^2 \Omega^2 (1 + a')^2 \\ &= r^2 \Omega^2 \left[ (1 + a')^2 + (1 - a)^2 \frac{1}{\lambda^2} \right] \end{aligned} \quad \text{A.41}$$

where  $U_\infty$  is the undisturbed up-wind axial wind speed,  $r$  is the radial location of the blade station relative to the axis of rotation,  $\Omega$  is the rotational speed,  $a$  is the axial induction factors and  $a'$  is the tangential induction factor.

Some approximations are in order:

$$\begin{aligned} C_L(\alpha) \cos(\varphi) &\gg C_D(\alpha) \sin(\varphi), \\ a' &\ll 1, \quad \cos(\varphi) \approx 1 \\ C_L(\alpha) &= C_{L_0} + C'_{L\alpha} \alpha = C_{L_0} + C'_{L\alpha} \varphi - C_{L\beta} \end{aligned} \quad \text{A.42}$$

where  $C_{L_0}$  is the lift due to camber at  $\alpha = 0$ ,  $C'_{L\alpha}$  is the linearised lift slope and  $C_{L\beta}$  is the lift reduction due to pitch angle.

Using approximation from equation A.42 and the local speed ratio, the flow angle relative to the plane of rotation can be approximated as:

$$\varphi \approx \tan(\varphi) = \frac{U_N}{U_T} = \frac{(1-a)}{(1+a')\lambda} \approx (1-a)\frac{1}{\lambda} \quad \text{A.43}$$

where  $U_N$  is the net stream-wise velocity at the blade element and  $U_T$  is the net tangential velocity at the blade element.

Using equation A.41 and approximations from equation A.42 and equation A.43, the axial force on a rotor blade can now be expressed as:

$$F_N = \frac{1}{2}\rho c U_T^2 \left[ 1 + (1-a)^2 \frac{1}{\lambda^2} \right] (C_{L_0} + C'_{L\alpha}\varphi - C_{L\beta}) \quad \text{A.44}$$

For small changes in wind experienced by the rotor blade,  $\delta U_N$  in the axial direction, and  $\delta U_T$  in the in-plane direction, the change in the axial force is:

$$\begin{aligned} \delta F_N = \delta t \frac{d}{dt} F_N = \frac{1}{2}\rho c \delta t \left\{ \left[ \frac{d}{dt} (U_T^2 + U_N^2) \right] (C_{L_0} + C'_{L\alpha}\varphi - C_{L\beta}) \right. \\ \left. + (U_T^2 + U_N^2) \left[ \frac{d}{dt} (C_{L_0} + C'_{L\alpha}\varphi - C_{L\beta}) \right] \right\} \quad \text{A.45} \end{aligned}$$

Equation A.45 can be rewritten as:

$$\begin{aligned} \frac{2\delta F_N}{\rho c} = \delta t \frac{d}{dt} (U_T^2 + U_N^2) (C_{L_0} + C'_{L\alpha}\varphi - C_{L\beta}) \\ + U_T^2 \left[ 1 + (1-a)^2 \frac{1}{\lambda^2} \right] \delta t \frac{d}{dt} (C_{L_0} + C'_{L\alpha}\varphi - C_{L\beta}) \quad \text{A.46} \end{aligned}$$

where

$$\begin{aligned} \delta t \frac{d}{dt} (U_T^2 + U_N^2) = 2U_T \delta U_T + 2U_N \delta U_N \\ \delta t \frac{d}{dt} (C_{L_0} + C'_{L\alpha}\varphi - C_{L\beta}) = C'_{L\alpha} \delta t \frac{d}{dt} \varphi \quad \text{A.47} \end{aligned}$$

Using quotient rule and equation A.43, equation A.47 can be further simplified as:

$$C'_{L\alpha} \delta t \frac{d}{dt} \varphi = C'_{L\alpha} \left( \frac{\delta U_N}{U_T} - \frac{\delta U_T U_N}{U_T^2} \right) = \frac{C'_{L\alpha}}{U_T} \left[ \delta U_N - \delta U_T (1-a) \frac{1}{\lambda} \right] \quad \text{A.48}$$

Using equation A.47 and equation A.48, equation A.45 can now be expressed as:

$$\begin{aligned} \frac{2\delta F_N}{\rho c} = & (2U_T \delta U_T + 2U_N \delta U_N) \left[ C_{L_0} + C'_{L\alpha} (1-a) \frac{1}{\lambda} - C_{L\beta} \right] \\ & + C'_{L\alpha} U_T \left[ 1 + (1-a)^2 \frac{1}{\lambda^2} \right] \left[ \delta U_N - \delta U_T (1-a) \frac{1}{\lambda} \right] \end{aligned} \quad \text{A.49}$$

Finally, with help of equation A.42 and equation A.43, equation A.49 can be simplified to:

$$\begin{aligned} \delta F_N = \rho c r \Omega \left\{ \delta U_T \left[ C_{L_0} + \frac{1}{2} C'_{L\alpha} (1-a) \frac{1}{\lambda} \left[ 1 - \frac{(1-a)^2}{\lambda^2} \right] - C_{L\beta} \right] \right. \\ \left. + \delta U_N \left[ C_{L_0} \frac{1-a}{\lambda} + \frac{1}{2} C'_{L\alpha} \left[ 1 + \frac{3(1-a)^2}{\lambda^2} \right] - C_{L\beta} \frac{1-a}{\lambda} \right] \right\} \end{aligned} \quad \text{A.50}$$

Equation A.50 shows that when and where there is little camber or it is cancelled out by pitch angle, then axial wind speed changes have the greater effect on the axial force by a factor of approximately the local tip-speed ratio. On the other hand, when and where there is significant lift due to camber or negative pitch, there might be quite significant contribution to the axial force from in-plane changes in speed.

## A1.8. Non-circulatory lift of oscillatory pitching

The non-circulatory lift coefficient for a blade subjected to plunging, time varying incident velocity and pitching, as given by [55], is:

$$C_L^{nc}(t) = \frac{\pi c}{2W^2} \left( \ddot{h} + \frac{d(W\alpha)}{dt} - \frac{ac\ddot{\alpha}}{2} \right) \quad \text{A.51}$$

where  $c$  is the chord length,  $W$  is the resultant velocity,  $\ddot{h}$  is the plunge acceleration,  $\alpha$  is the angle-of-attack and  $a$  is the pitch axis location measured in half-chords from the mid-chord and being positive towards the trailing edge.

The non-circulatory lift coefficient for a rigid blade or a blade that is not flapping as it is forced in pitch, when the free-stream velocity and rotational velocity is fixed, is:

$$C_L^{nc} = \frac{\pi c}{2W^2} \left( W\dot{\alpha} - \frac{ac\ddot{\alpha}}{2} \right) \quad \text{A.52}$$

Defining the pitch axis at the quarter chord distance ( $a = -0.5$ ), displacement in pitch as  $\bar{\alpha}e^{i\omega t}$  and inserting its first and second derivatives into equation A.51:

$$C_L^{nc} = \frac{\pi c * i\omega \bar{\alpha} e^{i\omega t}}{2W} - \frac{\pi c^2 * \omega^2 \bar{\alpha} e^{i\omega t}}{8W^2} \quad \text{A.53}$$

Using equation 2.1 ( $k = \frac{\omega c}{2W}$ ), the lift coefficient from the non-circulatory due to forcing in pitching becomes:

$$C_L^{nc} = \pi k \left( i - \frac{k}{2} \right) \bar{\alpha} e^{i\omega t} \quad \text{A.54}$$

For a comprehensive description and explanation of Theodorsen's theory and associated non-circulatory effects see [53, 55, 68, 121].

## A1.9. Excel spreadsheet

The majority of the necessary data to calculate the natural frequencies of the OC3-Hywind spar was taken from [46, 47], however some calculations, such as added mass and inertia, had to be performed in Excel.

### A1.9.1. Surge and sway

Natural frequency of a mechanical system oscillating in 1 DoF is purely a function of mass and stiffness.

$$f_{Hz} = \frac{1}{2\pi} \sqrt{\frac{k}{m + m'}} \quad \text{A.55}$$

The only restoring force in the surge and sway DsoF comes from the mooring system. The restoring constant,  $k$ , was calculated in FAST and given in [46] as 41,180 N/m. The mass of the systems,  $m$ , was augmented with the added mass of the water,  $m'$ , displaced when surging and/or swaying. The added mass has to be taken into account because of the relatively high density of water (normally ignored, when system is surrounded by air) and can be approximated as the mass of the water displaced by the spar. The mass and the add mass of the OC3-Hywind can be obtained from [46].

### A1.9.2. Heave

An identical approach to surge and sway calculations can be used in computing the natural frequency in heave. However, there are 2 main differences with the heave natural frequency. First, the restoring force in heave comes mainly from the extra buoyancy when the spar is displaced (there is a small component of restoring coming from the mooring system). Second, the added mass can be approximated as a half of a sphere of water beneath the spar.

### A1.9.3. Roll and pitch

Calculation of the roll and pitch natural frequencies are slightly more complicated. One needs to know the total inertia of the system,  $I_{xx,yy}$ , the added water inertia,  $I'_{xx,yy}$ , and the

distance between the centre of gravity (CoG) and the centre of buoyancy (CoB),  $\overline{GM}$ . The last being an approximation that can be used due to a very small cross-sectional area at the SWL compared to the length of the spar.

$$f_{Hz} = \frac{1}{2\pi} \sqrt{\frac{\overline{GM} \times m \times g + k}{I_{xx,yy} + I'_{xx,yy}}} \quad \text{A.56}$$

The distance between the CoG and CoB was taken as approx. 15.8 m and the total inertia of the system around the CoG approximated as 30,400,000,000 kgm<sup>2</sup> (includes solid and liquid inertia).

#### A1.9.4. Yaw

The yaw DoF is characterised in the OC3-Hywind as having the highest natural frequency. Its natural frequency depends on the system's inertia about the z-axis,  $I_z$ , the restoring constant from the mooring,  $k$ , and additional stiffness due to the delta connection of the mooring system to the spar,  $c$ . Only the solid inertia needs to be considered, as no water is displaced in the yaw DoF.

$$f_{Hz} = \frac{1}{2\pi} \sqrt{\frac{k + c}{I_{zz}}} \quad \text{A.57}$$

The mooring stiffness and additional stiffness in yaw, due to the delta connection used with the mooring system, are given in [46].

## A1.10. WAMIT RAOs

The following 4 figures (Figure 176, Figure 177, Figure 178 and Figure 179) show RAOs for the OC3-Hywind. Sway and roll RAOs are not shown, because of the symmetry of the system in surge and sway, and roll and pitch (there is a slight difference in the roll and pitch DsoF, but it is negligible and hence is ignored). The origin of the coordinate system in these figures and all WAMIT calculations performed in this study is located on the free surface and not at the CoG of the system. In this way the pitch and roll restoring of a floating body was not double booked, as it is intrinsically accounted for by FAST.

Figure 176 shows significant coupling between the surge and pitch DsoF. This is consistent with the results discussed in 3.1.5.2 and 3.2.3.

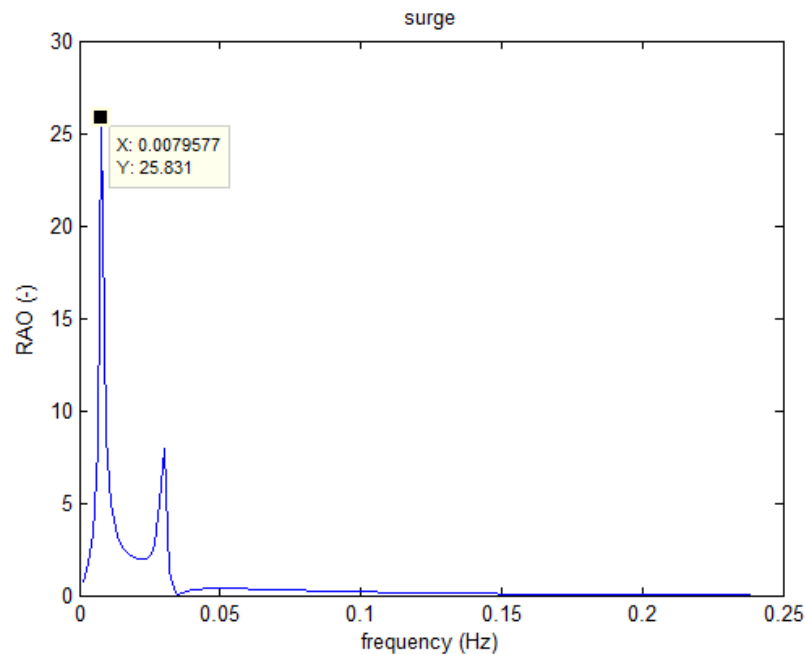


Figure 176 – RAO for surge/sway

The heave RAO in Figure 177 shows a peak at the heave's natural frequency (0.032 Hz) and an asymptotical tendency to 1 as the frequency decreases. However, it never reaches RAO = 1, as there is some stiffness in the heave DoF coming from the mooring system which prevents the system from following the wave input at very low wave frequencies.

Figure 178 shows RAO for the pitch and roll DsoF. The natural frequency of pitch mode can be easily identified at 0.03 Hz. Another, much smaller peak is also visible at a lower frequency. This is the natural frequency of surge. Compared to Figure 176, there is much less coupling between the DsoF, this is also consistent with the results obtained and described in [99].

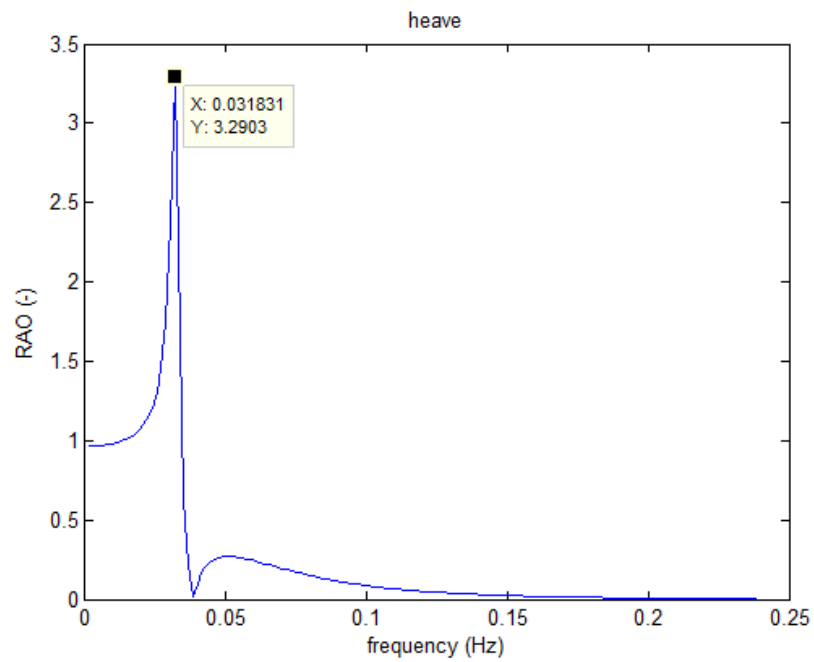


Figure 177 – RAO for heave

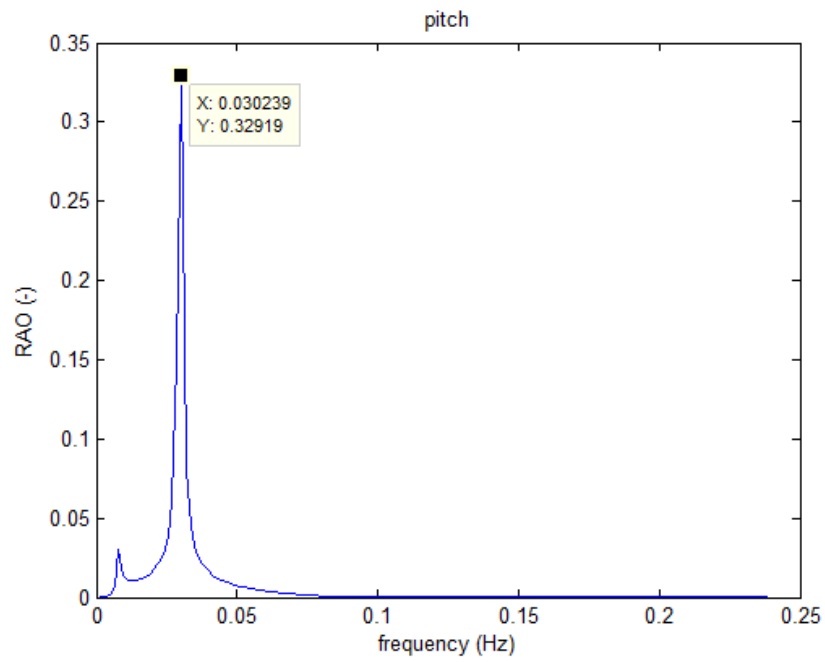


Figure 178 – RAO for pitch/roll

It is very hard to excite the OC3-Hywind in the yaw DoF, as the floater is rotationally symmetric. When waves are aligned with the positive x-axis, yaw response is 0. In Figure 179 waves were misaligned by 45 degrees and this produced a very small excitation in yaw, which was large enough to identify the natural frequency at 0.1178 Hz.

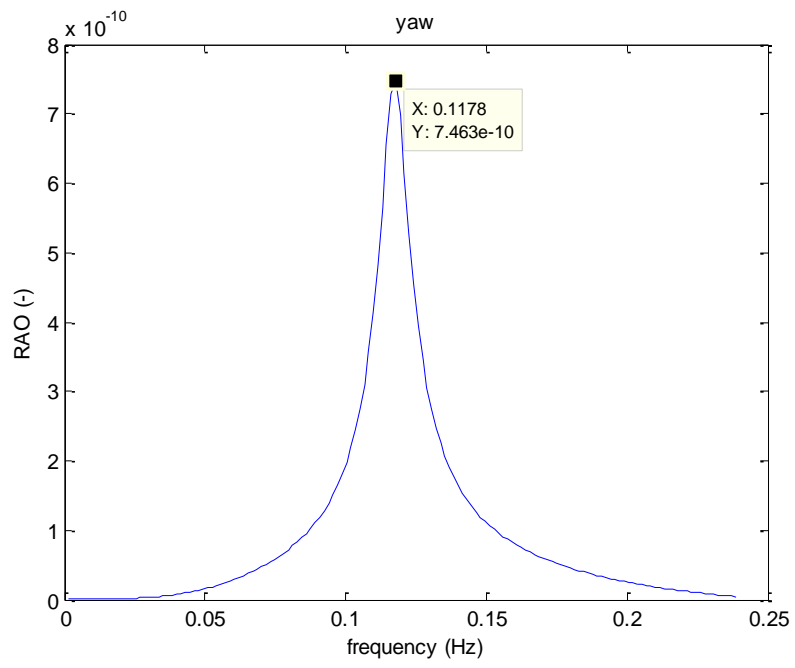


Figure 179 – RAO for yaw

## A1.11. Maximal stress points

Strain gauge locations in FAST simulations were chosen to be located at the weakest points of the OC3-Hywind tower and blades. These were identified using basic mathematical and mechanical identities.

### A1.11.1. Tower

Tower is a relatively simple structure when compared to blades. However, it can be even further simplified by assuming that there is a point load at the tower top and that the tower is cantilever to the platform (ignoring tower drag as it is very small compared to thrust on the rotor). Using a simple point load, the bending moment, as a function of the distance from the base,  $x$ , can be expressed as:

$$M(x) = F \times (l - x) \quad \text{A.58}$$

where  $0 \leq x \leq l$  and  $l$  is the length of the tower and the point load,  $F$ , acting on the tower top is the thrust on the rotor.

$$F = Thrust = \frac{1}{2} \rho U_{\infty}^2 A C_T \quad \text{A.59}$$

Assuming that the largest load on the tower is at the greatest thrust force on the rotor, the axial induction factor can be assumed to be  $\frac{1}{3}$  and  $U_{\infty}$  as 11.4 m/s (the rated wind speed for the NREL 5 MW turbine).

The maximal stress point can now be expressed as:

$$\sigma_{max} = |M_{max}| \times \frac{c}{I} = \left| \frac{F \times l}{S} \right| \quad \text{A.60}$$

where  $S$  is the section modulus, which is a geometric property for a given cross-section,  $I$  is the second moment of area and  $c$  is the tower thickness (point of the maximum tension and compression).

The towers used in wind turbines are normally coned, including the one used in the OC3-Hywind design or the NREL 5 MW. Its second area of moment can be calculated assuming that the tower consists of multiple diameter thin tubes.

Second area of moment for a thin tube is:

$$I_{x,y} = \frac{\pi}{4} \times (r_2^4 - r_1^4) \quad \text{A.61}$$

where  $r_1$  is the inner and  $r_2$  is the outer radius of the tube. The wall thickness and tower diameter is changing linearly with height, as provided in [46].

Using the OC3-Hywind data for tower structural properties and Young's modulus of 210 GPa (2<sup>nd</sup> moment of area calculated using tower fore-aft stiffness and Young's modulus), and tower geometric properties (2<sup>nd</sup> moment of area calculated using tower diameter and wall thickness distributions), the maximal stress distribution for the tower is shown below.

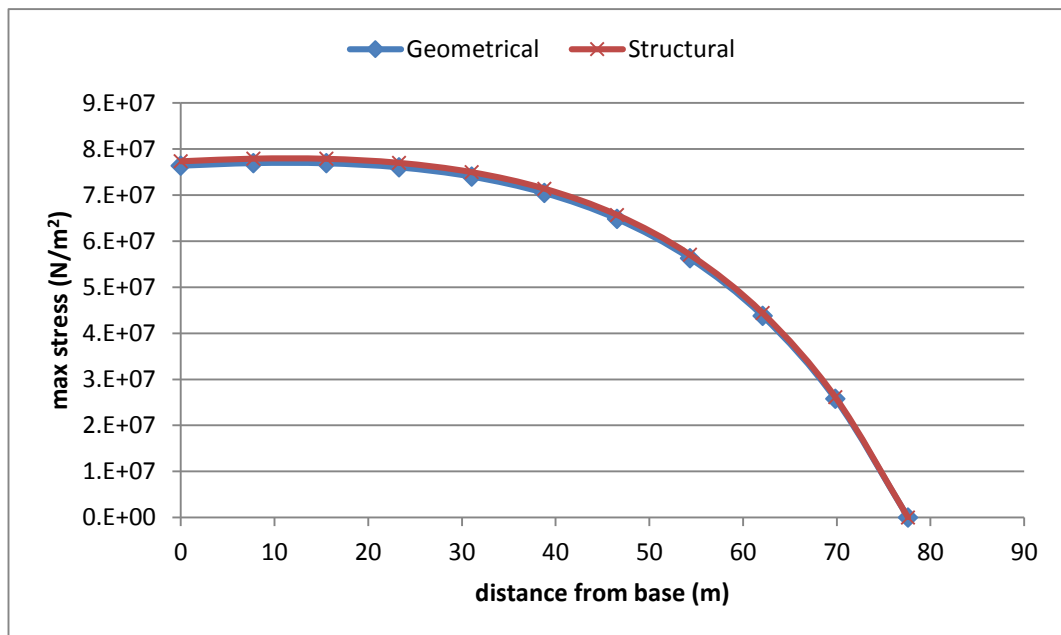


Figure 180 – Max. stress distribution along the tower's length

Both cases ('geometrical' and 'structural') yield almost identical results with the max stress point being located very close to the tower base. Using 11 stations along the tower length, station number 2 (7.76 m from the tower base) was identified as where the tower would most likely fail.

Two strain gauges were set-up for each FAST simulation. These were at the tower base, to measure the loads at the base of the tower, and at gauge location number 3 (9.7 m from the tower base, as strain gauge locations cannot be chosen completely freely in FAST), which is the closest gauge station to the identified 7.76 m point from the base.

### A1.11.2. Blades

Wind turbine blades are much more complicated structures compared to towers. Variation of the chord length, thickness, shell and spar thickness, etc. makes them slightly more complicated to model.

To calculate the maximum stress point location blade was modelled as a cantilevered beam with triangular loading. In the simplified calculations chord distribution was assumed to be linearly tapered and the cap spar width and depth proportional to the chord length (ignored shell thickness and webs).

Second moment of area for a rectangle (spar cap) is:

$$I = \frac{ab^3}{12} \quad \text{A.62}$$

where  $a$  is width and  $b$  is depth. Using parallel axis theorem the total second area of moment for a blade section, ignoring and accounting for the cap depth around the central axis, is:

$$I_{\text{ignoring}} = \frac{1}{6}ab^3 + \frac{abt^2}{2} \quad \text{A.63}$$

$$I_{\text{including}} = \frac{2}{3}a(b_1^3 - b_2^3)$$

where  $b_1$  and  $b_2$  are the distances from the centreline to the upper and lower sides of the cap and  $t$  is the half-thickness of the aerofoil.

With the chord length, cap width and depth expressed as:

$$\begin{aligned} c(x) &= c_0 + \frac{x(c_1 - c_0)}{L} \\ a(x) &= k_a c(x) \\ b(x) &= k_b c(x) \end{aligned} \quad \text{A.64}$$

where  $c_0$  and  $c_1$  are chord lengths at  $x = 0$  and  $x = L$ .

The total moment of inertia for any location along the blade length, ignoring thickness of the cap spar and using parallel axis theorem is:

$$I(x) = \frac{k_a k_b}{6} \left[ c_0 + \frac{x(c_1 - c_0)}{L} \right]^4 + \frac{k_a k_b t^2}{2} \left[ c_0 + \frac{x(c_1 - c_0)}{L} \right]^2 \quad \text{A.65}$$

Approximating thrust force on a blade as a triangular load,  $w$ , from the hub centre to the blade tip being proportional to the distance along the blade span, load can be expressed as:

$$w(x) = k_w (r_{hub} + x) \quad \text{A.66}$$

The total thrust force on a blade is:

$$\int_0^L w dx = Thrust = k_w r_{hub} L + \frac{k_w L^2}{2} \quad \text{A.67}$$

where  $r_{hub}$  is the hub radius and  $k_w$  is the proportionality coefficient between the load and distance along the blade length.

The proportionality coefficient,  $k_w$ , is:

$$k_w = \frac{Thrust}{r_{hub} L + \frac{L^2}{2}} \quad \text{A.68}$$

and the load at any point along the blade span is:

$$w(x) = \frac{Thrust}{r_{hub} L + \frac{L^2}{2}} (r_{hub} + x) \quad \text{A.69}$$

The shear force can now be expressed as:

$$S(x) = \int_x^L w(z)dz = k_w \left[ r_{hub}(L - x) + \frac{(L^2 - x^2)}{2} \right] \quad \text{A.70}$$

and bending moment as:

$$M(x) = \int_x^L S(z)dz = k_w \left[ \frac{L^3}{3} + \frac{r_{hub}L^2}{2} + \frac{x^3}{6} + \frac{r_{hub}x^2}{2} - xL \left( r_{hub} + \frac{L}{2} \right) \right] \quad \text{A.71}$$

Using identity:

$$\frac{\sigma}{y} = \frac{M}{I} \quad \text{A.72}$$

where  $\sigma$  is stress and  $y$  is the perpendicular distances to the neutral axis.

Stress, or max stress, can be expressed as:

$$\sigma = \frac{k_w \left[ \frac{L^3}{3} + \frac{r_{hub}L^2}{2} + \frac{x^3}{6} + \frac{r_{hub}x^2}{2} - xL \left( r_{hub} + \frac{L}{2} \right) \right] \times \frac{t}{2}}{\frac{k_a k_b}{6} \left[ c_0 + \frac{x(c_1 - c_0)}{L} \right]^4 + \frac{k_a k_b t^2}{2} \left[ c_0 + \frac{x(c_1 - c_0)}{L} \right]^2} \quad \text{A.73}$$

The following table summarises the values used with the equation above to produce Figure 181. Some of these values were taken from [47], while others (not given in [47]) were chosen by making an educated guess.

**Table 31 – Variables used in calculating maximum stress point on a blade**

Variable	Value (units)
$k_a$	0.4 (-)
$k_b$	0.01 (-)
$t_0/2$	2 m
$t_1/2$	0.25 m
$c_0$	4 m
$c_1$	1 m
$k_w$	100 (-)
$r_{hub}$	1.5 m
$L$	61.5 m

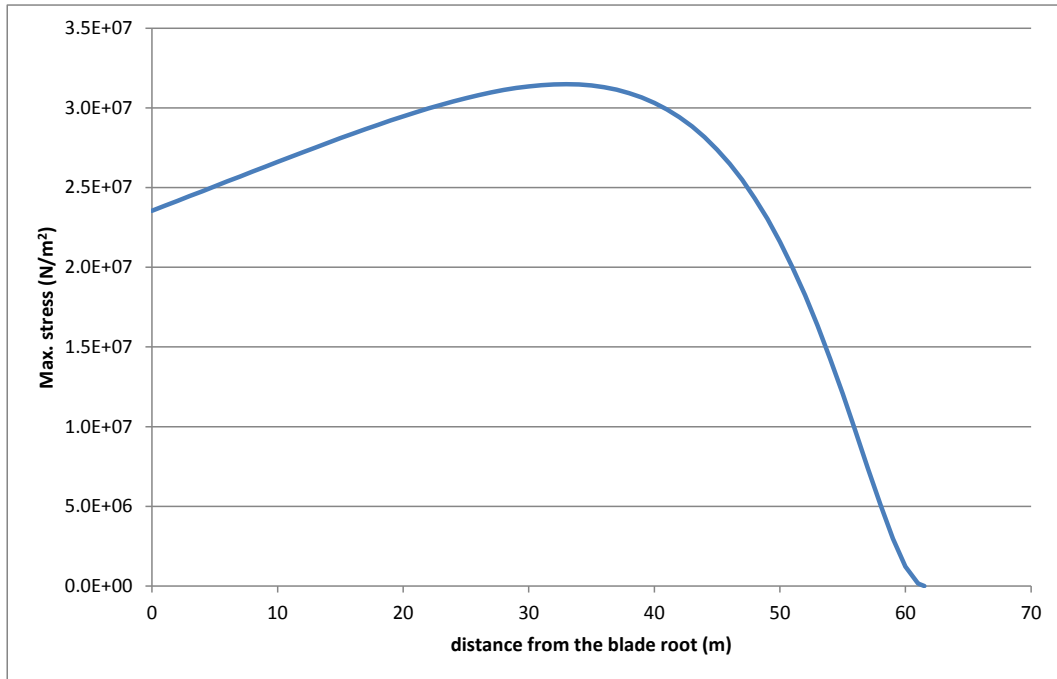


Figure 181 – Stress distribution along the blade’s span

Using the simplified approach detailed above, location 33 m along the blade length was identified as the weakest point on the blade. However, this approach is too simplistic and results were used only as a first estimate.

An alternative, a much better way to approximate where the blade could experience the max stress, is to use blade’s data published in [47].

Just like for the tower calculations, two different approaches were used:

- 49 point structural data (2<sup>nd</sup> moment of inertia was calculated from flapwise section stiffness and Young’s modulus; assumed to be 180 GPa for carbon fibre reinforced plastic).
- 17 point aerodynamic data (a much cruder data set as can be seen in Figure 182).

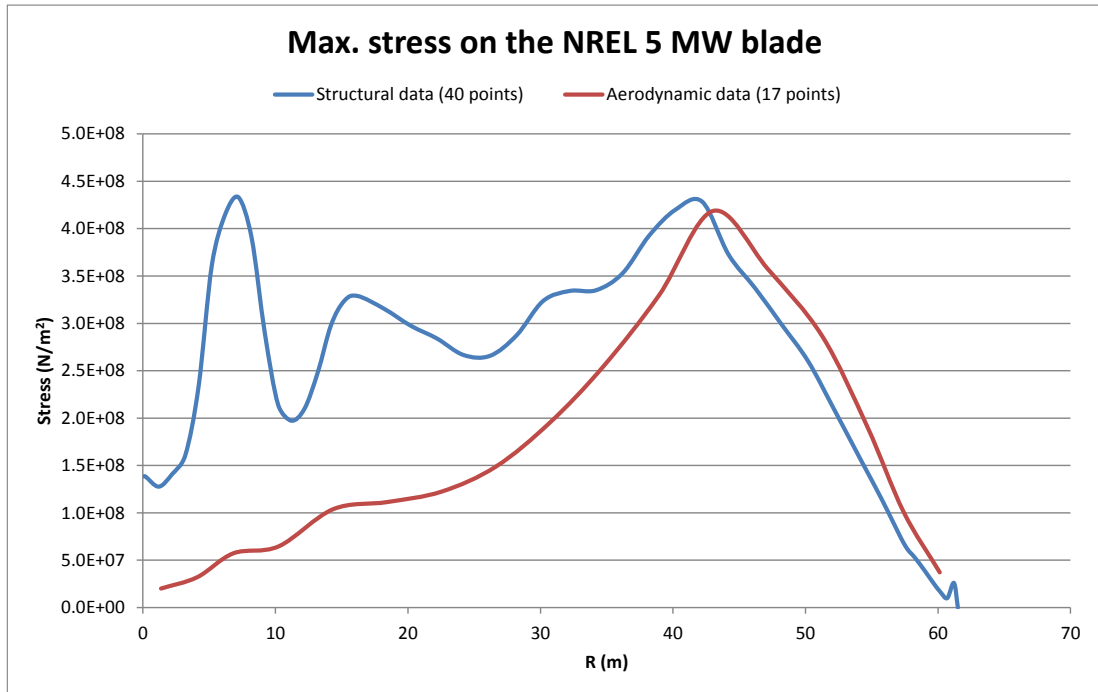


Figure 182 – Maximum stress points along the blade’s length

Curves in Figure 182 show similar trends and both identify section at 42-43 m as potentially the weakest point in the blade structure. However, when using the aerodynamic data, some points of high stresses are not identified, such as at around 7 m along the blade span. This corresponds to the point where the metallic flange, which is used to attach the blade to the hub, finishes. Also around the same point there is change in the number of composite layers used, resulting in very high stress concentration factors.

Due to its superior resolution and data fidelity, the structural data was used to identify the locations for placing strain gauges. These were placed at station 3 (6.83 m) and 12 (43.05 m from the blade root) to measure moments in flapwise and edgewise directions.

## A1.12. Most damaging degree-of-freedom

### A1.12.1. Rated

The rated conditions were simulated using the following environment: 11.4 m/s wind, and 3 m and 15 s regular waves. Figure 183 shows displacement in the surge and pitch DsoF for 3 different wave-excitation force-vectors.

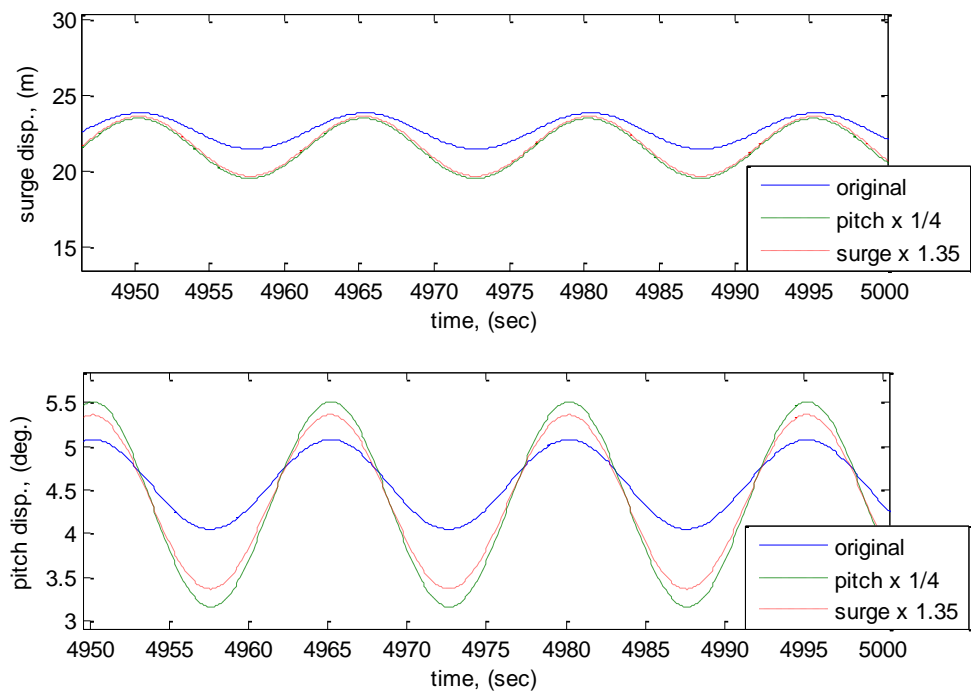


Figure 183 – Surge and pitch response in rated conditions and modified wave-excitation force-vector

Linear response in surge and pitch displacements is produced for scaling factors from 1 to 4 inclusive for surge wave-excitation force-vector. For pitch excitation these were found to be between 0.25 and 1.5. Compared to the below- and above-rated results, the rated simulations produce the highest difference in the mean displacement in the surge and pitch DsoF between the original and scaled runs (see Table 32). Most likely this is due to the fact that at the rated wind speed turbine operates in the most non-linear region and any change in the environmental conditions, or as in this case in the wave-excitations force-vectors, will result in different 'steady-state' values.

**Table 32 – Mean displacements in surge and pitch DsoF for 3 different operation states (original, pitch x 0.25 (scaled 1) and surge x 1.35 (scaled 2))**

	Below-rated			Rated			Above-rated		
	Original	Scaled 1	Scaled 2	Original	Scaled 1	Scaled 2	Original	Scaled 1	Scaled 2
<b>Surge (m)</b>	8.16	8.16	8.16	22.62	21.48	21.62	12.1	11.98	11.95
<b>Pitch (deg.)</b>	1.66	1.66	1.66	4.56	4.33	4.36	2.46	2.45	2.44

3 different wave-excitation force-vector simulations were compared. These included original (no scaling), pitch x 0.25 and surge x 1.35. The response in surge and pitch for each simulation is given in Table 33.

**Table 33 – Surge and pitch response ranges for rated simulations**

	Surge (m)	Pitch (deg.)
<b>Original</b>	2.39	1.03
<b>Pitch x 0.25</b>	3.96	2.35
<b>Surge x 1.35</b>	3.94	2

The difference between the surge response with pitch and surge wave-excitation force-vectors modified is 0.5%.

Table below summarises all loads and damage-equivalent loads per 1 m and 1 deg. and 2.39 m and 1.03 deg. displacements in the surge and pitch DsoF, calculated using pitch x 0.25 and surge x 1.35.

**Table 34 – Loads and DELs for tower and blade in surge and pitch DsoF in rated conditions**

	Surge		Pitch	
	per 1 m	per 2.39 m	per 1 deg.	per 1.03 deg.
<b>Tower base</b>	8,822.7 kNm	21,086.3 kNm	20,446.9 kNm	21,060.3 kNm
<b>Tower at 9.7 m</b>	7,447.4 kNm	17,799.3 kNm	17,905 kNm	18,442.1 kNm
<b>Blade root</b>	504.7 kNm	1,206.2 kNm	684.9 kNm	705.5 kNm
<b>Blade at 6.83 m</b>	555.4 kNm	1,327.4 kNm	529.3 kNm	545.2 kNm
<b>Blade at 43.05</b>	43.4 kNm/m	103.7 kNm	54.9 kNm	56.6 kNm

### A1.12.2. Above-rated

Results for the above-rated simulations with 18 m/s wind, and 5 m and 17 s regular waves are presented below.

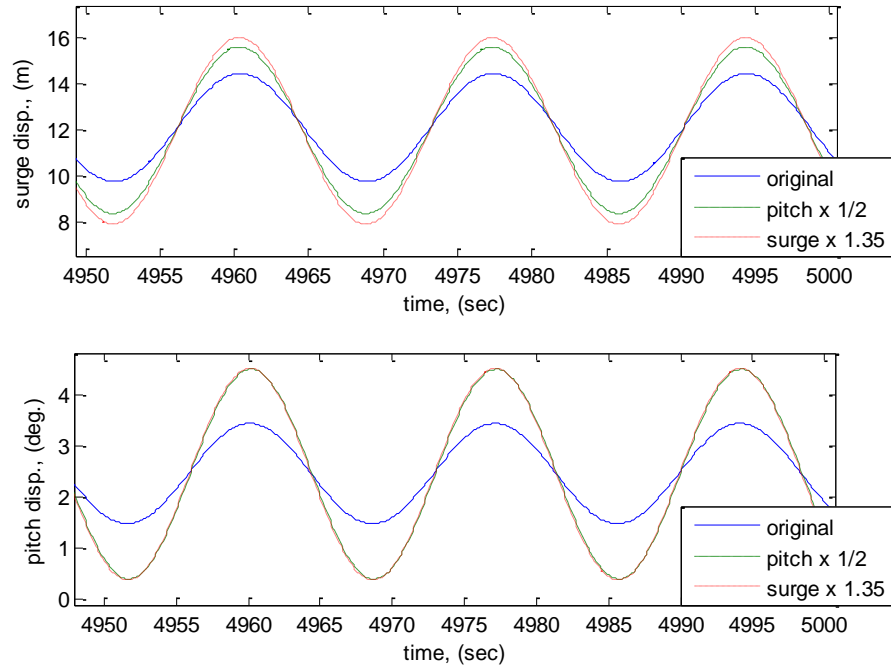


**Figure 184 – Surge and pitch response at above rated conditions for scaled wave-excitation force-vector**

Surge and pitch responses were found to be linear for scaling factors of 1 to 4 inclusive, when the surge DoF wave-excitation force vector was scaled. For the pitch DoF wave-excitation scaling, linearity was met between 0.25 and 1 scaling factors. The original run with no scaling of the wave-excitation force-vector yielded response of 4.666 m and 1.96 deg. ranges in surge and pitch.

To estimate the relative detrimental effect that motions in surge and pitch have on the fatigue, two different scaling factors were used.

**Table 35 – Surge and pitch response ranges for above-rated simulations**

	Surge (m)	Pitch (deg.)
<b>Pitch x 0.5</b>	7.20	4.11
<b>Surge x 1.35</b>	8.06	4.14

Whilst the pitch response was not matching between both simulation runs, it was within 1% error margin and was presumed to be sufficiently small to assume that the difference in the loading comes from the difference in the surge displacement.

**Table 36 – Loads and DELs for tower and blade in surge and pitch DsoF in above-rated conditions**

	Surge		Pitch	
	per 1 m	per 4.666 m	per 1 deg.	per 1.96 deg.
<b>Tower base</b>	7,191.5 kNm	33,555.5 kNm	15,757.9 kNm	30,885.5 kNm
<b>Tower at 9.7 m</b>	6,169.2 kNm	28,785.5 kNm	13,582.1 kNm	26,620.9 kNm
<b>Blade root</b>	270.9 kNm	1,264 kNm	628.5 kNm	1,231.9 kNm
<b>Blade at 6.83 m</b>	199.8 kNm	932.3 kNm	610.3 kNm	1,196.2 kNm
<b>Blade at 43.05</b>	20.6 kNm	96.1 kNm	44 kNm	86.2 kNm

Just like in the below-rated and rated cases, surge and pitch were shown to be of a comparable importance, with loads on the tower and blade, for the actual displacements in above-rated conditions, being of very similar magnitudes.

## A1.13. Correlational approach

In Table 37 to Table 44 the following abbreviations were used: blade edgewise and flapwise moments at the blade root (RootMEdg and RootMFlp), blade local edgewise and flapwise moments at 6.83 m and 43.05 m from the blade root (Spn1Mx, Spn1My and Spn2Mx and Spn2My), tower base fore-aft and side-to-side moments (TwrBsMy and TwrBsMx) and tower fore-aft and side-to-side moments at 7.76 m from the tower base (TwHt1My and TwHt1Mx).

### A1.13.1. Rated

The following eight figures show tower and blade load correlations with floater displacements and velocities in different DsoF. In the next 4 figures the rated wind turbine conditions are used: 11.4 m/s wind and 2.54 m significant wave height and 13.35 s wave peak spectral period.

Table 37 – Correlation matrix for tower loads with aligned wind and wave inputs in rated conditions

	Surge disp.	Sway disp.	Heave disp.	Roll disp.	Pitch disp.	Yaw disp.	Surge vel.	Sway vel.	Heave vel.	Roll vel.	Pitch vel.	Yaw vel.	TwrBsMx	TwrBsMy	TwHt1Mx	TwHt1My
Surge disp.	1	-0.2607	-0.3348	0.114	0.3669	0.1432	-0.1163	0.021	-0.1829	-0.0701	-0.1058	0.0411	0.0189	0.2872	0.0194	0.2869
Sway disp.	-0.2607	1	0.1764	-0.66	-0.2218	-0.1718	0.0864	-0.0189	0.1601	-0.0369	0.00682	-0.0467	-0.0951	-0.1272	-0.0872	-0.126
Heave disp.	-0.3348	0.1764	1	-0.1872	-0.0521	-0.1467	0.6908	-0.3392	0	0.5177	0.6413	0.468	-0.1286	-0.2489	-0.1363	-0.2537
Roll disp.	0.114	-0.66	-0.1872	1	0.3985	0.5551	-0.0196	0.1279	-0.4142	-0.0358	-0.063	0.0534	0.1323	0.3599	0.1182	0.3594
Pitch disp.	0.3669	-0.2218	-0.0521	0.3985	1	0.4423	0.0168	0.2027	-0.52	-0.0304	-0.0612	0.1482	-0.007	0.7257	-0.0154	0.7234
Yaw disp.	0.1432	-0.1718	-0.1467	0.5551	0.4423	1	-0.1553	0.1111	-0.6007	-0.0744	-0.2125	0	0.0606	0.5908	0.0531	0.5922
Surge vel.	-0.1163	0.0864	0.6908	-0.0196	0.0168	-0.1553	1	-0.3142	-0.1099	0.4814	0.917	0.5018	-0.1615	-0.2095	-0.1767	-0.216
Sway vel.	0.021	-0.0189	-0.3392	0.1279	0.2027	0.1111	-0.3142	1	0	-0.8273	-0.3392	-0.3215	0.0359	0.1633	0.0387	0.1644
Heave vel.	-0.1829	0.1601	0	-0.4142	-0.52	-0.6007	-0.1099	0	1	-0.1768	-0.0399	-0.296	0.044	-0.7756	0.0557	-0.7733
Roll vel.	-0.0701	-0.0369	0.5177	-0.0358	-0.0304	-0.0744	0.4814	-0.8273	-0.1768	1	0.4836	0.7755	-0.0759	0.0491	-0.0846	0.0458
Pitch vel.	-0.1058	0.00682	0.6413	-0.063	-0.0612	-0.2125	0.917	-0.3392	-0.0399	0.4836	1	0.461	-0.1638	-0.2932	-0.1776	-0.3
Yaw vel.	0.0411	-0.0467	0.468	0.0534	0.1482	0	0.5018	-0.3215	-0.296	0.7755	0.461	1	-0.0913	0.2576	-0.1024	0.2534
TwrBsMx	0.0189	-0.0951	-0.1286	0.1323	-0.007	0.0606	-0.1615	0.0359	0.044	-0.0759	-0.1638	-0.0913	1	0.0091	0.9992	0.0111
TwrBsMy	0.2872	-0.1272	-0.2489	0.3599	0.7257	0.5908	-0.2095	0.1633	-0.7756	0.0491	-0.2932	0.2576	0.0091	1	0	1
TwHt1Mx	0.0194	-0.0872	-0.1363	0.1182	-0.0154	0.0531	-0.1767	0.0387	0.0557	-0.0846	-0.1776	-0.1024	0.9992	0	1	0
TwHt1My	0.2869	-0.126	-0.2537	0.3594	0.7234	0.5922	-0.216	0.1644	-0.7733	0.0458	-0.3	0.2534	0.0111	1	0	1

**Table 38 – Correlation matrix for blade loads with aligned wind and wave inputs in rated conditions**

	Surge disp.	Sway disp.	Heave disp.	Roll disp.	Pitch disp.	Yaw disp.	Surge vel.	Sway vel.	Heave vel.	Roll vel.	Pitch vel.	Yaw vel.	RtMEdg	RtMFlp	Spn1Mx	Spn2Mx	Spn1My	Spn2My
Surge disp.	1	-0.2607	-0.3348	0.114	0.3669	0.1432	-0.1163	0.021	-0.1829	-0.0701	-0.1058	0.0411	0.0074	0.2232	-0.0061	0.0142	0.1575	0.2045
Sway disp.	-0.2607	1	0.1764	-0.66	-0.2218	-0.1718	0.0864	-0.0189	0.1601	-0.0369	-0.0682	-0.0467	0	-0.0344	0	0	-0.0218	-0.0235
Heave disp.	-0.3348	0.1764	1	-0.1872	-0.0521	-0.1467	0.6908	-0.3392	0	0.5177	0.6413	0.468	0	-0.4576	0.0262	0	-0.3152	-0.3912
Roll disp.	0.114	-0.66	-0.1872	1	0.3985	0.5551	-0.0196	0.1279	-0.4142	-0.0358	-0.063	0.0534	0.0052	0.2505	-0.0101	0.0137	0.1753	0.2324
Pitch disp.	0.3669	-0.2218	-0.0521	0.3985	1	0.4423	0.0168	0.2027	-0.52	-0.0304	-0.0612	0.1482	0.0154	0.4298	-0.0101	0.0325	0.3029	0.386
Yaw disp.	0.1432	-0.1718	-0.1467	0.5551	0.4423	1	-0.1553	0.1111	-0.6007	-0.0744	-0.2125	0	0.0148	0.5422	-0.0187	0.0274	0.3823	0.4973
Surge vel.	-0.1163	0.0864	0.6908	-0.0196	0.0168	-0.1553	1	-0.3142	-0.1099	0.4814	0.917	0.5018	0	-0.4966	0.0367	0.02	0.3358	-0.4029
Sway vel.	0.021	-0.0189	-0.3392	0.1279	0.2027	0.1111	-0.3142	1	0	-0.8273	-0.3392	-0.3215	0	0.2131	-0.0103	0	0.1471	0.1768
Heave vel.	-0.1829	0.1601	0	-0.4142	-0.52	-0.6007	-0.1099	0	1	-0.1768	-0.0399	-0.2896	-0.0176	-0.4097	0.0065	-0.0355	-0.2896	-0.3551
Roll vel.	-0.0701	-0.0369	0.5177	-0.0358	-0.0304	-0.0744	0.4814	-0.8273	-0.1768	1	0.4836	0.7755	0	-0.1952	0.0138	0.0104	-0.1339	-0.1682
Pitch vel.	-0.1058	-0.0682	0.6413	-0.063	-0.0612	-0.2125	0.917	-0.3392	-0.0399	0.4836	1	0.461	0	-0.5781	0.0381	0.013	-0.3946	-0.4836
Yaw vel.	0.0411	-0.0467	0.468	0.0534	0.1482	0	0.5018	-0.3215	-0.2896	0.7755	0.461	1	0.0056	-0.0977	0.0135	0.0204	-0.0648	-0.0876
RtMEdg	0.0074	0	0	0.0052	0.0154	0.0148	0	0	-0.0176	0	0	0.0056	1	0.2652	0.9982	0.9967	0.7517	0.2651
RtMFlp	0.2232	-0.0344	-0.4576	0.2505	0.4298	0.5422	-0.4966	0.2131	-0.4097	-0.1952	-0.5781	-0.0977	0.2652	1	0.2079	0.3034	0.8351	0.98
Spn1Mx	-0.0061	0	0.0262	-0.0101	-0.0101	-0.0187	0.0367	-0.0103	0.0065	0.0138	0.0381	0.0135	0.9982	0.2079	1	0.9929	0.7115	0.2096
Spn2Mx	0.0142	0	0	0.0137	0.0325	0.0274	0.02	0	-0.0355	0.0104	0.013	0.0204	0.9967	0.3034	0.9929	1	0.7758	0.3137
Spn1My	0.1575	-0.0218	-0.3152	0.1753	0.3029	0.3823	0.3358	0.1471	-0.2896	-0.1339	-0.3946	-0.0648	0.7517	0.8351	0.7115	0.7758	1	0.8216
Spn2My	0.2045	-0.0235	-0.3912	0.2324	0.386	0.4973	-0.4029	0.1768	-0.3551	-0.1682	-0.4836	-0.0876	0.2651	0.98	0.2096	0.3137	0.8216	1

**Table 39 – Correlation matrix for tower loads with misaligned wind and wave inputs in rated conditions**

	Surge disp.	Sway disp.	Heave disp.	Roll disp.	Pitch disp.	Yaw disp.	Surge vel.	Sway vel.	Heave vel.	Roll vel.	Pitch vel.	Yaw vel.	TwrBsMx	TwrBsMy	TwrHtMx	TwrHtMy
Surge disp.	1	0.0231	-0.5885	0	0.396	0	-0.0888	0	0.0222	0	-0.2496	0	0	0.4772	0	0.4764
Sway disp.	0.0231	1	0.0076	-0.9761	0.0343	-0.4494	0.0253	0	-0.9592	-0.1195	0.0694	-0.7353	-0.8929	0.0665	-0.892	0.0734
Heave disp.	-0.5885	0.0076	1	0.0643	-0.2814	0.5295	-0.064	0.6975	0	-0.6869	0.0539	-0.3281	-0.0112	-0.4224	-0.0116	-0.4228
Roll disp.	0	-0.9761	0.0643	1	-0.0188	0.5763	-0.0063	0.1208	0.9552	0	-0.0529	0.6842	0.8932	-0.0548	0.8922	-0.0617
Pitch disp.	0.396	0.0343	-0.2814	-0.0188	1	-0.0137	0.3487	-0.0209	0.0123	0.0132	-0.1942	0.0106	0	0.9199	0	0.9157
Yaw disp.	0	-0.4494	0.5295	0.5763	-0.0137	1	0.0116	0.7111	0.436	-0.6548	-0.0288	0	0.31	-0.0996	0.3087	-0.1044
Surge vel.	-0.0888	0.0253	-0.064	-0.0063	0.3487	0.0116	1	0	-0.1044	0	0.3756	-0.0165	-0.015	0.5166	-0.0153	0.5194
Sway vel.	0	0	0.6975	0.1208	-0.0209	0.7111	0	1	0.015	-0.988	0	-0.3435	0	-0.1428	0	-0.1452
Heave vel.	0.0222	-0.9592	0	0.9552	0.0123	0.436	-0.1044	0.015	1	0.1064	-0.1318	0.7367	0.8989	-0.0382	0.8982	-0.0454
Roll vel.	0	-0.1195	-0.6869	0	0.0132	-0.6548	0	-0.988	0.1064	1	-0.0207	0.4732	0.1076	0.1287	0.1081	0.13
Pitch vel.	-0.2496	0.0694	0.0539	-0.0529	-0.1942	-0.0288	0.3756	0	-0.1318	-0.0207	1	-0.0798	-0.0679	-0.1442	-0.0684	-0.1436
Yaw vel.	0	-0.7353	-0.3281	0.6842	0.0106	0	-0.0165	-0.3435	0.7367	0.4732	-0.0798	1	0.6616	0	0.6611	0
TwrBsMx	0	-0.8929	-0.0112	0.8932	0	0.31	-0.015	0	0.8989	0.1076	-0.0679	0.6616	1	-0.0202	1	-0.0256
TwrBsMy	0.4772	0.0665	-0.4224	-0.0548	0.9199	-0.0996	0.5166	-0.1428	-0.0382	0.1287	-0.1442	0	-0.0202	1	-0.02	0.9999
TwrHtMx	0	-0.892	-0.0116	0.8922	0	0.3087	-0.0153	0	0.8982	0.1081	-0.0684	0.6611	1	-0.02	1	-0.0254
TwrHtMy	0.4764	0.0734	-0.4228	-0.0617	0.9157	-0.1044	0.5194	-0.1452	-0.0454	0.13	-0.1436	0	-0.0256	0.9999	-0.0254	1

**Table 40 – Correlation matrix for blade loads in misaligned wind and wave inputs in rated conditions**

	Surge disp.	Sway disp.	Heave disp.	Roll disp.	Pitch disp.	Yaw disp.	Surge vel.	Sway vel.	Heave vel.	Roll vel.	Pitch vel.	Yaw vel.	RtMEdg	RtMFjp	Spn1Mx	Spn2Mx	Spn1My	Spn2My
Surge disp.	1	0.0231	-0.5885	0	0.396	0	-0.0888	0	0.0222	0	-0.2496	0	0.0127	0.2987	0	0.0191	0.1995	0.2504
Sway disp.	0.0231	1	0.0076	-0.9761	0.0343	-0.4494	0.0253	0	-0.9592	-0.1195	0.0694	-0.7353	0	0.0179	0	0.0058	0.0141	0.0246
Heave disp.	-0.5885	0.0076	1	0.0643	-0.2814	0.5295	-0.064	0.6975	0	-0.6869	0.0539	-0.3281	-0.0139	-0.2642	0	-0.0226	-0.1793	-0.228
Roll disp.	0	-0.9761	0.0643	1	-0.0188	0.5763	-0.0063	0.1208	0.9552	0	-0.0529	0.6842	0	0	0	0	0	0
Pitch disp.	0.396	0.0343	-0.2814	-0.0188	1	-0.0137	0.3487	-0.0209	0.0123	0.0132	-0.1942	0.0106	0.025	0.455	0	0.0491	0.3113	0.4138
Yaw disp.	0	-0.4494	0.5295	0.5763	-0.0137	1	0.0116	0.7111	0.436	-0.6548	-0.0288	0	0	-0.0288	0	0	-0.0196	-0.0226
Surge vel.	-0.0888	0.0253	-0.064	-0.0063	0.3487	0.0116	1	0	-0.1044	0	0.3756	-0.0165	0.0379	0.4484	0.0163	0.0746	0.3219	0.4586
Sway vel.	0	0	0.6975	0.1208	-0.0209	0.7111	0	1	0.015	-0.988	0	-0.3435	-0.0059	-0.0834	0	-0.0084	-0.0572	-0.0676
Heave vel.	0.0222	-0.9592	0	0.9552	0.0123	0.436	-0.1044	0.015	1	0.1064	-0.1318	0.7367	0	-0.0128	0	-0.0066	-0.0113	-0.0249
Roll vel.	0	-0.1195	-0.6869	0	0.0132	-0.6548	0	-0.988	0.1064	1	-0.0207	0.4732	0.0061	0.0798	0	0.0083	0.0549	0.0634
Pitch vel.	-0.2496	0.0694	0.0539	-0.0529	-0.1942	-0.0288	0.3756	0	-0.1318	-0.0207	1	-0.0798	0	-0.0645	0.0055	0.0083	-0.037	-0.0221
Yaw vel.	0	-0.7353	-0.3281	0.6842	0.0106	0	-0.0165	-0.3435	0.7367	0.4732	-0.0798	1	0	0.0172	0	0.012	0.005	
RtMEdg	0.0127	0	-0.0139	0	0.025	0	0.0379	-0.0059	0	0.0061	0	0	1	0.3032	0.9988	0.9955	0.7887	0.2814
RtMFjp	0.2987	0.0179	-0.2642	0	0.455	-0.0288	0.4484	-0.0834	-0.0128	0.0798	-0.0645	0.0172	0.3032	1	0.2566	0.3733	0.8245	0.9709
Spn1Mx	0	0	0	0	0	0	0.0163	0	0	0	0.0055	0	0.9988	0.2566	1	0.9908	0.758	0.2366
Spn2Mx	0.0191	0.0058	-0.0226	0	0.0491	0	0.0746	-0.0084	-0.0066	0.0083	0.0083	0	0.9955	0.3733	0.9908	1	0.8314	-0.3611
Spn1My	0.1995	0.0141	-0.1793	0	0.3113	-0.0196	0.3219	-0.0572	-0.0113	0.0549	-0.037	0.012	0.7887	0.8245	0.758	0.8314	1	0.7955
Spn2My	0.2504	0.0246	-0.228	0	0.4138	-0.0226	0.4586	-0.0676	-0.0249	0.0634	-0.0221	0.005	0.2814	0.9709	0.2366	0.3611	0.7955	1

**A1.13.2. Above-rated**

In the following four figures the above-rated wind turbine conditions are used: 18 m/s wind and 4.09 m and 15.33 s significant wave height and wave peak spectral period.

**Table 41 – Correlation matrix for tower loads in aligned wind and wave inputs in above-rated conditions**

	Surge disp.	Sway disp.	Heave disp.	Roll disp.	Pitch disp.	Yaw disp.	Surge vel.	Sway vel.	Heave vel.	Roll vel.	Pitch vel.	Yaw vel.	TwrBsMx	TwrBsMy	TwHt1Mx	TwHt1My
Surge disp.	1	0.0066	0.006	-0.0316	0.6671	0.0825	-0.0304	0.3732	-0.6688	-0.3889	-0.0811	-0.4805	-0.115	0.6446	-0.1008	0.6429
Sway disp.	0.0066	1	0.0488	-0.9707	0.2658	-0.2914	-0.2173	-0.0088	0.1003	-0.0233	-0.2344	-0.0538	-0.6869	0.0914	-0.6694	0.0925
Heave disp.	0.006	0.0488	1	-0.0209	0.119	0.6686	0.869	-0.2014	0	0.2215	0.786	0.1749	-0.2515	-0.1239	-0.2715	-0.1295
Roll disp.	-0.0316	-0.9707	-0.0209	1	-0.2397	0.3422	0.2464	0.0396	-0.1171	-0.006	0.2695	0.0453	0.6958	-0.0685	0.6777	-0.0698
Pitch disp.	0.6671	0.2658	0.119	-0.2397	1	0.1054	0.0651	0.4439	-0.7159	-0.4763	-0.0065	-0.5689	-0.3006	0.8081	-0.2826	0.8057
Yaw disp.	0.0825	-0.2914	0.6686	0.3422	0.1054	1	0.7355	0.0991	-0.1997	-0.0784	0.7192	-0.0058	0	0.167	-0.0104	0.1629
Surge vel.	-0.0304	-0.2173	0.869	0.2464	0.0651	0.7355	1	-0.046	0.0091	0.1001	0.9756	0.3122	-0.1035	-0.1728	-0.1319	-0.1794
Sway vel.	0.3732	-0.0088	-0.2014	0.0396	0.4439	0.0991	-0.046	1	-0.2252	-0.9894	-0.0103	-0.3155	-0.0269	0.3804	-0.0168	0.3798
Heave vel.	-0.6688	0.1003	0	-0.1171	-0.7159	-0.1997	0.0091	-0.2252	1	0.2752	0.0876	0.6442	0.0391	-0.8717	0.0209	-0.8704
Roll vel.	-0.3889	-0.0233	0.2215	-0.006	-0.4763	-0.0784	0.1001	-0.9894	0.2752	1	0.0756	0.425	0.0354	-0.424	0.0221	-0.424
Pitch vel.	-0.0811	-0.2344	0.786	0.2695	-0.0065	0.7192	0.9756	-0.0103	0.0876	0.0756	1	0.3701	-0.0801	-0.2405	-0.1099	0.247
Yaw vel.	-0.4805	-0.0538	0.1749	0.0453	-0.5689	-0.0058	0.3122	-0.3155	0.6442	0.425	0.3701	1	-0.0215	-0.6215	-0.0473	-0.6234
TwrBsMx	-0.115	-0.6869	-0.2515	0.6958	-0.3006	0	-0.1035	-0.0269	0.0391	0.0354	-0.0801	-0.0215	1	-0.1281	0.9988	-0.1259
TwrBsMy	0.6446	0.0914	-0.1239	-0.0685	0.8081	0.167	-0.1728	0.3804	-0.8717	-0.424	-0.2405	-0.6215	-0.1281	1	-0.102	1
TwHt1Mx	-0.1008	-0.6694	-0.2715	0.6777	-0.2826	-0.0104	-0.1319	-0.0168	0.0209	0.0221	-0.1099	-0.0473	0.9988	-0.102	1	-0.0995
TwHt1My	0.6429	0.0925	-0.1295	-0.0698	0.8057	0.1629	-0.1794	0.3798	-0.8704	-0.424	0.247	-0.6234	-0.1259	1	-0.0995	1

**Table 42 – Correlation matrix for blade loads in aligned wind and wave inputs in above-rated conditions**

	Surge disp.	Sway disp.	Heave disp.	Roll disp.	Pitch disp.	Yaw disp.	Surge vel.	Sway vel.	Heave vel.	Roll vel.	Pitch vel.	Yaw vel.	RtMEdg	RtMFlp	Spn1Mx	Spn2Mx	Spn1My	Spn2My
Surge disp.	1	0.0066	0.006	-0.0316	0.6671	0.0825	-0.0304	0.3732	-0.6688	-0.3889	-0.0811	-0.4805	-0.0286	0.3313	-0.06	-0.0641	0.238	0.3146
Sway disp.	0.0066	1	0.0488	-0.9707	0.2658	-0.2914	-0.2173	-0.0088	0.1003	-0.0233	-0.2344	-0.0538	-0.0065	0.1682	-0.0221	-0.0203	0.1254	0.1767
Heave disp.	0.006	0.0488	1	-0.0209	0.119	0.6686	0.869	-0.2014	0	0.2215	0.786	0.1749	0.0319	-0.4353	0.075	0.0855	-0.317	-0.4312
Roll disp.	-0.0316	-0.9707	-0.0209	1	-0.2397	0.3422	0.2464	0.0396	-0.1171	-0.006	0.2695	0.0453	0.0071	-0.1633	0.0225	0.0217	-0.1213	-0.1705
Pitch disp.	0.6671	0.2658	0.119	-0.2397	1	0.1054	0.0651	0.4439	-0.7159	-0.4763	-0.0065	-0.5689	-0.0283	0.464	-0.071	-0.0677	0.3412	0.4778
Yaw disp.	0.0825	-0.2914	0.6686	0.3422	0.1054	1	0.7355	0.0991	-0.1997	-0.0784	0.7192	-0.0058	0.0184	-0.1451	0.0345	0.0478	-0.0986	-0.1196
Surge vel.	-0.0304	-0.2173	0.869	0.2464	0.0651	0.7355	1	-0.046	0.0091	0.1001	0.9756	0.3122	0.0394	-0.5197	0.0909	0.1046	-0.3777	-0.5079
Sway vel.	0.3732	-0.0088	-0.2014	0.0396	0.4439	0.0991	-0.046	1	-0.2252	-0.9894	-0.1013	-0.3155	-0.0161	0.2703	-0.0414	-0.0412	0.2012	0.2915
Heave vel.	-0.6688	0.1003	0	-0.1171	-0.7159	-0.1997	0.0091	-0.2252	1	0.2752	0.0876	0.6442	0.0315	-0.5451	0.0818	0.0782	-0.4032	-0.559
Roll vel.	-0.3889	-0.0233	0.2215	-0.006	-0.4763	-0.0784	0.1001	-0.9894	0.2752	1	0.0756	0.425	0.0197	-0.3323	0.0511	0.0518	-0.2473	-0.3578
Pitch vel.	-0.0811	-0.2344	0.786	0.2695	-0.0065	0.7192	0.9756	-0.1013	0.0876	0.0756	1	0.3701	0.0416	-0.5477	0.0957	0.1094	0.3975	-0.5308
Yaw vel.	-0.4805	-0.0538	0.1749	0.0453	-0.5689	-0.0058	0.3122	-0.3155	0.6442	0.425	0.3701	1	0.0392	-0.6069	0.0972	0.1024	-0.4497	-0.6507
RtMEdg	-0.0286	-0.0065	0.0319	0.0071	-0.0283	0.0184	0.0394	-0.0161	0.0315	0.0197	0.0416	0.0392	1	0.3471	0.9963	0.996	0.6947	-0.0563
RtMFlp	0.3313	0.1682	-0.4353	-0.1633	0.464	-0.1451	-0.5197	0.2703	-0.5451	-0.3323	-0.5477	-0.6069	0.3471	1	0.2651	0.2726	0.9154	0.8992
Spn1Mx	-0.06	-0.0221	0.075	0.0225	-0.071	0.0345	0.0909	-0.0414	0.0818	0.0511	0.0957	0.0972	0.9963	0.2651	1	0.9993	0.6303	-0.1401
Spn2Mx	-0.0641	-0.0203	0.0855	0.0217	-0.0677	0.0478	0.1046	-0.0412	0.0782	0.0518	0.1094	0.996	0.2726	0.9993	1	0.6361	-0.1287	0.6687
Spn1My	0.238	0.1254	-0.317	-0.1213	0.3412	-0.0986	-0.3777	0.2012	-0.4032	-0.2473	0.3975	-0.4497	0.6947	0.9154	0.6303	0.6361	1	0.6687
Spn2My	0.3146	0.1767	-0.4312	-0.1705	0.4778	-0.1196	-0.5079	0.2915	-0.559	-0.3578	-0.5308	-0.6507	-0.0563	0.8992	-0.1401	-0.1287	0.6687	1

**Table 43 – Correlation matrix for tower loads in misaligned wind and wave inputs in above-rated conditions**

	Surge disp.	Sway disp.	Heave disp.	Roll disp.	Pitch disp.	Yaw disp.	Surge vel.	Sway vel.	Heave vel.	Roll vel.	Pitch vel.	Yaw vel.	TwrBsMx	TwrBsMy	TwrHtMx	TwrHtMy
Surge disp.	1	0.0859	-0.028	-0.0326	0.2933	-0.0301	-0.2003	0	0.0218	0	-0.099	0	-0.0147	0.2065	-0.0146	0.2019
Sway disp.	0.0859	1	0.0542	-0.9881	0.0488	-0.6864	0	0	-0.9616	0.0095	0.0659	-0.622	-0.8999	0.0223	-0.8992	0.0251
Heave disp.	-0.028	0.0542	1	-0.0796	0	0.5695	-0.0707	0.9216	0	-0.9051	-0.0773	-0.6496	-0.0387	-0.0154	-0.0381	0
Roll disp.	-0.0326	-0.9881	-0.0796	1	-0.0706	0.6843	-0.0212	-0.0097	0.9672	0	-0.0352	0.6414	0.9197	-0.0439	0.919	-0.047
Pitch disp.	0.2933	0.0488	0	-0.0706	1	-0.0619	-0.0183	-0.0298	0.0399	0.015	-0.0292	-0.0085	-0.033	0.9201	-0.0328	0.9146
Yaw disp.	-0.0301	-0.6864	0.5695	0.6843	-0.0619	1	0.0258	0.6457	0.7036	-0.6502	0.0251	0	0.5736	-0.0508	0.5733	-0.0442
Surge vel.	-0.2003	0	-0.0707	-0.0212	-0.0183	0.0258	1	0.051	-0.0778	-0.0541	0.8696	-0.0921	-0.0589	0.0825	-0.0589	0.0833
Sway vel.	0	0	0.9216	-0.0097	-0.0298	0.6457	0.051	1	0.042	-0.9982	0.0558	-0.6067	0	-0.0534	0	-0.0412
Heave vel.	0.0218	-0.9616	0	0.9672	0.0399	0.7036	-0.0778	0.042	1	-0.0496	-0.0909	0.624	0.9269	0.0546	0.9264	0.0516
Roll vel.	0	0.0095	-0.9051	0	0.015	-0.6502	-0.0541	-0.9982	-0.0496	1	-0.0618	0.5983	-0.0075	0.0397	-0.008	0.0275
Pitch vel.	-0.099	0.0659	-0.0773	-0.0352	-0.0292	0.0251	0.8696	0.0558	-0.0909	-0.0618	1	-0.1099	-0.0757	0.0586	-0.0757	0.0588
Yaw vel.	0	-0.622	-0.6496	0.6414	-0.0085	0	-0.0921	-0.6067	0.624	0.5983	-0.1099	1	0.6248	0.0147	0.6241	0
TwrBsMx	-0.0147	-0.8999	-0.0387	0.9197	-0.033	0.5736	-0.0589	0	0.9269	-0.0075	-0.0757	0.6248	1	-0.0074	1	-0.0107
TwrBsMy	0.2065	0.0223	-0.0154	-0.0439	0.9201	-0.0508	0.0825	-0.0534	0.0546	0.0397	0.0586	0.0147	-0.0074	1	-0.0072	0.9998
TwrHtMx	-0.0146	-0.8992	-0.0381	0.919	-0.0328	0.5733	-0.0589	0	0.9264	-0.008	-0.0757	0.6241	1	-0.0072	1	-0.0105
TwrHtMy	0.2019	0.0251	0	-0.047	0.9146	-0.0442	0.0833	-0.0412	0.0516	0.0275	0.0588	0	-0.0107	0.9998	-0.0105	1

**Table 44 – Correlation matrix for blade loads in misaligned wind and wave inputs in above-rated conditions**

	Surge disp.	Sway disp.	Heave disp.	Roll disp.	Pitch disp.	Yaw disp.	Surge vel.	Sway vel.	Heave vel.	Roll vel.	Pitch vel.	Yaw vel.	RtMEdg	RtMFlp	Spn1Mx	Spn2Mx	Spn1My	Spn2My
Surge disp.	1	0.0859	-0.028	-0.0326	0.2933	-0.0301	-0.2003	0	0.0218	0	-0.099	0	-0.0085	-0.1058	0	-0.0118	-0.0732	-0.1695
Sway disp.	0.0859	1	0.0542	-0.9881	0.0488	-0.6864	0	0	-0.9616	0.0095	0.0659	-0.622	0	-0.028	0	0	-0.0149	-0.0256
Heave disp.	-0.028	0.0542	1	-0.0796	0	0.5695	-0.0707	0.9216	0	-0.9051	-0.0773	-0.6496	0	-0.0243	0	0	-0.0149	0.029
Roll disp.	-0.0326	-0.9881	-0.0796	1	-0.0706	0.6843	-0.0212	-0.0097	0.9672	0	-0.0352	0.6414	0	0.0191	0	0	0.012	0.0158
Pitch disp.	0.2933	0.0488	0	-0.0706	1	-0.0619	-0.0183	-0.0298	0.0399	0.015	-0.0292	-0.0085	0.1844	-0.0201	-0.0198	0.103	0.1969	
Yaw disp.	-0.0301	-0.6864	0.5695	0.6843	-0.0619	1	0.0258	0.6457	0.7036	-0.6502	0.0251	0	0	0	0	0	0	0
Surge vel.	-0.2003	0	-0.0707	-0.0212	-0.0183	0.0258	1	0.051	-0.0778	-0.0541	0.8696	-0.0921	0.005	0.1488	0	0.0055	0.1004	0.2759
Sway vel.	0	0	0.9216	-0.0097	-0.0298	0.6457	0.051	1	0.042	-0.9982	0.0558	-0.6067	0	-0.0454	0	0	-0.0268	-0.0454
Heave vel.	0.0218	-0.9616	0	0.9672	0.0399	0.7036	-0.0778	0.042	1	-0.0496	-0.0909	0.624	0	0.034	0	0	0.0201	0.0268
Roll vel.	0	0.0095	-0.9051	0	0.015	-0.6502	-0.0541	-0.9982	-0.0496	1	-0.0618	0.5983	0	0.041	0	0	0.0242	0.0398
Pitch vel.	-0.099	0.0659	-0.0773	-0.0352	-0.0292	0.0251	0.8696	0.0558	-0.0909	-0.0618	1	-0.1099	0	0.1182	0	0	0.0823	0.241
Yaw vel.	0	-0.622	-0.6496	0.6414	-0.0085	0	-0.0921	-0.6067	0.624	0.5983	-0.1099	1	0	0.0369	0	0	0.0219	0.0296
RtMEdg	-0.0085	0	0	0	-0.0088	0	0.005	0	0	0	0	0	1	0.5995	0.999	0.9995	0.873	-0.0171
RtMFlp	-0.1058	-0.028	-0.0243	0.0191	0.1844	0	0.1488	-0.0454	0.034	0.041	0.1182	0.0369	0.5995	1	0.5628	0.5862	0.9131	0.7549
Spn1Mx	0	0	0	0	-0.0201	0	0	0	0	0	0	0	0.999	0.5628	1	0.9993	0.8502	-0.06
Spn2Mx	-0.0118	0	0	0	-0.0198	0	0.0055	0	0	0	0	0	0.9995	0.5862	0.9993	1	0.8649	-0.0296
Spn1My	-0.0732	-0.0172	-0.0149	0.012	0.103	0	0.1004	-0.0268	0.0201	0.0242	0.0823	0.0219	0.873	0.9131	0.8502	0.8649	1	0.4566
Spn2My	-0.1695	-0.0256	0.029	0.0158	0.1969	0	0.2759	-0.0454	0.0268	0.0398	0.241	0.0296	-0.0171	0.7549	-0.06	-0.0296	0.4566	1